Reduction of Lead Free Solder Aging Effects
Using Doped SAC Alloys

by

Zijie Cai

A dissertation submitted to the Graduate Faculty of
Auburn University
in partial fulfillment of the
requirements for the Degree of
Doctor of Philosophy

Auburn, Alabama
December 8, 2012

Keywords: lead-free solder, aging, dopant, constitutive models,
mechanical properties, microstructure

Approved by

Jeffrey C. Suhling, Chair, Quina Distinguished Professor of Mechanical Engineering
Pradeep Lall, Thomas Walter Professor of Mechanical Engineering
John L. Evans, Thomas Walter Professor of Industrial and Systems Engineering
Michael J. Bozack, Professor of Physics

Abstract

The microstructure, mechanical response, and failure behavior of lead free solder joints in electronic assemblies are constantly evolving when exposed to isothermal aging and/or thermal cycling environments. Large degradations that occur in the material properties (stiffness and strength) and creep behavior of Sn-Ag-Cu (SAC) lead free solders during aging have been demonstrated in the past several years. These effects are universally detrimental to reliability and are exacerbated as the aging temperature and aging time increases. Conversely, changes due to aging are relatively small in conventional Sn-Pb solders.

In an attempt to reduce the aging induced degradation of the material behavior of SAC solders, several doped SAC-X alloys have been explored and studied. The doped materials are lead free SAC solders that have been modified by the addition of small percentages of one or more additional elements (X). Using dopants (e.g. Bi, In, Ge, Ni, La, Mg, Mn, Ce, Co, Ti, Zn, Fe, etc.) has become widespread to enhance shock/drop reliability, wetting, and other properties; and this approach has been extended to examine the ability of dopants to reduce the effects of aging and extend thermal cycling reliability. In this research, four popular doped lead free solder alloys, including SACX0307 (SAC-X, where X is 0.1%Bi), SAC-Zn (0.21%Zn), SN100C (0.05%Ni + 0.01%Ge) and SN96CI (0.05%Co), have been scrutinized. Also, the enhancement of aging resistance of doped lead free solders has been explored when compared to corresponding reference

SAC alloys (SAC105, SAC205, SAC3595, Sn-0.7Cu, SAC3810).

The effects of aging on mechanical behavior have been examined by performing stress-strain and creep tests on solder samples that were aged for various durations (0-12 months) at room temperature (25 ^{o}C), and several elevated temperatures (50, 75, 100, and 125 ^{o}C). For all of the solders, variations of the mechanical and creep properties (effective modulus, yield stress, ultimate strength, creep compliance, etc.) were observed and modeled as a function of aging time and aging temperature. The doped SAC-X alloys illustrated reduced degradations with aging for all of the aging temperatures considered. Also, the stress-strain and creep mechanical properties of doped solders are better than those of reference solders after short durations of aging. After long term aging, doped solder alloys were found to have more stable behaviors than those of the standard SAC alloys.

A parallel microstructure study has shown that aging effects have significant influence on phase coarsening and degradation, grain/sub-grain growth and internal residual stress relaxation. However, the changes in microstructure have been demonstrated to be smaller in doped solder materials when compared to non-doped solders after severe aging.

Acknowledgments

I would like to heartily express my gratitude to my major advisor Dr. Jeffrey C. Suhling for the support, guidance and mentorship throughout this research. Sincere appreciation is sent to my advisory committee members including Dr. Pradeep Lall, Dr. John L. Evans, and Dr. Michael J. Bozack for their insightful instruction and discussion regarding this research. Special thanks are also extended to all my co-workers and friends, Dr. Hongtao Ma, Dr. Chang Lin, Dr. Yifei Zhang, Jordan Roberts, Mohammad Motalab, Muhannad Mustafa, Nusratjahan Chhanda, Safina Hussain, Kun-yen Wang, Michael Palmer and John Marcell for their help, encouragement and friendship.

I am in debt to my parents, Longhai Cai and Qiu Li, for their endless love and support to my life and study in the United States. Lastly, I solemnly dedicate this dissertation and all achievements in pursuit of doctoral degree to my wife, Wenrui Bi and daughter Veronica Qinxin Cai, for their endurance, perseverance and heartfelt consideration.

Table of Contents

List of Tables

List of Figures

CHAPTER 1

INTRODUCTION

1.1 Lead Free Solders in Microelectronics

Throughout the history of electronics packaging, eutectic 63Sn-37Pb has been the most extensively used soldering alloy. This eutectic Sn-Pb solder has a relatively low melting temperature (183 ℃), features excellent ductility and outstanding reliability, and provides superior wettability and compatibility with most substrates and devices [1, 2].

However, despite the advantages of Sn-Pb solders, they have been prohibited in many countries due to environmental and health concern [3-6]. The Waste Electrical and Electronic Equipment (WEEE), Restriction of Hazardous Substances (RoHs), and European Commission's (EC) draft directives have approved banning the use of lead in electronics effective in July 2006 in European Union countries [5]. Furthermore, several Japanese electronics manufacturers have successfully created a market differentiation and increased market share based on "green" products that use Pb-free solders [7]. Therefore, the conversion to Pb-free solders in the global electronics assembly business appears imminent [8].

As a result, efforts to develop alternatives to Pb-bearing solders have been continuously increasing in recent years. Although there is no standard for the "perfect" replacement for eutectic Sn-Pb, some must-have features are still required. In general, good candidates are expected to have [9]:

- physical behavior (melting temperature, etc) similar to eutectic Sn-Pb
- adequate wettability for the metallization used in the electronics industry
- good fatigue resistance, electrical performance and reliability
- compatibility with existing liquid flux systems
- adequate shelf life and performance as a solder paste
- low dross formation when used in a wave soldering operation
- low cost

So far, approximately 70 Pb-free solder alloy compositions have been proposed, including binary, ternary and even quaternary alloys [10]. Among them, the majority of the alloys are Sn-based alloys, that is, Sn is the preferred major constituant. Even though researchers still have not indentified any "drop in" replacements for eutectic Sn-Pb solder in all applications, alloys involving elements such as Sn, Ag, Cu, Bi, and Zn have been recognized as promising candidates. In fact, Sn-rich lead free alloys have occupied more than 80% in the wave solder market share and more than 90% in the reflow solder market share (Figure 1.1) [11].

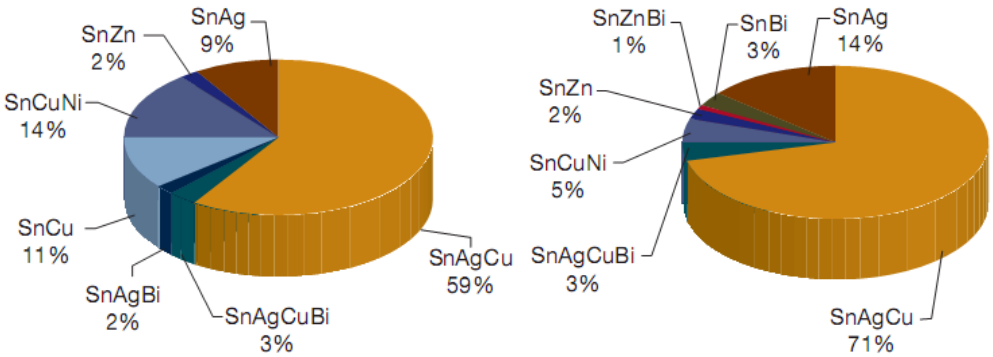

(a) Wave Solders (b) Reflow Solders

Figure 1.1 Lead Free Solder Market Share [11]

1.2 Prevailing Lead Free Choices

As illustrated in Figure 1.1, Sn-based lead free solders are widely used and have been regarded as the best option for replacing eutectic Sn-Pb solder thus far. Actually, most of these lead free candidates originate from binary alloy systems and some are further optimized by adding small amount of third chemical elements in order to lower the melting point and/or increase the wettability and reliability [12]. Figure 1.2 summarizes popular lead free choices available on the market and their current applications.

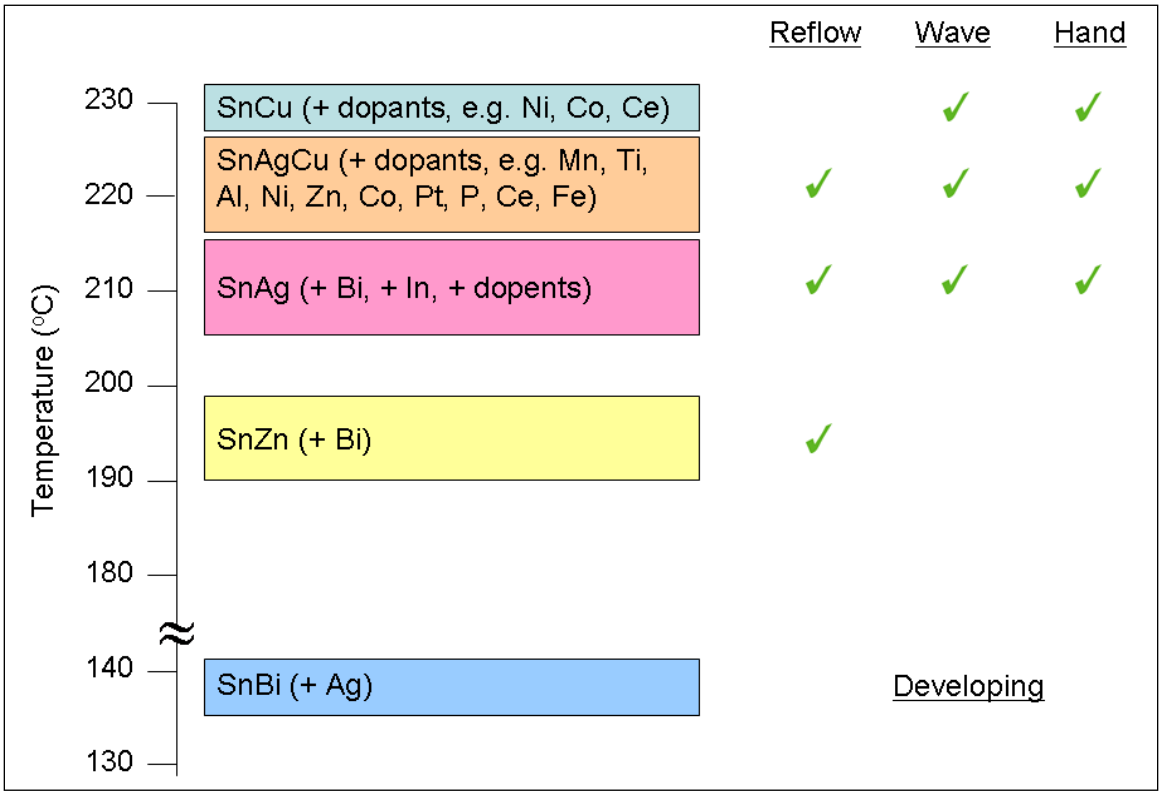

(Lee, C. N., Professional Development Course, ECTC 2011)

Figure 1.2 Prevailing Lead Free Choices and Their Applications

1.2.1 Sn-Cu System

The eutectic composition of binary Sn-Cu alloy is 99.3Sn-0.7Cu, with a melting temperature at 227 ^{o}C. According to the Sn-Cu binary phase diagram shown in Figure 1.3, Cu_6Sn_5 is the only intermetallic compound dispersed in the β-Sn matrix. This alloy is now mainly used in wave soldering, and might be suitable for high temperature applications required by the automotive industry. However, this solder material is easily contaminated and has unsatisfactory wettability as well as mechanical properties [13]. It also has low thermal resistance and is known for causing corrosion in equipment.

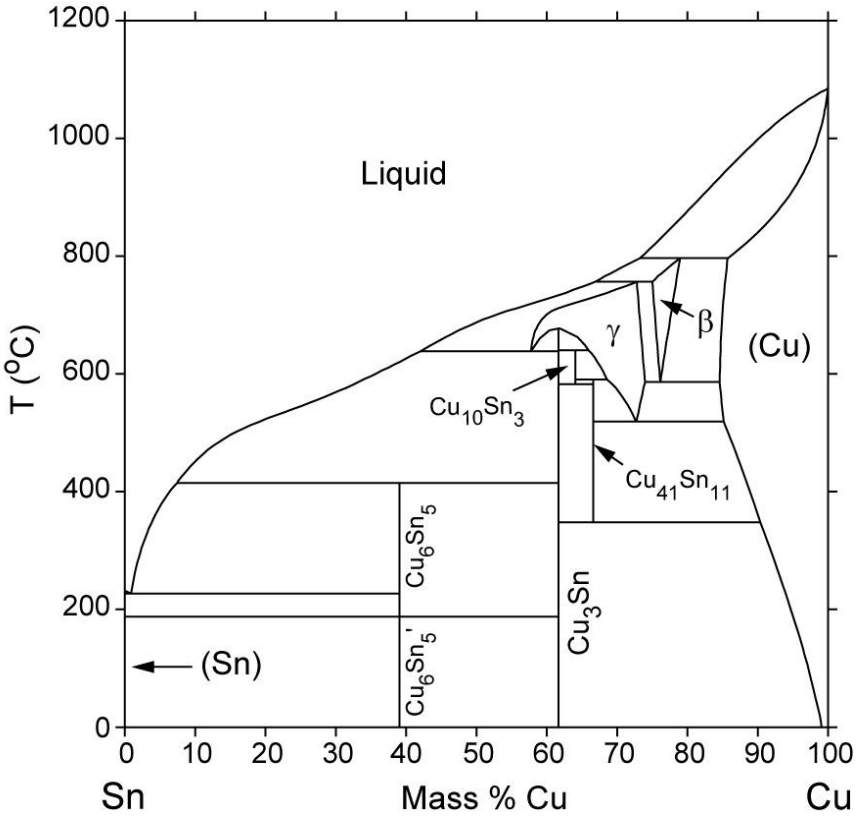

(http://www.metallurgy.nist.gov/phase/solder/cusn-w.jpg)

Figure 1.3 Sn-Cu Binary Phase Diagram

1.2.2 Sn-Ag System

The Sn-Ag binary system has a eutectic composition of 96.5Sn-3.5Ag in weight percentage and a eutectic temperature of 221 ℃. From the Sn-Ag binary phase diagram (Figure 1.4), the eutectic microstructure is composed of β-Sn matrix as primary phase with a eutectic dispersion of Ag_3Sn precipitates [14]. This alloy exhibits marginal wettability but strong joint strength [15]. However, when soldered to copper base metal, the diffusion rate for Cu from the Cu base into the solder is accelerated by high reflow temperatures as well as the concentration gradient of Sn between solder and base metal. As a result, a layer of brittle Cu_6Sn_5 intermetallics is often observed near the interface between Cu pads and bulk solder balls, which is known to be detrimental to the reliability of the electronic assembly.

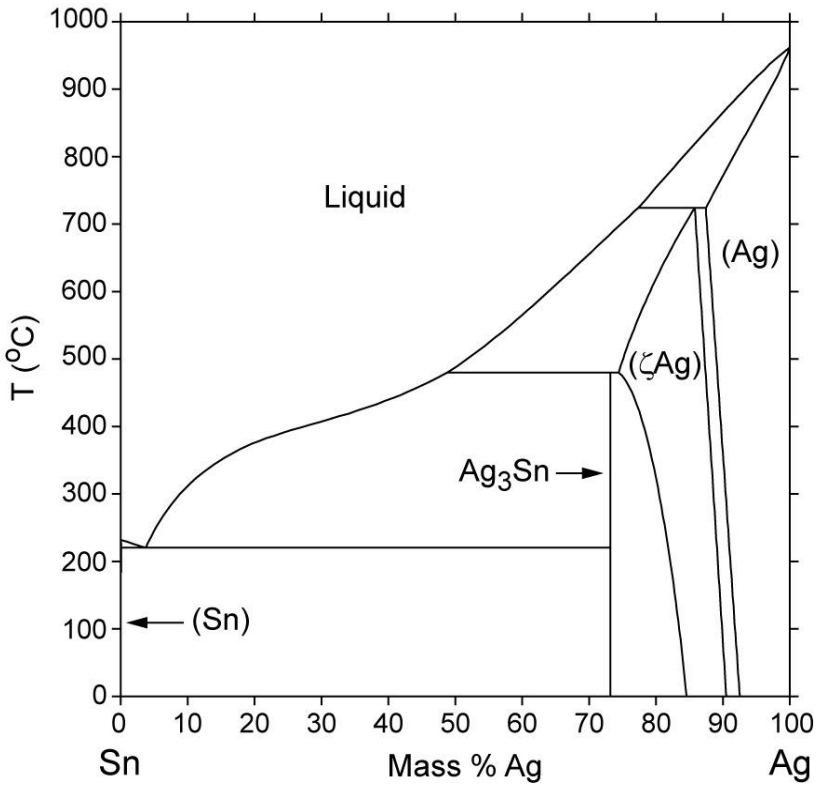

(http://www.metallurgy.nist.gov/phase/solder/agsn-w.jpg)

Figure 1.4 Sn-Ag Binary Phase Diagram

1.2.3 Sn-Zn System

The eutectic composition of the Sn-Zn binary system is 91Sn-9Zn with a melting temperature at 199 °C [13]. The lamellar microstructure consists of alternating Sn-rich and Zn-rich phases, which is similar to the eutectic Sn-Pb system. However, Zn-Cu phases are known to decrease the reliability of Sn-Zn/Cu assemblies. The presence of Zn in solder alloys easily leads to oxidation and corrosion due to the high oxidation potential of Zn. Zinc-containing solder alloys are also known to react with the flux medium. Despite the questionable compatibility with fluxes and storage stability, Sn-Zn solder has an average wettability in reflow soldering, and produces excessive dross in wave soldering.

1.2.4 Sn-Bi System

The Sn-Bi alloy has an eutectic composition of 42Sn-58Bi and a relatively low eutectic temperature of 139 ^{o}C. The low melting temperature makes the eutectic Sn-Bi alloy a promising replacement for Sn-Pb solders. Additionally, eutectic Sn-Bi solder has proven to have better manufacturability than Pb-Sn. However, Bi precipitates from the solder matrix aggregate along boundaries of grains through which cracking occurs. The segregation of Bi often results in unpredictable early failures of solder joints due to the embrittlement of the interface between the Cu trace and bulk Sn-Bi solder joint [16, 17].

1.2.5 Sn-Ag-Cu System

As shown in Figure 1.1, SnAgCu (SAC) has been the most popular, widely used lead free solder in today's market. Although they are still not indentified as the "drop in" replacement for all applications, a variety of SAC alloys with different chemical compositions have been the proposed by various user groups and industry experts. These

include: SAC105 (98.5Sn-1.0Ag-0.5Cu), SAC205 (97.5Sn-2.0Ag-0.5Cu), SAC305 (96.5Sn-3.0Ag-0.5Cu), and SAC405 (95.5Sn-4.0Ag-0.5Cu), known as the SACN05 series; SAC387 (95.5Sn-3.8Ag-0.7Cu), SAC396 (95.5Sn-3.9Ag-0.6Cu), and SAC357 (95.2Sn-3.5Ag-0.7Cu), identified as near eutectic SAC choices; SAC3810 (95.2Sn-3.8Ag-1.0Cu), SAC3595 (95.55Sn-3.5Ag-0.95Cu), SAC0307 (9Sn-0.3Ag-0.7Cu), and SAC107 (98.3Sn-1.0Ag-0.7Cu), designed for special needs such as high temperature application, drop and shock optimization, etc. The main benefits of the various SAC alloy systems are their relatively low melting temperatures compared with the 96.5Sn-3.5Ag binary eutectic alloy, as well as their superior mechanical and manufacturability properties when compared to other lead free solders [18].

It is known that the eutectic SAC alloy composition is near Sn-3.5Ag-0.9Cu, with a eutectic temperature at 217 ^{o}C [19, 20]. Figure 1.5 contains the Sn-Ag-Cu ternary phase diagram near the pure Sn side with an enlarged scale. The contours in the figure represent the isothermal lines. The red boxed region indicates the region containing SAC alloy compositions currently available on the market.

The ternary phase diagram also shows two possible precipitates near the eutectic SnAgCu region: Ag_3Sn and Cu_6Sn_5. The ternary eutectic microstructure of SAC solders consists of β-Sn dendrites (primary phase), eutectic Sn-Ag regions (needle-shape Ag_3Sn intermetallic dispersed within β-Sn matrix), and eutectic Sn-Cu regions (scallop-shape Cu_6Sn_5 intermetallic dispersed within β-Sn matrix), as shown in Figure 1.6. These interspersed fine intermetallic particles are capable of pinning and blocking the movement of dislocations, and will thus enhance mechanical strength and reliability of solder joints when compared to eutectic Sn-Pb alloy [21, 22].

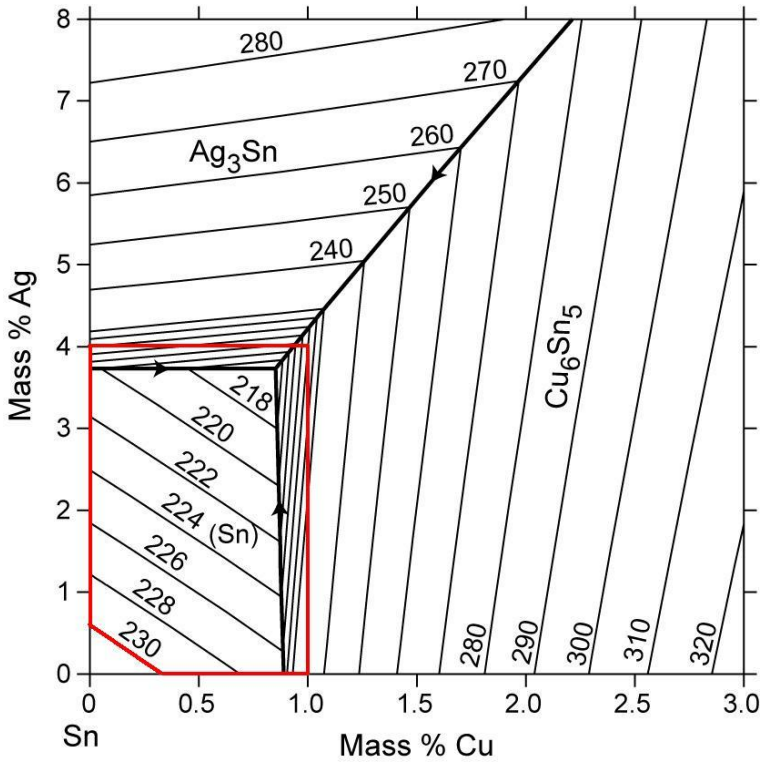

(http://www.metallurgy.nist.gov/phase/solder/agcusn-ll.jpg)

Figure 1.5 Sn-Ag-Cu Ternary Phase Diagram

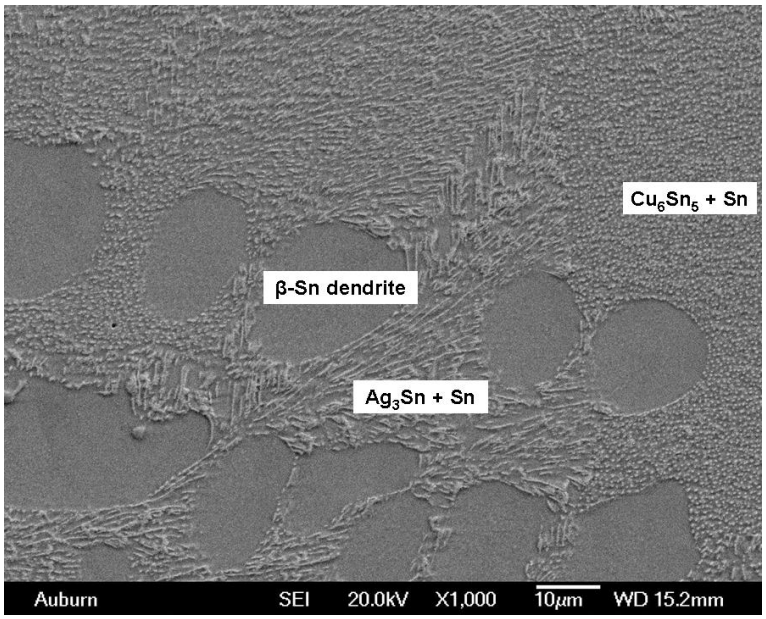

Figure 1.6 SEM Micrograph of Typical Sn-Ag-Cu Solder

Despite the benefits mentioned above, SAC family solders sometimes are still questionable as complete substitutes for eutectic Sn-Pb because of costs, some patent issues (particularly outside Europe), aesthetic consideration (dross problem of SAC solders), and relatively high melting temperature (217 ^{o}C vs. 183 ^{o}C).

1.2.6 Sn-Ag-Cu + X System

SnAgCu alloys have shown potential to be successful substitutes for eutectic Sn-Pb, however, the industry is still looking for a "perfect" solution. According to the results of many recent studies, performance characteristics of solder alloys are able to be optimized by doping, that is, by adding a small amount of other alloying elements into the SAC solder alloys.

The proposed doping element candidates include Bi, Ni, Co, Ge, Zn, La, Mg, Mn, Ce, Ti, Fe, In, B, etc. For example, adding 0.05% (wt.) Ni can successfully stabilize the microstructure, inhibit the excessive consumption of metal base and thus increase the reliability of the solder joints [23-25]. In addition, doping rear earth (RE) elements can significantly enhance wettability, refine microstructure and improve ductility of SAC alloys [26-29].

Even though dopants can greatly alter the mechanical, electrical and physical behavior of SAC solders, the effect on melting temperature, however, is found to be negligible. This is another advantage for doped solder alloys because manufacturers can still use the same processing conditions as conventional SAC alloys.

Meanwhile, the known issues for SAC-X solders are also apparent. For instance, the material properties and interfacial behavior of solder alloys have been demonstrated

to be very sensitive to the quantity of the X-additive. As a result, it takes much more time and cost to figure out the optimal composition levels for the dopants.

1.3 Mechanical Properties of Solder Materials

In electronics, solder joints are used to mount chips and components onto printed circuit boards (PCB) and thus create an electrical circuit. Therefore, an ideal solder material needs not only excellent conductivity to transmit signals, but also adequate strength to provide mechanical support and connection. Since most failures in electronic packages are caused by fatigue/fracture under certain thermal conditions [30], fully understanding of mechanical behavior of solder materials will be extremely critical.

1.3.1 Tensile

Tensile properties indicate how the material will react to forces being applied in tension. Although solder joints are rarely under pure tensile/compressive loading, tensile properties are still crucial indicators for design purposes. Through tensile tests, several material properties can be determined, such as effective modulus, yield strength (YS), ultimate tensile strength (UTS), elongation, etc. The tensile behavior of a solder material is usually described by a load vs. elongation curve, which is then converted into a stress vs. strain curve. It is often the case that engineering stress-strain curves are mostly employed because the physical size and shape changes of the material are neglected.

Figure 1.7 shows a typical engineering stress strain curve. In engineering practice, the engineering stress and engineering strain are defined as follows [31]:

$$\sigma_e = \frac{F}{A_0} \tag{1.1}$$

$$\varepsilon_e = \frac{\Delta L}{L} = \frac{L_f - L_0}{L_0} \tag{1.2}$$

where F is the applied force, A_0 the original (unstressed) cross-sectional area, L_f the final (current) gage length and L_0 the initial gage length.

Note that the stress and strain initially increase with a linear relationship. This is the linear-elastic portion of the curve where no plastic deformation has occurred. This means that when the stress is reduced, the material will return to its original shape. In this linear region, the material obeys the relationship defined by Hooke's Law where the ratio of stress to strain is a constant:

$$\sigma = E\varepsilon \tag{1.3}$$

where E is called the effective modulus, which is the slope of initial part of a stress-strain curve. However, since the effective modulus includes small inelastic deformations or time-dependent deformations such as creep, it is usually smaller than the dynamic modulus measured by the acoustic or ultrasonic wave method, which largely eliminates the inelastic deformation due to rapid wave propagation [33-35].

As strain progresses, many materials (e.g. solder) eventually deviate from this linear proportionality, the point of departure being termed the proportional limit. This nonlinearity is usually associated with stress-induced plastic flow in the specimen. At this stage the material is undergoing a rearrangement of its internal molecular or microscopic structure, in which atoms are being moved to new equilibrium positions. This plasticity requires a mechanism for molecular mobility, which in crystalline materials can arise from dislocation motion. A closely related term is the yield stress, denoted σ_{YS} in Figure 1.7; this is the stress needed to induce plastic deformation in the specimen. Since it is often difficult to pinpoint the exact stress at which plastic

deformation begins, the yield stress is usually taken to be the stress needed to induce a specified amount of permanent strain, typically 0.2%. By drawing a parallel line to the elastic portion of the engineering stress-strain curve but offset from the origin by 0.002 strain, this "0.2% offset yield stress" is then determined as the intersection between the stress-strain curve and the offset line.

The ultimate tensile strength (UTS) or, more simply, the tensile strength, is the maximum engineering stress level reached in a tension test. The strength of a material is its ability to withstand external forces without breaking. In ductile materials, the UTS will be well outside of the elastic portion into the plastic portion of the stress-strain curve. The engineering stress will decrease after the UTS is reached as necking occurs in the specimen. However, this type of localized deformation is beyond my research scope and will not be further discussed in this dissertation.

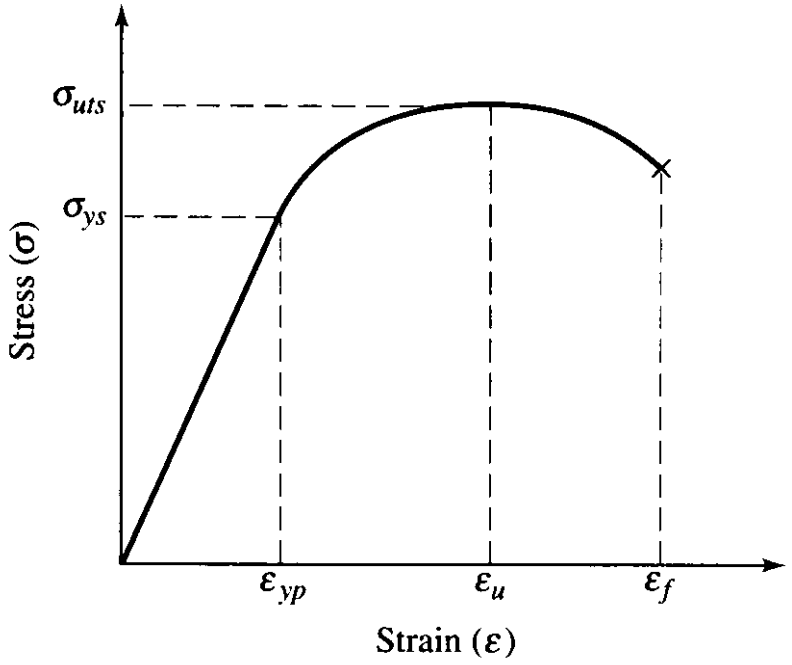

(http://www.benbest.com/cryonics/lessons.html)

Figure 1.7 Typical Stress-Strain Response for Ductile Materials

1.3.2 Creep

Solder joints are often placed in service at 'relatively high temperatures' and thus exposed to static mechanical stresses due to the Coefficient of Thermal Expansion (CTE) mismatch between silicon chip and PCB. These stresses are less than the yield strength of solder materials but nevertheless can cause plastic deformation to take place – particularly over a long period of service time. This type of time-dependent yet permanent deformation of a material while under an applied load that is below its yield strength is known as creep deformation. Creep is often regarded as one of the major failure modes of solder joints in microelectronic packaging modules [36].

In engineering practice, creep data are usually obtained under conditions of constant uniaxial loading and constant temperature. Results of tests are plotted as strain vs. time up to rupture. As indicated in Figure 1.8, the response begins with a quick transition to the initial "elastic" strain level, followed by three stages; namely, primary, secondary, and tertiary creep. In the primary stage, strain occurs at a relatively rapid rate after the instantaneous strain but then the rate gradually decreases until it becomes approximately constant during the secondary stage. This constant creep rate due to the dynamic balance of strain hardening and recrystallization [31] is defined as the steady state creep rate. It is often used by practicing engineers as one of the key material parameters for solder in Finite Element (FE) simulations used to predict solder joint reliability. The tertiary creep region occurs when rupture is imminent, and typically features an abrupt change to a nearly constant but significantly increased creep rate.

In spite of similar shapes of creep responses, the deformation mechanism of creep varies with applied load and service temperature. Figure 1.9 maps the possible creep

deformation mechanisms of eutectic Sn-Pb solder material. This diagram features with axes of normalized stress τ/G and homologous temperature, T/T_M (where τ is shear stress, G the shear modulus, T the ambient temperature, and T_M the melting temperature). The map is divided into fields, which show the regions of stress and temperature over which each of the deformation mechanisms is dominant. Superimposed on the fields are contours of constant strain-rate: these show the net strain-rate (due to an appropriate superposition of all the mechanisms) that a given combination of stress and temperature will produce. For most cases, creep is considered critical with a homologous temperature larger than 0.5. Therefore, creep is not negligible for most solder materials even at room temperature (RT) due to their large homologous temperatures:

$$H_T = \frac{T}{T_M} = \frac{298K}{456K} = 0.65 \qquad \text{for eutectic Sn-Pb} \tag{1.4}$$

$$H_T = \frac{T}{T_M} = \frac{298K}{490K} = 0.61 \qquad \text{for Sn-Ag-Cu} \tag{1.5}$$

In practice, solder joints are subject to high ambient temperatures and/or low stress levels in most cases. Thus, it is believed that dislocation-controlled creep and lattice diffusion-controlled creep are the major deformation modes for eutectic Sn-Pb solder [37]. At high homologous temperatures, the thermally activated dislocations are able to move along preferred slip plans or cut through dislocation barriers [38, 39], and the interstitial atoms and lattice vacancies tend to migrate along the gradient of a grain boundary in the presence of tensile or compressive pressure in reversed directions [40].

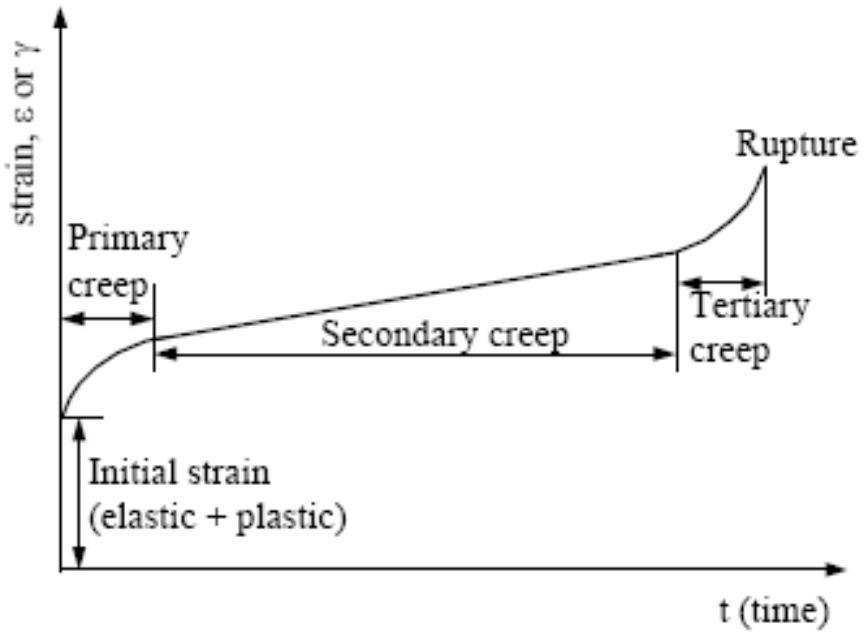

(http://www.metallurgy.nist.gov/solder/clech/Sn-Pb_Creep.htm)

Figure 1.8 Typical Creep Response for Ductile Materials

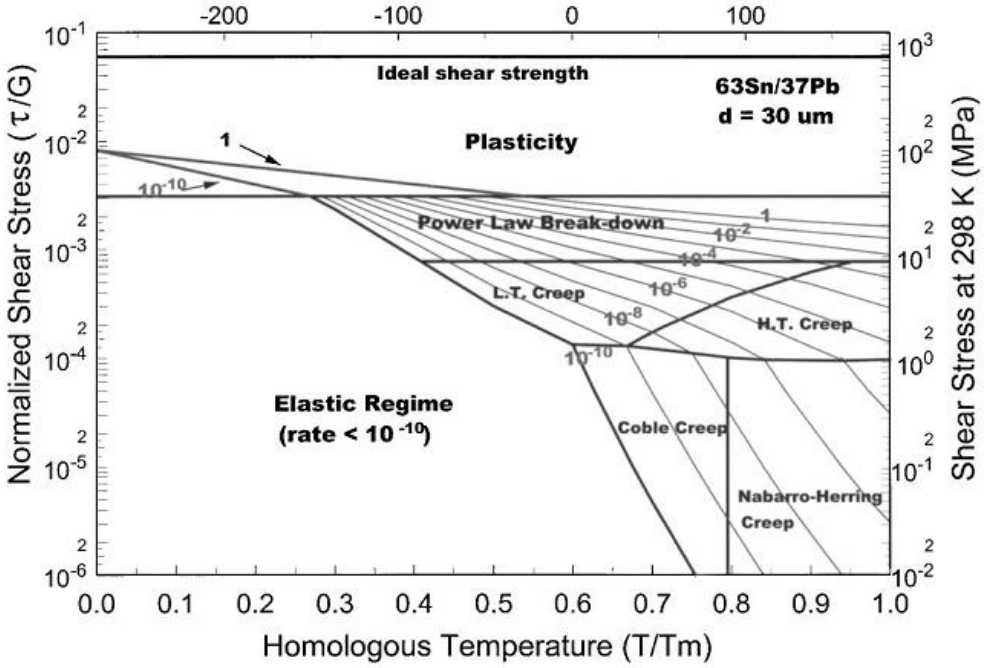

Figure 1.9 Creep Deformation Mechanism Map for Eutectic Sn-Pb Solder [37]

1.3.3 Fatigue

Thermally cycling induced solder joint fatigue is a common failure mode in electronic packaging. When subjected to temperature changes, stresses in electronic assemblies are typically developed due to the mismatches in CTE of the soldered components and the PCB. Cyclic temperature changes, either due to external environment or power switching, can therefore lead to substantial alternating stresses and strains within the solder joints. During cyclic loading, micro cracks form within the solder material followed by macro cracks which leads to damage and ultimately to fatigue failure (see Figure 1.10). The facts that the original bulk design strengths are not exceeded and the only warning sign of an impending fracture is an often unable-to-see internal crack, makes fatigue damage especially dangerous for electronic packages.

Fatigue test results (see Figure 1.11) are obtained by cycling smooth or notched specimens until failure, and are presented in a form of *S*-*N* diagram (where *S* is the stress amplitude, and *N* the number of cycles to failure). Since the 1950's, researchers have developed several models to predict the number of cycles to failure including the Engelmaier-Wild equation [41], Palmgren-Miner linear damage law, Coffin-Manson relation [43], etc.

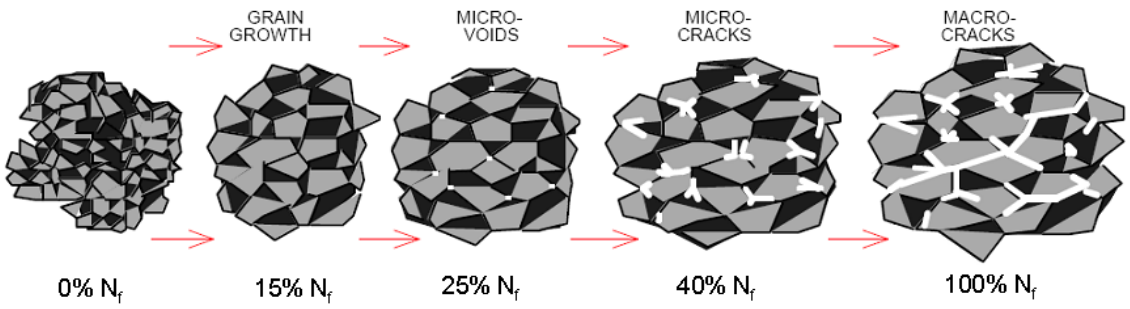

Figure 1.10 Depiction of the Effects of the Accumulating Fatigue Damage [41]

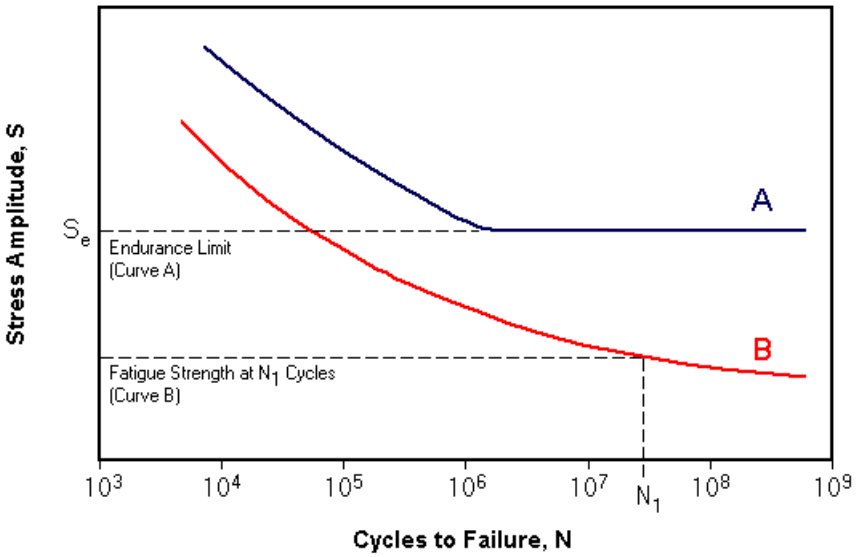

(http://www.mdme.info/MEMmods/MEM30007A/properties/Properties.html)

Figure 1.11 Typical S-N Curve for Ductile Materials

1.3.4 Shear

It is known that solder joints in microelectronics systems often experience shear loading due to the CTE mismatch. Similar to tensile stress-strain curves, Hooke's Law also holds for shear stress-strain responses at small shear strains, as shown in Figure 1.12:

$$\tau = G\gamma \tag{1.6}$$

Here shear stress and shear strain, τ and γ, can be similarly obtained by:

$$\tau = \frac{F}{A_0} \tag{1.7}$$

$$\gamma = \frac{\Delta x}{h} \tag{1.8}$$

where F is the applied shear force, A_0 the cross-sectional area, Δx the transverse displacement, h the initial length.

In Eq. 1.6, *G* is called the shear modulus or modulus of rigidity, measured as the slope of the linear portion on the shear stress-strain response. The shear modulus can also be estimated from the elastic modulus and Poisson's ratio by the equation [31]:

$$G = \frac{E}{2(1+\nu)} \tag{1.9}$$

In addition, stress/strain in shear testing can also be converted into the equivalent stress/strain in tensile testing by using von-Mises relationship:

$$\sigma = \sqrt{3}\tau \tag{1.10}$$

$$\varepsilon = \gamma / \sqrt{3} \tag{1.11}$$

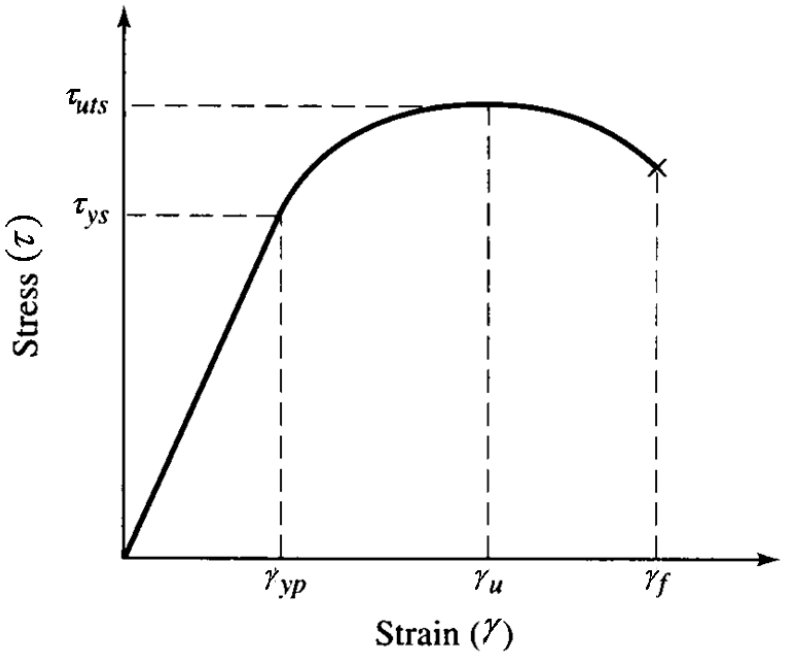

(http://www.benbest.com/cryonics/lessons.html)

Figure 1.12 Typical Shear Stress-Strain Response for Ductile Materials

1.4 Objectives of This Research

The motivation of this research is to systematically study the effects of aging on mechanical behavior and microstructure evolution of lead free solder alloys. In order to find possible solutions to minimize aging effects as well as expand the current database of solder material properties for finite element analysis (FEA) purposes, the following objectives will be achieved in this research:

(1) Develop specimen preparation procedures that produce uniaxial testing coupons with consistent microstructures comparable to actual lead free solder joints in commercial electronic packages;

(2) Examine physical properties of lead free solders of interest and explore the application in real packaging assemblies;

(3) Develop DoE test matrix to systematically study aging effects on material properties of lead free solders;

(4) Perform uniaxial tensile and creep tests for doped/reference lead free solders over a wide range of aging conditions;

(5) Develop constitutive models for predicting uniaxial tensile and creep behaviors, and models of aging for estimating mechanical properties of lead free solders;

(6) Investigate the effects of aging, casting method, testing conditions and dopants on material properties of solder alloys;

(7) Examine the effects of aging on microstructure, grain structure and internal residual stress.

1.5 Organization of the Dissertation

This dissertation mainly focuses on understanding aging effects on mechanical properties of lead free solder materials and is presented in the following chapters:

Chapter 1: Introduction to lead free solders alloys and mechanical properties of solder materials.

Chapter 2: Literature review on isothermal aging effects, mechanical properties, constitutive models, microstructure evolution and metallurgical modification/optimization of lead free solder alloys.

Chapter 3: Description of experimental procedure, uniaxial tensile and creep tests and data processing.

Chapter 4: Investigation of aging effects on mechanical properties of lead free solder alloys.

Chapter 5: Study on using dopants to reduce aging effects on mechanical behaviors of lead free solder alloys.

Chapter 6: Study on the effect of cooling profile and testing condition on mechanical properties of lead free solder alloys.

Chapter 7: Investigation of aging effects on microstructure evolution and residual stress relaxation in lead free solder alloys.

Chapter 8: Summary and conclusions of the dissertation.

CHAPTER 2

LITERATURE REVIEW

2.1 Introduction

The ongoing transition to lead free soldering has been motivated by environmental concerns, legislative mandates, and market differentiation. Although Sn-Ag, Sn-Ag-Cu (SAC), and other alloys involving elements such as Sn, Ag, Cu, Bi, In, and Zn have been identified as potential replacements for standard 63Sn-37Pb eutectic solder, there is still no "drop in" replacement identified for all applications. Even worse, large discrepancies are found in the published data from various groups [44]. The observed disagreements in the test results are largely attributed to the lack of "standards" including variations in the as-cast/solidified microstructures of the test specimens, and differences in the test methods and data acquisition. All of these possibilities might make the measured data incomparable to each other. Moreover, aging effects, mostly neglected in majority of the studies, may further exacerbate these problems.

In real applications, solder joints are continuously exposed to aging/thermal cycling during service. It has been well documented that the microstructure, mechanical response, and failure behavior of solder materials are constantly evolving under such circumstances [25, 45-62, 69, 71, 74, 78, 89, 102-112, 114, 117, 120]. It has also been demonstrated that aging effects are universally detrimental to reliability and cause reductions in stiffness, yield stress, ultimate strength, and strain to failure, as well as

highly accelerated creep. Solder joints with highly degraded microstructure and material properties are so vulnerable that the service life of the package is often severely shortened.

Reliable, consistent, and comprehensive solder constitutive equations are also needed for use in mechanical design, reliability assessment, and process optimization. Among all the widely used constitutive models, however, none of them take aging effects into account. This drawback may significantly hinder the application of finite element modeling to reach its full potential. Therefore, it is necessary to conduct an in-depth study on the constitutive models for lead free solder materials, not only for the better interpretation of experimentally measured data, but also for the incorporation of aging effects into the models.

2.2 Aging Effects on Material Properties

Studies of aging effects on Sn-Pb solders can be traced back to the 1950s. In 1956, Medvedev [45] reported a 30% loss of tensile strength for bulk Sn-Pb solder after 450 days of room temperature (RT) aging, and a 23% loss in tensile strength for solder joints under a similar exposure. Similar work has also been conducted by Lampe [46], who observed an up to 20% loss in both strength and hardness of Sn-Pb and Sn-Pb-Sb solders after 30 days of RT aging.

Meanwhile, the effect of aging on tensile properties of Pb-free solders has been studied extensively in recently years. Ding, *et al.* [47] investigated the influence of aging treatment on deformation behavior of Sn-3.5Ag solder during in situ tensile tests. They observed a quick softening effect on solder samples subject to 180 ^{o}C isothermal exposure for 120 hours. Xiao, *et al.* [48] recorded the tensile behavior of SAC396 solder

alloy subject to both RT aging and elevated temperature (HT) aging (180 ^{o}C) for various durations. They observed a 25% reduction of tensile strength for 35 days of RT aging, but a 33% reduction for merely 9 days of HT aging. Ma, *et al.* [49] investigated the evolution and saturation of Young's modulus, yield strength, and ultimate tensile strength of SAC305 and SAC405 solder alloys under various aging conditions. They found that the material properties decreased exponentially in the first 20 days for both RT and HT aging, followed by a "steady" linear degradation. Zhang, *et al.* [50] also systematically studied the aging effects on tensile properties of SACN05 (N = 1, 2, 3, 4) series solders. They performed uniaxial tensile tests on micro-scale bulk solder samples with a full aging test matrix. They also proposed several empirical models to correlate the degradation in tensile properties with aging.

In addition, isothermal aging effects were also reported to reduce the shear strength and change the failure mode of lead free solder joints. Chen, *et al.* [51] conducted a study on both Sn-Pb and Sn-3.5Ag solders and measured the variations in solder bump shear strength with aging. They concluded that shear strength for both solder materials decreases slightly after aging at 150% for 1500 hours, 8.9% for Sn-Pb solder bumps and 5.3% for Sn-3.5Ag. Similar results were achieved by Kim, *et al.* [52]. They observed an average 5% decrease in joint strength in stud bump samples for the first 300 hours of aging at 150 ^{o}C. They also reported that the degradation was almost negligible afterwards. Anderson, *et al.* [53] extended the study to a wide selection of SAC alloys, including SAC305, SAC3810, SAC379 and SAC396. Despite the significant change in ductility, the solder materials were severely softened with long term HT aging.

Moreover, the literature has also documented the significant influence of aging on creep behavior of lead free solder alloys. Ma, *et al.* [49] initiated a parametric study of aging on SAC305 and SAC405 solders, and found that the secondary creep rates were increased up to 10X and 100X, respectively. A more systematic study was conducted by Zhang, *et al.* [50]. They recorded the evolution of creep curves and corresponding steady state creep rates as a function of aging (aging temperature + aging time), and observed up to a 9,700X deterioration in the secondary creep rate for aging up to 6 months. Similar aging induced degradations in creep properties were also reported in bulk samples by Xiao, *et al.* [54], Mysore, *et al.* [55], and in solder joints by Chavali, *et al.* [56].

Furthermore, several previous studies have been conducted with respect to aging effects on the fatigue behavior of lead free solders. Bansal, *et al.* [57] observed a significant degradation in reliability after 500 hours of aging at 150 ^{o}C for both SAC105 and SAC305 solder joints in 0.5 mm pitch BGAs and MLF packages. Elevated temperature aging effects on shear fatigue behavior was studied by Venkatadri and coworkers [58] on a SMD test vehicle with SAC305 solder joints. A decrease of more than 70% in fatigue resistance was observed after 3000 hours of aging at 125 ^{o}C. A more systematic study of aging induced evolution of hysteresis loops for SAC solders was conducted by Mustafa, *et al.* [59]. They reported a decrease in loop area with aging for all SACN05 alloys, indicating reduction of energy dissipation in the material.

2.3 Aging Induced Microstructure Evolution

Aging effects on microstructure evolution of lead free solders have been studied extensively on both bulk samples and solder joints in packages. In general, isothermal aging leads to phase coarsening of both β-Sn and precipitates, the dispensing and

coalescing of IMC particles, as well as the accelerated growth of grains, and the interfacial IMC thickness between Cu trace and bulk solder joints.

Allen, *et al.* [60] investigated phase coarsening in SAC alloy from a kinetics aspect. They concluded that phase coarsening is governed by a $r^3 \propto t$ relationship:

$$\rho^{-\frac{3}{2}} - \rho_0^{-\frac{3}{2}} = \frac{Kt}{RT}\exp\left(-\frac{Q_S + Q_D}{RT}\right) \tag{2.1}$$

where K is a constant containing terms such as the particle/matrix interfacial energy and volume fraction effects, Q_S is the heat of solution for the rate-controlling species in the matrix, and Q_D is the activation energy for diffusion of the rate-controlling species in the matrix. The sum of Q_S and Q_D, however, is assumed to be the effective activation energy. By measuring the volume fraction of Cu_6Sn_5 IMC particles in each of the light optical micrographs shown in Figure 2.1, they estimated the effective activation energy to be 69 ± 5 kJ/mol, which perfectly matches the results from other researchers (as tabulated in Table 2.1), indicating that the coarsening of the Cu_6Sn_5 rods was the dominant process ($Q_S + Q_D = 36 + 33 = 69$ kJ/mol).

Similar research was also conducted by Fix, *et al.* [61]. They applied the same procedure to determine the activation energy from Figure 2.2 and the result was compared to Allen's observation. However, they made a different conclusion and suggested a Sn diffusion controlled process for 175 ^{o}C aging.

Aging effects on dispensing and coalescing of IMC particles were also investigated by several researchers. Xiao, *et al.* [54] captured the IMC phase growth with aging in bulk SAC396 samples (Figure 2.3), and Yao, *et al.* [62] graphed the growth of the IMC particles near the SAC/Cu(Ni) interface, as shown in Figure 2.4.

Solute	Solvent	Q (kJ/mol)
Ag	Sn (c axis)	55 (D)
Ag	Sn (a axis)	77 (D)
Cu	Sn (a axis)	33 (D)
Sn	Sn (c axis)	107 (D)
Sn	Sn (a axis)	123 (D)
Ag	Sn Grain Boundaries	28 (D)
Sn	Sn Grain Boundaries	40 (D)
Ag	Sn	26 (S)
Cu	Sn	36 (S)

Table 2.1 Activation Energies for Diffusion and the Heats of Solution for Sn, Ag , Cu [60]

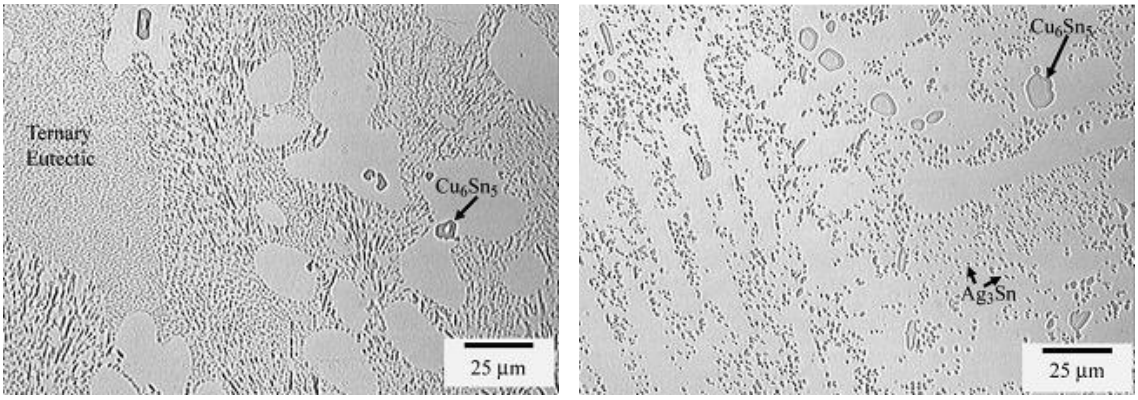

(a) As Soldering (b) 4 Weeks at 152 ^{o}C

Figure 2.1 Microstructure Evolution of SAC405 Solder Joints (Example 1) [60]

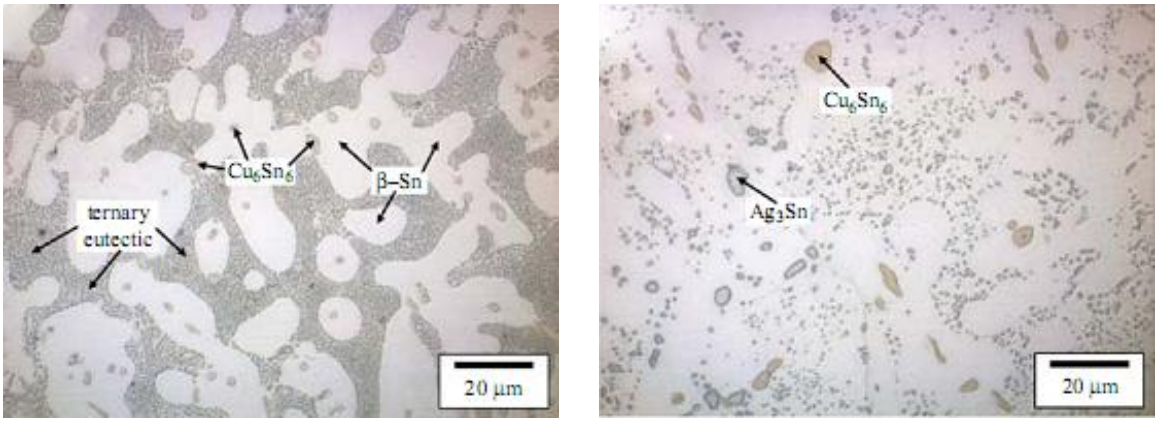

(a) As Soldered (b) 500 Hours at 175 ^{o}C

Figure 2.2 Microstructure Evolution of SAC405 Solder Joints (Example 2) [61]

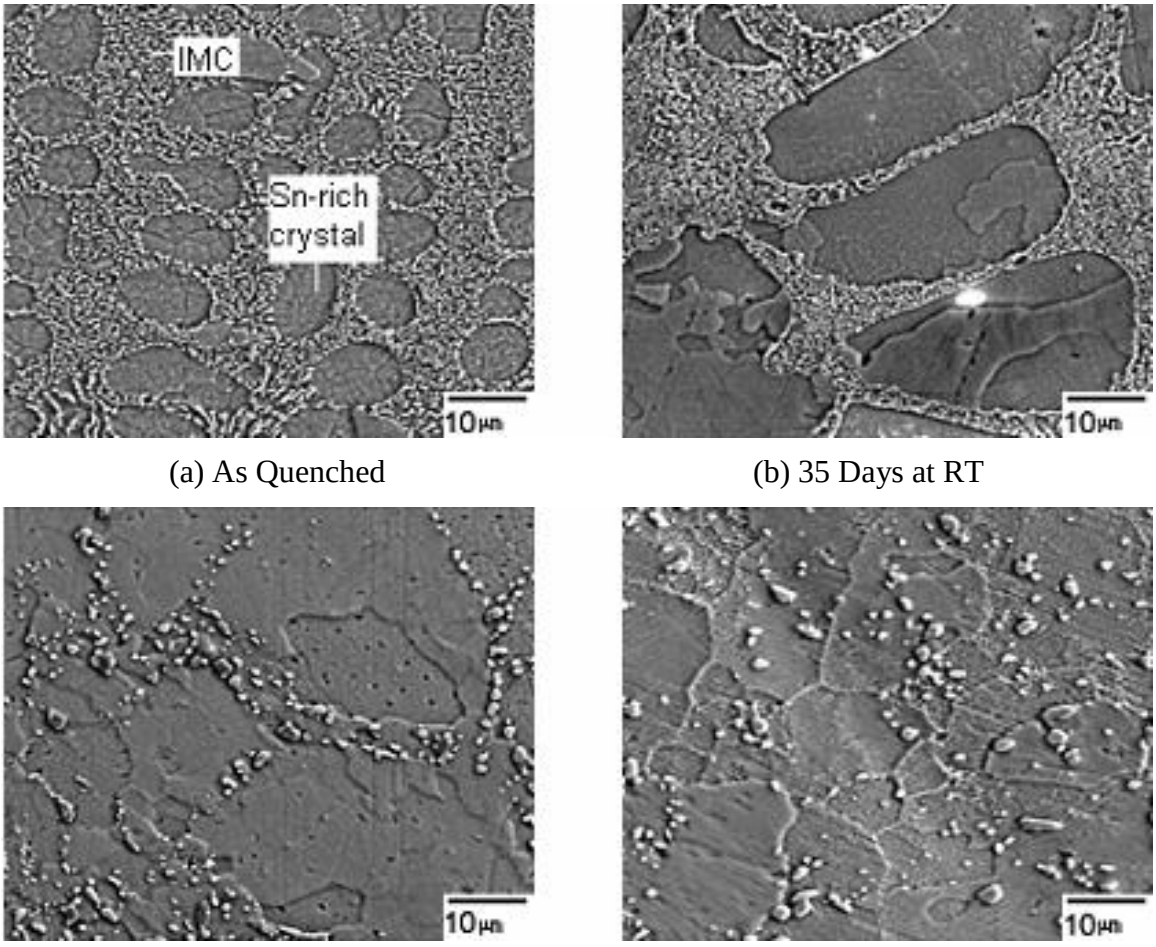

(a) As Quenched (b) 35 Days at RT

(c) 1 Day at 180 ^{o}C (d) 3 Day at 180 ^{o}C

Figure 2.3 SEM Micrograph of As-Aged SAC396 Samples [54]

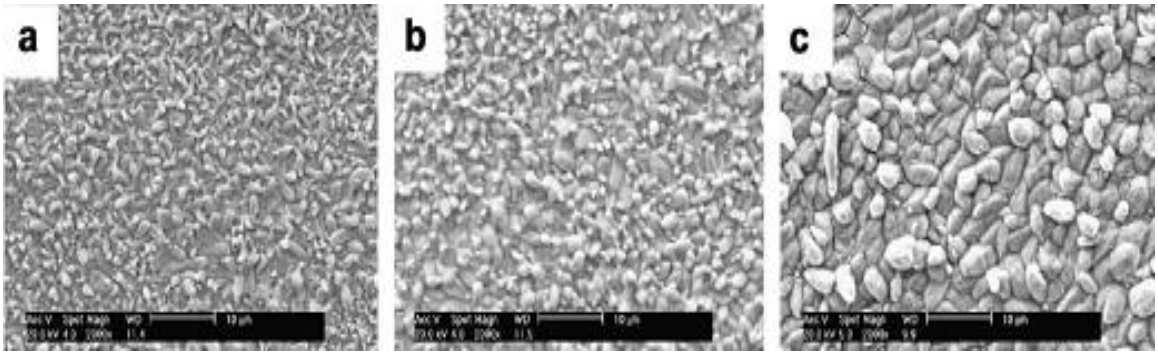

(a) 50 Hours (b) 200 Hours (c) 1000 Hours

Figure 2.4 Top Viewed SEM Micrographs of SAC/Ni Interfaces
Aged for Various Durations at 150 ^{o}C [62]

Additionally, aging effects on the interfacial structure of lead free solders have been well documented in the past few years [63-74]. As a rule of thumb, the growth kinetics of an IMC layer is express as a function of the exposure time at a given temperature:

$$X_t - X_0 = \sqrt{D_0 e^{-\frac{Q}{RT}} t} \tag{2.2}$$

where X_0 and X_t are the IMC thinkness at time t = 0 and t = t, respectively; D_0 is the diffusion constant; Q is the effective activation energy; R is the universal gas constant equal to 8.314 J/mol K, T is the isothermal aging temperature in K; and t is the aging time. Table 2.2 summarizes the literature results of activation energy estimation from several researchers and groups.

Solder/Substrate Couple	Soldering Method	Temperature Range (^{o}C)	IMC Layer	Q (kJ/mol)	Ref.
Sn37Pb/ Ni	CSP SJ	80-160	Ni_3Sn_4	45.4	[63]
Sn/Cu	Electroplated	70-170	Cu_6Sn_5 + Cu_3Sn	66	[64]
Sn/Cu	Dipped	100-170	Cu_6Sn_5 + Cu_3Sn	77	[65]
Sn0.6Cu0.05Ni/Cu	Wave	80-150	Cu_6Sn_5 + Cu_3Sn	76.16	[66]
Sn58Bi/Cu	Dipping	55-120	Cu_6Sn_5	55	[67]
Sn3.3Ag4.8Bi/Cu	Immersing	70-170	Cu_6Sn_5 + Cu_3Sn	49 $\pm$8	[68]
Sn3.5Ag5Bi/Cu	Spreading	70-200	Cu_6Sn_5 + Cu_3Sn	88.6	[69]
Sn3.5Ag5Bi/NiP/Cu	Spreading	100-170	Ni_3Sn_4	52.85	[69]
Sn3.5Ag/Cu	SJ	70-170	Cu_6Sn_5 + Cu_3Sn	64.82	[70]
Sn3.5Ag/Cu	Sandwich	70-180	Cu_6Sn_5	116	[71]
Sn3.5Ag/Cu	Dipping	70-205	Cu_6Sn_5 + Cu_3Sn	59	[72]
Sn3.5Ag/Cu	Speading	70-200	Cu_6Sn_5 + Cu_3Sn	65.4	[73]
Sn3.8Ag0.7Cu/Cu	Reflow	100-150	Cu_6Sn_5 + Cu_3Sn	41.7	[74]

Sn3.8Ag0.7Cu/Ni	Reflow	100-150	$(Ni_{1-x}Cu_x)_3Sn_4$	72.9	[74]

Table 2.2 Reported Effective Activation Energies for the Growth of IMC Layers

It is also known that the elevated temperature aging attributes to the crack initiation and propagation near solder substrate interfaces. Zeng, *et al.* [75] captured a series of SEM micrographs (Figure 2.5), illustrating the development of Kirkendall voids (pointed out by white arrows) as aging progressed. It is widely acknowledged that Kirkendall voids are formed due to the unbalanced inter-diffusion rates between Cu and Sn. In particular, Cu atoms diffuse from the Cu pad into the bulk solder joints at a faster rate than Sn atoms diffuse from solder joint into Cu. The diffusion of Cu is further accelerated by elevated temperature aging, leads to the coalescing of vacancies, and finally causes the formation of micro-voids/cracks.

Several studies have documented aging effects on grain growth in lead free Sn-rich solder materials. Telang, *et al.* [76] quantitatively compared the size, number, and misorientation of grains within six different types of lead free solders by using OIM. Figure 2.6 is an example of their OIM data, illustrating the apparent growth of the grains. Table 2.3 summarized their findings on the aging induced evolution of grains and misorientation.

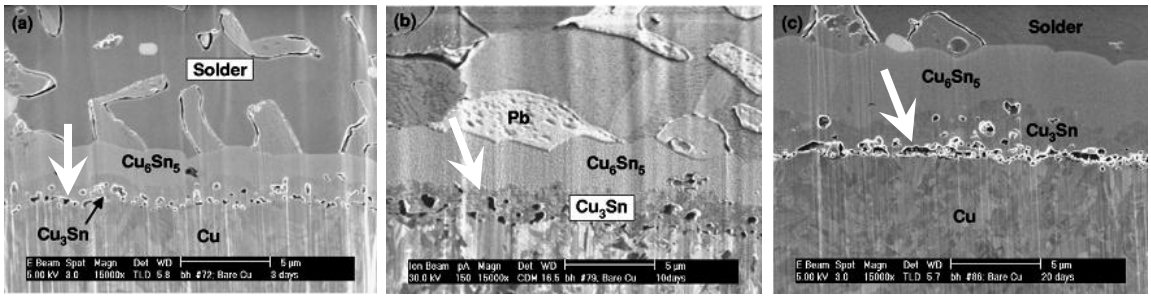

(a) 3 day (b) 10 day (c) 20 day

Figure 2.5 Micrographs for Formation of Kirkendall Voids with Aging at 150 ^{o}C [75]

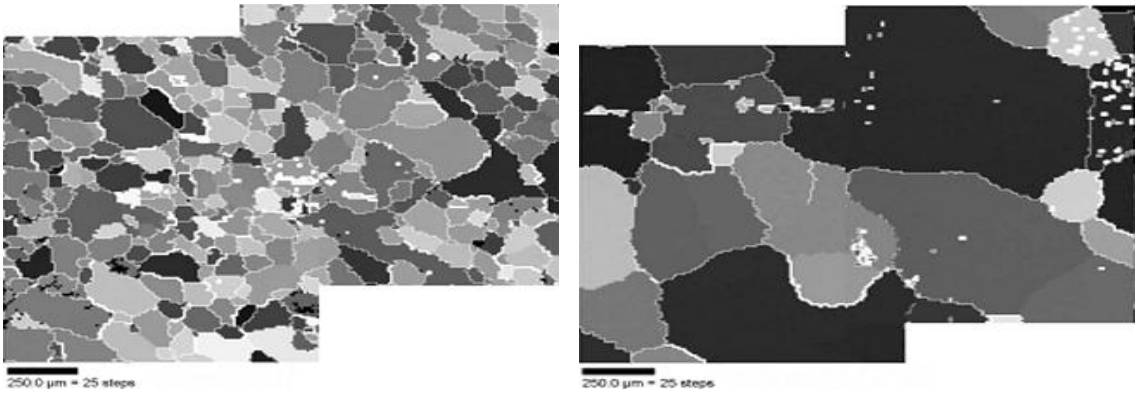

(a) As Reflowed (b) Aging at 150 ^{o}C for 200 Hours

Figure 2.6 Evolution of Grain Size and Orientation with Aging for Reflowed Pure Sn [76]

Specimen	Aging History	Grain Size	Grain Boundary Misorientation
Pure Sn ingot	As received	50-150 μm, equiaxed	Sharp peaks at 45^{o} and 60^{o}
	Aged 200 hours at 150 ^{o}C	>500 μm, irregular	Fewer boundaries, peaks at 45^{o}, 60^{o} and 70^{o}
Pure Sn, reflowed	As reflowed	100-250 μm, equiaxed	Many small peaks
	Aged 200 hours at 150 ^{o}C	>500 μm, irregular	Very strong peak at 45^{o}, other small peaks
Eutectic Sn-3.5Ag	As received	10-30 μm, equiaxed	Nearly random distribution of higher angle grain boundary misorientation, regardless of aging time
	Aged 200, 400 hours at 150 ^{o}C	20-60 μm, equiaxed	
Eutectic Sn3.8Ag0.7Cu	As received	10-30 μm, equiaxed	Random + low angle, 60^{o}, 80^{o} peaks superposed
	Aged 200 hours at 150 ^{o}C	20-100 μm, equiaxed	Randomness decreases with aging, peaks sharpen
Solder ball Sn-1.63Ag	As fabricated	15-20 μm, equiaxed	Bi-modal; <15^{o} low angle, and large 50-70^{o} peak
Solder ball Sn-3.0Ag	As fabricated	40-250 μm, irregular shapes	Several small peaks <25^{o}, 55-60^{o}, 70-80^{o}
Solder ball	As fabricated	100-600 μm,	Not scanned

Sn-3.0Ag-0.6Cu	large, irregular

Table 2.3 Summary of Typical Grain Size and Misorientation in Solders Samples [76]

2.4 Effect of Fabrication and Testing Conditions on Material Properties

The solidification cooling rate has a significant effect on the microstructure of solder materials by determining the initial size, distribution and morphology of IMC phases (e.g. Ag_3Sn and Cu_6Sn_5) [77]. For bulk solder, fast cooling rates result in relatively thin and planar IMCs, while slow cooling rates lead to a relatively thick and scalloped IMC morphology. For a solder/substrate interface, fast cooling rates reduce the thickness of the interfacial IMC layer, as well as the size of IMC particles [78]. Liang, *et al.* [79] compared the mechanical properties and macro/micro-structure of SAC387 formed with different cooling rates. Figure 2.7 illustrates the typical macrostructure of as-solidified test samples (etched by 10% HCl). They found that fast solidification could significantly lower the Sn dendrite arm spacing and enhance the creep resistance of solder material.

Tensile properties of solder materials are known to be strongly rate and temperature dependent. In the 1980's, Anand [80] proposed a unified plastic/creep constitutive model for describing the viscoplastic behavior of metals. The flow equation in the Anand model establishes the relationship between flow stress and plastic strain, with strain rate and ambient temperature as parameters. This model has been shown to work well on solder materials and is widely used in finite element simulations. Pang, *et al.* [81] modified the Ramberg-Osgood model by introducing testing temperature and strain rate, in an attempt to predict the stress-strain behavior for SAC387. Nie, *et al.* [82] characterized the rate-dependent behavior of SAC387 solder over a wide range of strain

rates, from 10^{-6} to 10^{-2}. Although two different experimental setups were utilized, the test results demonstrated a remarkably consistent relationship between the yield stress and the strain rate over eight decades of strain rate. It has also been demonstrated by several researchers [8, 33, 37, 54], that both stress level and testing temperature have a strong effect on the steady state creep rate of solder materials. In general, higher loading of stress/temperature significantly accelerates the creep and reduces the strain-to-rupture.

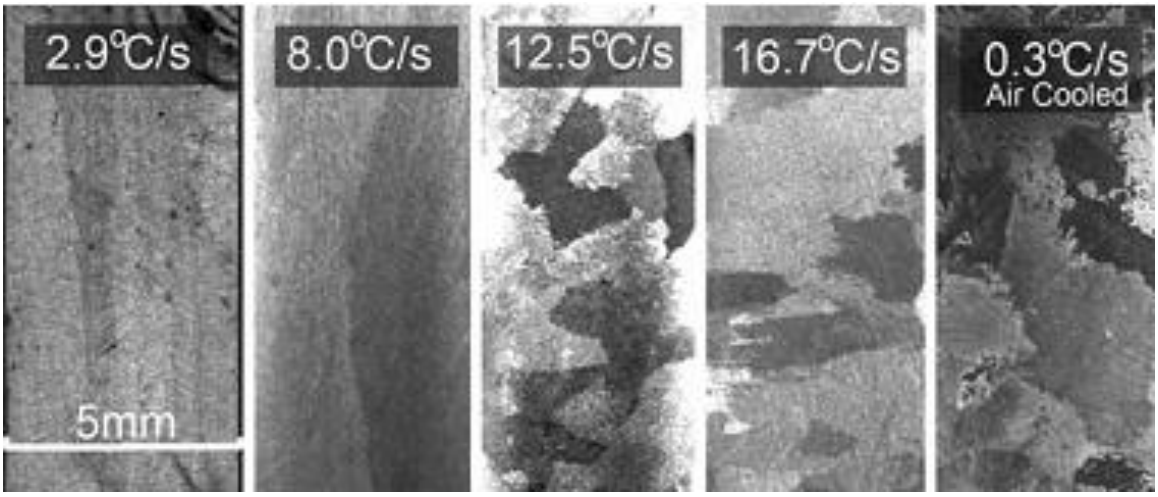

Figure 2.7 As-Solidified Macrostructures of SAC387 [79]

2.5 Solder Material Optimization by Using Dopants

The ongoing transition to lead free soldering has been motivated by environmental concerns, legislative mandates, and market differentiation. However, there is still no single replacement that has been identified for challenging operating environments, i.e. high temperatures and stress levels, as well as impact loading. To this end, studies concerning to isothermal aging and thermal cycling have concentrated on near eutectic Sn-Ag-Cu (SAC) solders. An ideal SAC solder alloy should not only possess enhanced mechanical properties, but also resistance to isothermal aging effects

and thermal-mechanical fatigue for a wide range of temperatures. Therefore, there is much interest in the industry on establishing optimal SAC-based lead free solder alloys to meet all demands. According to the results of many recent studies, these goals can be accomplished by metallurgical approaches, i.e. micro-alloying, to strengthening the solder matrix or the matrix/intermetallic interface regions of the solder joint.

Bi additions to lead free solders have been the subject of many investigations. It has been shown that Bi can lower the solidus temperature, improve the wetting and alloy spreading, refine the Sn matrix through precipitation hardening, and suppress the formation of large Ag_3Sn IMCs in the bulk solder [83]. On the negative side, it is also reported that Bi atoms segregate along the Cu/IMC interface and lead to brittle fracture [84]. However, according to the observation of Pandher and his coworkers [85], using the appropriate amount of Bi doping is highly important. They found that the addition of 0.01% Bi resulted in improved drop shock and ball pull response for low silver content SAC solder, i.e. SAC0307. In addition, they also observed the reduction in the IMC growth and the partition to the Cu/IMC interface for Bi-doped SAC0307 solder. Tateyama, *et al.* [86] conducted a study on the effects of Bi content on mechanical properties and bump interconnection reliability of Sn-Ag solder alloys. They suggested a 3% or less Bi doping level in Sn-Ag solder so that the optimal enhancement could be achieved.

The effect of Ni doping has been discussed by several authors [23-25], i.e. a thorough review by Tegehall [87]. It is reported that Ni doping can inhibit the allotropic transformation of Cu_6Sn_5 [23], suppress the formation of Kirkendall voids, and slow the growth of interfacial IMC layers [25]. On the other hand, it has also been demonstrated

that the introduction of Ni would soften the SAC solder material and form brittle Cu-Ni-Sn ternary IMCs [24]. Pandher, *et al.* [85] proposed a 0.05% Ni doping to SAC0307 + 0.1% Bi solder to obtain the optimal drop resistance and tarnish resistance.

With respect to mechanical properties, Zn modified SAC alloys have been reported to exhibit a combination of high tensile strength and great ductility [88]. The most tremendous benefit of Zn doping is attributed to its enhancement of microstructure stability and aging resistance [89]. Song, *et al.* [88] studied the effect of Zn doping on the microstructure characteristics of SAC solder. They found that the addition of 0.5% Zn significantly reduced the degree of undercooling for Sn-3.3Ag-0.5Cu solder, and thus suppressed the formation of large Ag_3Sn platelets. In addition, Zn-doped SAC solders were observed to have an increased volume fraction of eutectic phases without formation of any Zn-bearing IMCs. Anderson, *et al.* [89] reported that no significant microstructure evolution in bulk Sn-3.5Ag-0.74Cu-0.21Zn solder joints was observed even after 1000 hours of aging at 150 ^{o}C. Similar work was also performed by Kang, *et al.* [90]. They concluded that a minor addition of Zn (<1%) to SAC387 was very effective in suppressing the IMC growth on Cu pads.

It has been demonstrated that other transition metals such as Co and Fe can refine the microstructure for bulk solder joints, as well as hinder the IMC growth near the interface [91-92]. According to the microstructure studies conducted by Anderson, *et al.* [91], Co exhibited a solidification catalysis effect on Cu_6Sn_5 phase in the Sn-3.7Ag-0.6Cu-0.3Co solder matrix with a desirable (reduced) volume fraction and size (smaller). They also observed the significant effect that the minor substitution of iron for copper promoted highly refined Sn dendrites in the solidified solder matrix. Syed, *et al.* [92]

carried out package level tests on a wide selection of SAC-X solders, indicating that SAC355Co solder had the best performance in both ball pull and ball shear tests regardless of aging conditions. Based on their observations, they also suggested that the refined, stabilized microstructure of Co-doped SAC solder was the fundamental reason resulting in the improved resistance to deformation.

Rare Earth (RE) elements (e.g. La, Ce) are also popular options for low level doping in SAC solders. Wu and Wong [93] performed a thorough review discussing the advantages and issues of RE-doped SAC solders. They concluded that small addition of RE elements can improve the tensile strength, creep strength, and wettability. From the microstructure aspect, RE-doped alloys were demonstrated to generate well-controlled interfacial IMC layers, especially in BGA packages. On the other hand, they also suggested that more studies should be conducted regarding soldering behavior under common processes (i.e. SMT), as RE elements were known to be easily oxidized. The addition of RE elements was also reported to significantly improve the ductility of SAC solders. Dudek, *et al.* [94] modified conventional SAC397 solder by adding small amount of La and they measured a more than a 1.5X increase in failure strain with a negligible loss in shear strength.

Other doping choices for optimizing SAC solders, such as Mn, Cr, Ge, Ti, Si, B, Al, In, etc, have also been studied extensively by various researchers and groups. Liu and Lee [95] compared the interfacial IMC growth and drop performance for 14 different doped solder alloys, and concluded that SAC105 + 0.13Mn alloy outperformed all other alloys, including conventional Sn-Pb solder. Anderson, *et al.* [89] claimed that the aging resistance of SAC3595 improved tremendously by merely adding 0.05% Al. Amagai, *et*

al. [96] found that doping with In could reduce Kirkendall voiding but had little effect on the growth of Cu_3Sn IMC. Ge, different from other "diffusion compensators" such as Ni and Co, is acknowledged to refine the Sn matrix as well as improve corrosion behavior [85].

2.6 Constitutive Modeling for Solder Materials

It is widely acknowledged that solder materials exhibit elasto-viscoplastic behavior when subject to deformation. In general, the expression of total strain can be partitioned by decoupling the elastic and plastic parts:

$$\varepsilon = \varepsilon_e + \varepsilon_{vp} \tag{2.3}$$

where ε_e is the elastic strain; ε_{vp} is the viscoplastic strain. If the strain hardening effect (the stress continues to increase after yielding) is also taken into consideration, the constitutive model may be expressed in generic terms as:

$$\begin{aligned} \varepsilon = \varepsilon_e &= \frac{\sigma}{E} && \text{for } \|\sigma\| < \sigma_{ys} \\ \dot{\varepsilon} = \dot{\varepsilon}_e + \dot{\varepsilon}_{vp} &= \frac{\dot{\sigma}}{E} + f\left(\sigma, \sigma_{ys}, \varepsilon_{vp}\right)\sigma && \text{for } \|\sigma\| \geq \sigma_{ys} \end{aligned} \tag{2.4}$$

Based on the fact that the mechanical behavior, such as yield stress, ductility, and tensile strength, of materials will change with strain rate and temperature, an ideal viscoplastic model for solder materials should consist of at least the following four elements:

$$\sigma_{vp} = f\left(\varepsilon_{vp}, \dot{\varepsilon}_{vp}, T\right) \tag{2.5}$$

where σ_{vp} is the von-Mises flow stress; ε_{vp} is the equivalent plastic strain; $\dot{\varepsilon}_{vp}$ is the equivalent plastic strain rate; and T is the absolute temperature. In the past few decades, several physically and phenomenologically based models have been proposed for use in

material characterization, including tensile and creep responses. In this section, four constitutive models with approximately the same number of material constants, Johnson-Cook (J-C) model, Zerilli-Armstrong (Z-A) model, Khan-Huang (K-H) model, and Anand model will be discussed.

2.6.1 J-C Model

In 1983, Johnson and Cook [97] proposed a constitutive model for metals subjected to large strains, high strain rates, and high temperatures. This particular model is widely used due to its simplicity and the availability of parameters for various materials of interest, although it is purely empirical. In the J-C model, the von Mises flow stress, σ is expressed as:

$$\sigma(\varepsilon, \dot{\varepsilon}, T) = \left(A + B\varepsilon^n\right)\left(1 + C\ln\dot{\varepsilon}^*\right)\left(1 - T^{*m}\right) \tag{2.6}$$

where A, B, C, m, n are material constants; $\dot{\varepsilon}^* = \dot{\varepsilon}/\dot{\varepsilon}_0$ is the dimensionless strain rate ($\dot{\varepsilon}_0$ is normally taken to be 1.0 $\sec^{-1}$), and $T^* = (T - T_r)/(T_m - T_r)$ where T_r is the reference temperature (lowest temperature of interest) and T_m is the melting temperature of the material. With merely one term, the J-C model in its multiplication form is appropriate for describing the temperature dependence of metals. However, this model will be invalid for modeling any metals where the work hardening rate decreases with an increased strain rate. In addition, this model exhibits unrealistically small strain-rate dependence at high temperatures.

2.6.2 Z-A Model

In 1987, Zerilli and Armstrong [98] proposed constitutive relations based on a dislocation mechanism. Despite the relatively simple expression compared to other

microstructure-aware constitutive relations, the Z-A model still includes the effects of strain hardening, strain-rate hardening, and thermal softening based on the thermal activation analysis. The general form of the equation for the flow stress is:

$$\sigma(\varepsilon,\dot{\varepsilon},T)=\sigma_a+B\exp(-\beta\dot{\varepsilon}T)+B_0\sqrt{\varepsilon}\exp(-\alpha\dot{\varepsilon}T) \tag{2.7}$$

In this model, σ_a is the thermal component of the flow stress given by:

$$\sigma_a=\sigma_g+\frac{k_h}{\sqrt{l}}+K\varepsilon^n \tag{2.8}$$

where σ_g is the contribution due to solutes and initial dislocation density, k_h is the microstructural stress intensity, l is the average grain diameter, and K, B, B_0 are material constants. Note that in the thermally activated terms, the functional forms of the exponents α and β are

$$\begin{aligned}\alpha&=\alpha_0-\alpha_1\ln(\dot{\varepsilon})\\ \beta&=\beta_0-\beta_1\ln(\dot{\varepsilon})\end{aligned} \tag{2.9}$$

where α_0, α_1, β_0, β_1 are material parameters that depend on the crystal structure (e.g. FCC, BCC, HCP).

2.6.3 K-H Model

Based on the study of Bordner and Partom [99], Khan and Huang [100] developed a new constitutive model to predict the mechanical behavior of 1100 aluminum in the strain rate range from 10^{-5} to 10^{4} sec^{-1}. In their study, the model proposed was:

$$J_2=f_1(\varepsilon_2)f_2(D_2) \tag{2.10}$$

where ε_2 is the equivalent plastic strain defined by:

$$\varepsilon_2=\frac{1}{2}\varepsilon_{ij}\varepsilon_{ij} \tag{2.11}$$

Considering the one dimensional case, Eq. 2.11 can be rewritten as:

$$\sigma = g_1(\varepsilon) g_2(\dot{\varepsilon}) \tag{2.12}$$

where g_1 and g_2 are expressed as:

$$\begin{aligned} g_1(\varepsilon) &= \left[3 f_1\left(\frac{3}{4}(\dot{\varepsilon})^2 \right) \right]^{1/2} \\ g_2(\dot{\varepsilon}) &= \left[f_2\left(\frac{3}{4}(\dot{\varepsilon})^2 \right) \right]^{1/2} \end{aligned} \tag{2.13}$$

An example of the particular forms of g_1 and g_2 were given in their study:

$$\begin{aligned} g_1(\varepsilon) &= \sigma_0 + E_\infty \varepsilon - a e^{-\alpha\varepsilon} \\ g_2(\dot{\varepsilon}) &= \left(1 - \frac{\ln(\dot{\varepsilon})}{\ln(D_0)} \right)^{-n} \end{aligned} \tag{2.14}$$

where n, E_∞, σ_0, a and α. are constants, and D_0 was arbitrarily chosen to be 10^6 sec^{-1} in their work. Compared to the J-C model, the K-H model is more capable of predicting strong work-hardening behavior over a large strain-rate range. However, since the K-H model does not incorporate temperature effects into the proposed equations, modifications are needed so that the temperature-dependent characteristics of a material can be fully predicted.

2.6.4 Anand Model

In 1985, Anand [101] proposed a simple set of constitutive equations for large isotropic viscoplastic deformations but small elastic deformations. This constitutive model has been embedded in commercial finite element simulation software such as ANSYS, and is now widely used in prediction of electronic packaging reliability. There

are three constitutive equations in Anand model; namely the stress equation, flow equation and evolution equation.

The stress equation is defined by:

$$\sigma = cs \qquad (c < 1) \tag{2.15}$$

where s is the deformation resistance, c is a material constant defined as:

$$c = \frac{1}{\xi}\sinh^{-1}\left[\left(\frac{\dot{\varepsilon}}{A}e^{Q/RT}\right)^{m}\right] \tag{2.16}$$

where ξ is the multiplier of stress, $\dot{\varepsilon}$ is the inelastic strain rate, A is the pre-exponential factor, Q is the activation energy, m is the strain rate sensitivity, R is the universal gas constant, and T is the absolute temperature.

The flow equation was selected to accommodate the strain rate dependence on the stress, and is given by:

$$\dot{\varepsilon} = A\exp\left(-\frac{Q}{RT}\right)\left[\sinh\left(\xi\frac{\sigma}{s}\right)\right]^{1/m} \tag{2.17}$$

Note that temperature dependence has been incorporated into the model via an Arrhenius term, while the stress and state dependence were modified to be in form of the hyperbolic sine from the original power law relationship.

The evolution equation for the internal variable s is assumed to be:

$$s = f(\dot{\varepsilon}, \varepsilon, T) \tag{2.18}$$

An explicit form of evolution equation is expressed as:

$$\dot{s} = \left[h_0\left(1-\frac{s}{s^*}\right)^{a} sign\left(1-\frac{s}{s^*}\right)\right]\dot{\varepsilon} \qquad (a > 1) \tag{2.19}$$

where h_0 is a constant for the dynamic process, a is the strain rate sensitivity of the dynamic process, and s^* represents a saturation value of s associated with a given set of testing conditions given by:

$$s^* = \hat{s}\left[\frac{\dot{\varepsilon}}{A}\exp\left(\frac{Q}{RT}\right)\right]^n \tag{2.20}$$

where $\hat{s}$ is a constant and n is the strain rate sensitivity for the saturation value of deformation resistance.

To summarize, the Anand model has nine material constants, i.e. s_0, Q, A, ξ, m, h_0, $\hat{s}$, n, and a (note that s_0 is the initial value of deformation resistance). These constants can be determined from either stress-strain responses or creep responses characterized over a wide temperature range. The Anand model successfully unifies both rate-dependent creep behavior and rate-independent plastic behavior occurring concurrently in the alloys and it has been demonstrated to work well on solder materials. On the other hand, there are still some limitations of the Anand model, such as incapability of predicting the primary and tertiary creep responses, no incorporation with aging effects, etc.

2.7 Summary and Discussion

In this chapter, an extensive review has been performed on three major topics in solder material characterization including aging effects, X-additive modification, and constitutive modeling.

Aging effects are acknowledged to be responsible for the large discrepancies existing in the mechanical property databases for solder materials. A vast body of studies has already demonstrated that isothermal aging is the root cause for the ever-changing

microstructure of lead free solders and thus gives rise to the softening effect on the material properties. Most lead free solders, especially the Sn-Ag-Cu solder family, experience dramatic loss in strength (both tensile and shear), stiffness and creep resistance as aging progresses. This effect was found to be exacerbated for elevated temperature exposure. With respect to soldered components on substrates, aging has also been extensively reported to accelerate the unfavorable interfacial IMC growth, cause the formation of Kirkendall voids, and result in the coarsening of the phases in bulk solder joints.

The effects of cooling profile and testing conditions on mechanical properties of solder alloys were also discussed through reviewing previous work. In general, fast cooling rates (i.e. water quenching) during solidification yield finer/smaller phases in the microstructure, which in turn strengthens the solder material. However, quickly cooled samples may also exhibit more brittle behavior when subject to deformation, indicating a loss in strain-to-failure. Testing conditions such as strain rate, stress level, and testing temperature are also known to be key factors affecting the mechanical properties of solders. In general, higher strain rates during tensile tests cause strain hardening, and thus increase the strength and stiffness of the material. In creep testing, the response is highly accelerated by small increases in the applied stress loading. Softening effects in material properties have been reported for both tensile and creep tests performed under elevated temperatures.

In an attempt to optimize the performance of lead free solders (e.g. aging resistance, drop resistance, etc.) researchers have modified lead free solders by micro-alloying. The possible candidates of the X-additive include Bi, Zn, Co, Ni, Mn, Cr, Ge,

Ti, Si, B, Al, In, etc. It has been demonstrated that appropriate amounts of additives will not only refine the grains, phases and IMC particles in the bulk solder joints, but also control the growth of interfacial IMC layers between the bulk joint and the copper pads on the substrate.

Lastly, four widely used constitutive models for viscoplastic materials were discussed. In particular, the Anand viscoplastic model, which successfully incorporates rate-dependent creep behavior with rate-independent plastic behavior during deformation, has been often adopted for solder materials. However, modifications to the Anond model will be necessary to incorporate aging effects.

CHAPTER 3

SPECIMEN PREPARATION AND EXPERIMENTAL

3.1 Introduction

In this chapter, a novel specimen preparation technique is presented. This unique approach is able to fabricate micro-scale uniaxial tensile specimens without further modification and machining. The test specimens are formed in glass tubes with rectangular cross-section by using a vacuum suction system. The specimens are then cooled by either a water quenched cooling profile or a specifically designated reflow profile. For the current work, uniaxial samples with nominal dimensions of 80 (length) × 3 (width) × 0.5 (height) mm were utilized. Uniaxial tensile and creep tests were then carried out by using a micro tension torsion testing system. Several empirical constitutive models were adopted to represent the collected raw data and to extract the desired mechanical properties of the solder materials of interest.

In this work, microstructure analysis was conducted on testing coupons mounted upon epoxy stubs by using a Scanning Electron Microscope (SEM), Normaski Optical Microscope (OM), and Energy Dispersive X-ray analysis (EDX). Differential Scanning Calorimetry (DSC) was also used to study melting behavior of the solder alloys such as pasty range, melting point, phase transition temperature, etc. Also, 2-dimensional X-ray Diffraction (2D-XRD) was utilized to measure internal residual stresses induced by the specimen solidification process.

3.2 Uniaxial Test Specimen Preparation Procedure

Solder uniaxial samples have been fabricated by machining of bulk solder material [102], or by melting of solder paste in a mold [48, 54, 103, 104]. Use of a bulk solder bars is undesirable, because they will have significantly different microstructures than those present in the small solder joints used in microelectronics assembly. In addition, machining can develop internal/residual stresses in the specimen, and heat generated during turning operations can cause localized microstructural changes on the exterior of the specimens. Reflow of solder paste in a mold causes challenges with flux removal, minimization of voids, microstructure control, and extraction of the sample from the mold. In addition, many of the developed specimens have shapes that significantly deviate from being long slender rods. Thus, undesired non-uniaxial stress states will be produced during loading.

Other investigators have attempted to extract constitutive properties of solders by direct shear or tensile loading [105-107], or indenting [108], of actual solder joints (e.g. flip chip solder bumps or BGA solder balls). While such approaches are attractive because the true solder microstructure is involved, the unavoidable non-uniform stress and strain states in the joint make the extraction of the correct mechanical properties and stress-strain curves from the recorded load-displacement data very challenging. Also it can be difficult to separate the various contributions to the observed behavior from the solder material and other materials in the assembly (bond pads, silicon die, PCB/substrate, etc.).

In an attempt to avoid many of the specimen preparation pitfalls identified above, a novel specimen preparation procedure was developed. Compared with other specimen

fabrication approaches, this unique technique is able to make micro-scale uniaxial tensile specimens with no requirement of further machining/cutting. The solder specimens in this study were formed in high precision rectangular cross-section glass tubes using a vacuum suction process. The tubes were then cooled by water quenching and sent through a SMT reflow to re-melt the solder in the tubes and subject them to any desired temperature profile (i.e. same as actual solder joints). The solder is first melted in a quartz crucible using a pair of circular heating elements (see Figure 3.1). A thermocouple attached on the crucible and a temperature control module is used to direct the melting process. One end of the glass tube is inserted into the molten solder, and suction is applied to the other end via a rubber tube connected to the house vacuum system. The suction forces are controlled through a regulator on the vacuum line so that only a desired amount of solder is drawn into the tube. The specimens are then cooled to room temperature using a user-selected cooling profile.

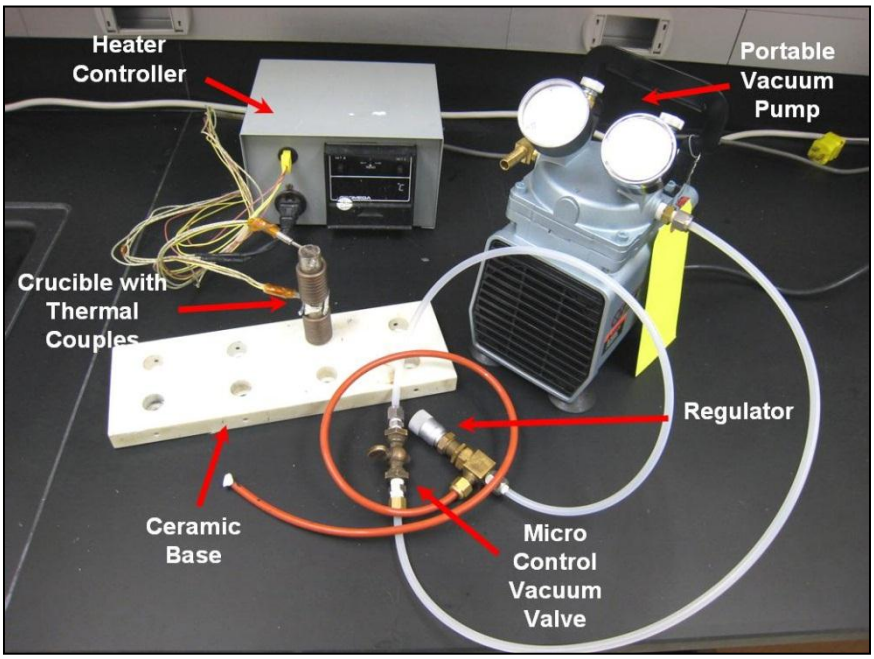

Figure 3.1 Specimen Preparation Hardware

In order to see the extreme variations possible in the mechanical behavior and microstructure, two different cooling profiles were employed in this work:

(1) Water Quenching (W.Q.): water quenching of the tubes (fast cooling rate),

(2) Reflowed (R.F.): controlled cooling using a surface mount technology solder reflow oven.

Typical temperature versus time plot for water quenching is shown in Figure 3.2(a). For the reflow oven controlled cooling, the tubes are first cooled by water quenching, and they are then sent through a reflow oven (9 zone Heller 1800EXL, see Figure 3.3) to re-melt the solder in the tube and subject it to the desired temperature profile. Thermo-couples are attached to the glass tubes and monitored continuously using a radio-frequency KIC temperature profiling system to ensure that the samples are formed using the desired temperature profile (same as actual solder joints). Figure 3.2(b) illustrates the reflow temperature profile used in this work for lead free solder specimens.

Typical glass tube assemblies filled with solder and final extracted specimens are shown in Figure 3.4. For some cooling rates and solder alloys, the final solidified solder samples can be easily pulled from the tubes due to the differential expansions that occur when cooling the low CTE glass tube and higher CTE solder alloy. Other options for more destructive sample removal involve breaking the glass or chemical etching of the glass. The final test specimen dimensions are governed by the useable length of the tube that can be filled with solder, and the cross-sectional dimensions of the hole running the length of the tube. In the current work, uniaxial samples were formed with nominal dimensions of 80 x 3 x 0.5 mm. A thickness of 0.5 mm was chosen because it matches the height of typical BGA solder balls. The specimens were stored in the aging oven

immediately after the reflow process to eliminate possible room temperature aging effects.

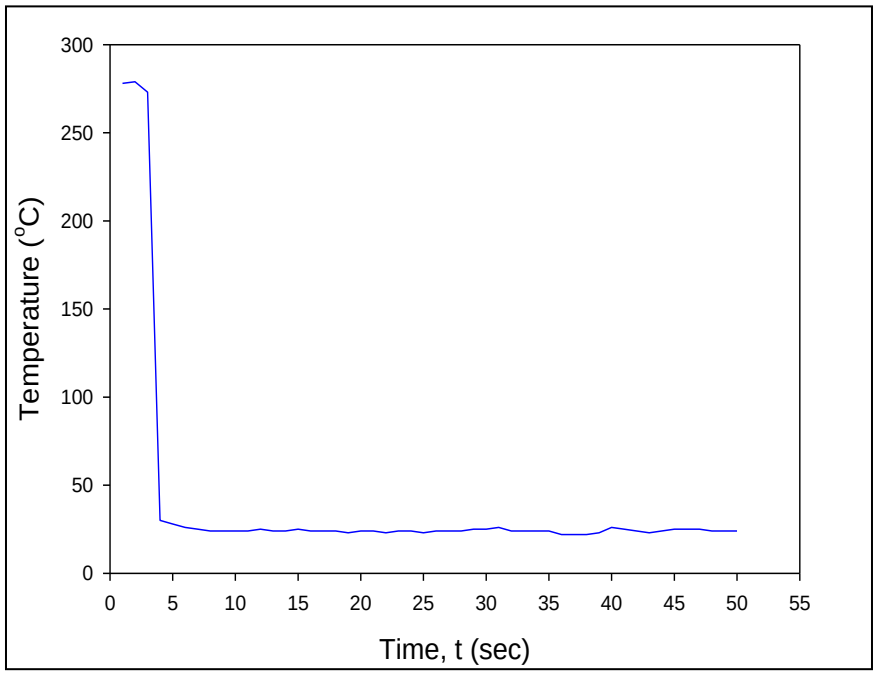

(a) Water Quenching Profile, W.Q.

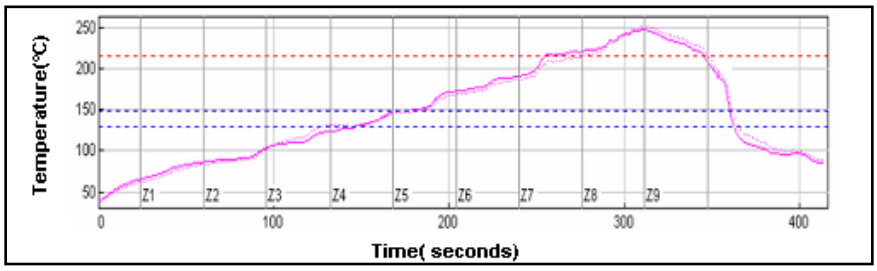

(b) Reflow Profile, R.F.

Figure 3.2 Specimen Cooling/Reflow Profiles

Figure 3.3 Heller 1800EXL Reflow Oven

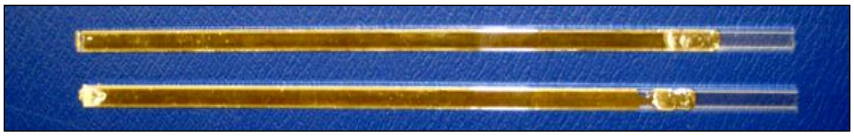

(a) Within Glass Tubes

(b) After Extraction

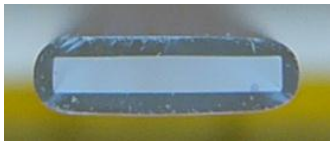

(c) Cross-Section

Figure 3.4 Solder Uniaxial Test Specimens

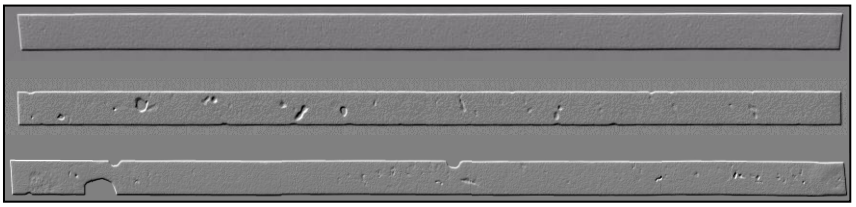

Figure 3.5 X-Ray Inspection of Solder Test Specimens (Good and Bad Samples)

The described sample preparation procedure yielded repeatable samples with controlled cooling profile (i.e. microstructure), oxide free surface, and uniform dimensions. By extensively cross-sectioned on several specimens, the microstructure of any given sample is proven to be very consistent throughout the volume of the sample. In addition, the specimen preparation method has been demonstrated to yield repeatable sample microstructures for a given solidification temperature profile. Samples were inspected using a micro-focus x-ray system to detect flaws (e.g. notches and external indentations) and/or internal voids (non-visible). Figure 3.5 illustrates results for good and poor specimens. With proper experimental techniques, samples with no flaws and voids were generated.

3.3 Mechanical Testing System

A MT-200 tension/torsion thermo-mechanical test system from Wisdom Technology, Inc., as shown in Figure 3.6, has been used to test the samples in this study. The system provides an axial displacement resolution of 0.1 micron and a rotation resolution of 0.001 °. Testing can be performed in tension, shear, torsion, bending, and in combinations of these loadings, on small specimens such as thin films, solder joints, gold wire, fibers, etc. Cyclic (fatigue) testing can also be performed at frequencies up to 5 Hz. In addition, a universal 6-axis load cell was utilized to simultaneously monitor three forces and three moments/torques during sample mounting and testing. Environmental chambers added to the system allow samples to be tested over a temperature range of -185 to +300 ℃.

During uniaxial testing, forces and displacements were measured. The axial stress and axial strain were calculated from the applied force and measured cross-head

displacement using:

$$\sigma = \frac{F}{A} \qquad \varepsilon = \frac{\Delta L}{L} = \frac{\delta}{L} \tag{3.1}$$

where σ is the uniaxial stress, ε is the uniaxial strain, F is the measured uniaxial force, A is the original cross-sectional area, δ is the measured crosshead displacement, and L is the specimen gage length (initial length between the grips). The gage length of the specimens in this study was 60 mm, so that the specimen length to width aspect ratio was 20 to 1 (insuring true uniaxial stress states).

Two major types of testing in the current work, including uniaxial tension and creep, were both conducted at room temperature (25 ℃). The strain rates for the stress-strain testing were $\dot{\varepsilon}$ = 0.01 and 0.001 sec^{-1}, while the applied stresses for the creep testing were σ = 10 and 15 MPa.

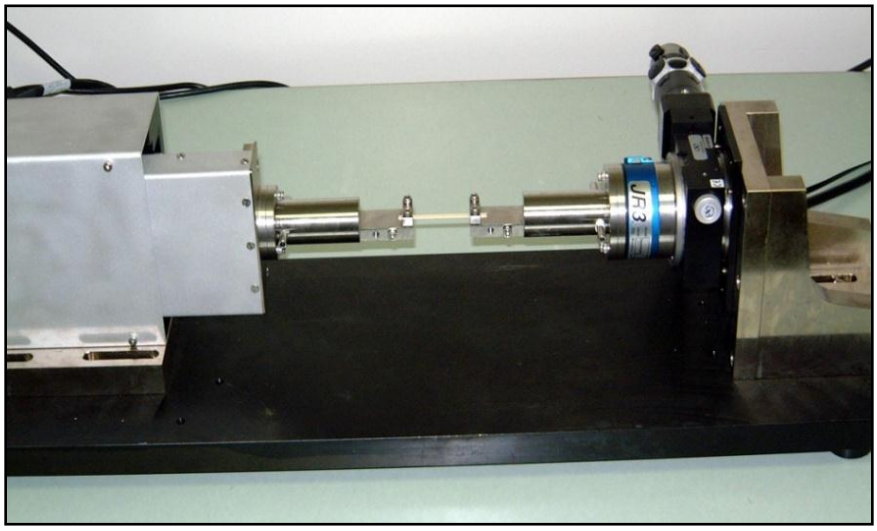

Figure 3.6 MT-200 Testing System with Solder Sample

3.4 Typical Testing Data and Data Processing

Typical Testing Data

A typical recorded tensile stress strain curve for solder with labeled standard material properties is shown in Figure 3.7. The notation "*E*" is taken to be the effective modulus, which is the initial slope of the stress-strain curve. Since solder is viscoplastic, this effective modulus will be rate dependent, and will approach the true elastic modulus as the testing strain rate approaches infinity. The yield stress σ_Y (YS) is taken to be the

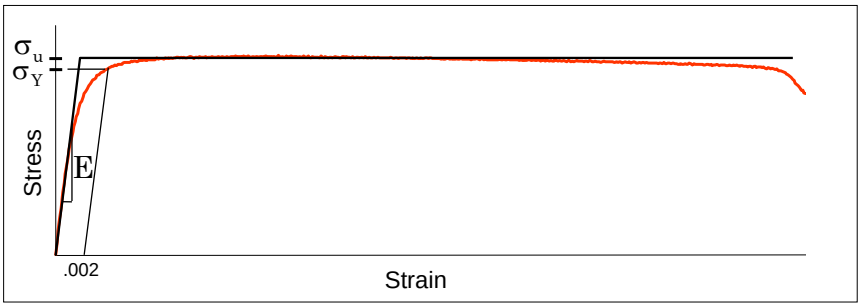

(a) Typical Solder Stress-Strain Curve (Whole Curve)

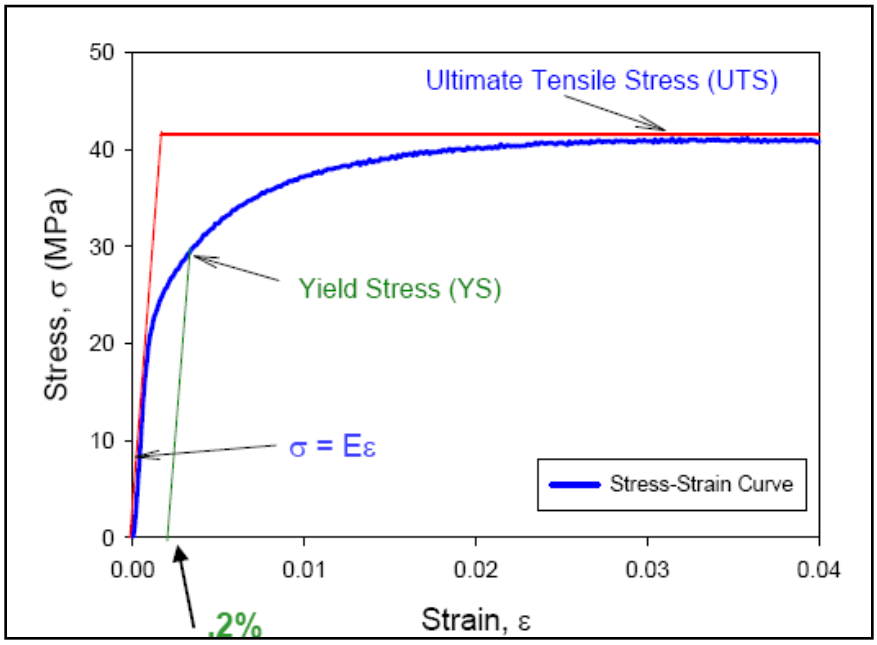

(b) Typical Solder Stress-Strain Curve (Enlarged at Small Strain Range)

Figure 3.7 Typical Solder Stress-Strain Curve and Material Properties

standard 0.2% yield stress (upon unloading, the permanent strain is equal to ε = 0.002). Finally, the ultimate tensile strength σ_u (UTS) is taken to be the maximum stress realized in the stress-strain data. As shown in Figure 3.7(a), the solders tested in this work illustrated nearly perfect elastic-plastic behavior (with the exception of a small transition region connecting the elastic and plastic regions). As the strain level becomes extremely high and failure is imminent, extensive localized necking takes place. These visible reductions in cross-sectional area lead to non-uniform stress-states in the specimen and drops in the applied loading near the end of the stress-strain curve.

Figure 3.8 illustrates a typical solder creep curve (strain vs. time response for a constant applied stress). The load input of a creep test was calculated as:

$$F = \sigma \times w \times t \times 10^3 \ (g) \tag{3.2}$$

where F is the input holding force in gram, σ is the chosen stress level for the creep test in MPa, w is the specimen width in mm, t is the specimen thickness in mm, and g is the acceleration of gravity (9.8 N/kg).

Creep response begins with a quick transition to the initial "elastic" strain level, followed by regions of primary, secondary, and tertiary creep. Depending on the applied stress level, the primary creep region can be more extensive for the SAC alloys. The secondary creep region is typically characterized by a very long duration of nearly constant slope. This slope is referred to as the "steady state" secondary creep rate, and it is often used by practicing engineers as one of the key material parameters for solder in finite element simulations used to predict solder joint reliability. In this work, the measured creep rates were taken to be the minimum slope values in the secondary creep regions of the observed $\dot{\varepsilon}$ versus t responses. The tertiary creep region occurs when

rupture is imminent, and typically features an abrupt change to a nearly constant but significantly increased creep rate.

Creep response begins with a quick transition to the initial "elastic" strain level, followed by regions of primary, secondary, and tertiary creep. Depending on the applied stress level, the primary creep region can be more extensive for the SAC alloys. The secondary creep region is typically characterized by a very long duration of nearly constant slope. This slope is referred to as the "steady state" secondary creep rate, and it is often used by practicing engineers as one of the key material parameters for solder in finite element simulations used to predict solder joint reliability. In this work, the measured creep rates were taken to be the minimum slope values in the secondary creep regions of the observed $\dot{\varepsilon}$ versus t responses. The tertiary creep region occurs when rupture is imminent, and typically features an abrupt change to a nearly constant but significantly increased creep rate.

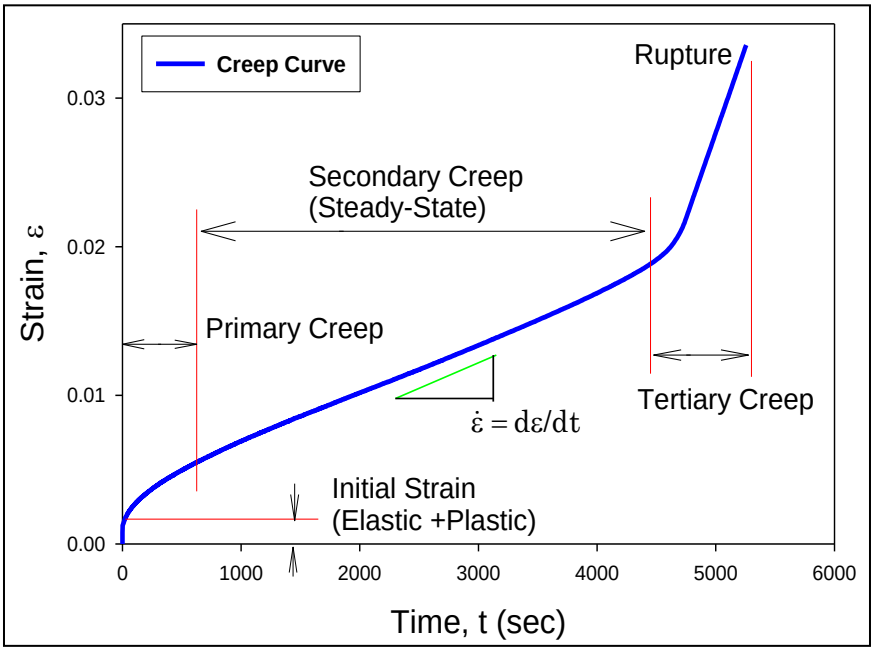

Figure 3.8 Typical Solder Creep Curve and Material Properties

Testing Data Processing

For the uniaxial stress-strain tests, a total of 10 specimens have been tested at a specific aging/testing condition. From the recorded stress-strain data, a set of averaged material properties were extracted. Variations of the average mechanical properties (effective modulus, yield stress, ultimate strength, creep compliance, etc.) with aging were observed and then modeled as a function of aging time. In this work, a single "average" curve was generated to represent a set of 10 recorded stress-strain curves for a certain testing configuration. Although, several different mathematical models can be used to represent the observed data, an empirical four parameter dual hyperbolic tangent model has been demonstrated to be the best option for accurately capturing the variations in both elastic and visco-plastic regions:

$$\sigma(\varepsilon) = C_1 \tanh(C_2\varepsilon) + C_3 \tanh(C_4\varepsilon) \tag{3.3}$$

where C_1, C_2, C_3, C_4 are material constants to be determined.

When consider extreme small strain situation ($\varepsilon \to 0$), the effective modulus (E) can be estimated as:

$$\begin{aligned} \lim_{\varepsilon\to 0} \frac{d\sigma(\varepsilon)}{d\varepsilon} &= \lim_{\varepsilon\to 0} C_1C_2\left\{\left(1-\tanh^2(C_2\varepsilon)\right)+C_3C_4\left(1-\tanh^2(C_4\varepsilon)\right)\right\} \\ &= C_1C_2 + C_3C_4 \end{aligned} \tag{3.4}$$

When consider extreme large strain situation ($\varepsilon \to \infty$), the ultimate tensile strength (UTS) can be obtained by:

$$\lim_{\varepsilon\to\infty} \sigma(\varepsilon) = C_1 + C_3 \tag{3.5}$$

Figure 3.9 illustrates a typical set of 10 solder stress strain curves measured under similar conditions, and the corresponding curve fitting of Eq. 3.3 to the data. Ten raw stress-strain curves are truncated at their UTS and then fitted by the proposed model. The

excellent representation provided by the four parameter empirical model suggests that it indeed provides a mathematical description of a suitable "average" stress-strain curve for a set of experimental curves measured under fixed preconditioning/testing conditions. From the various stress-strain curves obtained at a given aging temperature, the variations in the material properties (effective modulus, yield stress, and ultimate tensile strength) were also able to be determined and modeled as a function of aging time.

In the solder creep experiments, constant stress levels on the order of 25-50% of the observed UTS were applied. In this work, the applied stress as were σ = 10 and 15 MPa, which are approximately 50% of the non-aged UTS value for the SAC-X alloy tested. Due to the long testing time involved, only 5 specimens were tested for each alloy and set of aging/testing conditions. The curves in each set were fitted with an empirical strain-time model to generate an "average" representation of the creep response for those conditions. For the range of test conditions considered in this work, the raw strain versus

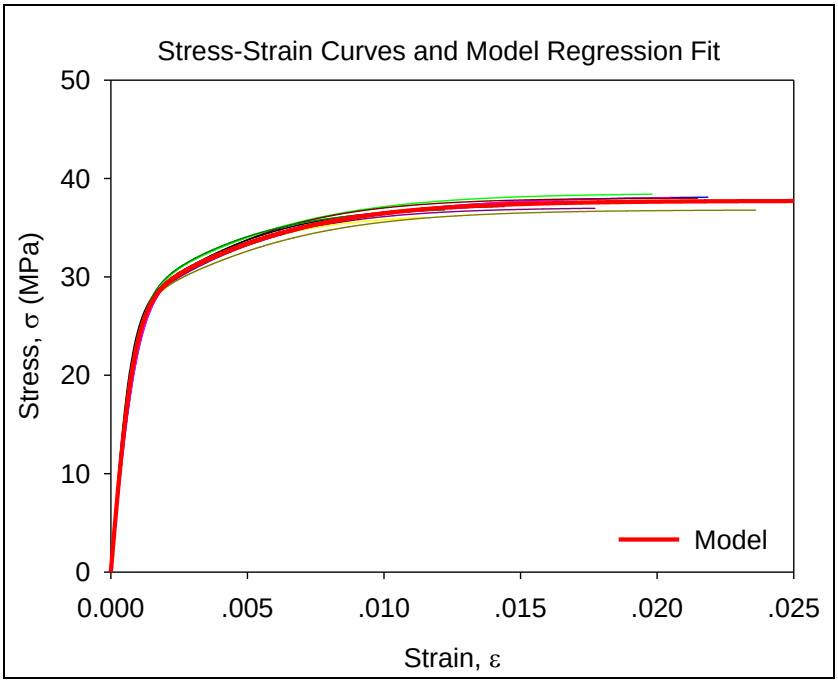

Figure 3.9 Solder Stress-Strain Curves and Empirical Model

time data in the primary and secondary creep regions were found to be well fitted by creep response of the four parameter Burger's (spring-dashpot) model (see Figure 3.10):

$$\varepsilon = \varepsilon(t) = k_0 + k_1 t + k_2\left(1 - e^{-k_3 t}\right) \tag{3.6}$$

From the recorded strain vs. time curves under constant stress, the "steady state" creep strain rates (k_1) have been extracted. In practice, the measured creep rate for each curve was also compared to numerical evaluation of the minimum slope value in the secondary creep region for the observed $\dot{\varepsilon}$ versus t response (see Figure 3.11). Variations of the average creep rates with aging were determined and then modeled as a function of aging time.

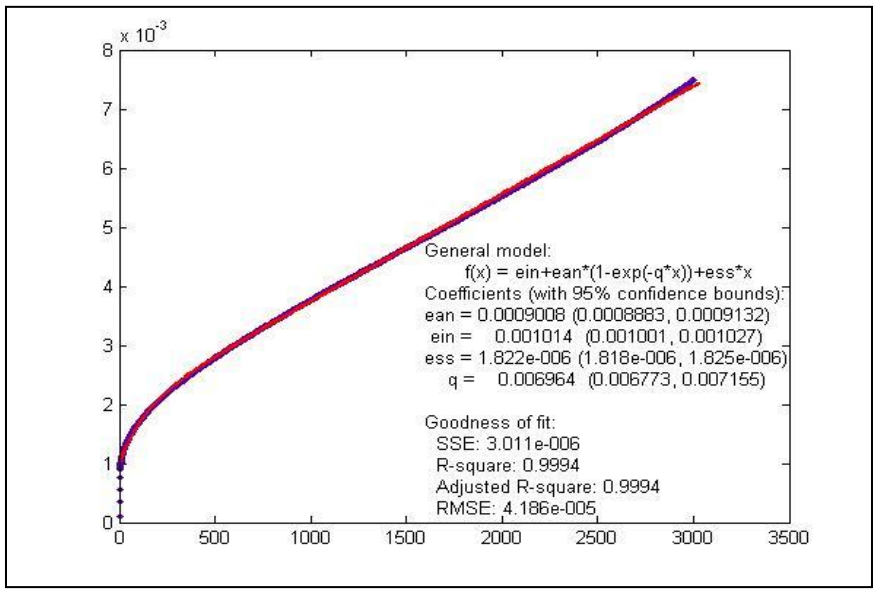

Figure 3.10 Solder Creep Curve and Burger's Model

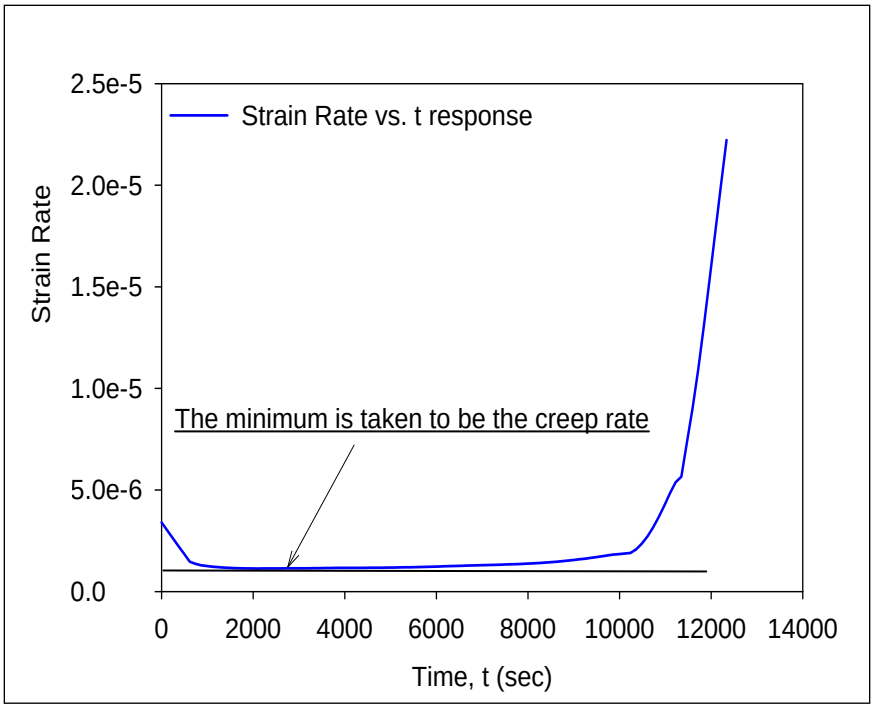

Figure 3.11 Extraction of "Steady State" Creep Rate

3.5 Microstructure Study and Physical Property Investigation

After fabrication by the process discussed in Chapter 3.2, solder specimens were quickly cut into shorter lengths and attached to a pre-prepared epoxy resin stubs by using double-sided carbon tape. This procedure minimized any aging induced microstructure evolution at room temperature. The exposed cross-sectional area of the uniaxial specimens were then grinded using silicon carbide (SiC) sand papers with 320, 600, 1200 in grit size on a metallographic rotating disk. The subsequent fine polishing process included using a 3-μm-particle-size polycrystalline diamond suspension as the abrasive on a woven silk cloth, as well as a 0.05-μm-particle-size BUEHLER MasterPrep alumina polishing suspension on a porous neoprene cloth. The polished surface was then rinsed by distilled water to remove the residuals introduced during polishing process. In order to create a better metallographic structure, a chemical etchant with a mixture of 5%

hydrochloride and 95% methanol was applied for 3-8 seconds, depending on chemical composition of solder alloy. Lastly, the specimen was thoroughly cleaned by ethanol and dried by compressed air.

Microstructure analysis studies of the solder alloys were then conducted on mounted testing coupons, by using an OLYMPUS BX60 Optical Microscope (Figure 3.12) equipped with Normaski prism for grain orientation/structure, and a JEOL JSM-7000F Field Emission Scanning Electron Microscope (Figure 3.13) for morphology. In addition, EDS/EDX was employed to identify intermetallic compounds (IMCs) and map the distribution of chemical elements of interest.

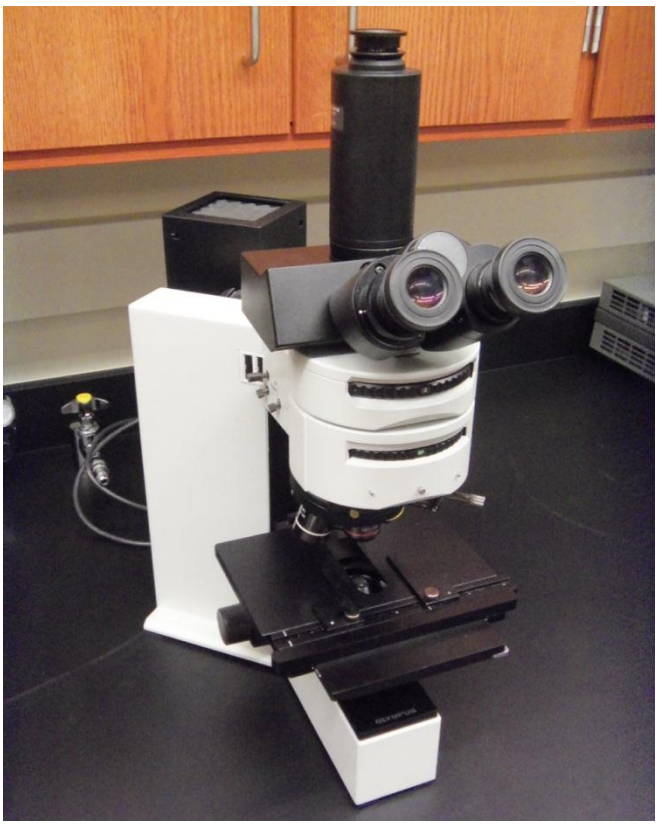

Figure 3.12 OLYMPUS BX60 Optical Microscope

Figure 3.13 JEOL JSM-7000F Field Emission SEM

Furthermore, residual stress analysis was performed on solder samples utilizing a Bruker Discover D8 General Area Detector Diffraction System (GADDS), as shown in Figure 3.14. The cutting-edge 2-D XRD technique enables precise measurements of the internal residual stresses induced by solidification processes.

DSC (Figure 3.15) analysis was also applied to investigate the physical properties of solder materials, such as melting temperature, pasty range, phase transition temperature, etc. The solder specimens were trimmed into small pieces (around 10 mg) and then a relative heat flow (aluminum served as a reference) vs. temperature curve was recorded.

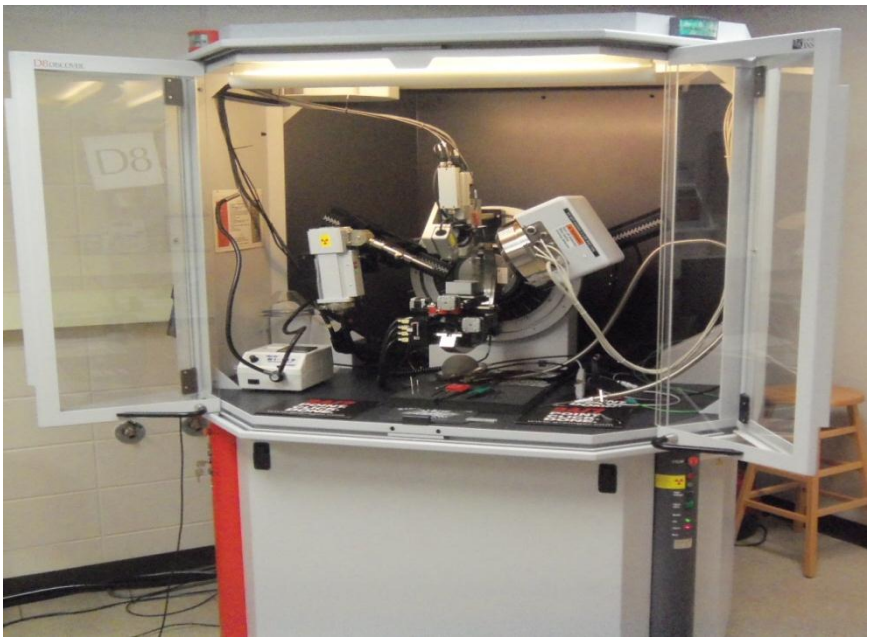

Figure 3.14 Bruker Discover D8 GADDS and Goniometer Setup

Figure 3.15 DSC Device Setup

3.6 Summary and Discussion

A unique specimen preparation procedure was developed in this study to fabricate micro-scale uniaxial tensile specimens. All solder specimens were formed in glass tubes with rectangular cross-section by using a vacuum suction system. Two cooling profiles were adapted in this study, including water quenching and controlled reflow oven cooling. Typical uniaxial samples with nominal dimensions of 80 × 3 × 0.5 mm were utilized.

Uniaxial tensile and creep tests were performed by using a multifunctional microtester. In this study, the experimental data were modeled by empirical constitutive laws so that the corresponding mechanical properties of solder materials could be extracted.

Microstructure analysis was conducted on specimens that were taped upon pre-made epoxy stubs by using SEM and Normaski OM. DSC analysis was also performed to study melting/solidification behavior of solder alloys. Furthermore, residual stresses in the test samples were evaluated by using 2D-XRD technique.

CHAPTER 4

EFFECT OF AGING ON MECHANICAL PROPERTIES OF LEAD FREE SOLDER ALLOYS

4.1 Introduction

Due to the transition from Pb-bearing to Pb-free solders, more efforts have been put in exploring the microstructure, mechanical properties, and failure behavior of lead free solder joints in microelectronic package assemblies. As reviewed by Ma, *et al.* [44], there exists a large discrepancy in the current solder material database even though considerable amount of work has been done on solder material characterization. It is believed that this issue is mainly caused by variations in specimen geometry, fabrication procedure, data acquisition accuracy, and microstructure of the specimens. However, people began to realize that isothermal aging was not a negligible effect for lead free solder alloys, and it might also contribute to the disagreement of the current solder data. It has been known that the microstructure of lead free solder joints is constantly evolving when exposed to isothermal aging and/or thermal cycling environments, and the induced variations in material behavior of lead free solders during aging were unexpectedly large and universally detrimental to reliability [109].

In this chapter, aging effects on solder material properties have been characterized by performing tensile and creep tests over a wide range of aging conditions. The parametric study on aging effects was conducted on SACX0307 (or SACX), a low silver content SAC alloy that has been proposed as a lower cost SAC variation suitable for

enhancing drop reliability. Prior to testing, SACX uniaxial specimens were pre-conditioned according to a full aging test matrix. Reductions in stiffness, yield stress, and ultimate strength were observed and correlated with aging. In addition, dramatic evolution was observed in the creep response of aged SACX solders (up to 1000X increase).

4.2 Effect of Aging on Tensile Behavior

Reflowed SACX specimens for tensile testing were prepared by sample preparation procedure described in Chapter 3. Aging was then performed at five different conditions including room temperature (25 ^{o}C) and four elevated temperatures (50, 75, 100 and 125 ^{o}C) for various durations up to 12 months before test. The aging test matrix is shown in Table 4.1. In this section, all tensile tests were carried out under a constant strain rate of 0.001 sec^{-1} at room temperature (T = 25 ^{o}C). Also, a set of ten specimens were tested under each aging condition.

Aging Temp / Aging Time	25 ^{o}C	50 ^{o}C	75 ^{o}C	100 ^{o}C	125 ^{o}C
As Reflowed	X	X	X	X	X
5 Days	X	X	X	X	X
10 Days	X	X	X	X	X
20 Days	X	X	X	X	X
30 Days	X	X	X	X	X
60 Days	X	X	X	X	X
120 Days	X	X	X	X	X
180 Days	X	X	X	X	X
270 Days	X	X	X	X	X
360 Days	X	X	X	X	X

Table 4.1 SACX Aging Test Matrix (Tensile)

4.2.1 Aging Effects on Stress-Strain Responses

Figure 4.1 illustrates plots of the average stress-strain curves for SACX for aging at 25, 50, 75, 100, and 125 ^{o}C. In each graph, the average stress-strain curves are shown for each aging time (0-360 days). Each average curve represents the fit of Eq. 3.3 to the 10 recorded experimental measurements for a given set of aging conditions. The highest/top curve (red color) in each plot is the stress-strain curve for the non-aged solder (tested immediately after solidification and cool down). As shown in Figure 4.1, the tensile strength as well as the initial slope of stress-strain curves decreases with preconditioning duration at all of the aging temperatures.

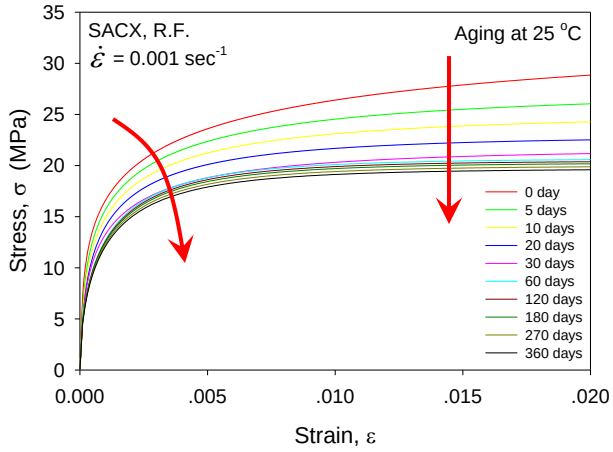

(a) Aging at T = 25 ^{o}C

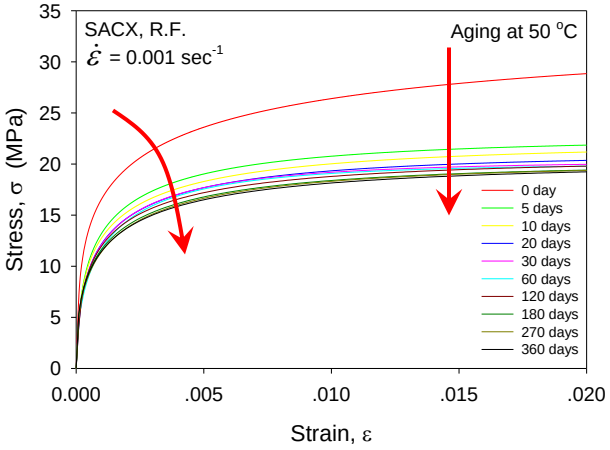

(b) Aging at T = 50 ^{o}C

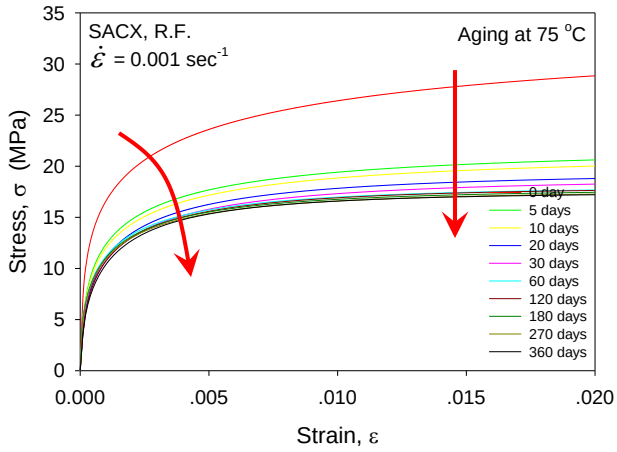

(c) Aging at T = 75 °C

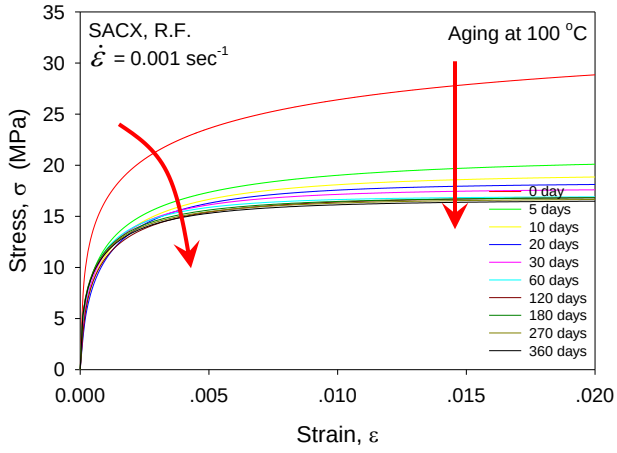

(d) Aging at T = 100 °C

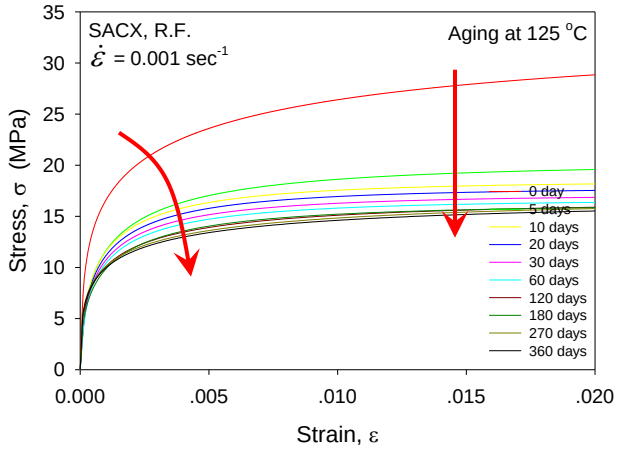

(e) Aging at T = 125 °C

Figure 4.1 Stress-Strain Curves for SACX (R.F., Aged for 0-360 Days)

4.2.2 Aging Effects on Tensile Properties

By following the data processing procedures described in Chapter 3.4, the tensile properties of SACX under each aging condition were extracted from every stress-strain curve shown in Figure 4.1, and then characterized as a function of aging (see Figure 4.2). From the recorded data, it is observed that each tensile property starts with the same point, but afterward decreases dramatically within a short period of time (around 20 days of aging) at all aging temperatures, and finally degrades continuously at a constant rate. The strength and stiffness of SACX under several representative aging conditions are compared in Table 4.2, while the corresponding percentage changes of material properties (Aged vs. Non-aged) are summarized in Table 4.3. For example, the average ultimate tensile stress of as-reflowed (non-aged) SACX specimens was measured to be 29.57 MPa. However, after 360 days of aging at room temperature (T = 25 ^{o}C), the material lost nearly 30% of its tensile strength (21.19 MPa), and the degradation was even more severe after elevated temperature isothermal exposure (e.g. UTS degraded to 16.68 MPa at 125 ^{o}C aging, which led to a more than 40% loss in strength).

	No Aging	25 ^{o}C	50 ^{o}C	75 ^{o}C	100 ^{o}C	125 ^{o}C
E (GPa)	31.87	24.32	22.70	21.58	20.21	20.02
UTS (MPa)	29.57	21.19	20.40	18.08	16.71	16.68
YS (MPa)	21.87	15.71	15.06	13.81	12.68	12.43

Table 4.2 Comparisons of Tensile Properties of SACX Aged up to 360 Days

	25 ^{o}C	50 ^{o}C	75 ^{o}C	100 ^{o}C	125 ^{o}C
E	23.69%	28.77%	32.29%	36.59%	37.18%
UTS	28.34%	31.01%	38.86%	43.49%	43.59%
YS	28.17%	31.14%	36.85%	42.02%	43.16%

Table 4.3 Percentage of loss in Tensile Properties of SACX Aged up to 360 Days

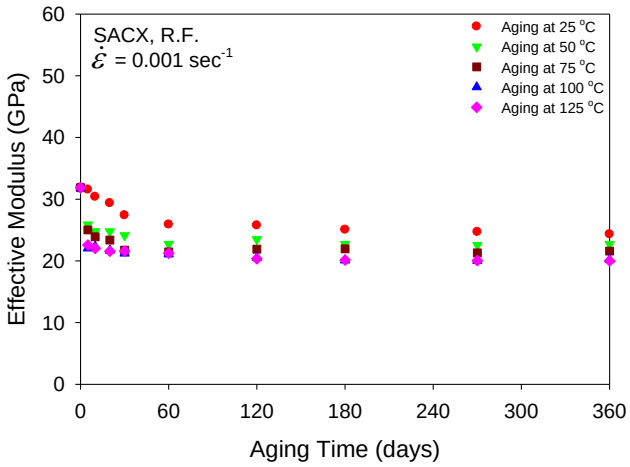

(a) E

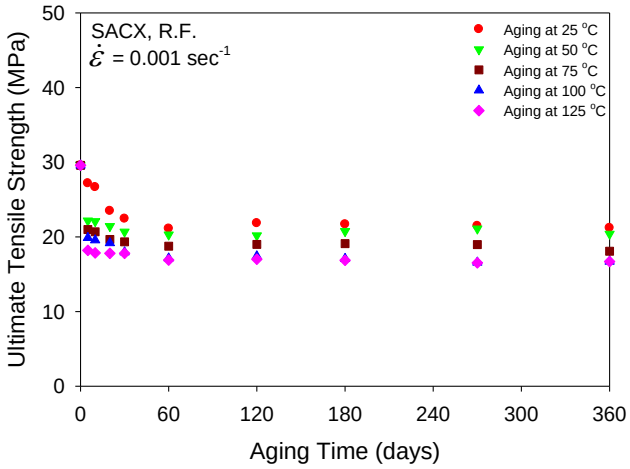

(b) UTS

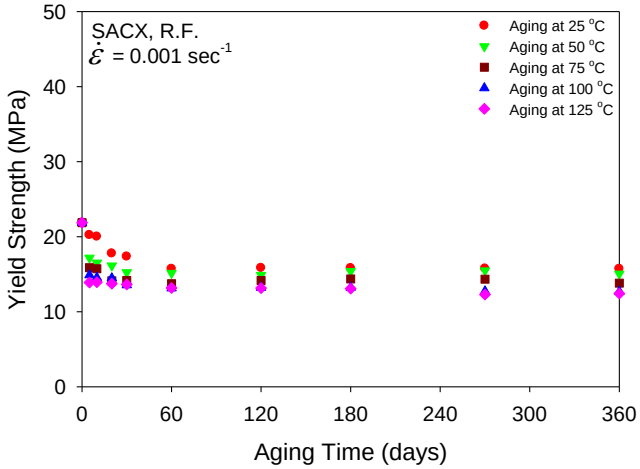

(c) YS

Figure 4.2 Variations in Tensile Properties with Aging for SACX (Data)

4.2.3 Modeling of Aging on Tensile Properties

In this study, the aging induced degradation of SACX tensile properties were modeled by a five-parameter non-linear relationship:

$$y(E,UTS,YS) = y\left(E,UTS,YS\right)_{\infty} + (C_0 + C_1 e^{-\frac{Q}{RT}} t)^{-\frac{1}{2n}} \tag{4.1}$$

where y_{∞}, C_0, C_1, Q and n are material constants, and R = 8.314 $\frac{J}{mol \cdot K}$ is the universal gas constant.

The derivation of this model started from correlating aging effects to the yield stress of solder materials. To begin with, the yield stress of the polycrystalline material, which is inversely proportional to its grain size, can be expressed by Hall-Petch Equation [31]:

$$\sigma_{ys} = \sigma_0 + kd^{-\frac{1}{2}} \tag{4.2}$$

where σ_0 is a material constant representing the overall resistance of the lattice to dislocation movement; k is a constant measuring the contribution of hardening due to grain boundaries; and d is the grain size of the polycrystalline material. On the other hand, the rate of grain growth is known to be proportional to the driving force, while the driving force is proportional to the total amount of grain boundary energy. Therefore, the time t required to reach a given grain size can be approximated by the Grain Growth Equation [31]:

$$d^n - d_0^n = At \tag{4.3}$$

where d_0 is the initial grain size, d is the grain size after aging, n is the exponent (n = 2 for most cases), and A is an Arrhenius type temperature dependent constant given by an exponential law:

$$A = A_0 e^{-\frac{Q}{RT}} \tag{4.4}$$

where A_0 is a material constant, T is the absolute temperature of aging, and Q is the activation energy for boundary mobility. Note that the activation energy for boundary mobility should in theory equal that for self-diffusion, but this is often found not to be the case. By rearranging Eq. 4.3 and replacing d into Eq. 4.2, the yield strength can be expressed in terms of the aging time and aging temperatures:

$$\sigma_{ys} = \sigma_0 + (d_0^n k^{-2n} + A_0 k^{-2n} e^{-\frac{Q}{RT}} t)^{-\frac{1}{2n}} \tag{4.5}$$

For brevity, Eq. 4.5 can be rewritten as:

$$YS = YS_\infty + (C_0 + C_1 e^{-\frac{Q}{RT}} t)^{-\frac{1}{2n}} \tag{4.6}$$

where $C_0 = d_0^n k^{-2n}$, $C_1 = A_0 k^{-2n}$, and $YS_\infty = \sigma_0$. Due to the high correlation between effective modulus, yield stress and ultimate tensile stress, it is also reasonable to extend the aging-YS relationship in Eq. 4.6 to E and UTS. Thus, a multivariate non-linear model describing aging effects on the tensile properties of SACX solder has been developed and expressed in the form of Eq. 4.1. However, due to the lack of evidence showing that grain growth is the most dominant factor affecting the changes in tensile properties of SACX, the proposed model was alternatively validated from a statistical point of view by using the Adaptive Neyman Test (A-N test) on SACN05 (where N = 1, 2, 3, 4) series data measured by Zhang [50]. Detailed Goodness-of-Fit test procedure and model validation are discussed in detail in Appendix A.

Figure 4.3 contains an example regression fit of the proposed model to the measured yield stress data. As illustrated in Figure 4.3(a), the five curves in different

colors represent predicted variations in yield stress of reflowed SACX for different aging temperatures. As mentioned earlier, all curves have the same starting point but continue to degrade at different rates according to the storage (aging) temperature prior to testing. The common starting point, literally the yield stress of a non-aged SACX specimen, can be estimated by simply taking $t = 0$ in Eq. 4.1:

$$YS\big|_{t=0} = YS_\infty + (C_0 + 0)^{-\frac{1}{2n}} = YS_\infty + C_0^{-\frac{1}{2n}} \tag{4.7}$$

In addition, if an infinite aging time is considered ($t = \infty$), the yield stress of SACX converges to a single constant value independent of the aging temperature:

$$YS\big|_{t=\infty} = YS_\infty + (C_0 + \infty)^{-\frac{1}{2n}} = YS_\infty \tag{4.8}$$

Furthermore, the transition region (aging time less than 20 days) is mostly dominated by C_0, C_1 and n; while the spacing and degradation rate of long-term aging are determined by the activation energy Q. Finally, since the model is based on an Arrhenius relationship, the $e^{-\frac{Q}{RT}}t$ term can thus be regarded as an indicator to the state of aging, and the application of Arrhenius acceleration factor holds as well:

$$AF = \frac{t_1}{t_2} = e^{\frac{Q}{R}\left(\frac{1}{T_1} - \frac{1}{T_2}\right)} \tag{4.9}$$

Similarly, the effective modulus and tensile strength data were also modeled by Eq. 4.1 and the results are shown in Figure 4.4. The calculated model constants are tabulated in Table 4.4. The average effective activation energy Q and exponent factor n for SACX are approximately 70 kJ and 2.33, respectively. The performance of the proposed model in predicting the experimentally measured data is also examined in 3-D plots, as shown in Figure 4.5.

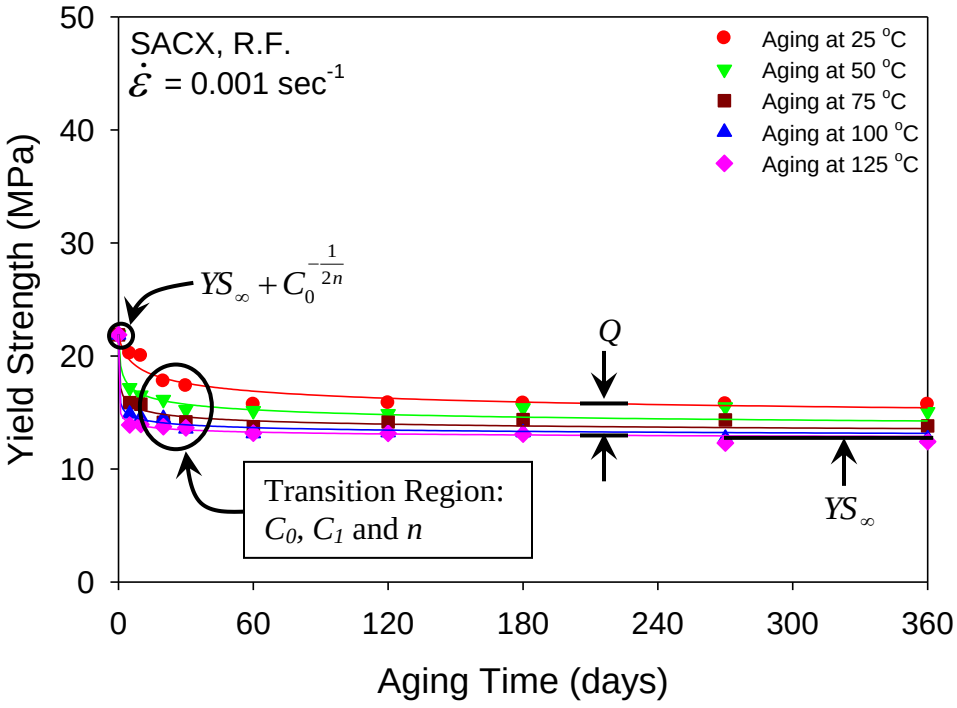

(a) Experimental Data vs. Model

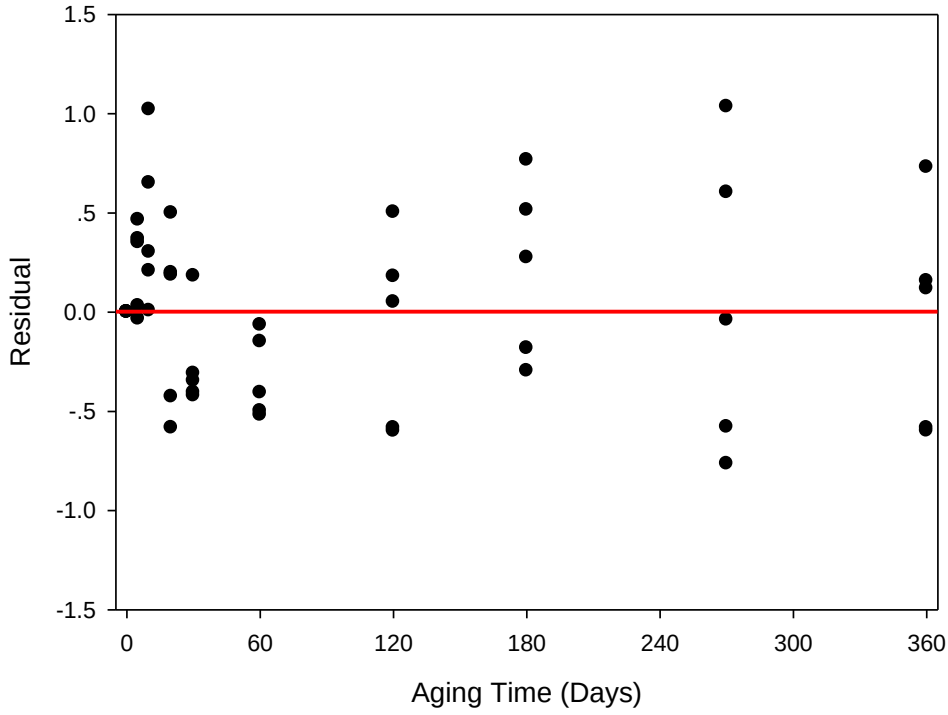

(b) Residual Plot (Absolute Residuals)

Figure 4.3 Variations in YS with Aging Time for SACX (Data + Model)

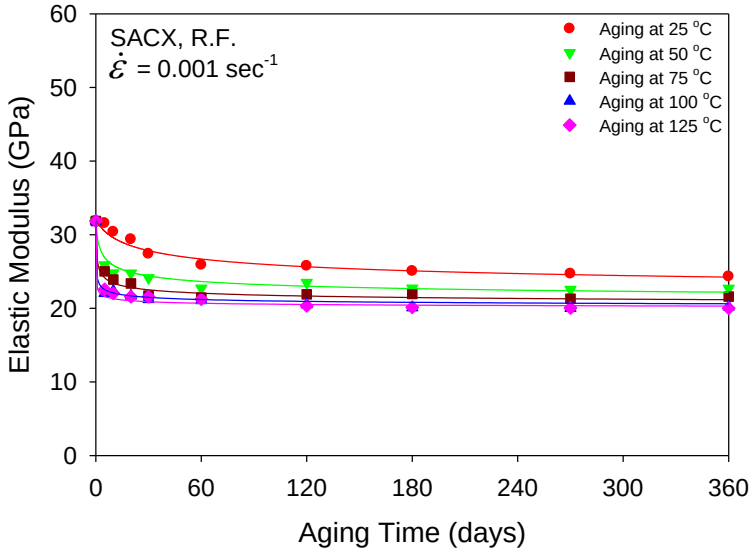

(a) E vs. Aging Time

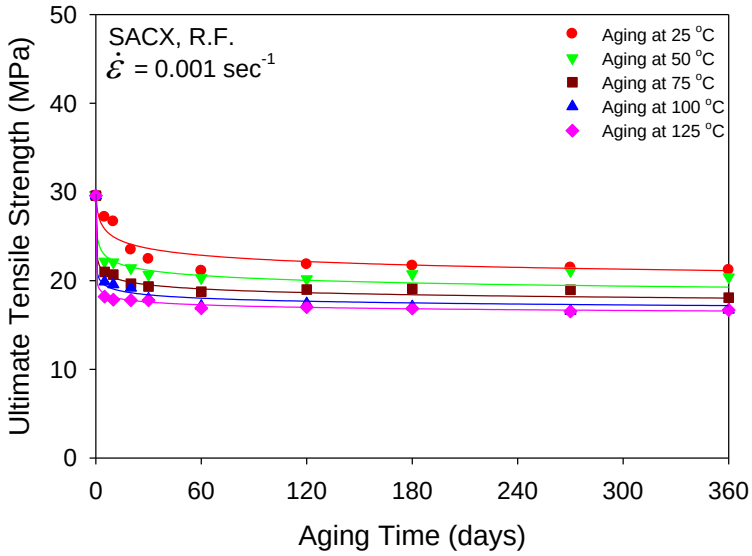

(b) UTS vs. Aging Time

Figure 4.4 Variations in E and UTS with Aging Time for SACX (Data + Model)

	y_∞	C_0	C_1	Q (kJ)	n
E	19.63	4.76×10^{-5}	9.74×10^{7}	75.28	1.99
UTS	15.92	2.40×10^{-6}	3.87×10^{6}	71.44	2.48
YS	11.77	5.26×10^{-6}	1.49×10^{6}	66.87	2.62

Table 4.4 Constants in Model for Tensile Properties vs. Aging for Reflowed SACX

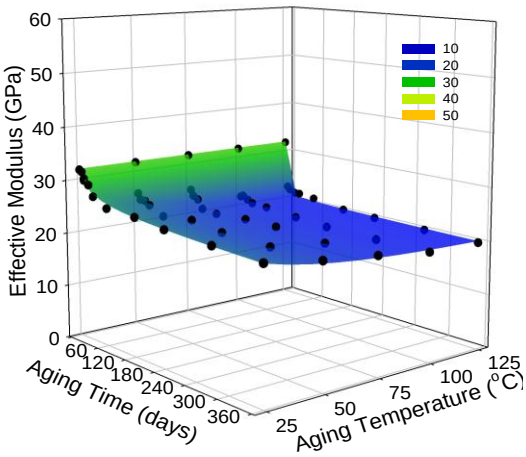

(a) E

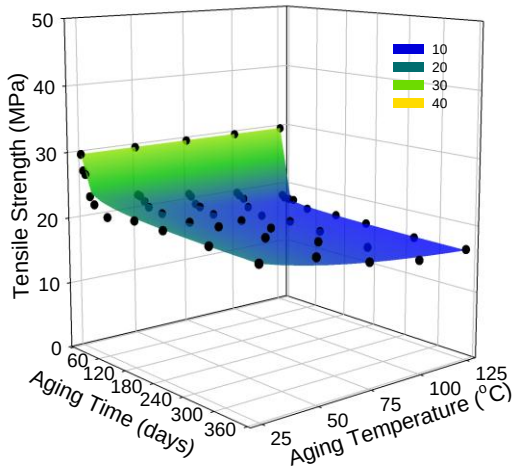

(b) UTS

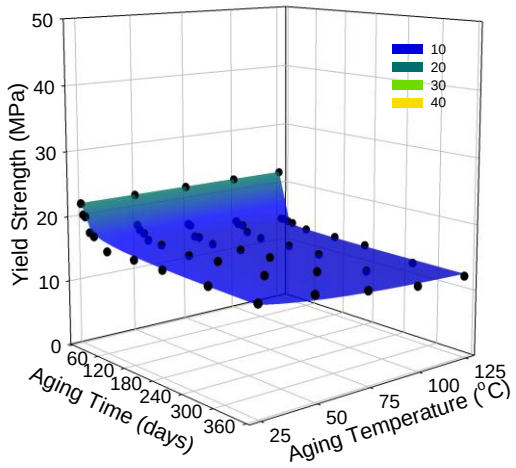

(c) YS

Figure 4.5 Variations in Tensile Properties with Aging for SACX (3D Plots)

4.3 Effect of Aging on Creep Behavior

Uniaxial specimens were fabricated for creep testing by using the casting method described in Chapter 3. After reflow, the creep test specimens were prepared in sets of five, which were then subjected to a specific set of aging conditions as tabulated in Table 4.5. Testing specimens were exposed to five different aging temperatures (T = 25, 50, 75, 100 and 125 ^{o}C) for up to 12 months. All creep tests in this parametric study were conducted at room temperature (T = 25 ^{o}C) with a constant applied stress level σ = 15 MPa.

Aging Temp / Aging Time	25 ^{o}C	50 ^{o}C	75 ^{o}C	100 ^{o}C	125 ^{o}C
As Reflowed	X	X	X	X	X
0.5 Months	X	X	X	X	X
1 Month	X	X	X	X	X
2 Months	X	X	X	X	X
3 Months	X	X	X	X	X
4 Months	X	X	X	X	X
5 Months	X	X	X	X	X
6 Months	X	X	X	X	X
9 Months	X	X	X	X	X
12 Months	X	X	X	X	X

Table 4.5 SACX Aging Test Matrix (Creep)

4.3.1 Aging Effects on Creep Responses

Figure 4.6 illustrates typical recorded creep curves for the five different aging temperatures (T = 25, 50, 75, 100, and 125 ^{o}C). Each graph is for a given aging temperature, and the various creep curves in a particular plot are for different aging times, illustrating the evolution of the creep response with duration of aging. The lowest (red)

curve in each plot represents the creep response for the non-aged SACX solder (tested immediately after solidification and cool down). For brevity and clarity of the presentation, only one of the five available creep curves is shown in each plot for each set of aging conditions. The plots in Figure 4.6 clearly indicate a dramatic evolution of the creep response at all of the aging temperatures. The slope of the secondary creep region changes by several orders of magnitude as aging progresses.

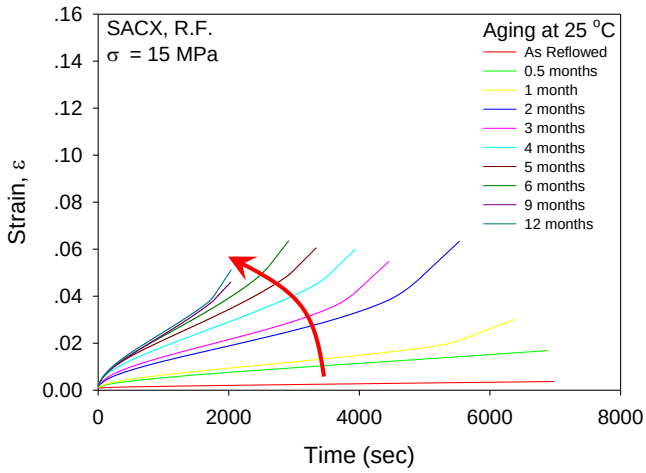

(a) Aging at T = 25 °C

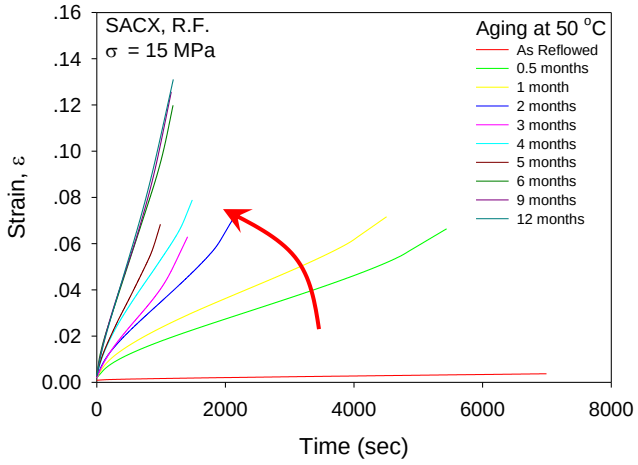

(b) Aging at T = 50 °C

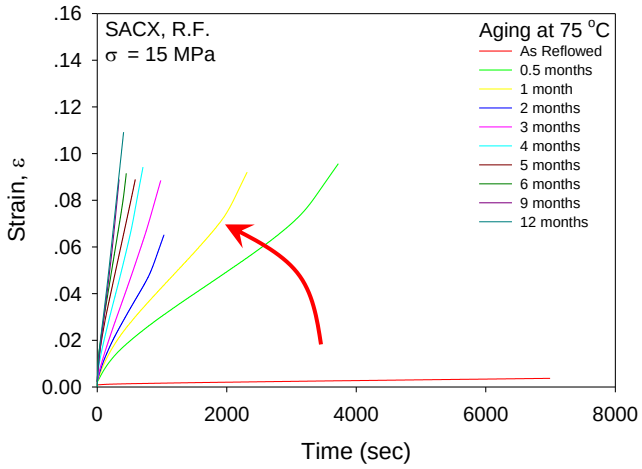

(c) Aging at T = 75 °C

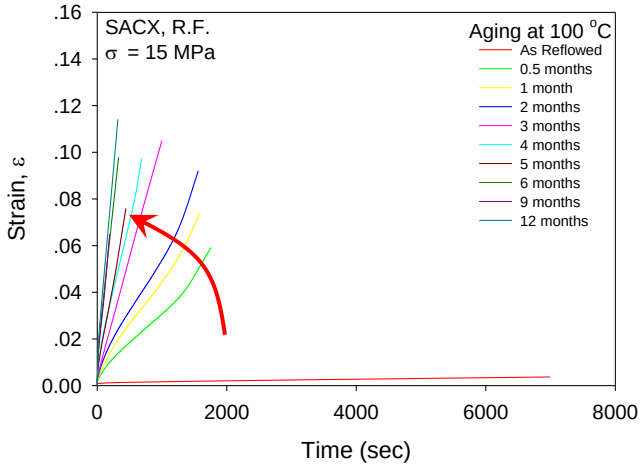

(d) Aging at T = 100 °C

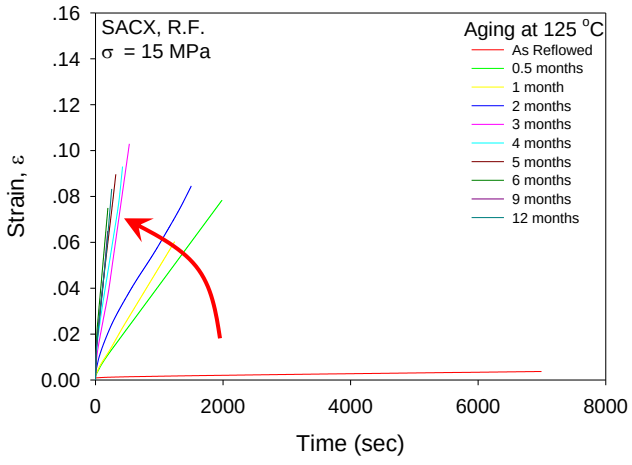

(e) Aging at T = 125 °C

Figure 4.6 Creep Curves for SACX (R.F., Aged for 0-12 Months)

4.3.2 Aging Effects on Creep Properties

The effects of aging on the creep rate can be better explored by plotting the extracted secondary creep rates versus the aging time. The creep rates for SACX under various aging conditions were obtained from each creep curve in Figure 4.6 and then plotted in Figure 4.7. In this plot, the creep rate evolution is indicated for each of the five aging temperatures. Each data point represents the average creep rate measured for the five samples tested at a given set of aging conditions. According to Figure 4.7, it is apparent that SACX experiences dramatic changes in creep rate for elevated temperature aging. It is also observed that the functional variations with aging at 50, 75, 100, and 125 ^{o}C become approximately "in parallel" with long term aging and are closely spaced. They are also significantly separated from the variation occurring with room temperature aging. After the large changes that occur during the first month of aging, the variations of the creep rate (log scale) for all aging temperatures become nearly linear with longer aging times (1-6 months approximately). However, it can be seen that some stabilization of evolution of the creep rate has occurred after 6 months of aging, and that the rapid degradation has stopped.

Table 4.6-4.7 lists the secondary creep rates of SACX under several representative aging conditions and the corresponding increases in steady state strain rate when compared to the non-aged samples. For example, the creep rate of SACX increases by a factor of 56X after 12 months room temperature aging (T = 25 ^{o}C), while experiences nearly 1000X increase after same duration of isothermal exposure at elevated temperature (T = 125 ^{o}C).

	25 °C	75 °C	125 °C
No Aging		3.27×10^{-7}	
1 Month	2.77×10^{-6}	2.99×10^{-5}	4.60×10^{-5}
3 Months	7.44×10^{-6}	8.05×10^{-5}	1.47×10^{-4}
6 Months	1.60×10^{-5}	1.69×10^{-4}	3.12×10^{-4}
12 Months	1.82×10^{-5}	2.60×10^{-4}	3.16×10^{-4}

Table 4.6 Comparisons of Creep Rate (sec^{-1}) for SACX Aged up to 12 Months

	25 °C	75 °C	125 °C
1 Month	8.48X	91.04X	140.57X
3 Months	22.77X	246.04X	449.63X
6 Months	49.04X	515.78X	953.58X
12 Months	55.66X	795.54X	966.94X

Table 4.7 Increases in Creep Rates for SACX Aged up to 12 Months
(Aged vs. Non-aged, Non-aged as Baseline)

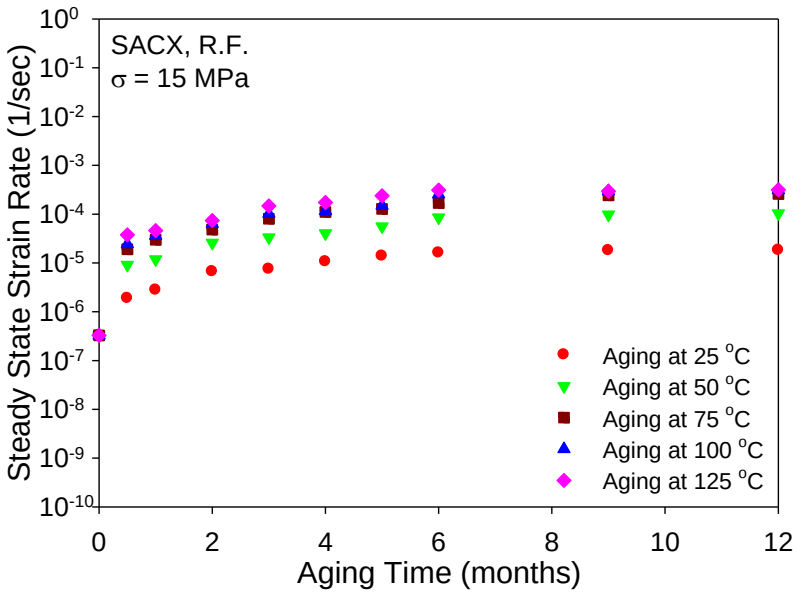

Figure 4.7 Evolution of Creep Strain Rate with Aging for SACX (Data)

4.3.3 Modeling of Aging on Creep Properties

For each aging temperature, the evolution of the creep rate was fit with a non-linear relationship for the data up to 6 months of aging:

$$\dot{\varepsilon} = e^{C_0 + C_1 t + C_2\left(1 - e^{-C_3 t}\right)} \tag{4.10}$$

$$\log \dot{\varepsilon} = C_0 + C_1 t + C_2\left(1 - e^{-C_3 t}\right) \tag{4.11}$$

If the strain rate versus aging time data are plotted with a log scale on the vertical axis (as in Figures 4.8), constant C_0 is the intercept and constant C_1 is the slope of the linear part of the curve for large aging times. Constants C_2 and C_3 are associated with the nonlinear transition region in the first 20-30 days of aging.

The model has been demonstrated to work well for up to 6 months of aging at all temperatures for SACX (Figure 4.9) as well as other SAC alloys including SAC105, SAC205, SAC305 and SAC405 [110]. However, the model does break down for SACX if 9 and 12 month aging data are also included. As shown in Figure 4.10, model predictions clearly deviated from the actual measurements for all aging temperatures after long-term aging.

Due to the breakdown of the proposed model (Eq. 4.10) in predicting long-term creep-aging behavior of SACX, another model of aging on creep rate of solder materials has been developed. It is based on the empirical model of aging on effective modulus (Eq. 4.1) as well as a creep model proposed by Darveaux and Banerji [111]:

$$\dot{\gamma} = A\left(\frac{G}{T}\right)\left[\sinh\left(\beta\frac{\tau}{G}\right)\right]^m e^{-\frac{Q}{RT}} \tag{4.12}$$

In this model, shear strain rate $\dot{\gamma}$ is determined as a function of testing temperature T, applied shear stress τ, activation energy Q, and shear modulus G. In addition, by using

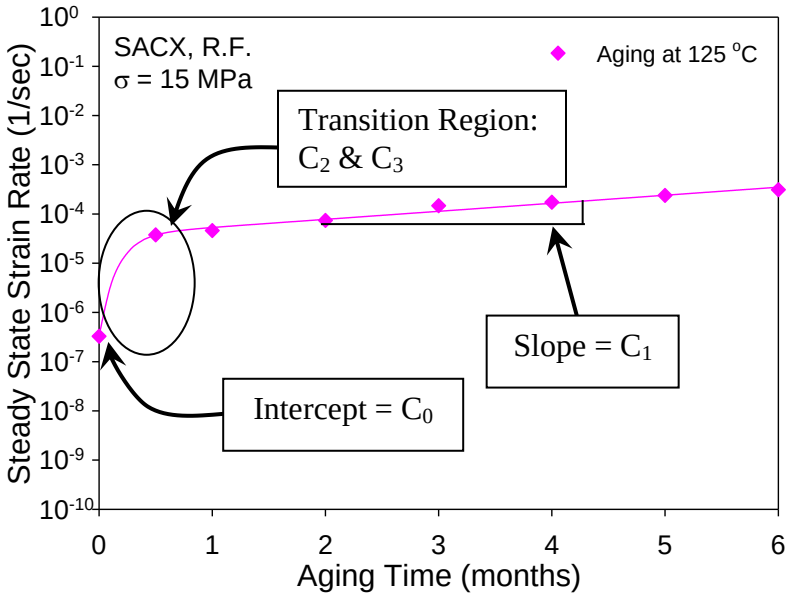

Figure 4.8 Example of Curve Fitting with the Proposed Aging Model

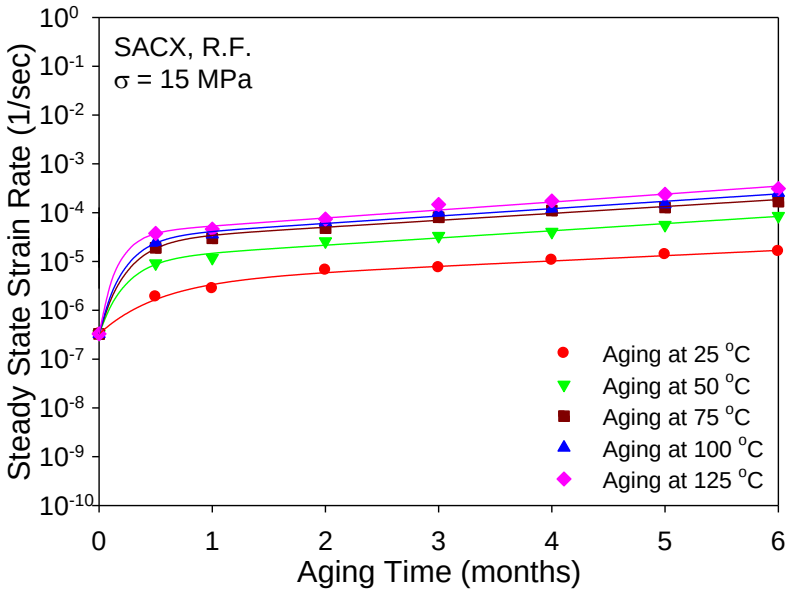

Figure 4.9 Variations in Creep Rate with Aging Time for SACX (Data + Model)

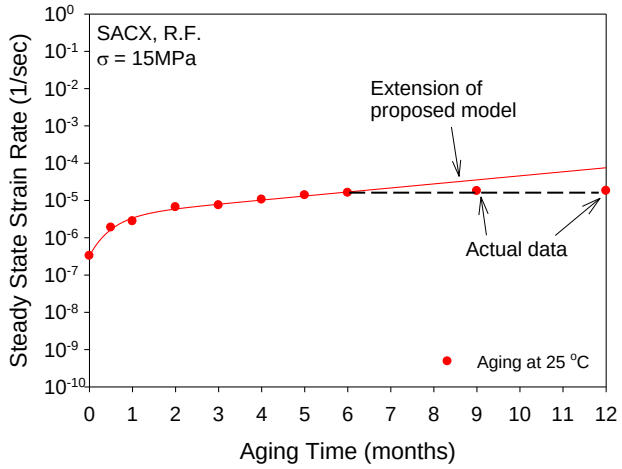

(a) Aging at T = 25 °C

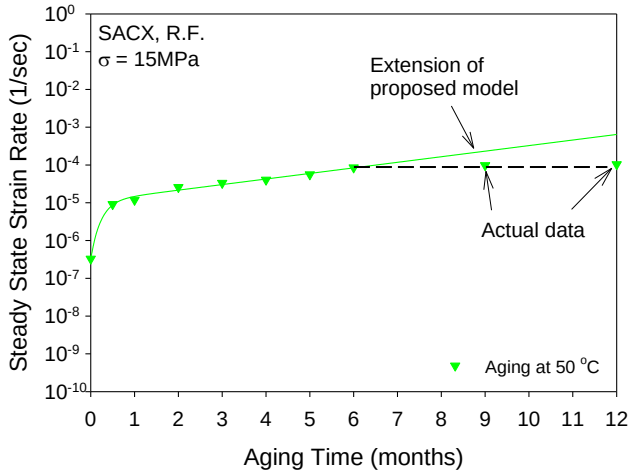

(b) Aging at T = 50 °C

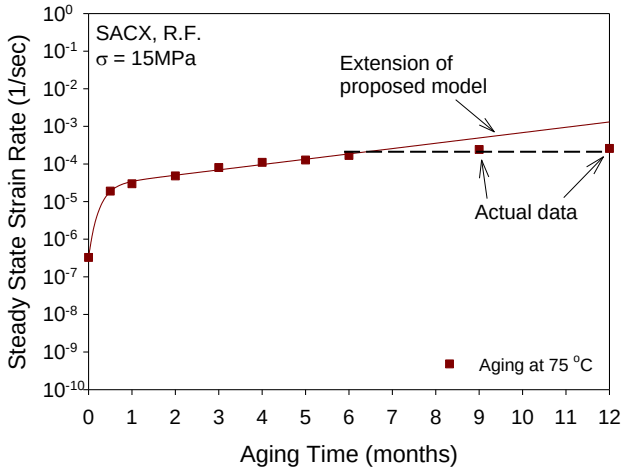

(c) Aging at T = 75 °C

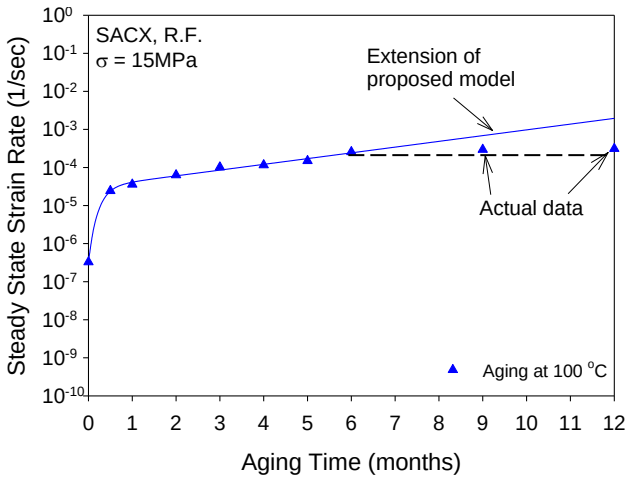

(d) Aging at T = 100 °C

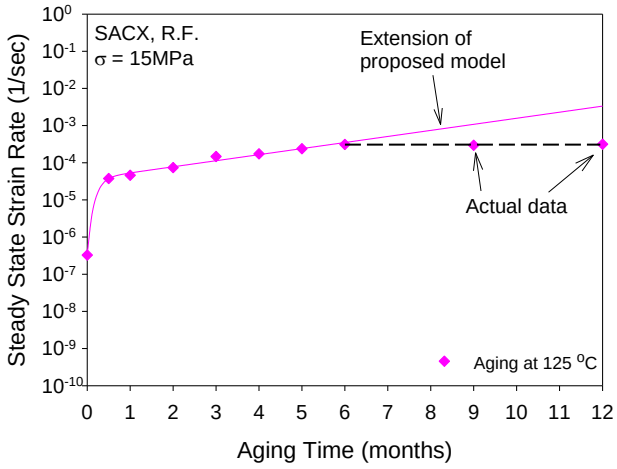

(e) Aging at T = 125 °C

Figure 4.10 Breakdown of the Aging Model for the Creep Rate of SACX

Eq. 1.9-1.11, Darveaux's Model can be rewritten as:

$$\dot{\varepsilon} = \frac{1}{\sqrt{3}} \frac{A}{T} \frac{E}{2(1+\nu)} \left[\sinh\left(\beta \frac{2(1+\nu)}{\sqrt{3}} \frac{\sigma}{E} \right) \right]^m e^{-\frac{Q}{RT}}$$

(4.13)

where $\dot{\varepsilon}$ is the tensile creep strain rate, E is the effective modulus, σ is the applied stress level, ν is the Poisson's ratio, T is testing temperature, and A, β are material constants. Since all creep tests were performed under the same testing condition (T = 25 ^{o}C and σ = 15 MPa), Eq. 4.13 can thus be further simplified to:

$$\dot{\varepsilon} = D_1 E(T,t) \left[\sinh\left(\frac{D_2}{E(T,t)} \right) \right]^m \tag{4.14}$$

by letting $D_1 = \frac{1}{2\sqrt{3}(1+\nu)} \frac{A}{T} e^{-\frac{Q}{RT}}$ and $D_2 = \frac{2(1+\nu)}{\sqrt{3}} \beta$. Note that the effective modulus $E(T,t)$ in Eq. 4.14 is aging-dependent and can be associated with aging temperature and aging time by using $E(T,t) = E_\infty + (C_0 + C_1 e^{-\frac{Q}{RT}} t)^{-\frac{1}{2n}}$ (Eq. 4.1), where T and t are for aging temperature and aging time, respectively.

Model predictions and the experimental measurements are compared and plotted in Figure 4.11-4.12. The estimated constants (tabulated in Table 4.8) are chosen to be consistent with the results obtained from the tensile data. Overall, the new aging-creep model can accurately represent most of the experimentally measured data points except for the transition regions with elevated temperature aging. This issue might be fixed by adding another term d^{-p} in Eq. 4.14 to include grain size effects:

$$\dot{\varepsilon} = D_1 E(T,t) [d(T,t)]^{-p} \left[\sinh\left(\frac{D_2}{E(T,t)} \right) \right]^m \tag{4.15}$$

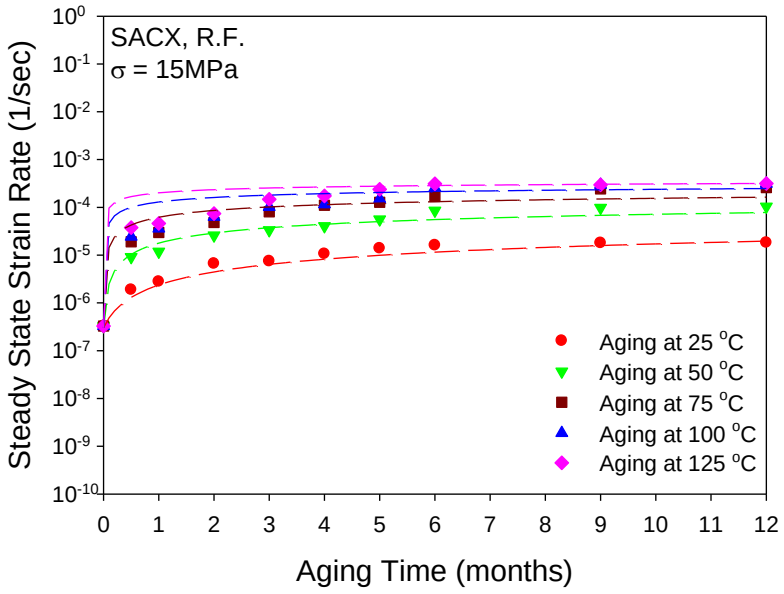

Figure 4.11 Variations in Strain Rate with Aging for SACX (New Model)

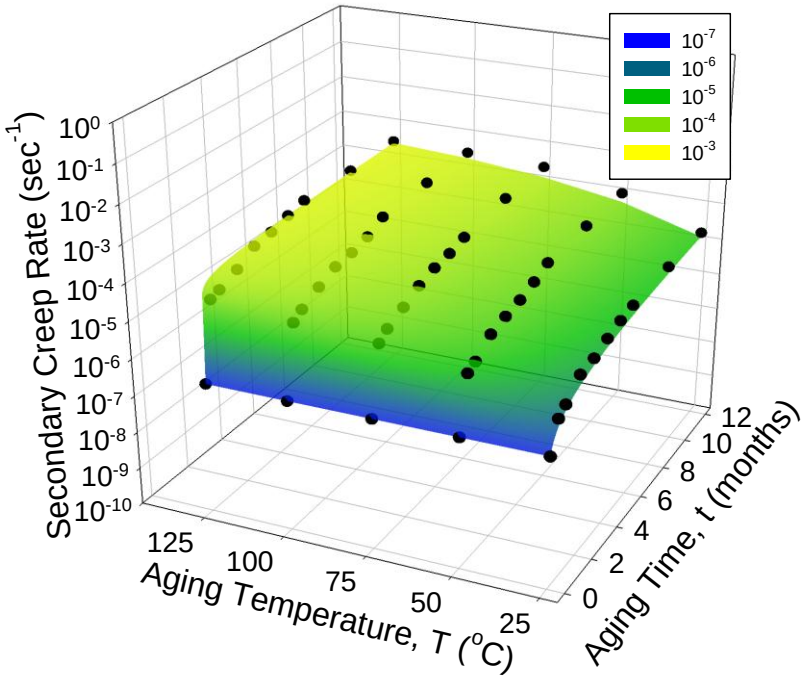

Figure 4.12 Variations in Strain Rate with Aging for SACX (3D Plot)

	E_∞	C_0	C_1	Q (kJ)	n	D_1	D_2	m
This model	19.46	4.19×10^{-5}	9.66×10^{5}	71.03	2.00	0.93	9.93	16.4
Tensile model	19.63	4.76×10^{-5}	9.74×10^{7}	75.28	1.99	/	/	/

Table 4.8 Constants in Model for Strain Rate vs. Aging for Reflowed SACX

4.4 Summary and Discussion

In this chapter, the effects of aging on mechanical behavior have been examined by performing stress-strain and creep tests on SACX solder samples that were aged for various durations (0-12 months) at room temperature (25 ^{o}C), and several elevated temperatures (50, 75, 100, and 125 ^{o}C). Under each aging condition, a set of 10 tests were conducted for stress-strain testing while 5 tests were performed for creep testing. All tests were carried out by a micro-tester at room temperature (T = 25 ^{o}C). The experimentally measured stress-strain curves and creep curves were then fitted by using constitutive models discussed in Chapter 3. The material properties (such as effective modulus, yield stress, ultimate strength, steady state creep rate, etc) under each aging condition were determined from the model fitting curves.

The variations of tensile and creep properties were observed as a function of aging (aging time and aging temperature). As expected, the mechanical properties and creep rates evolved (degraded) more dramatically when the aging temperature was increased. The recorded data also demonstrate that the majority of degradation occurs within first month of aging. Afterwards, the material properties continue to decrease by a linear manner with aging time.

A four parameter non-linear aging model fit well to the SACX creep data up to 6 months of aging; however, the extension of the model deviated from the experimental measurements of samples with 9 and 12 months of aging. The creep rate was found to be nearly constant after 6 months of isothermal exposure, and thus a saturation point for the degradation of the creep rate was reached.

Two models of aging for solder materials have been established. It has been

shown that both models can interpret data well and estimate the material properties for a given aging temperature T and aging time t. Moreover, an aging indicator was proposed to quantitatively estimate the state of aging. This concept might be useful for applications such as life prediction of solder joints.

CHAPTER 5

ENHANCED AGING RESPONSE USING DOPED LEAD FREE SOLDER ALLOYS

5.1 Introduction

As demonstrated in the previous chapters, dramatic changes occur in the constitutive and failure behavior of solder materials and solder joint interfaces during isothermal aging. However, these effects have been largely ignored in most studies involving solder material characterization or finite element predictions of solder joint reliability during thermal cycling. It is also widely acknowledged that the large discrepancies in measured solder mechanical properties from one study to another are due to differences in the microstructures of the tested samples. This problem is further exacerbated by the aging issue, as it is clear that the microstructure and material behavior of the samples used in even a single investigation are moving targets that are evolving rapidly even at room temperature. Aging induced evolution of the solder material properties also greatly complicates the use of finite element analysis to make accurate reliability predictions. For all of these reasons, there is much interest in the industry in establishing optimal lead free solder alloys that minimize aging effects and thus enhance thermal cycling and elevated temperature reliability.

In this study, aging was performed on four sets of lead free solders. Doped solder materials under consideration include SACX, SN100C, SAC-Zn and SN96CI. Variations in material properties were observed and modeled as a function of aging. Analogous

tests were performed on "standard" (non-doped) lead free solder alloys for comparison purposes. Table 5.1 summarizes the designed (ideal) chemical compositions of doped/non-doped solder alloys. As is indicated, most dopants are added into the alloy as "replacements" for copper, but the amount of silver remains unchanged.

All solder specimens were prepared by using the same casting process and reflow profile (controlled solidification) as mentioned in the previous chapters. For Set 1, design of experiments and partial test results of SACX have already been presented in Chapter 4, while analogous data for SAC105 and SAC205 are available in Zhang's Dissertation [112]. Initial studies of aging effects on lead free solders from sets 2-4 were also conducted by performing both uniaxial tensile and creep tests on samples with various aging conditions. For simplicity, the specimens from sets 2-4 were pre-conditioned for up to 180 days but only one aging temperature (T = 100 ^{o}C) was utilized. The detailed design of experiments is summarized in Table 5.2.

		Ag	Cu	Bi	Ni	Zn	Co	Sn
Set 1	SACX	0.30	0.70	0.10	/	/	/	Balanced
	SAC105*	1.00	0.50	/	/	/	/	
	SAC205*	2.00	0.50	/	/	/	/	
Set 2	SN100C	/	0.65	/	0.05	/	/	
	Sn-0.7Cu	/	0.70	/	/	/	/	
Set 3	SAC-Zn	3.50	0.74	/	/	0.21	/	
	SAC3595	3.50	0.95	/	/	/	/	
Set 4	SN96CI	3.80	0.97	/	/	/	0.03	
	SAC3810	3.80	1.00	/	/	/	/	

*: Test Results of SAC105 and SAC205 are available in Zhang's Dissertation [112]

Table 5.1 Chemical Compositions of Doped/Non-Doped Solder Materials (in wt.%)

Solder Materials	SN100C and Sn-0.7Cu SAC-Zn and SAC3595 SN96CI and SAC3810
Casting Condition	R.F.
Testing Conditions	$T_{testing}$ = 25 ^{o}C (RT) for all tests $\dot{\varepsilon}$ = 0.001 sec^{-1} for tensile tests σ = 15 MPa for creep tests
Aging Temperature	100 ^{o}C
Aging Times	0, 5, 10, 20, 30, 60, 120, 180 days for tensile 0, 0.5, 1, 2, 3, 4, 5, 6 months for creep

Table 5.2 Design of Experiment for Doped/Non-Doped Solders

5.2 Effect of Dopants on Aging Resistance in Stress-Strain Behavior

By using the data processing procedures from Chapter 3, average stress-strain curves for solders of interest were generated under the chosen set of aging conditions. Then, the tensile properties were extracted from each stress-strain curve and plotted and modeled against aging. Thus, the aging induced degradations of the tensile stress-strain properties of doped solders could be compared to those without dopants by evaluating the variations in effective modulus, yield stress, and ultimate tensile stress of the solders.

5.2.1 SACX, SAC105, and SAC205

The tensile behavior of SACX has been presented in Chapter 4 (Figure 4.1 for stress-strain responses and Figure 4.2 for variations in tensile properties), while plots for SAC105 and SAC205 can be found in Ref [112]. Figure 5.1 contains an example set of graphs that illustrates the evolution of the effective effective modulus (E), ultimate tensile strength (UTS), and yield stress (YS) of the three alloys for aging at 100 ^{o}C. It is observed that the mechanical properties of SACX are better than those of SAC105 and

approach those of SAC205 with longer aging times. This is surprising given the low silver content of the SACX alloy since it has been documented that the strength of SAC alloy highly depends on the amount and size of fine Ag_3Sn particles [113]. High silver content SAC alloys are supposed to contain more Ag_3Sn intermetallic compounds and thus be much stiffer as well as stronger than low silver content SAC alloys. However, due to the existence of 0.1% Bi, the strength properties of SACX (with only 0.3% Ag) exceed those of SAC105 (with 1% Ag) for all aging times, while a cross-over occurs for the effective modulus variation near the 20 day point for elevated temperature aging. As demonstrated in Figures 5.2-5.5, similar trends were observed for the other four aging temperatures (T = 25, 50, 75, and 125 ^{o}C). Thus, it is valid to conclude that for long term aging at any temperature:

$$E_{SAC105} < E_{SACX} < E_{SAC205} \tag{5.1}$$

$$YS_{SAC105} < YS_{SACX} < YS_{SAC205} \tag{5.2}$$

$$UTS_{SAC105} < UTS_{SACX} < UTS_{SAC205} \tag{5.3}$$

It can also be seen that the strength and stiffness properties of the SACX alloy stabilize much more quickly with aging. After 10-20 days of aging, the properties of SACX are basically constant, while those for SAC105 and SAC205 continue to decline/degrade in a linear manner with time.

Similar comparisons were also drawn on water quenched samples for SACX and SAC105 (see Figures 5.6-5.8). Further discussion of water quenched results will appear in Chapter 6.

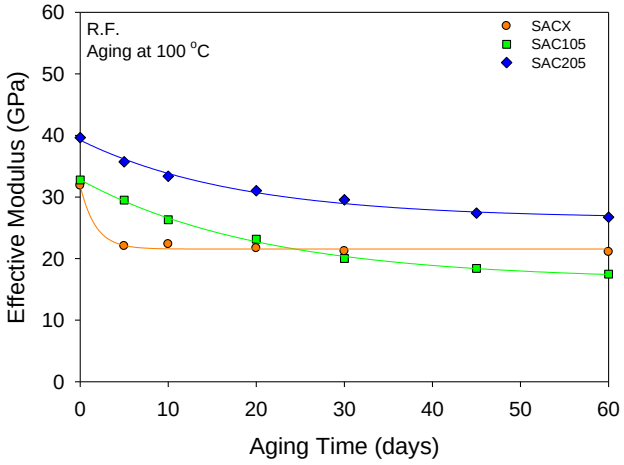

(a) E

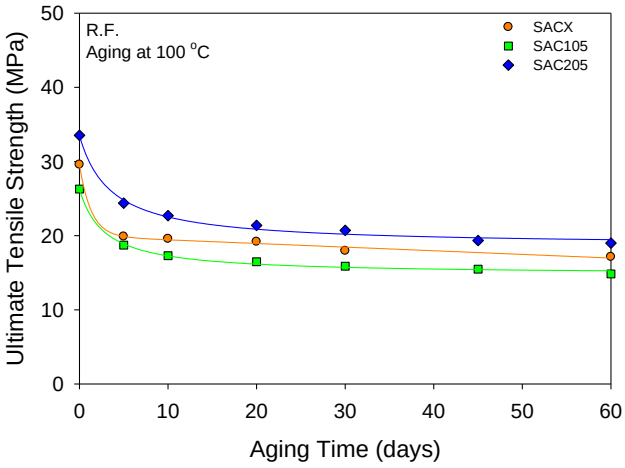

(b) UTS

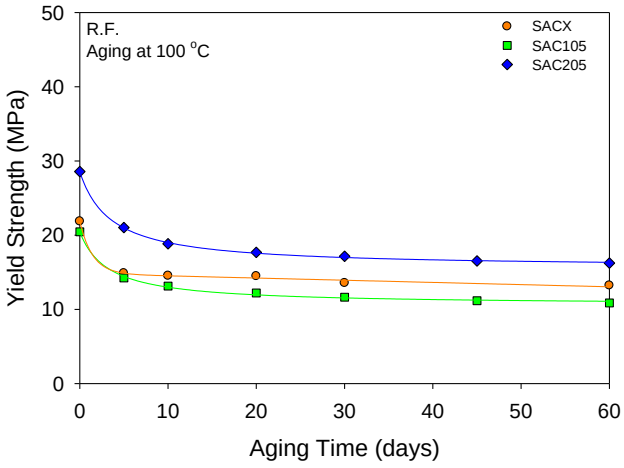

(c) YS

Figure 5.1 Effect of Dopants on the Evolution of Tensile Properties with Aging (SACX, SAC105, SAC205, R.F., Aging at 100 °C for up to 60 Days)

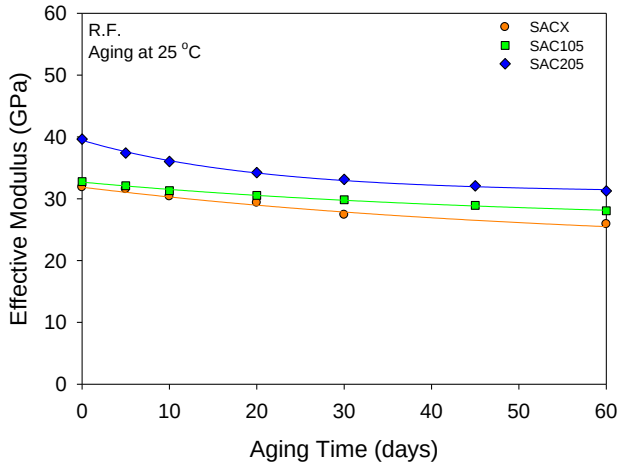

(a) E

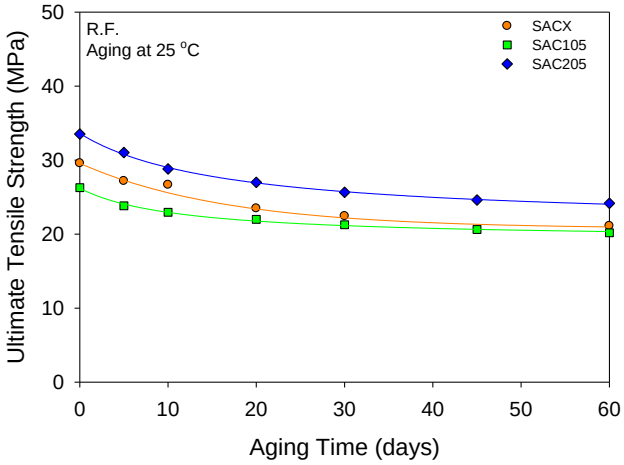

(b) UTS

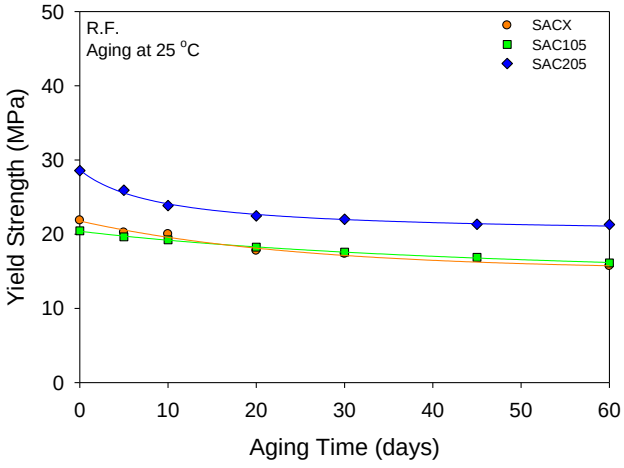

(c) YS

Figure 5.2 Effect of Dopants on the Evolution of Tensile Properties with Aging (SACX, SAC105, SAC205, R.F., Aging at 25 °C for up to 60 Days)

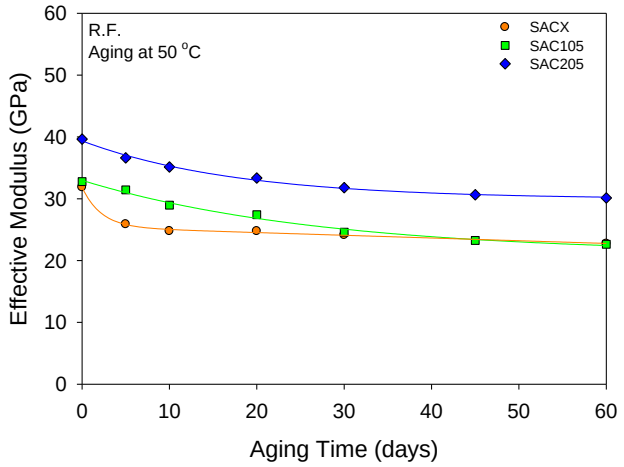

(a) E

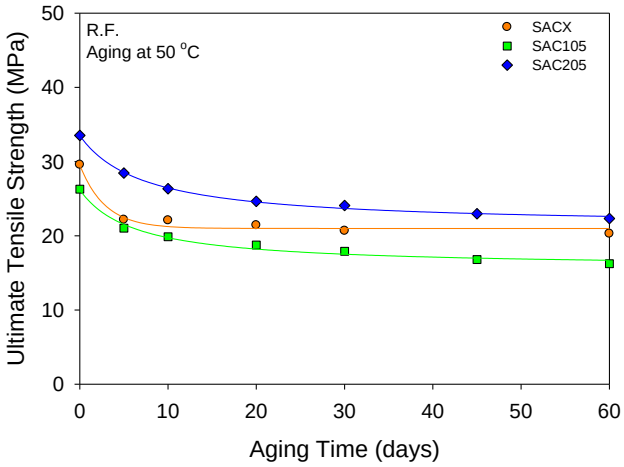

(b) UTS

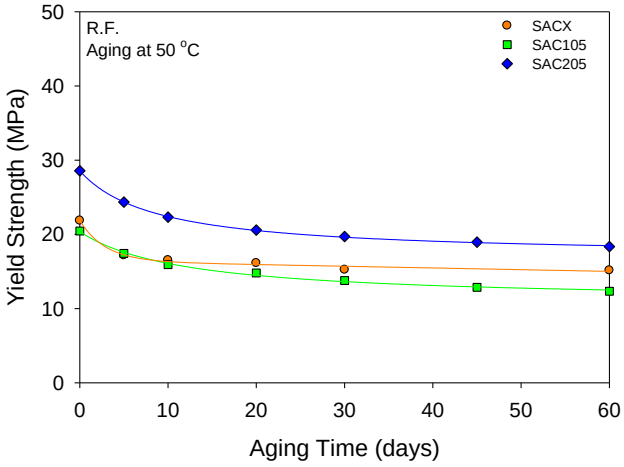

(c) YS

Figure 5.3 Effect of Dopants on the Evolution of Tensile Properties with Aging (SACX, SAC105, SAC205, R.F., Aging at 50 °C for up to 60 Days)

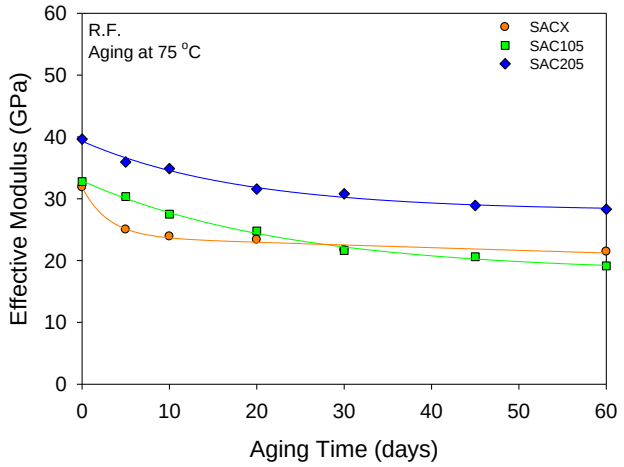

(a) E

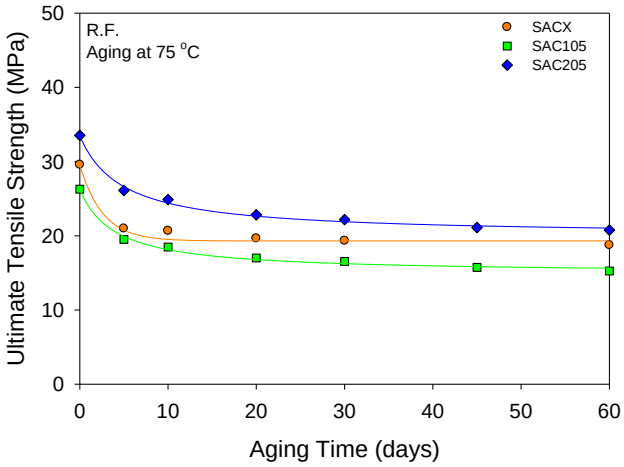

(b) UTS

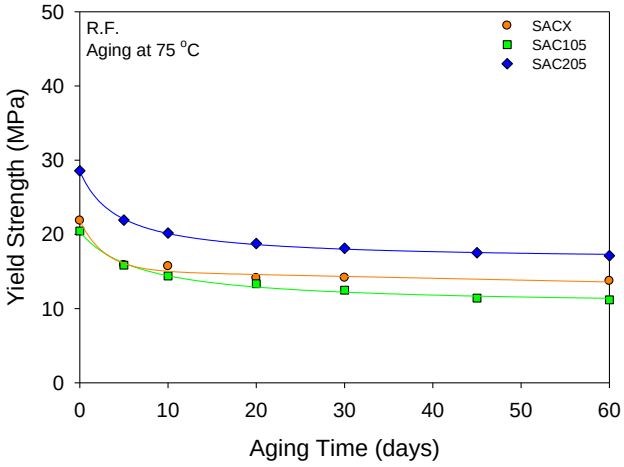

(c) YS

Figure 5.4 Effect of Dopants on the Evolution of Tensile Properties with Aging (SACX, SAC105, SAC205, R.F., Aging at 75 °C for up to 60 Days)

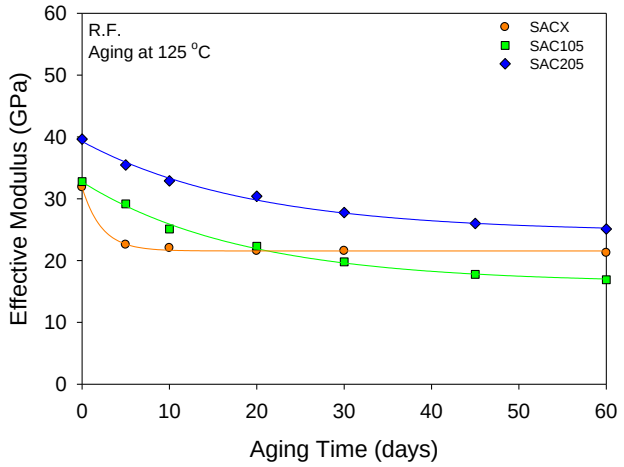

(a) E

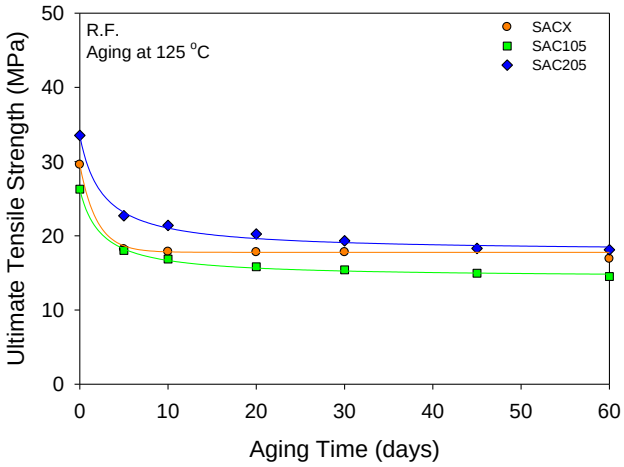

(b) UTS

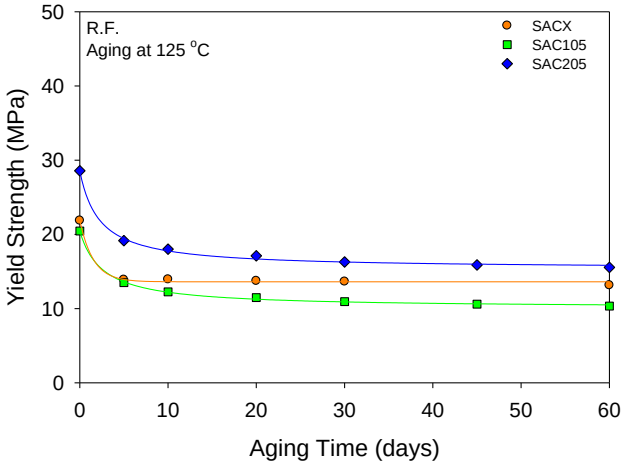

(c) YS

Figure 5.5 Effect of Dopants on the Evolution of Tensile Properties with Aging (SACX, SAC105, SAC205, R.F., Aging at 125 °C for up to 60 Days)

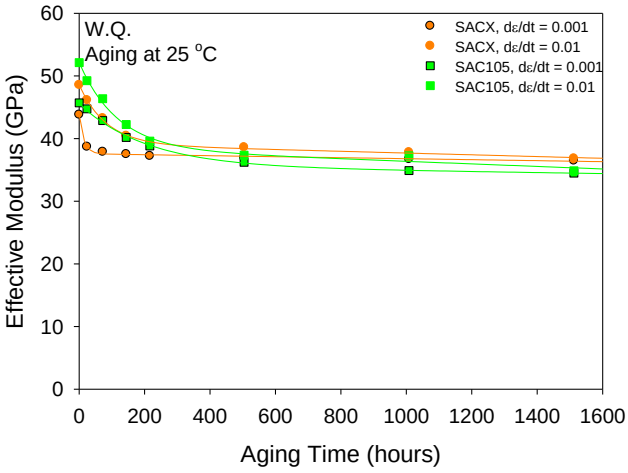

(a) E

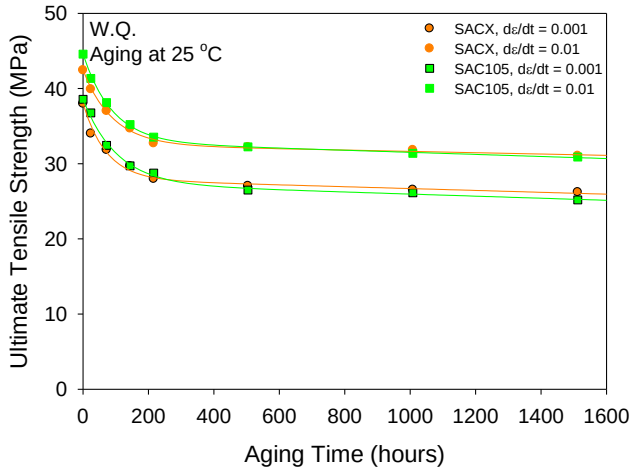

(b) UTS

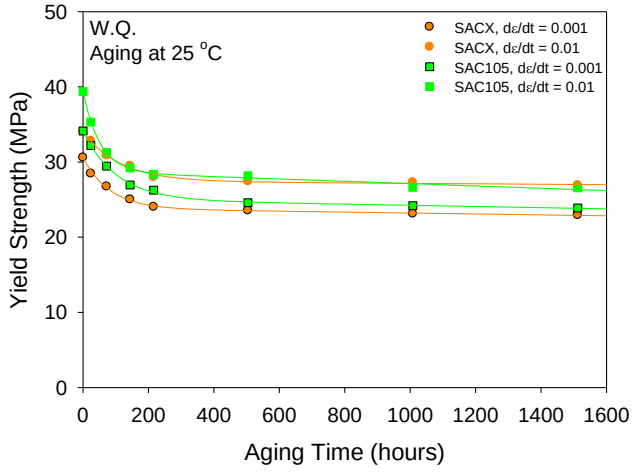

(c) YS

Figure 5.6 Effect of Dopants on the Evolution of Tensile Properties with Aging (SACX, SAC105, SAC205, W.Q., Aging at 25 °C for up to 60 Days)

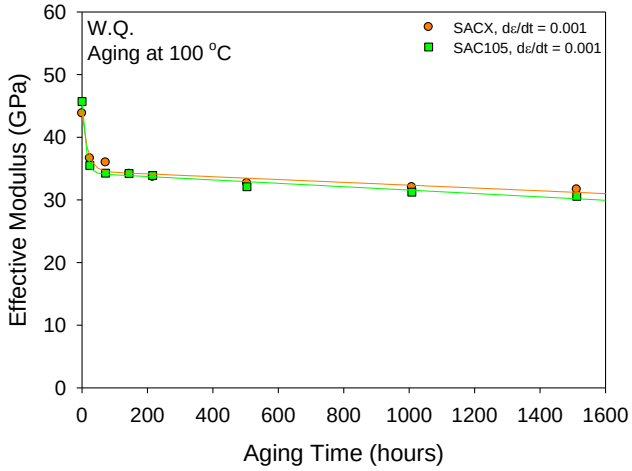

(a) E

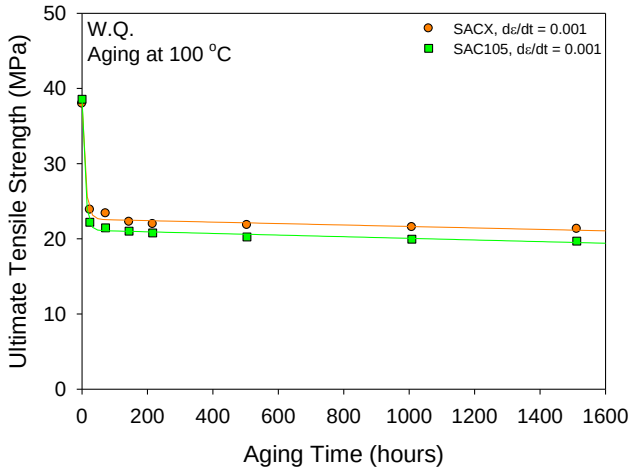

(b) UTS

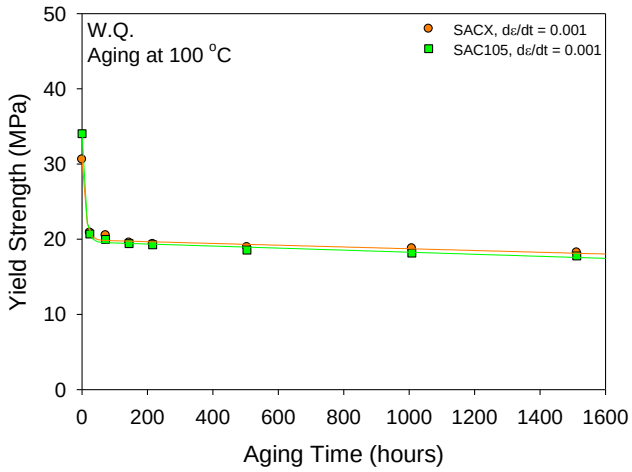

(c) YS

Figure 5.7 Effect of Dopants on the Evolution of Tensile Properties with Aging (SACX, SAC105, SAC205, W.Q., Aging at 100 °C for up to 60 Days)

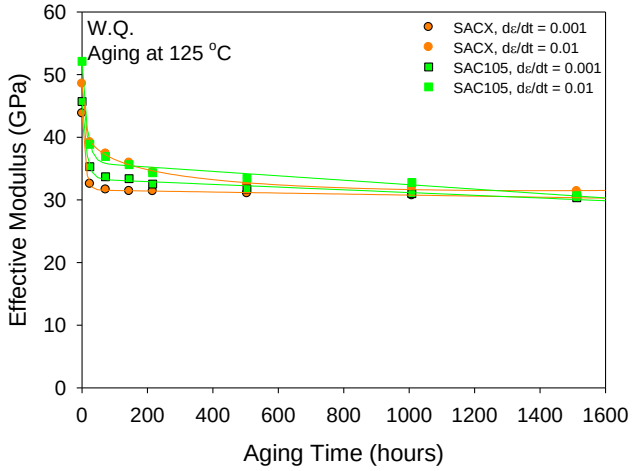

(a) E

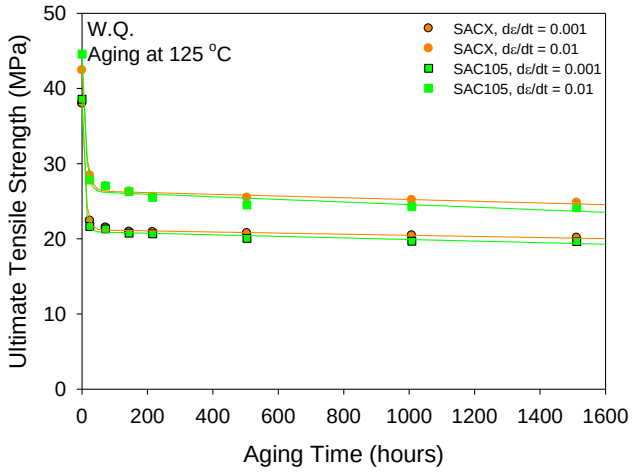

(b) UTS

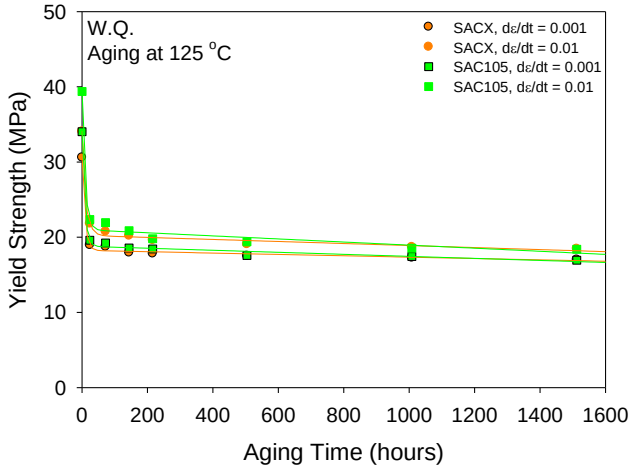

(c) YS

Figure 5.8 Effect of Dopants on the Evolution of Tensile Properties with Aging (SACX, SAC105, SAC205, W.Q., Aging at 125 °C for up to 60 Days)

5.2.2 SN100C and Sn-0.7Cu

Average stress-strain curves for SN100C/Sn-0.7Cu solders aged at 100 ^{o}C for various durations are illustrated in Figure 5.9. The corresponding tensile properties were extracted from each stress-strain response, and then plotted with aging time on one graph for comparison purposes (Figure 5.10). It was found that the Ni-doped SN100C solder has higher stiffness but worse strength than eutectic Sn-Cu. In addition, an apparent reduction in aging effects was observed for the SN100C solder.

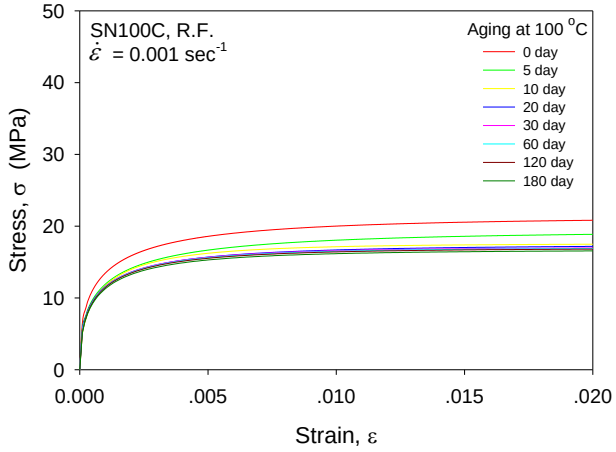

(a) SN100C

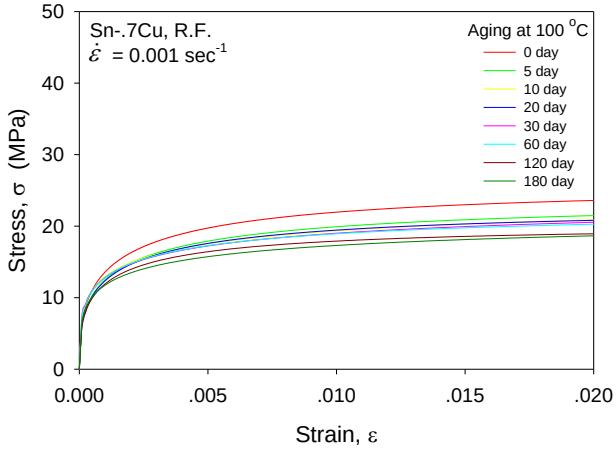

(b) Sn-0.7Cu

Figure 5.9 Stress-Strain Curves for SN100C/Sn-0.7Cu
(R.F., Aging at 100 ^{o}C for 0-180 Days)

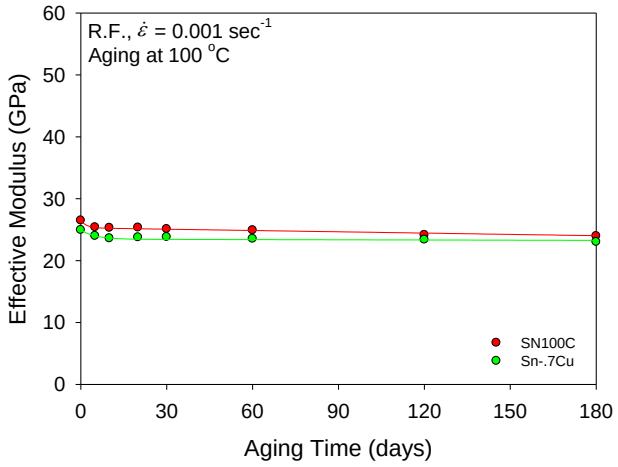

(a) E

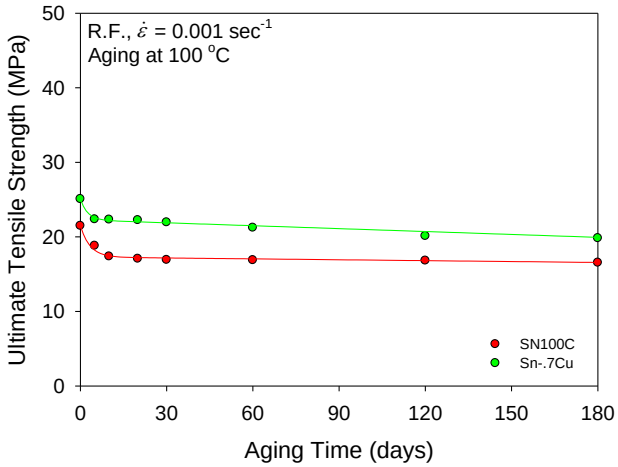

(b) UTS

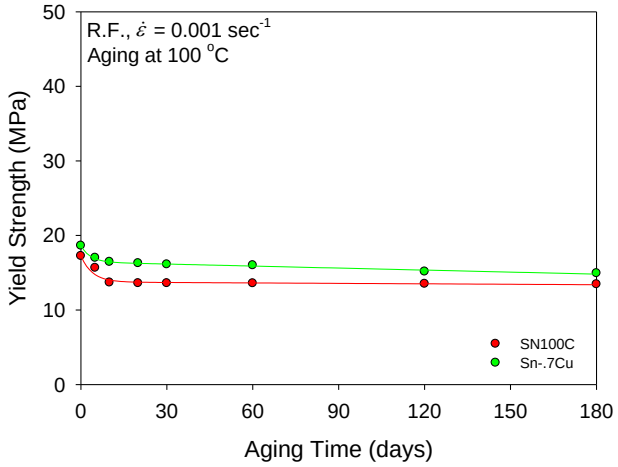

(c) YS

Figure 5.10 Effect of Dopants on the Evolution of Tensile Properties with Aging (SN100C and Sn-0.7Cu, R.F., Aging at 100 °C for up to 180 Days)

5.2.3 SAC-Zn and SAC3595

Figure 5.11 illustrates the evolution of the average stress-strain response for SAC-Zn/SAC3595 for 100 ^{o}C aging. The tensile properties were extracted from these results and are plotted in Figure 5.12. It can be seen that the inclusion of the Zn dopant not only improves the material properties of the solder, but increases the aging resistance as well.

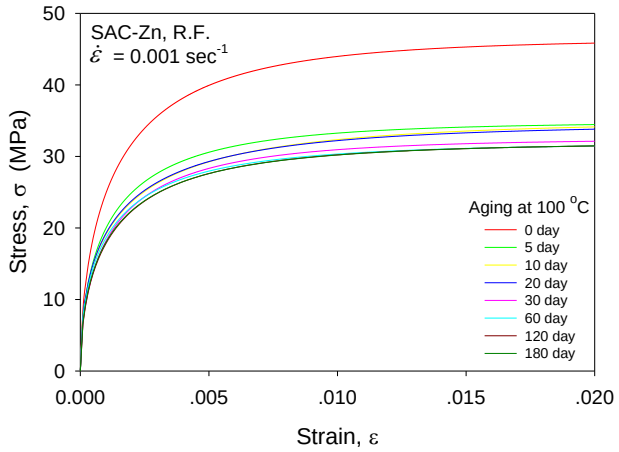

(a) SAC-Zn

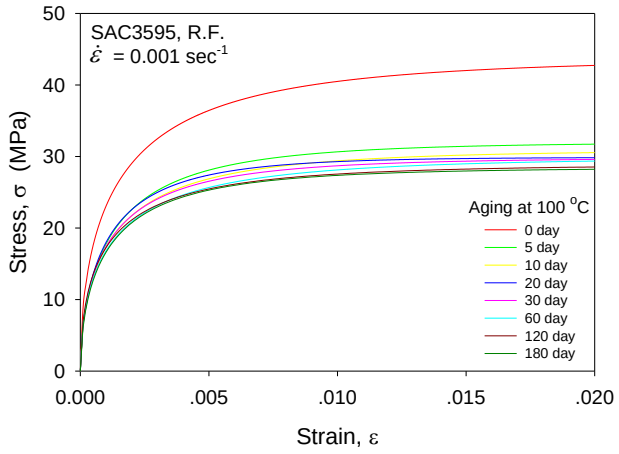

(b) SAC3595

Figure 5.11 Stress-Strain Curves for SAC-Zn/SAC3595
(R.F., Aging at 100 ^{o}C for 0-180 Days)

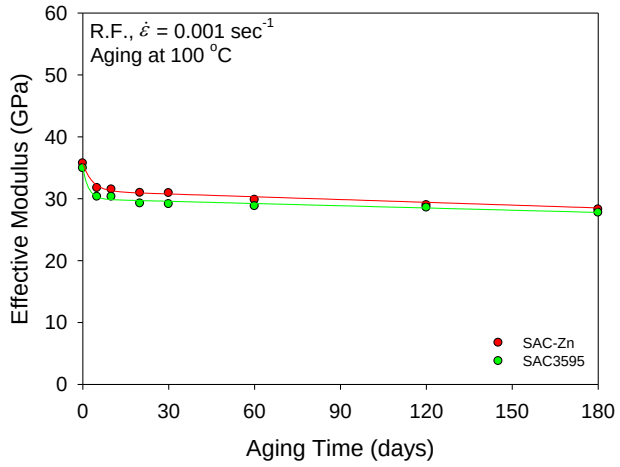

(a) E

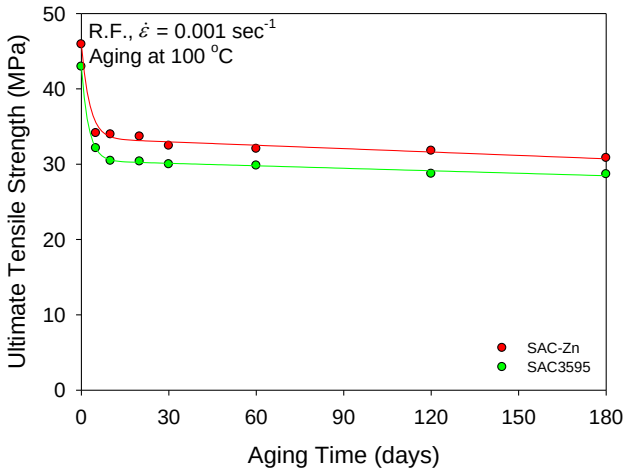

(b) UTS

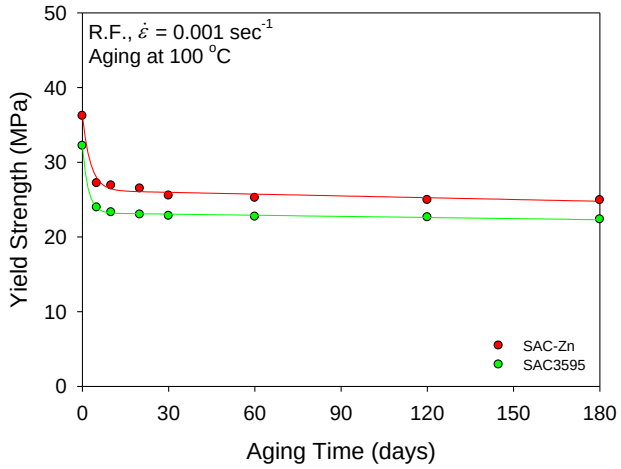

(c) YS

Figure 5.12 Effect of Dopants on the Evolution of Tensile Properties with Aging (SAC-Zn and SAC3595, R.F., Aging at 100 °C for up to 180 Days)

5.2.4 SN96CI and SAC3810

Figures 5.13-5.14 present the stress-strain behaviors and variations of the tensile properties of SN96CI/SAC3810 solders under different aging conditions. Although addition of 0.05 wt.% Cobalt does not help to improve the tensile behavior of SN96CI solder, the aging resistance was enhanced as with the other doped solders. For long term aging, the material properties of SN96CI were observed to degrade at a slower rate than those for SAC3810, although stabilization did not occur for either solder.

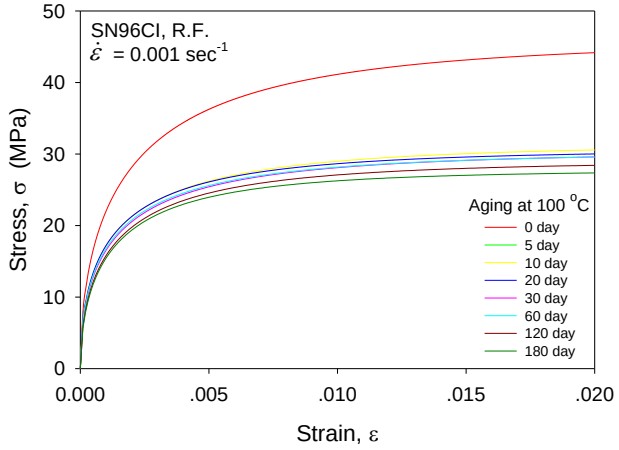

(a) SN96CI

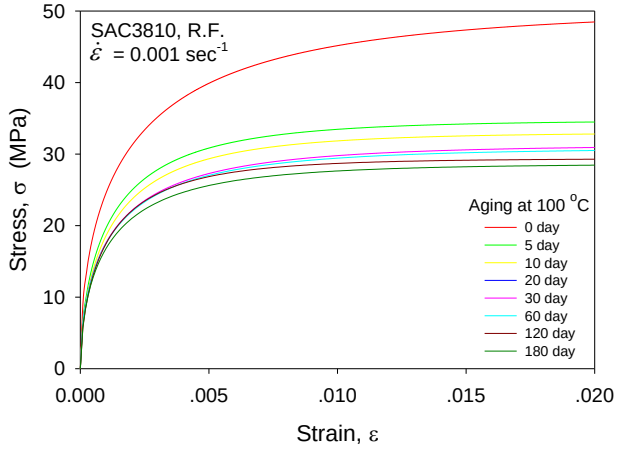

(b) SAC3810

Figure 5.13 Stress-Strain Curves for SN96CI/SAC3810 (R.F., Aging at 100 °C for 0-180 Days)

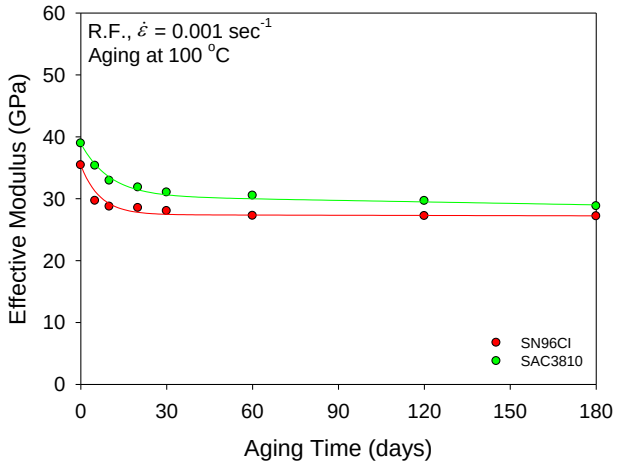

(a) E

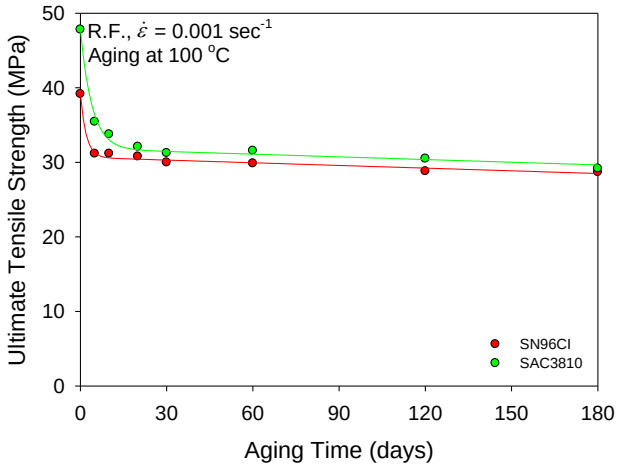

(b) UTS

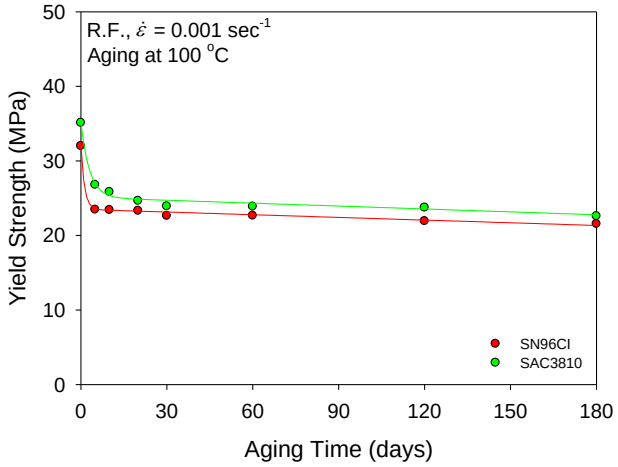

(c) YS

Figure 5.14 Effect of Dopants on the Evolution of Tensile Properties with Aging (SN96CI and SAC3810, R.F., Aging at 100 °C for up to 180 Days)

5.3 Effect of Dopants on Aging Resistance in Creep Behavior

The recorded strain-time responses for solders of interest subjected to creep loading were first fitted by Burger's Model, and then the steady state strain rates were obtained from the calculated k_1 values in Eq. 3.6. The evolution of the secondary creep rates of solders were then compared by plotting $\dot{\varepsilon}$ vs. aging on one graph. In this section, the effect of dopants on the aging resistance in creep behavior of solders was evaluated.

5.3.1 SACX, SAC105, and SAC205

Creep behaviors of SACX subject to various aging conditions have already been shown in Chapter 4 (Figure 4.6 for creep curves and Figure 4.7 for evolution of secondary creep rate), while data for SAC105 and SAC205 are available in Zhang's dissertation [112]. To compare the aging induced degradation of the creep properties of SACX to those for SAC105 and SAC205, the $\dot{\varepsilon}$-aging diagrams have been re-plotted so that all three alloys are included on each graph. Figure 5.15 contain plots of the secondary creep rates versus aging time for the 3 solders at each of the five aging temperatures. The non-linear model in Eq. 4.10 was again used to fit the experimental data. At zero aging time (non-aged sample), the SACX alloy has the highest creep rate:

$$\dot{\varepsilon}_{SACX} > \dot{\varepsilon}_{SAC105} > \dot{\varepsilon}_{SAC205} \qquad \text{(no aging)} \tag{5.4}$$

This is expected due to its low silver content (0.3%) relative to SAC105 (1% Ag) and SAC205 (2% Ag). However, as aging progresses, the creep rate of SACX increases at a slower rate than those of both SAC105 and SAC205. For all 5 aging temperatures, a cross-over takes place where SAC105 begins to creep faster than SACX:

$$\dot{\varepsilon}_{SAC105} > \dot{\varepsilon}_{SACX} > \dot{\varepsilon}_{SAC205} \qquad \text{(with aging)} \tag{5.5}$$

For elevated temperature aging (50, 75, 100, 125 ^{o}C), these cross-over points occurred within the first few days of aging. For room temperature aging, the cross-over took place after approximately 4 months of aging.

Quantitatively, the reduction of the creep rate degradation during aging is quite dramatic for the doped SAC alloy. The changes of the creep rates of SACX are approximately 10X less than those of SAC105 at all five of the aging temperatures (see tabulated values in Table 5.3). For example, the creep rate of SAC105 increases by a factor of 9700X after 6 months aging at 125 ^{o}C, while the creep rate of SACX increases by 954X over the same exposure.

For water quenched samples, the evolutions of the secondary creep rates of SACX and SAC105 solders converge for room temperature aging; while cross-over points can be observed in the data for elevated temperature aging (Figure 5.16). In general, the relationship in Eq. 5.4-5.5 still holds for water quenched specimens:

$$\dot{\varepsilon}_{SACX} > \dot{\varepsilon}_{SAC105} \qquad \text{(no aging)} \tag{5.6}$$

$$\dot{\varepsilon}_{SAC105} > \dot{\varepsilon}_{SACX} \qquad \text{(with aging)} \tag{5.7}$$

In general, it has been demonstrated that addition of 0.1 wt.% Bi can stabilize the degradation of the creep rate for SACX. Due to the lower silver content, SACX creeps at a faster rate than SAC105 before aging occurs. However, the reverse trend is observed for aged solder samples despite the testing and solidification conditions.

	25 °C	50 °C	75 °C	100 °C	125 °C
SAC105	420X	5700X	7100X	9200X	9700X
SAC205	9X	473X	1342X	1684X	2895X
SACX	49X	261X	516X	783X	954X

Table 5.3 Increases in Creep Rates for SACX, SAC105, and SAC205 after 6 Months of Aging (Aged vs. Non-aged, Non-aged as Baseline)

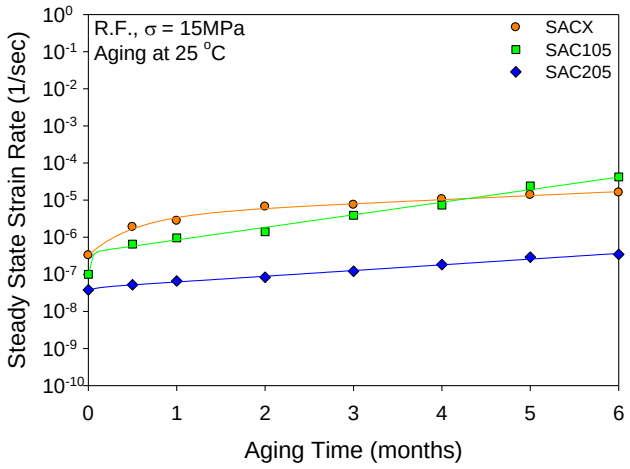

(a) Aging at T = 25 °C

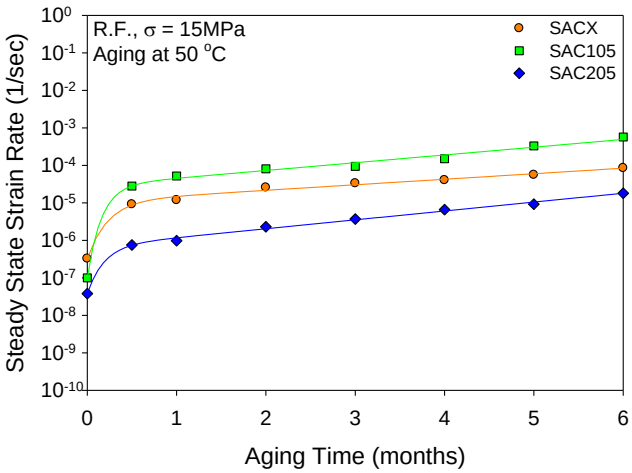

(b) Aging at T = 50 °C

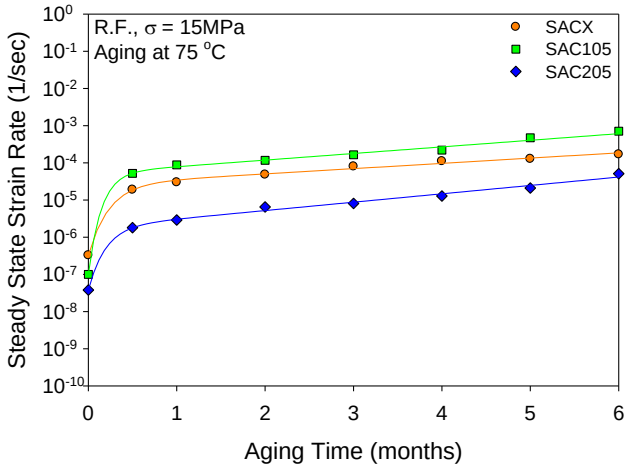

(c) Aging at T = 75 °C

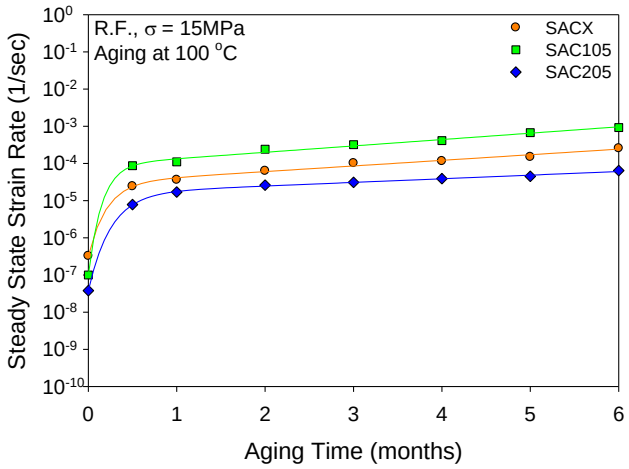

(d) Aging at T = 100 °C

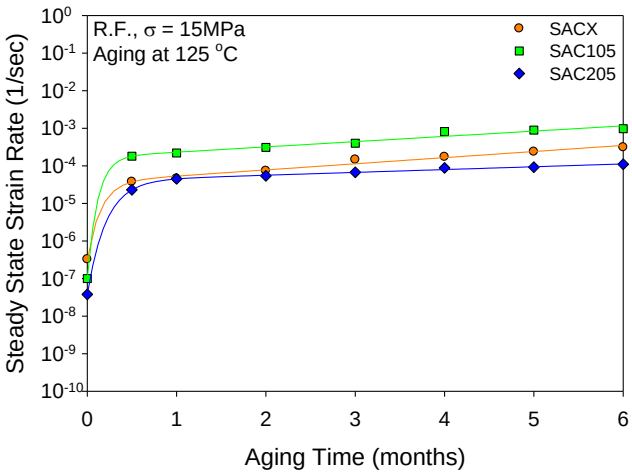

(e) Aging at T = 125 °C

Figure 5.15 Effect of Dopants on the Evolution of Creep Rate with Aging (SACX, SAC105, SAC205, R.F., Aging up to 6 Months)

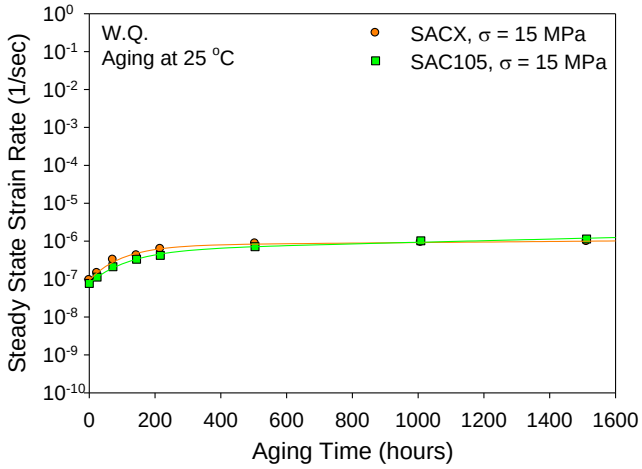

(a) Aging at T = 25 °C

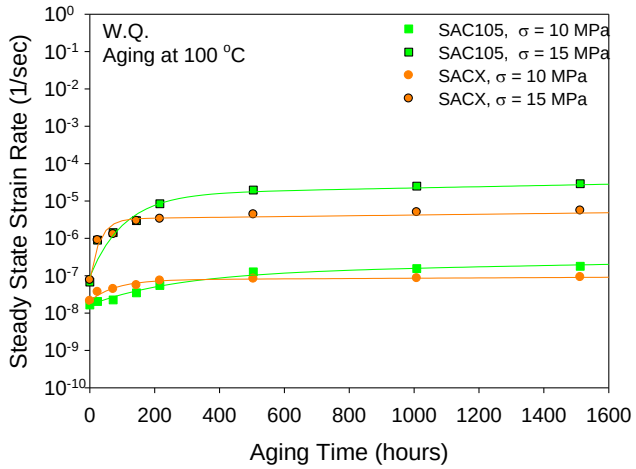

(b) Aging at T = 100 °C

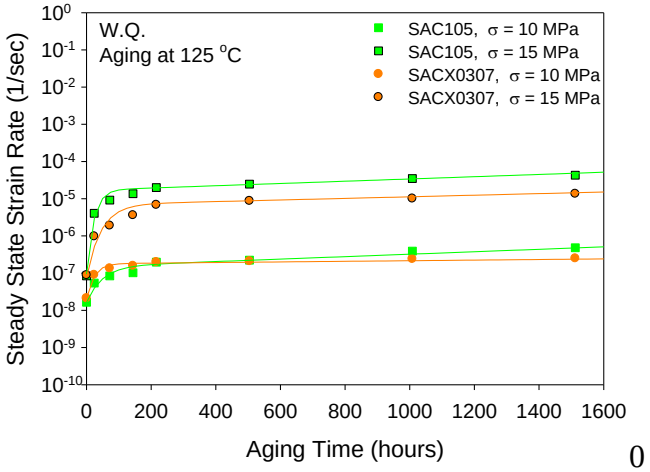

0

(c) Aging at T = 125 °C

Figure 5.16 Effect of Dopants on the Evolution of Creep Rate with Aging (SACX, SAC105, SAC205, W.Q., Aging up to 2 Months)

5.3.2 SN100C and Sn-0.7Cu

The representative creep curves for SN100C/Sn-0.7Cu solders under 100 ^{o}C of aging for various durations are illustrated in Figure 5.17. It can be seen that the evolutions in slope of the secondary creep region with aging are significantly different for the two solders. This has been demonstrated quantitatively by plotting $\dot{\varepsilon}$ vs. t diagrams for both solders in one graph (Figure 5.18). Another observation is that SN100C has a better aging resistance than Sn-0.7Cu even though it always creeps at a faster rate for up to 6 months of aging.

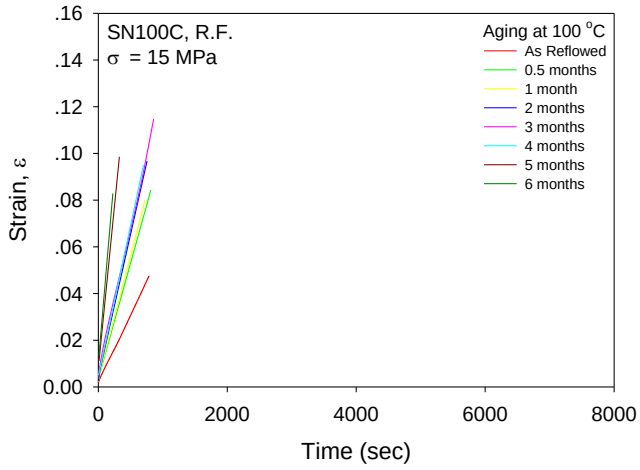

(a) SN100C

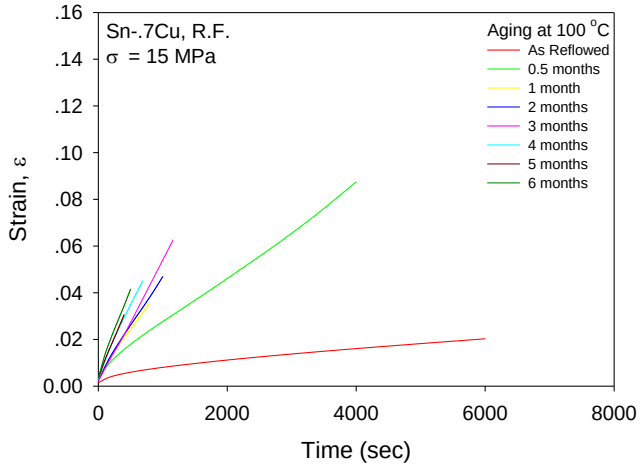

(b) Sn-0.7Cu

Figure 5.17 Creep Curves for SN100C/Sn-0.7Cu (R.F., Aging at 100 ^{o}C for 0-6 Months)

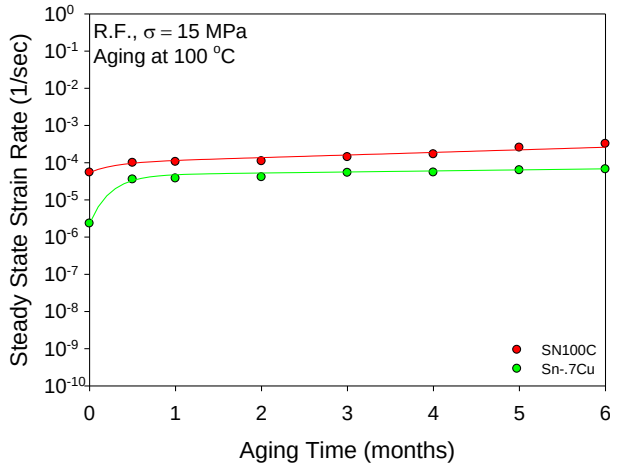

Figure 5.18 Effect of Dopants on the Evolution of Creep Rate with Aging (SN100C and Sn-0.7Cu, R.F., Aging at 100 °C for up to 6 Months)

5.3.3 SAC-Zn and SAC3595

Figure 5.19 illustrates the evolutions of the creep responses of SAC-Zn/SAC3595 solders for aging at 100 °C. Most of the creep curves are closely spaced in the two graphs. This is due to the chosen scale on the strain axis (a maximum strain of 0.16 was chosen for all 4 sets of solder materials for comparison purpose). The aging resistances and the degradations of the creep rate can be evaluated from Figure 5.20. Similar to the observations for stress-strain testing, the creep resistance and aging resistance of SAC-Zn are both better than those of SAC3595 for up to 6 months of aging.

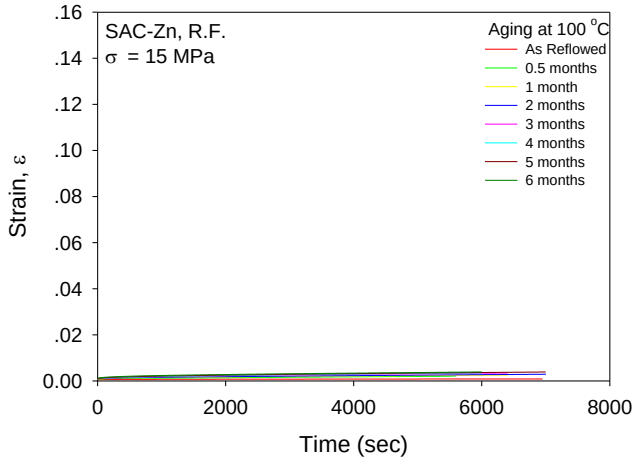

(a) SAC-Zn

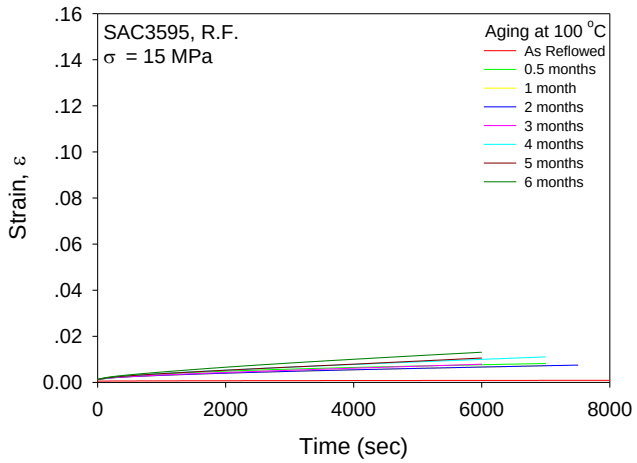

(b) SAC3595

Figure 5.19 Creep Curves for SAC-Zn and SAC3595
(R.F., Aging at 100 °C for 0-6 Months)

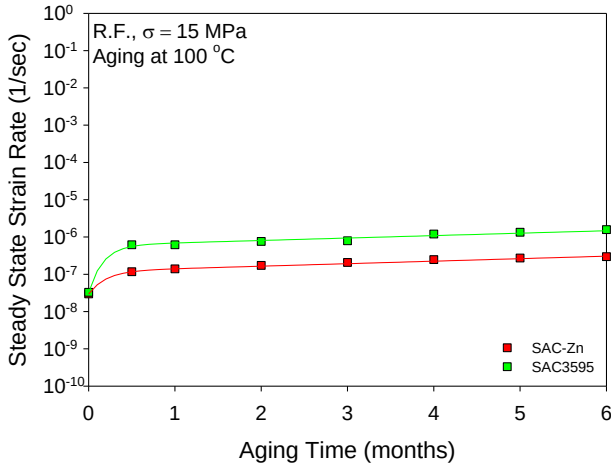

Figure 5.20 Effect of Dopants on the Evolution of Creep Rate with Aging
(SAC-Zn and SAC3595, R.F., Aging at 100 °C for up to 6 Months)

5.3.4 SN96CI and SAC3810

The creep responses under different aging conditions and the corresponding evolutions of the steady state strain rate of SN96CI/SAC3810 are plotted in Figures 5.21-5.22. It can be seen that even though SN96CI creeps faster than SAC3810 for up to 6 months of aging at 100 °C, it is more resistant to aging. In other words, the degradation of creep rate for SN96CI is slower than for the non-doped SAC3810 solder, and eventually a cross-over point is expected.

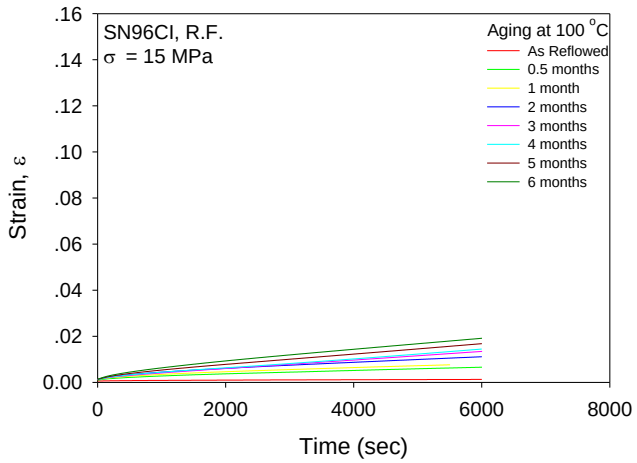

(a) SN96CI

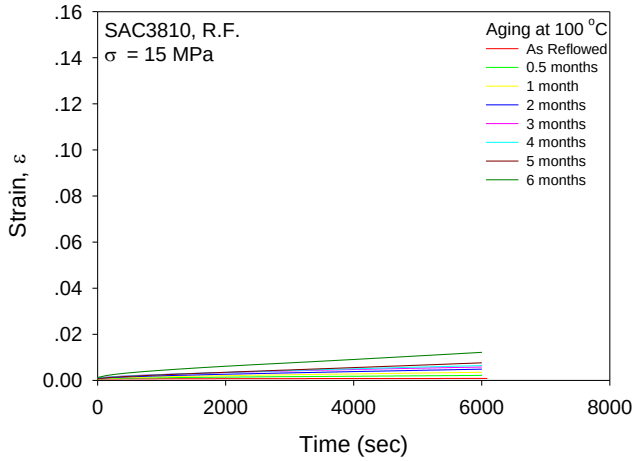

(b) SAC3810

Figure 5.21 Creep Curves for SN96CI/SAC3810
(R.F., Aging at 100 °C for 0-6 Months)

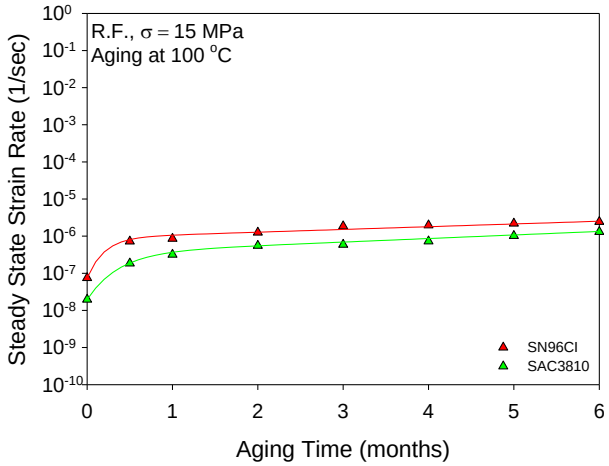

Figure 5.22 Effect of Dopants on the Evolution of Creep Rate with Aging
(SN96CI and SAC3810, R.F., Aging at 100 °C for up to 6 Months)

5.4 Summary and Discussion

In the previous chapter, the effect of aging on material behavior of lead free solders has been investigated by performing both tensile and creep test with a full matrix of aging time and aging temperature. Also, it was observed that the material properties of doped SACX solder stabilize quickly with aging. In this chapter, a wide selection of doped lead free solders was examined, and analogous tests were performed on the corresponding "standard" solders (without dopants) so that the effects of dopants on aging resistance of lead free solder materials could be studied.

In this study, a total of 9 different lead free solders were separated into 4 sets:

Set 1: SACX, SAC105 and SAC205

Set 2: SN100C, Sn-0.7Cu

Set 3: SAC-Zn, SAC3595

Set 4: SN96CI, SAC3810

The chemical compositions of solders are tabulated in Table 5.1. The design of experiment is summarized in Table 4.1 (for Set 1) and Table 5.2 (for Sets 2-4). All tests were performed at room temperature (T = 25 ^{o}C).

Table 5.4 summarizes the material properties with/without aging and the corresponding aging induced degradation for all the solders in this study. The "As R.F." data were obtained from the tests that were conducted immediately after the samples solidified. The "aged" data were extracted from the test results of the samples aged at 100 ^{o}C for 60 days. The effects of dopants on enhancing the aging resistance of lead free solders were then studied by comparing the percentage change (ratio) in material properties between the aged and non-aged samples.

In general, it is observed from Table 5.4 that dopants are able to improve aging resistance for lead free solders. Contrary to non-doped solders, the material properties of doped solders, including effective modulus (E), ultimate tensile strength (UTS), yield strength (YS) and steady state strain rate ($\dot{\varepsilon}$), stabilize quickly with aging. This result is more obvious for the tensile properties of the doped solders, which becomes nearly constant after 10-20 days of aging. In contrast, the tensile properties of the "standard" solders without dopants continue to degrade in a linear manner with time.

Additionally, some X-additives were discovered to improve the material properties of the solders. For example, due to the existence of 0.21 wt.% Zn, SAC-Zn solder has better stiffness and strength than "standard" SAC3595, as well as a more favorable creep resistance. Another example is that SACX (0.3% Ag) shows superior strength properties to SAC105 (1% Ag) after long-term aging at all aging temperatures regardless of its lower silver content.

In summary, aging effects have been reported to be universally detrimental to the material properties of lead free solders [45, 46, 48, 54, 103, 105, 106, 114-121]. Based on the test results reported in this chapter, it has been demonstrated that metallurgical approaches (e.g. doping) can reduce the effects of aging on the degradation of material properties. These observations can be explained by using material science theories for mechanisms of dislocation movement, solid solution strengthening, etc. Further discussions are given in Chapter 7.

Property / Solder	E (GPa)			UTS (MPa)			YS (MPa)			$\dot{\varepsilon}$ (1×10^{-6} sec^{-1})		
	As R.F.	Aged	Decrease	As R.F.	Aged	Decrease	As R.F.	Aged	Decrease	As R.F.	Aged	Increase
SACX	31.87	21.07	33.89%	29.57	17.13	42.07%	21.87	13.23	39.51%	0.33	63.41	192X
SAC105	32.77	17.47	46.49%	26.28	14.84	43.53%	20.45	10.87	46.85%	0.1	240	2400X
SN100C	26.49	24.92	5.93%	21.49	16.89	21.41%	17.25	13.59	21.21%	54.7	110.3	2X
Sn-0.7Cu	24.95	23.53	5.69%	25.08	21.23	15.35%	18.63	16.01	14.06%	2.31	40.62	18X
SAC-Zn	35.72	29.84	16.46%	45.92	32.04	30.23%	36.22	25.23	30.34%	0.03	0.17	6X
SAC3595	34.94	28.79	17.60%	42.95	29.82	30.57%	32.21	22.73	29.43%	0.03	0.76	25X
SN96CI	35.42	27.24	23.09%	39.16	29.86	23.75%	32.00	22.66	29.19%	0.07	1.26	18X
SAC3810	38.95	30.50	21.69%	47.82	31.56	34.00%	35.11	23.87	32.01%	0.02	0.56	28X

Table 5.4 Changes of Material Properties with Aging for Lead Free Solders
(Doped and Non-doped, R.F., Aging at 100 ^{o}C for 60 Days)

CHAPTER 6

EFFECT OF COOLING PROFILE AND TESTING CONDITIONS ON MECHANICAL PROPERTIES OF LEAD FREE SOLDER ALLOYS

6.1 Introduction

It is well known that the mechanical properties and initial microstructure of solder joints in microelectronic modules change significantly when different reflow/cooling profiles are adopted. These differences will affect the reliability of the assemblies for various working conditions.

In this chapter, the effects of solidification cooling profile and testing conditions on mechanical properties of lead free solder alloys, such as SACX (or SACX0307, Sn-0.3Ag-0.7Cu-0.1Bi) and SAC105, were characterized. Two different types of cooling profiles, Water Quenching Profile and Reflow Profile, were utilized in the current study. The reflow profile was chosen to match a typical profile used for PBGA assembly to PCBs. Although in actual practice, solder joints are never water quenched after melting, this extremely fast cooling profile is still valuable because it yields a near optimal initial microstructure for solder materials. The test specimens were fabricated with the casting procedure described in Chapter 3, and the design of experiments is summarized in Table 6.1.

Uniaxial stress-strain tests and creep tests for SACX and SAC105 were performed at Room Temperature (RT = 25 ^{o}C) on both Water Quenched (W.Q.) and Reflowed (R.F.) samples. Prior to testing, specimens were pre-conditioned at three different aging

temperatures including RT and two Elevated Temperatures (HT = 100, 125 ^{o}C) for various durations up to two months. Two strain rates, $\dot{\varepsilon}$ = 0.01 and 0.001 sec^{-1}, were used for the tensile stress-strain tests, while two stress levels, σ = 10 and 15 MPa, were applied for the creep tests. For each aging/testing condition, 10 tensile tests and 5 creep tests were performed, and the results were averaged as discussed in Chapter 3.

Solder Materials		SACX and SAC105
Casting Conditions		W.Q. and R.F.
Testing Conditions		$T_{testing}$ = 25 ^{o}C (RT) for all tests $\dot{\varepsilon}$ =0.001, 0.01 sec^{-1} for tensile tests σ =10, 15 MPa for creep tests
Aging Temperatures		25 ^{o}C (RT), 100 ^{o}C, 125 ^{o}C
Aging Times	Tensile	0, 25, 75, 150, 225, 500, 1000, 1500 hours for W.Q. 0, 5, 10, 20, 30, 60 days for R.F.
	Creep	0, 25, 75, 150, 225, 500, 1000, 1500 hours for W.Q. 0, 15, 30, 60 days for R.F.

Table 6.1 Design of Experiments for SACX and SAC105
(Effect of Cooling Profile and Testing Conditions)

6.2 Effect of Cooling Profile on Tensile Behavior

In this section, the effects of solidification cooling profile on the tensile behavior of lead free solder alloys are reported. All of the tensile tests were conducted at a constant strain rate of 0.001 sec^{-1}. The tensile properties were extracted and modeled as a function of aging time, and the results for reflowed samples were then compared to the water quenched samples.

Figures 6.1-6.4 illustrate the experimentally measured averaged stress-strain curves for W.Q./R.F. SACX and SAC105. Each figure contains three plots for the three

different aging temperatures (T = 25, 100 and 125 ^{o}C). In each plot, each individual stress-strain curve represents an average of 10 recorded stress-strain responses under the same aging/testing condition. When compared, it is obvious that water quenched results in Figures 6.1 and 6.3 illustrate much higher strengths and stiffnesses than the analogous results for the reflowed samples in Figures 6.2 and 6.4.

The tensile properties of SACX and SAC105 under different aging and casting conditions were extracted from the stress-strain curves in Figure 6.1-6.4. Similar to previous discussion, the effective modulus and tensile strength of solder materials were estimated using Eq. 3.4 and Eq. 3.5 respectively, while the standard 0.2% offset yield strength was also used. The tensile properties of the solder materials were then plotted against aging time and modeled by using Eq. 4.1, as shown in Figures 6.5-6.6. The curves in red are curve fits for the water quenched data; and the curves in blue are for the reflowed data. According to data listed in Tables 6.2 and 6.3, the water quenched specimens of both SAC solder materials showed an increase in tensile properties from 19-80% relative to the reflowed samples, if compared with the same aging conditions. Another interesting finding is that the aging resistance of the two SAC solders seemed to be independent of the casting condition, with the tensile properties for both materials degrading approximately 35% after isothermal aging regardless of cooling profile.

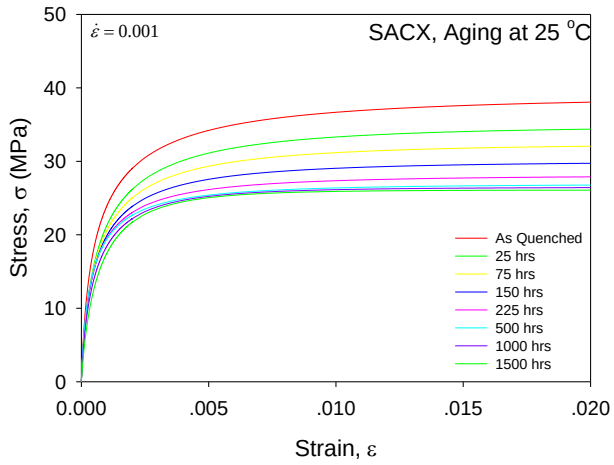

(a) Aging at T = 25 °C

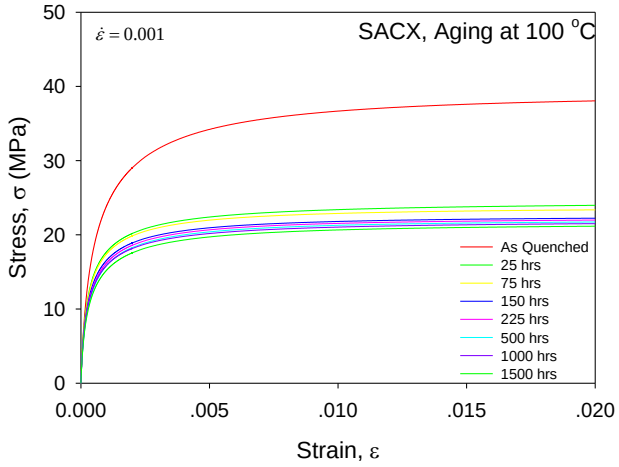

(b) Aging at T = 100 °C

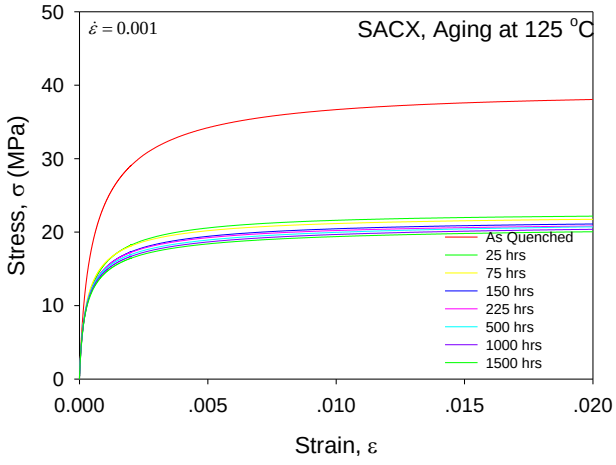

(c) Aging at T = 125 °C

Figure 6.1 Stress-Strain Curves for SACX
(W.Q., $\dot{\varepsilon}$ = 0.001 sec^{-1}, Aging for 0-60 Days)

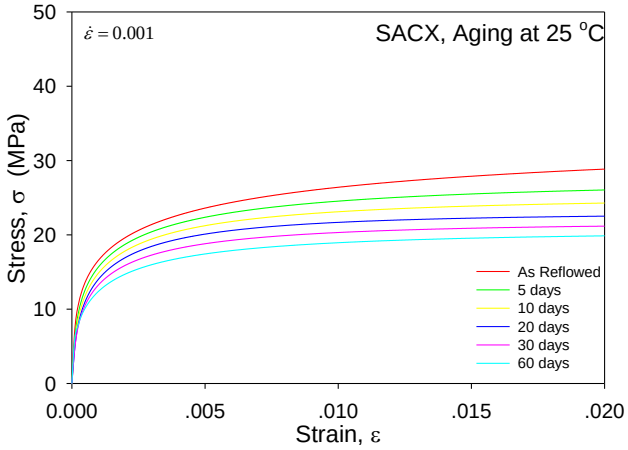

(a) Aging at T = 25 °C

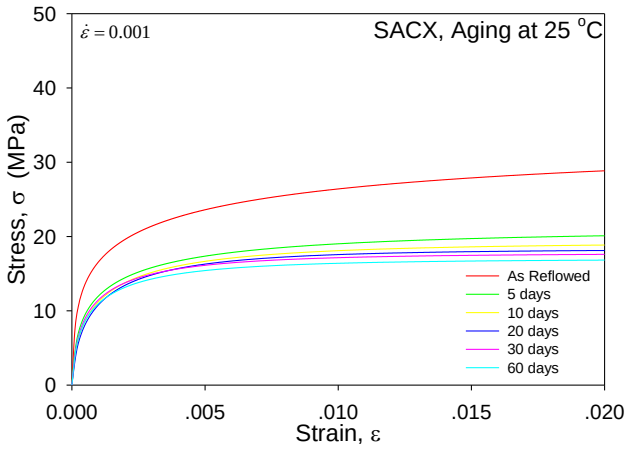

(b) Aging at T = 100 °C

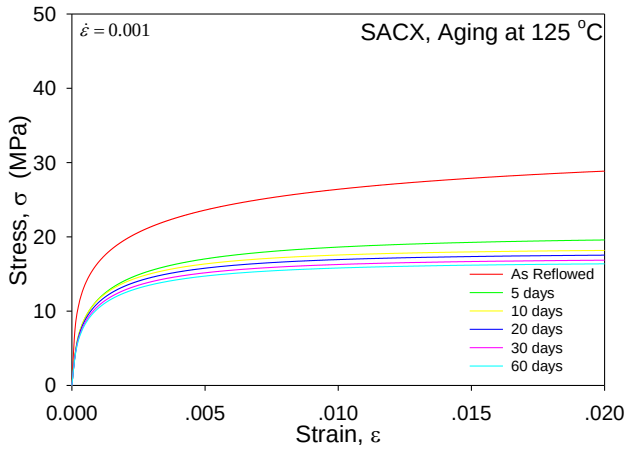

(c) Aging at T = 125 °C

Figure 6.2 Stress-Strain Curves for SACX
(R.F., $\dot{\varepsilon}$ = 0.001 sec^{-1}, Aging for 0-60 Days)

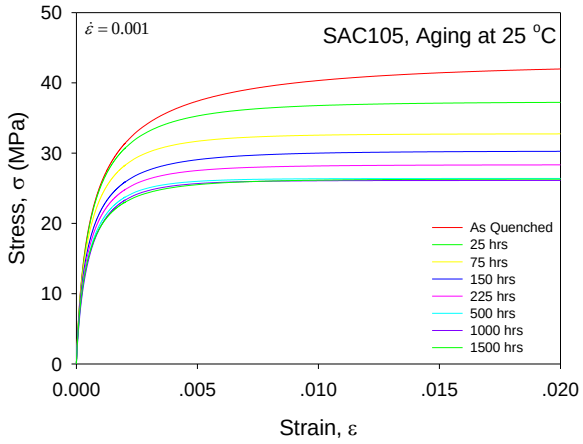

(a) Aging at T = 25 °C

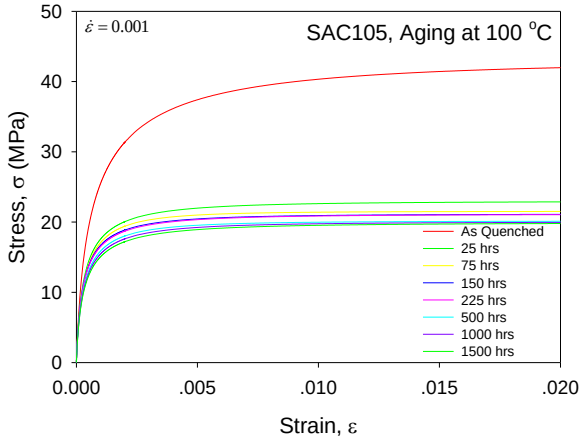

(b) Aging at T = 100 °C

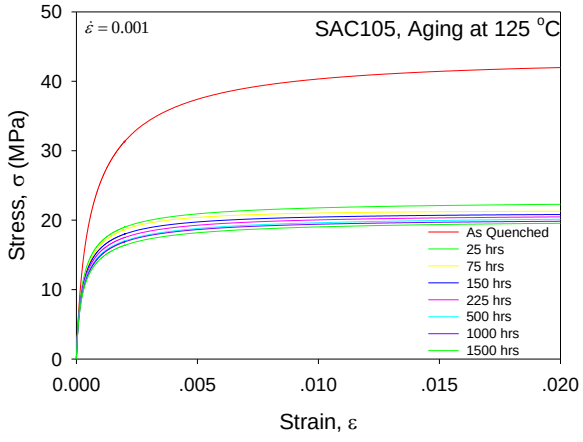

(c) Aging at T = 125 °C

Figure 6.3 Stress-Strain Curves for SAC105
(W.Q., $\dot{\varepsilon}$ = 0.001 sec^{-1}, Aging for 0-60 Days)

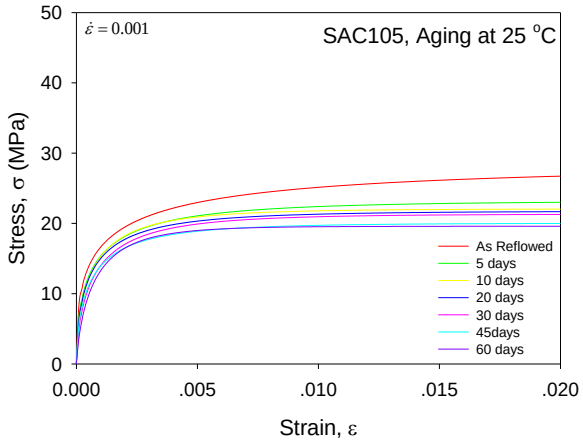

(a) Aging at T = 25 °C

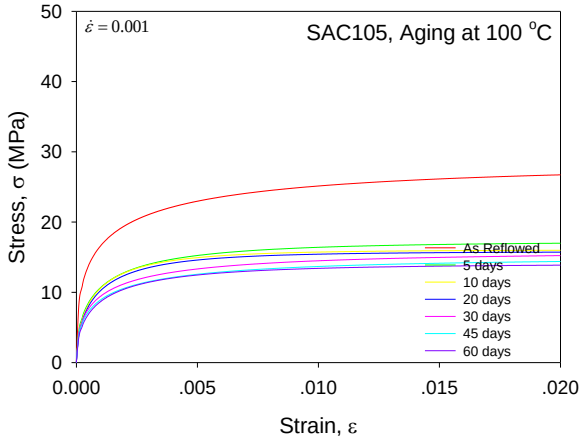

(b) Aging at T = 100 °C

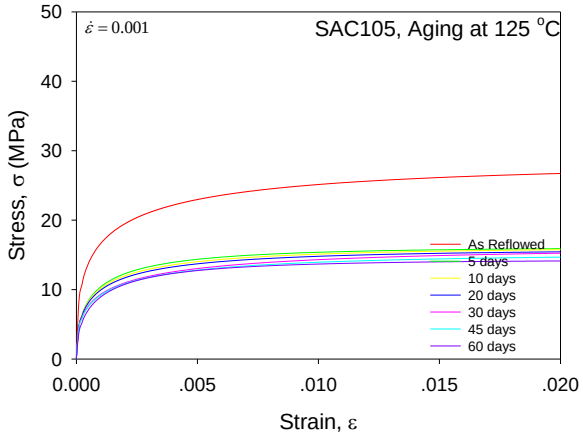

(c) Aging at T = 125 °C

Figure 6.4 Stress-Strain Curves for SAC105 (R.F., $\dot{\varepsilon}$ = 0.001 sec^{-1}, Aging for 0-60 Days)

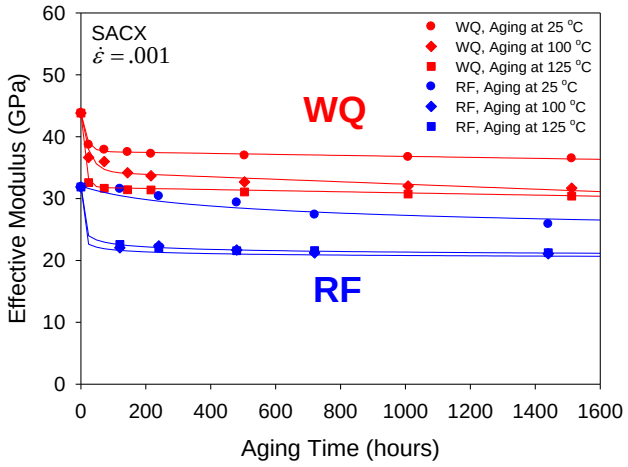

(a) E

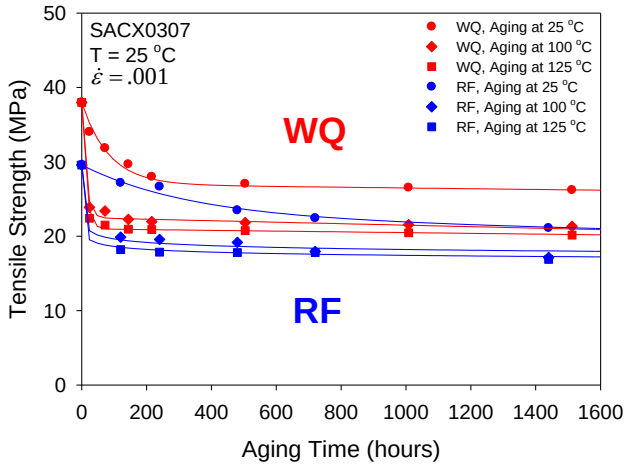

(b) UTS

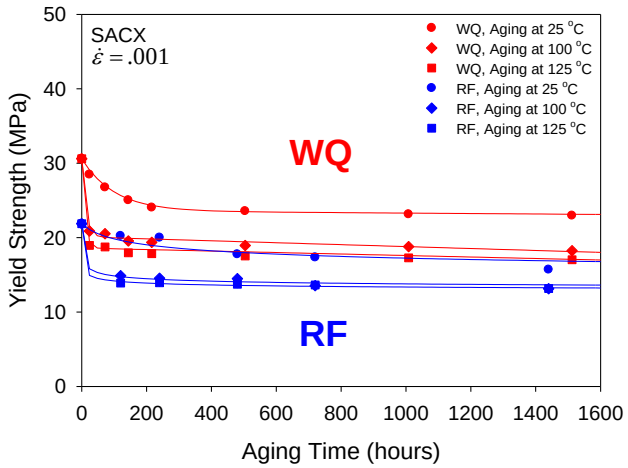

(c) YS

Figure 6.5 Effect of Solidification Cooling Profile on the Tensile Properties of SACX (W.Q. and R.F.)

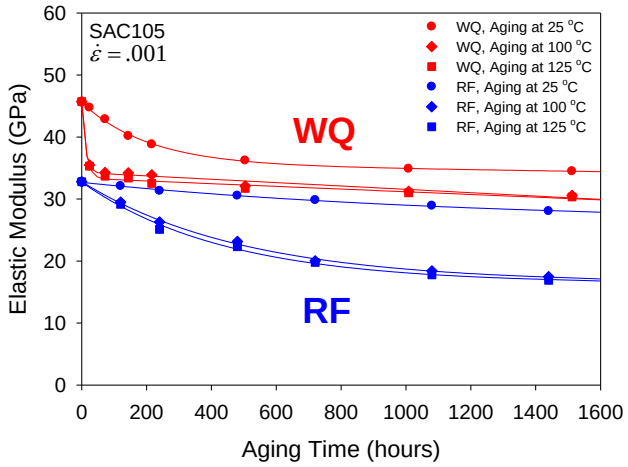

(a) E

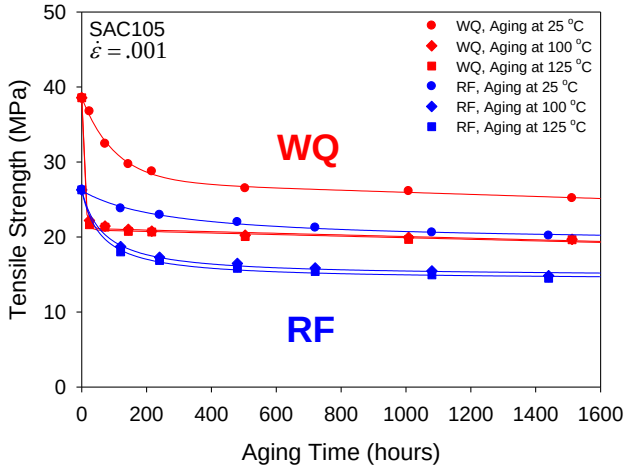

(b) UTS

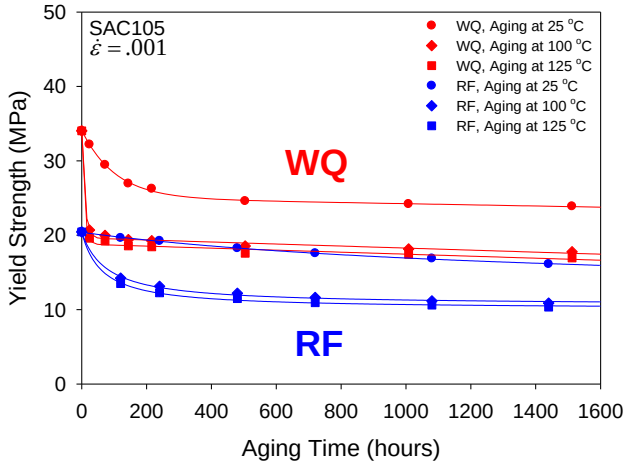

(c) YS

Figure 6.6 Effect of Solidification Cooling Profile on the Tensile Properties of SAC105 (W.Q. and R.F.)

	No Aging	60 Days @ 25 °C	60 Days @ 100 °C	60 Days @ 125 °C
E	1.38X	1.41X	1.50X	1.43X
UTS	1.28X	1.24X	1.25X	1.19X
YS	1.40X	1.46X	1.39X	1.29X

Table 6.2 Increases in Mechanical Properties of SACX
(W.Q. vs. R.F., R.F. as Baseline)

	No Aging	60 Days @ 25 °C	60 Days @ 100 °C	60 Days @ 125 °C
E	1.39X	1.23X	1.75X	1.80X
UTS	1.47X	1.25X	1.33X	1.35X
YS	1.66X	1.48X	1.64X	1.64X

Table 6.3 Increases in Mechanical Properties of SAC105
(W.Q. vs. R.F., R.F. as Baseline)

6.3 Effect of Cooling Profile on Creep Behavior

In this section, results for creep tests performed at a constant stress level of 15 MPa are presented. The steady state creep rates were obtained from the measured creep curves, and then modeled as a function of aging time. Moreover, the influence of solidification cooling profile on the steady state strain rates was investigated.

The creep responses of W.Q./R.F. SACX and SAC105 specimens are shown in Figures 6.7-6.10. Each Figure contains three ε vs. t plots for the three aging temperatures (T = 25, 100 and 125 °C). In each plot, a set of representative creep curves for different aging times are illustrated. Large differences in the slopes of secondary creep regions of the water quenched (Figure 6.7 and 6.9) and reflowed (Figure 6.8 and 6.10) specimens can be observed for analogous aging conditions.

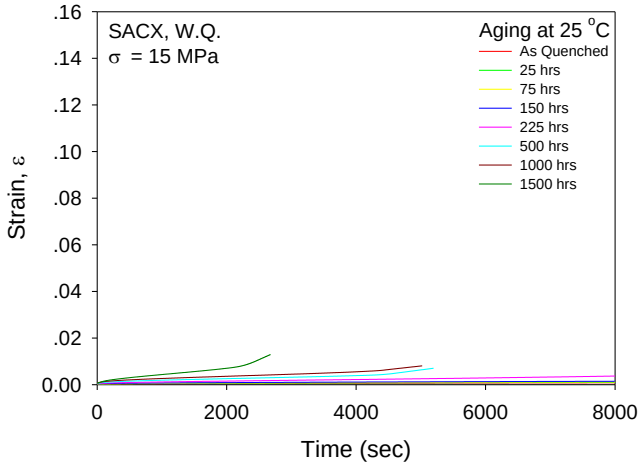

(a) Aging at T = 25 °C

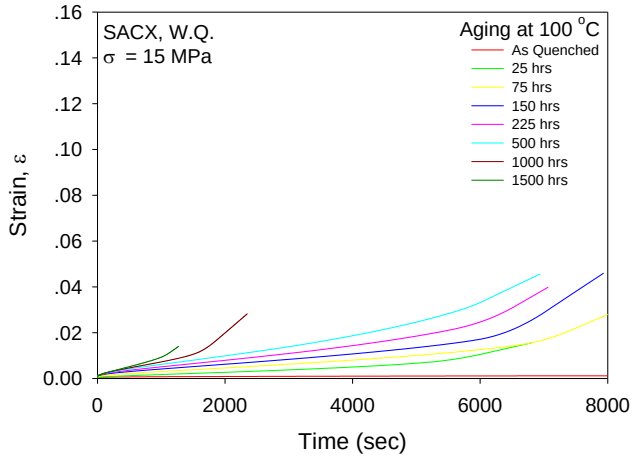

(b) Aging at T = 100 °C

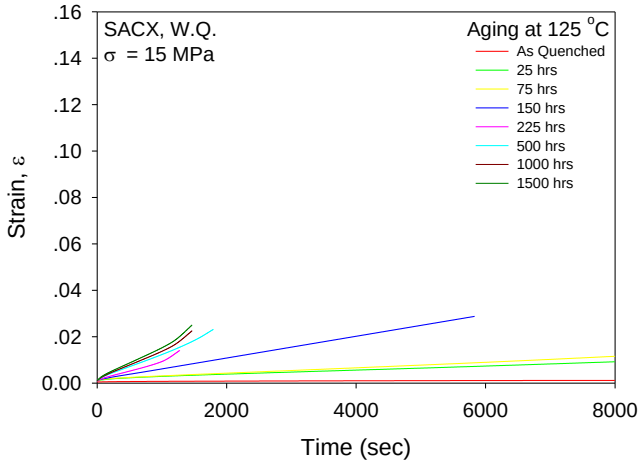

(c) Aging at T = 125 °C

Figure 6.7 Creep Curves for SACX
(W.Q., σ = 15 MPa, Aging for 0-60 Days)

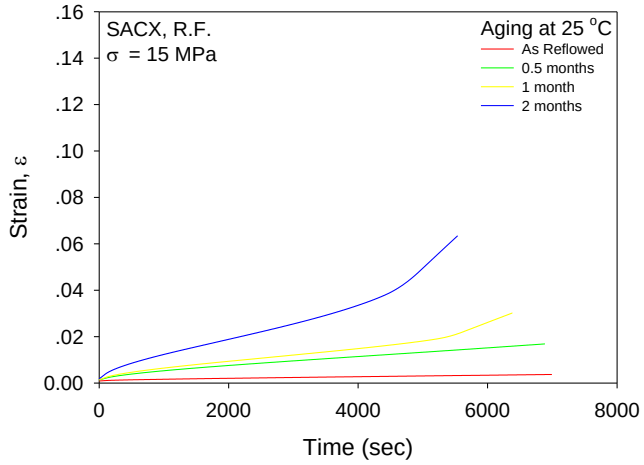

(a) Aging at T = 25 °C

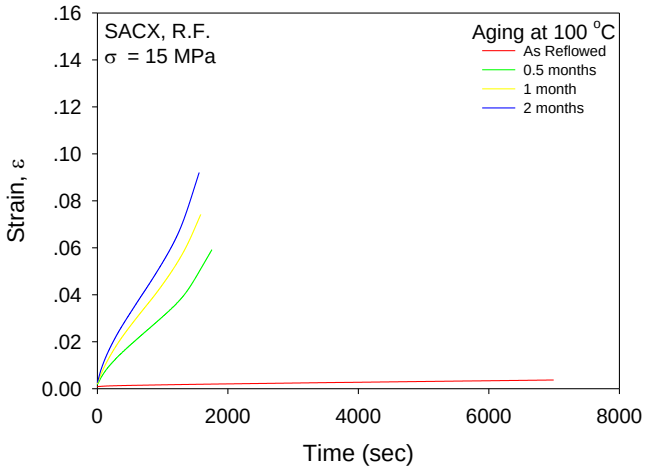

(b) Aging at T = 100 °C

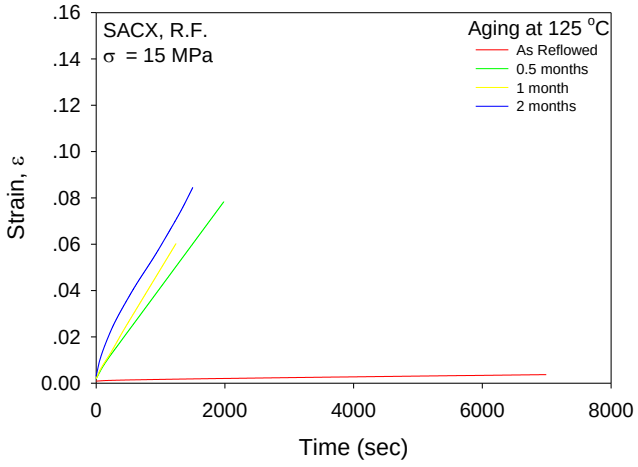

(c) Aging at T = 125 °C

Figure 6.8 Creep Curves for SACX
(R.F., σ = 15 MPa, Aging for 0-60 Days)

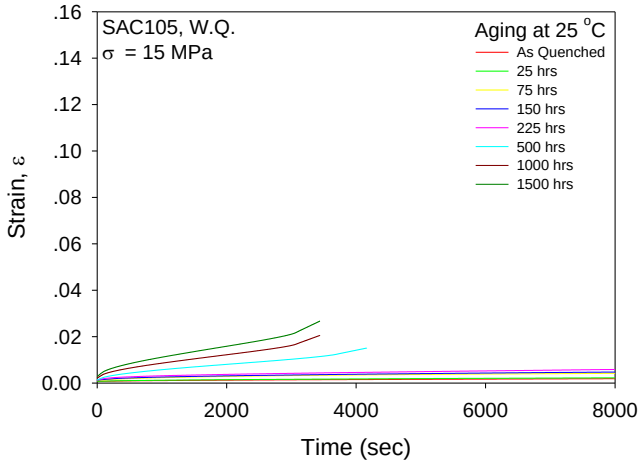

(a) Aging at T = 25 °C

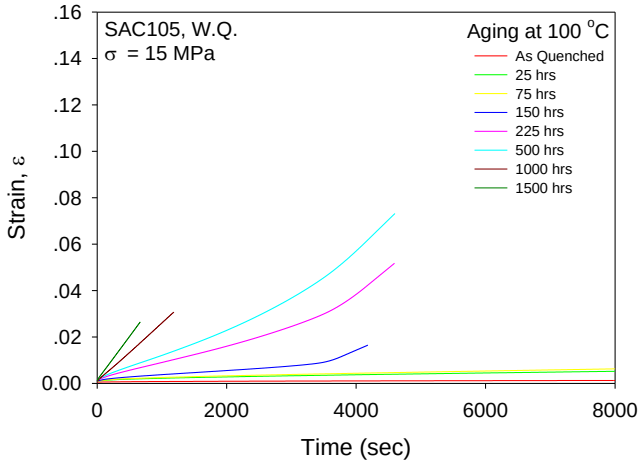

(b) Aging at T = 100 °C

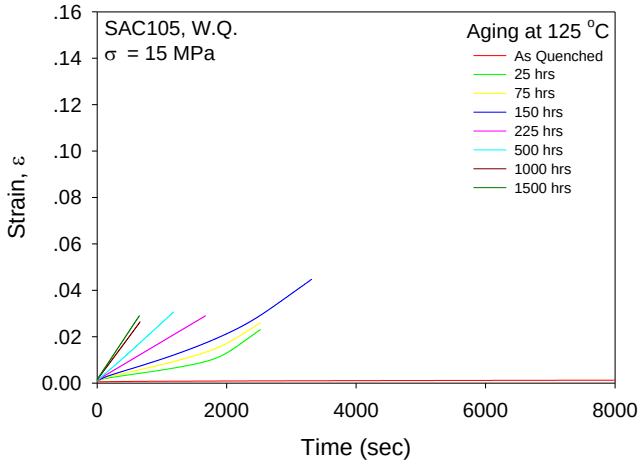

(c) Aging at T = 125 °C

Figure 6.9 Creep Curves for SAC105
(W.Q., σ = 15 MPa, Aging for 0-60 Days)

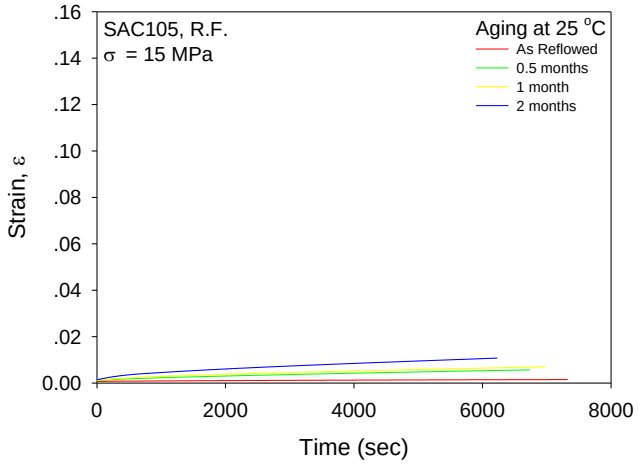

(a) Aging at T = 25 °C

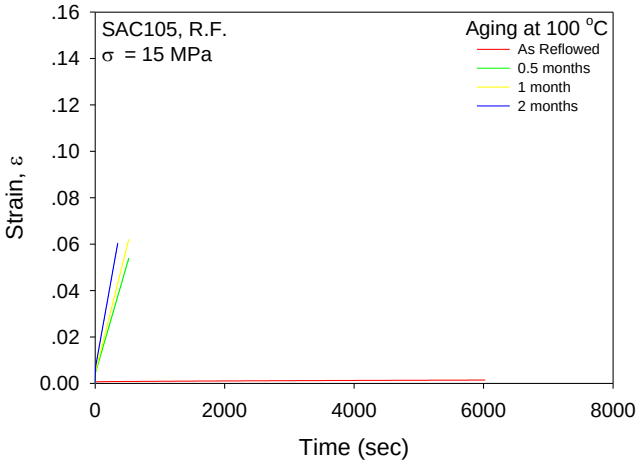

(b) Aging at T = 100 °C

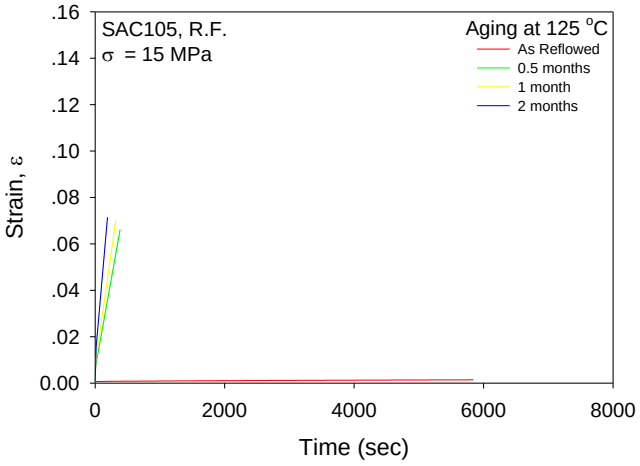

(c) Aging at T = 125 °C

Figure 6.10 Creep Curves for SAC105
(R.F., σ = 15 MPa, Aging for 0-60 Days)

As discussed in Chapter 3, the steady state strain rates of the creep curves shown in Figures 6.7-6.10 were extracted by using Eq. 3.6, and then plotted and modeled against aging time, as illustrated in Figures 6.11-6.12. Similar to the previous Figures, the curves in red are for the water quenched samples; and the curves in blue are for the reflowed samples. It is clear that the water quenched solder samples creep much slower, in other words, have better creep resistances than the reflowed samples. The increases in steady state creep rates (R.F. vs. W.Q., W.Q. as reference) are tabulated in Table 6.4. Even after severe aging conditions, for example, 60 days of aging at 100 ^{o}C, reflowed SACX samples still crept 11X faster than the analogous water quenched samples. However, similar to the situation of tensile properties discussed in Chapter 6.2.2, the aging induced degradation of the creep resistance of lead free solder alloys appears to be insensitive to the solidification cooling profile utilized for casting the samples.

	No Aging	60 Days @ 25 ^{o}C	60 Days @ 100 ^{o}C	60 Days @ 125 ^{o}C
SACX	4.25X	5.83X	11.35X	5.43X
SAC105	1.06X	1.60X	8.29X	7.21X

Table 6.4 Increases in Creep Rate (R.F. vs. W.Q., W.Q. as Baseline)

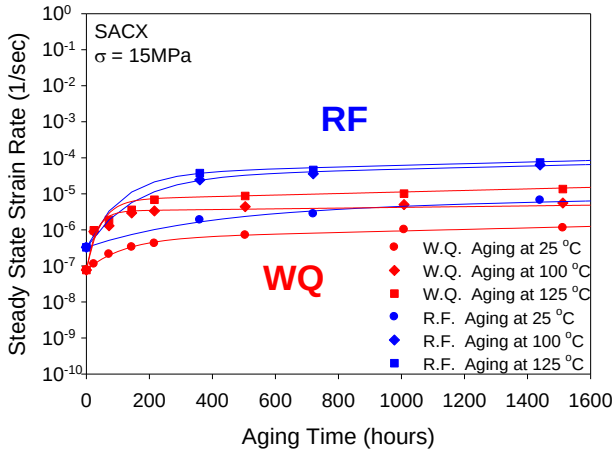

Figure 6.11 Effect of Cooling Rate on Creep Rate for SACX (W.Q. and R.F.)

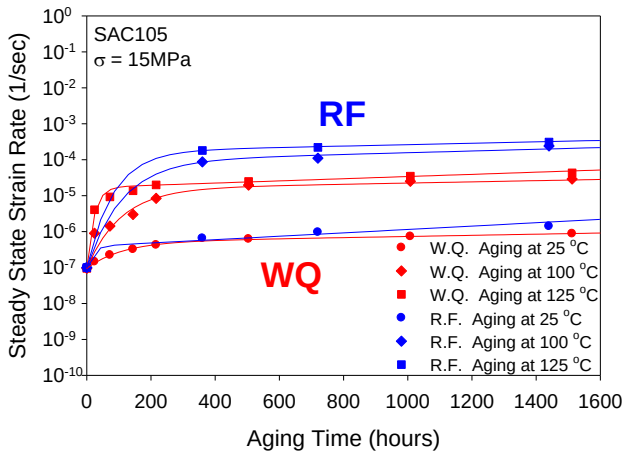

Figure 6.12 Effect of Cooling Rate on Creep Rate for SAC105 (W.Q. and R.F.)

6.4 Effect of Strain Rate on Tensile Behavior

The rate-dependent stress-strain behavior of solder materials has been reviewed in Chapter 2. It is widely acknowledged that the tensile properties of lead free solder materials, such as effective modulus, tensile strength, etc., are highly sensitive to the strain rate during testing. Therefore, most constitutive models for tensile behavior of lead free solder materials are rate dependent, such as the well-known Anand viscoplastic model. In this chapter, a brief study of strain rate effects on tensile behavior of lead free solder materials is presented.

The stress-strain responses at a higher testing rate ($\dot{\varepsilon}$ = 0.01 sec^{-1}) are depicted in Figures 6.13-6.14 for SACX and SAC105. These tests were conducted on water quenched specimens after various durations of isothermal aging exposure at RT (25 ^{o}C) and HT (125 ^{o}C). As before, the averaged stress-strain curves in these Figures were obtained by non-linear fitting of the ten individual experimental measurements. The results were then compared to the stress-strain data measured at the slower strain rate of 0.001 sec^{-1} as plotted in Figure 6.1 (a), (c) and Figure 6.3 (a), (c). An example of the

strain rate effects on the stress-strain responses is given in Figure 6.15. The conclusion is clear and as expected: a faster testing rate yields a higher stiffness and a better tensile strength for equally pre-conditioned (aged) lead free solder materials.

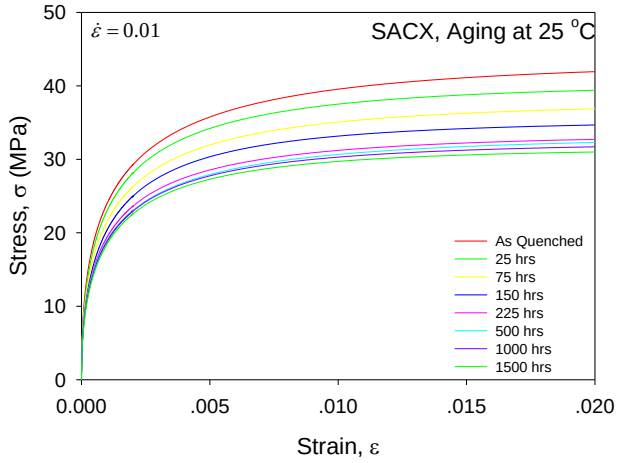

(a) Aging at T = 25 °C

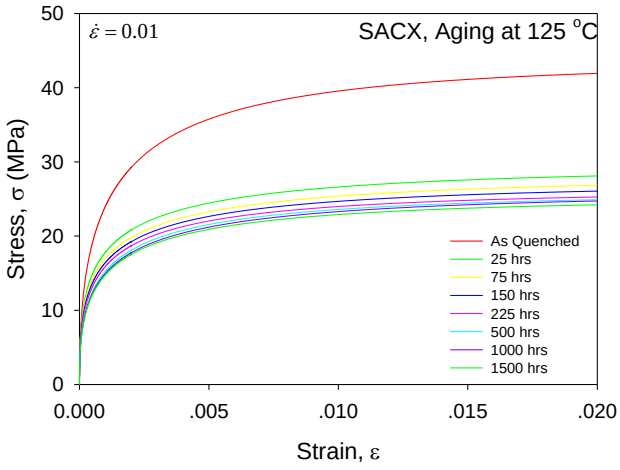

(b) Aging at T = 125 °C

Figure 6.13 Stress-Strain Curves for SACX
(W.Q., $\dot{\varepsilon}$ = 0.01 sec^{-1}, Aging for 0-60 Days)

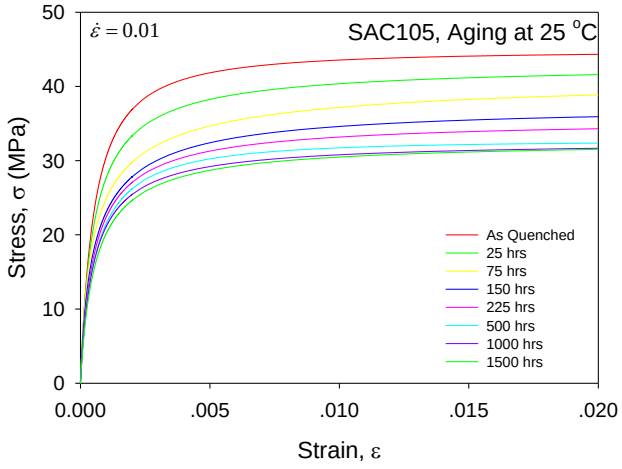

(a) Aging at T = 25 °C

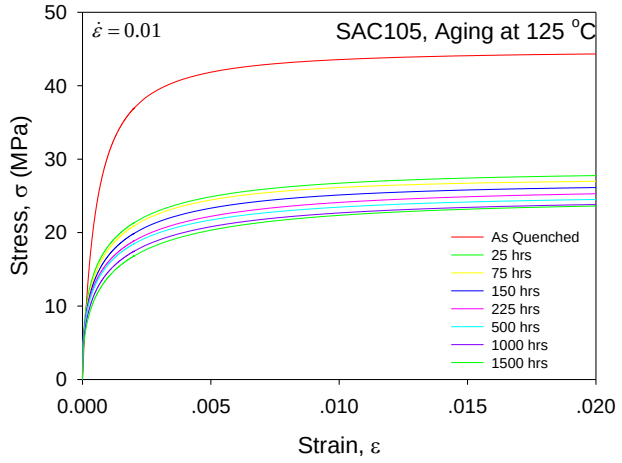

(b) Aging at T = 125 °C

Figure 6.14 Stress-Strain Curves for SAC105
(W.Q., $\dot{\varepsilon}$ = 0.01 sec^{-1}, Aging for 0-60 Days)

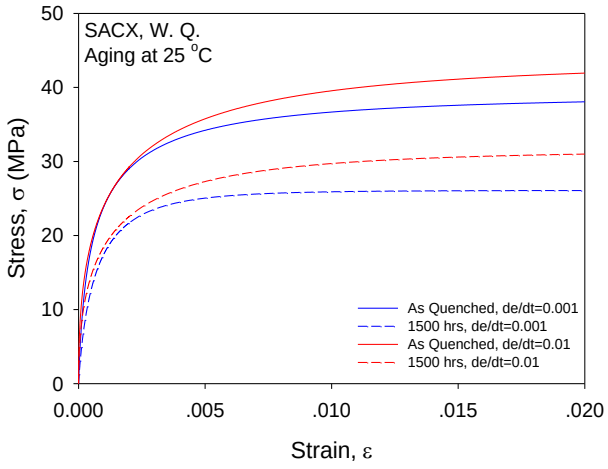

(a) SACX

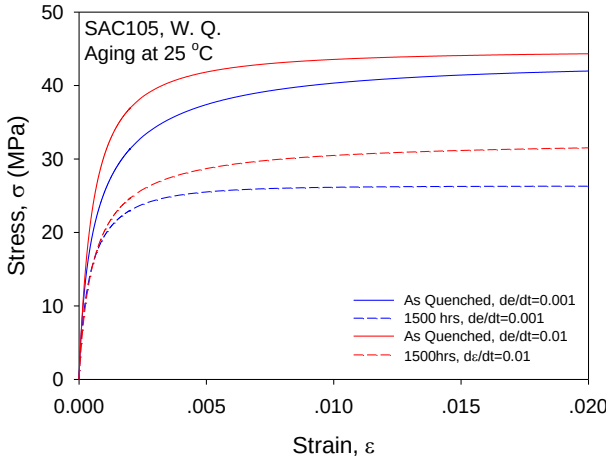

(b) SAC105

Figure 6.15 Effect of Strain Rate on the Stress-Strain Curves of SACX and SAC105

By applying the same procedures described previously, the tensile properties of SACX and SAC105 were extracted from the average stress-strain curves shown in Figures 6.13-6.14. The obtained data points were then plotted and modeled against aging time. As illustrated in Figures 6.16-6.17, all of the tensile properties are dramatically increased for the higher testing speed when comparing data for the same aging time. It is observed that the tensile strength of SACX and SAC105 increased approximately 20% for the higher strain rate testing. Tables 6.5-6.6 summarize the increases in the mechanical properties with the higher strain rate.

	No Aging	1500 Hours @ 25 ^{o}C	1500 Hours @ 125 ^{o}C
E	1.11X	1.01X	1.03X
UTS	1.12X	1.18X	1.23X
YS	1.02X	1.04X	1.08X

Table 6.5 Increases in Mechanical Properties of SACX
(high $\dot{\varepsilon}$ vs. low $\dot{\varepsilon}$, low $\dot{\varepsilon}$ as Baseline)

	No Aging	1500 Hours @ 25 ^{o}C	1500 Hours @ 125 ^{o}C
E	1.14X	1.01X	1.01X
UTS	1.16X	1.23X	1.23X
YS	1.16X	1.11X	1.09X

Table 6.6 Increases in Mechanical Properties of SAC105
(high $\dot{\varepsilon}$ vs. low $\dot{\varepsilon}$, low $\dot{\varepsilon}$ as Baseline)

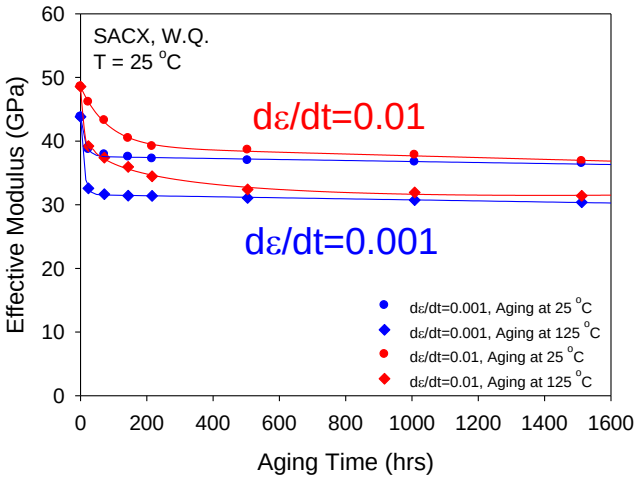

(a) E

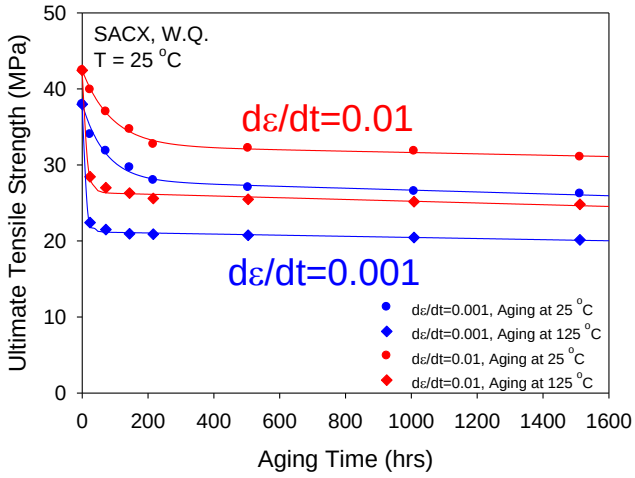

(b) UTS

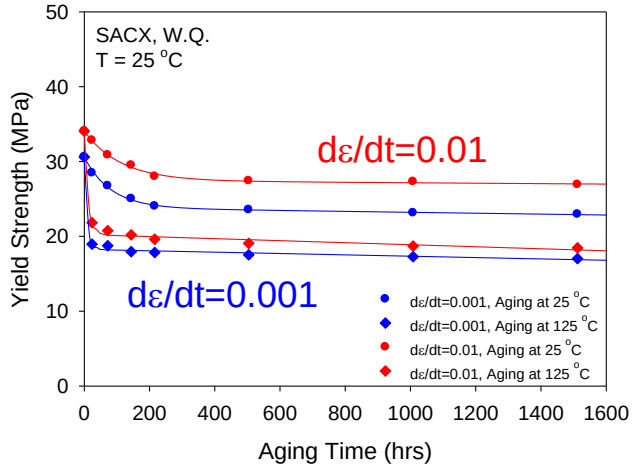

(c) YS

Figure 6.16 Effect of Strain Rate on Tensile Properties of SACX

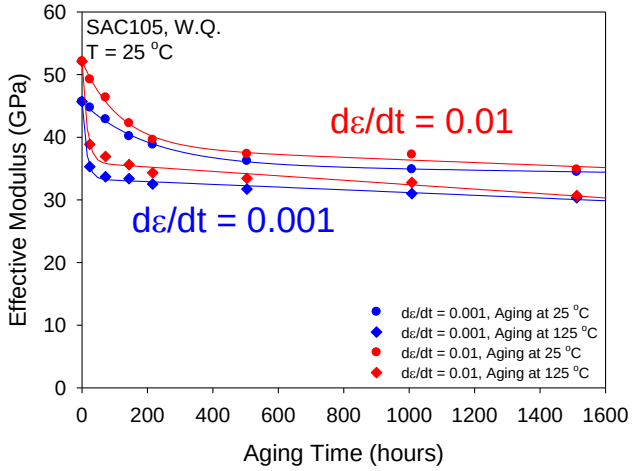

(a) E

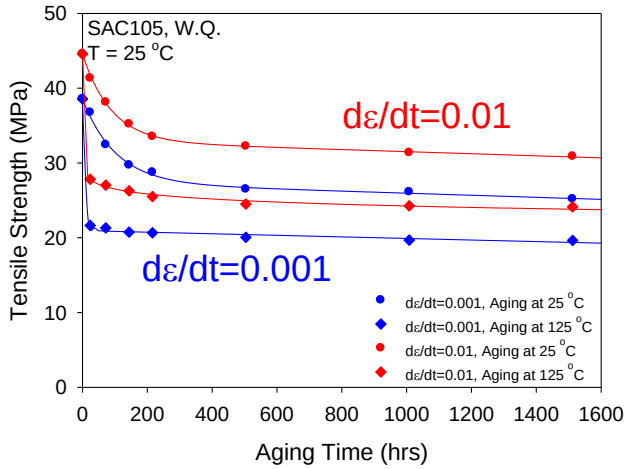

(b) UTS

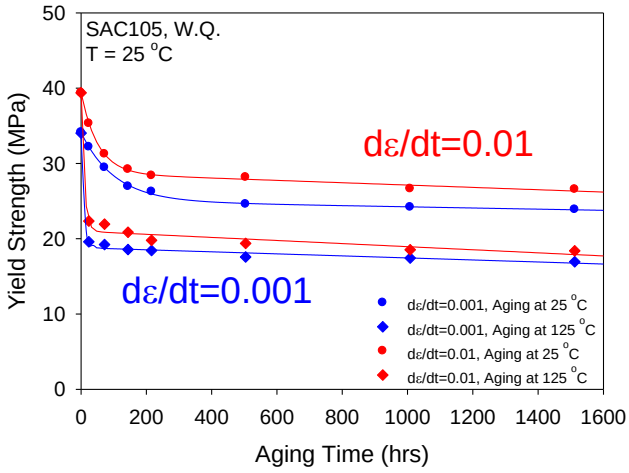

(c) YS

Figure 6.17 Effect of Strain Rate on Tensile Properties of SAC105

6.5 Effect of Stress Level on Creep Behavior

It is well known that the creep behavior of solder materials is notably affected by the magnitude of the applied load. In this section, the effect of stress level on creep behavior is reported. Water quenched specimens were aged at 100 ^{o}C and 125 ^{o}C for up to 1500 hours before creep testing at loads of 10 and 15 MPa. The representative creep curves under each aging condition were plotted and the corresponding steady state creep rates were calculated.

The creep curves for aged SACX and SAC105 specimens subjected to σ = 10 MPa are shown in Figures 6.18-6.19. These data were compared with the creep data for σ = 15 MPa shown earlier in Figures 6.7 (b), (c) and Figures 6.8 (b), (c). The various creep curves were fit using Eq. 3.6, and then the extracted steady state strain rate data were plotted against aging time, as shown in Figures 6.20-6.21. In these plots, specimens tested under a stress level of 15 MPa are colored in blue; while those for 10 MPa are in red. As stated in the previous chapters, the creep behavior of solder materials is strongly influenced by the applied stress level. Even an increase of 5 MPa in stress caused drastic increases in the creep rates of the SAC alloys. More detailed comparisons are summarized in Table 6.7 for two solder materials and three different aging conditions. Interestingly, the effect of stress level was relatively small for the non-aged SAC solder materials, but became an order of magnitude larger for the aged samples. Therefore, it is valid to conclude that the effect of stress level on the creep rate is highly exacerbated by aging.

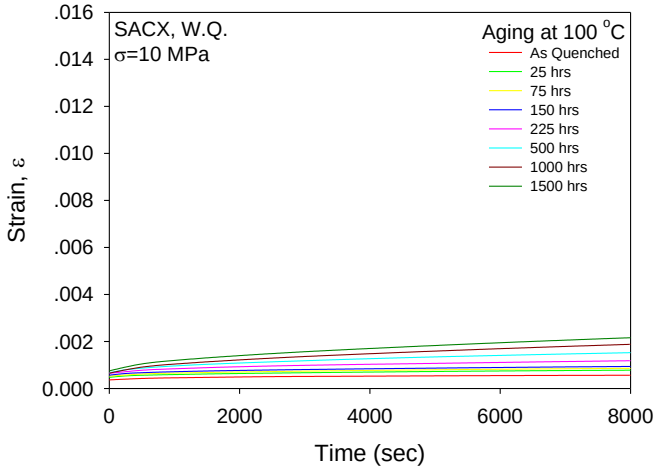

(a) Aging at T = 100 °C

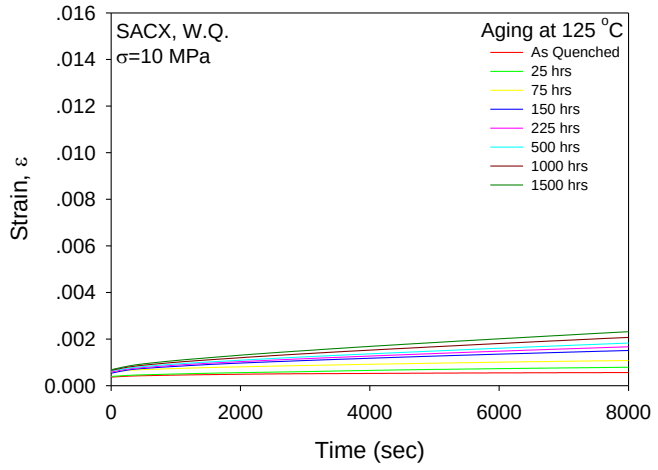

(b) Aging at T = 125 °C

Figure 6.18 Creep Curves for SACX
(W.Q., σ = 10 MPa, Aging for 0-60 Days)

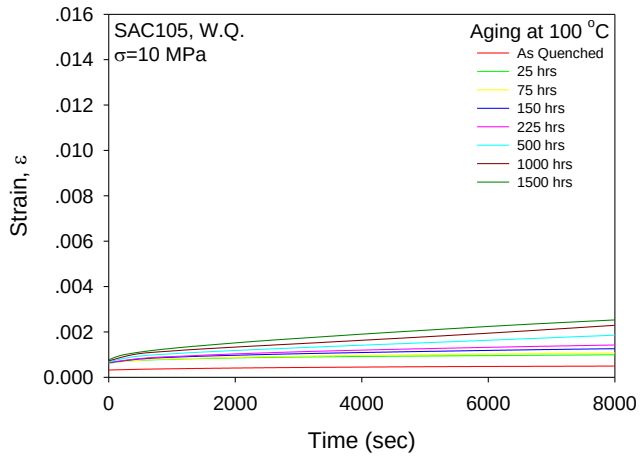

(a) Aging at T = 100 °C

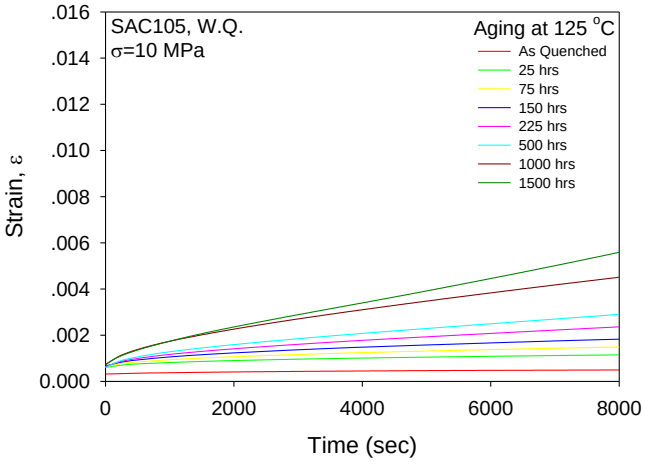

(b) Aging at T = 125 °C

Figure 6.19 Creep Curves for SAC105
(W.Q., σ = 10 MPa, Aging for 0-60 Days)

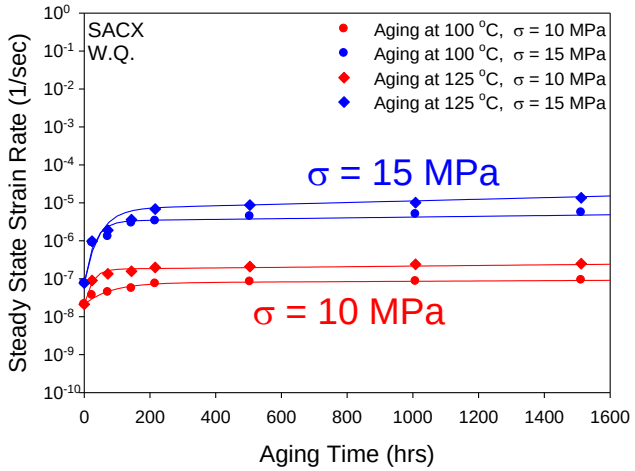

Figure 6.20 Effect of Stress Level on Creep Rate for SACX

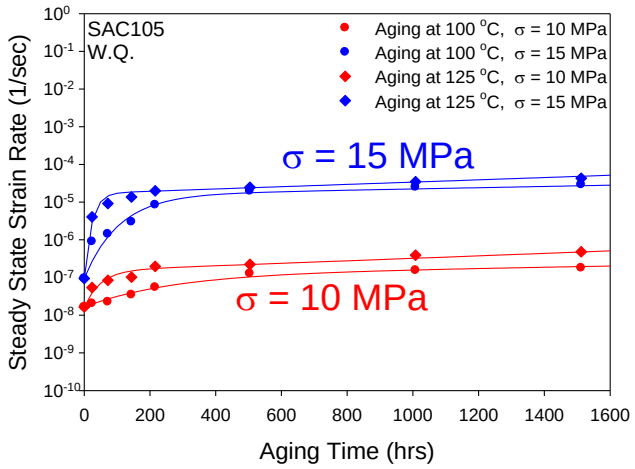

Figure 6.21 Effect of Stress Level on Creep Rate for SAC105

	No Aging	1500 Hours @ 100 °C	1500 Hours @ 125 °C
SACX	3.61X	60.59X	54.38X
SAC105	5.72X	162.19X	89.58X

Table 6.7 Increases in Creep Rate
(high σ vs. low σ, low σ as Baseline)

6.6 Summary and Discussion

In this chapter, the effects of solidification cooling profile and testing conditions on the material properties of SAC alloys have been examined by performing a series of tensile and creep tests. The specimens were prepared with two different types of cooling profile, namely, Water Quenching Profile and Reflow Profile. The testing specimens were subject to isothermal aging exposures (3 aging temperatures and up to 8 aging time durations) before testing. The tensile tests were performed at two different strain rates ($\dot{\varepsilon}$ = 0.01 and 0.001 sec^{-1}), while the creep tests were conducted under two different applied stresses (σ = 10 and 15 MPa).

It has been demonstrated that the higher cooling rate (water quenching) resulted in enhanced material properties for both SAC solder materials under the same testing condition. The water quenched samples have higher stiffness, better tensile and yield strength, as well as larger creep resistance than the analogous reflowed specimens. Although it is impossible to "water quench" real electronic packages, the water quenched data is still meaningful because it approaches the optimal case of extremely fine microstructure, and can serve as a guideline for design purposes. The effects of testing conditions (such as strain rate effect for tensile and effect of stress level for creep) were also presented in this chapter. The testing results in this study agreed with prior studies in the literature. Higher strain rates led to enhanced tensile performance for both SAC solder materials. Additionally, the steady state strain rate in creep has proven to be significantly sensitive to the applied stress level.

In general, it was found that neither the adoption of a different solidification cooling profile or the use of other testing conditions were able to reduce aging effects. In

fact, the use of higher stress levels in creep tended to exacerbate the observed degradations due to aging.

CHAPTER 7

AGING INDUCED MICROSTRUCTURE EVOLUTION AND RESIDUAL STRESS RELAXATION OF LEAD FREE SOLDER ALLOYS

7.1 Introduction

The work in this dissertation has documented the dramatic changes occurring in the constitutive and failure behavior of solder materials and solder joint interfaces during isothermal aging. It is also acknowledged that the microstructure and material behavior of the samples used in even a single investigation are moving targets that are evolving rapidly even at room temperature. Furthermore, the effects of aging on solder behavior must be better understood so that more accurate viscoplastic constitutive equations can be developed for lead free solders. Without such relations, it is doubtful that finite element reliability predictions can ever reach their full potential.

In Chapter 4, a parametric study of aging effects on material properties of lead free solder alloy has been conducted. A low silver content solder, SACX0307 (X = 0.1 wt.% Bi), has been characterized by performing both tensile and creep testing with a full aging test matrix (aging temperature + aging time). It has been found that aging is detrimental to the material properties of SACX; in other words, SACX continues to lose its strength as well as stiffness as aging progresses.

In Chapter 5, however, it has been demonstrated that the aging induced degradation in mechanical properties can be mitigated by metallurgical approaches such as doping. By adding small amount of X elements (i.e. Bi, Ni, Ge, Co, La, Zn, Al, Fe,

Mn, Mg, etc) into the lead free SAC+X solder, the material properties were observed to stabilize quickly with aging.

Along with the study of aging effects on extrinsic mechanical properties of solders, it is also necessary to examine the intrinsic responses of solder material to aging, namely, the aging induced microstructure evolution, so that the aging effects on mechanical behavior of lead free solders can be fully understood. Therefore, this chapter will concentrate on the presentation of results on correlation of aging effects and three possible factors that affect the material properties: phase coarsening, grain/sub-grain growth, and relaxation of internal residual stress.

7.2 Melting Behavior of Lead Free Solder Alloys

To start with, a study on melting behavior of lead free solder alloys was performed by DSC analysis. The data was collected over a temperature range from 190 ^{o}C to 250 ^{o}C, at a heating rate of 10 ^{o}C/min. The results are plotted as shown in Figure 7.1. Such information is useful for a microstructure study because any phase reaction, especially which occurs during melting process, will be indicated on the heat flow-temperature diagram. Thus, the possible phases that exist in solidified solder materials can be extrapolated. For example, the two peaks in Figure 7.1 (a) indicate the occurrence of two phase reactions for SACX solder during heating process:

(1) $Ag_3Sn^{(s)} + Cu_6Sn_5^{(s)} + Sn^{(s)} \rightarrow L$

(2) $Cu_6Sn_5^{(s)} + Sn^{(s)} \rightarrow L$

Therefore, 3 possible phases that may exist in as-solidified SACX solder are Ag_3Sn, Cu_6Sn_5, and β-Sn as the matrix. The melting temperature of SACX can be obtained from the location of the first peak (T_m = 218.78 ^{o}C). The pasty range is approximated by

estimating the difference between the onset temperature (218.03 ^{o}C) and the location of the last peak (227.89 ^{o}C), which yields 9.86 ^{o}C in this case.

Similar calculations were performed on all other solders using the graphs in Figure 7.1 to extract the melting temperature, pasty range and major phase reactions that occur during heating. The results are summarized in Table 7.1. Note that the large pasty ranges of SACX and SAC105 are caused by their hypo-eutectic compositions. For the doped solders, the amount of dopant is so small that the variation in heat flow cannot be noticed even though there exist phase reactions involving the doping element.

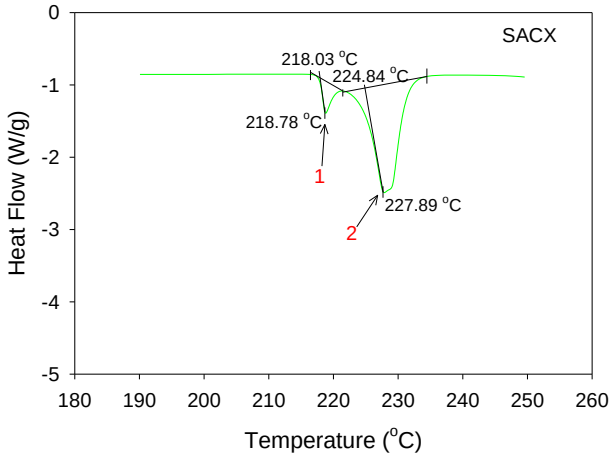

(a) SACX

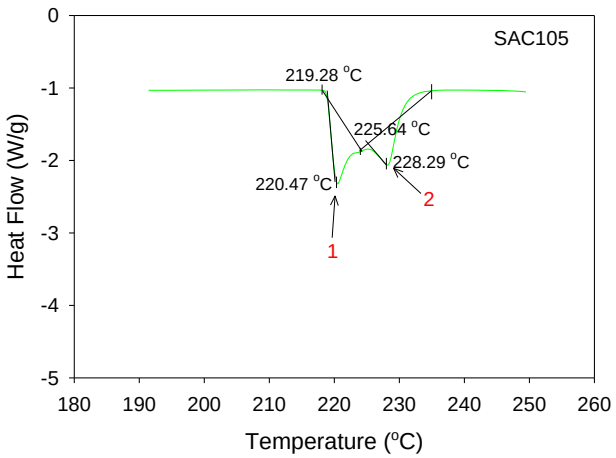

(b) SAC105

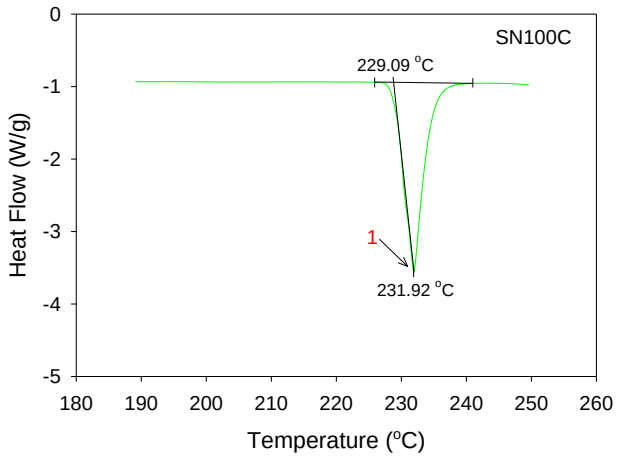

(c) SN100C

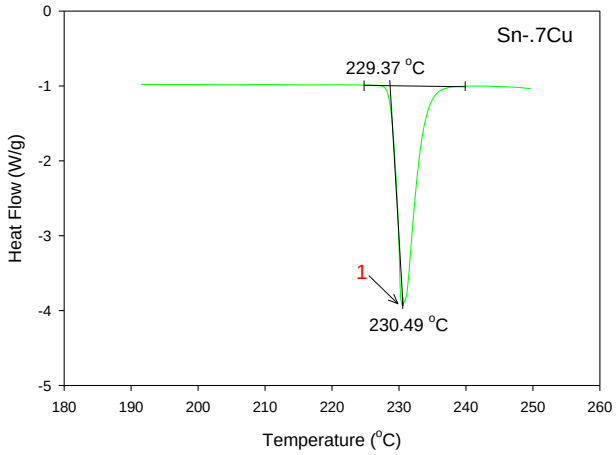

(d) Sn-0.7Cu

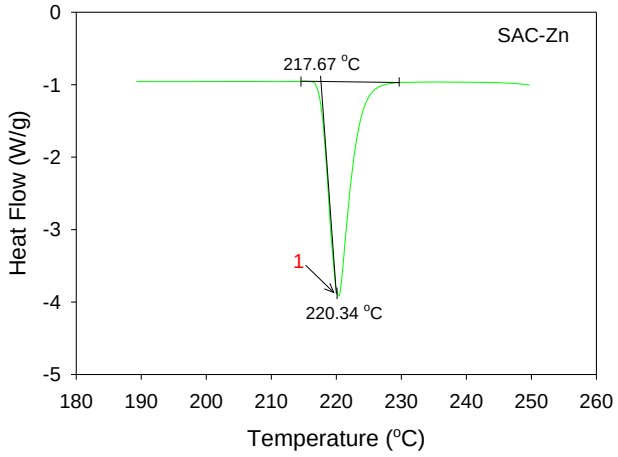

(e) SAC-Zn

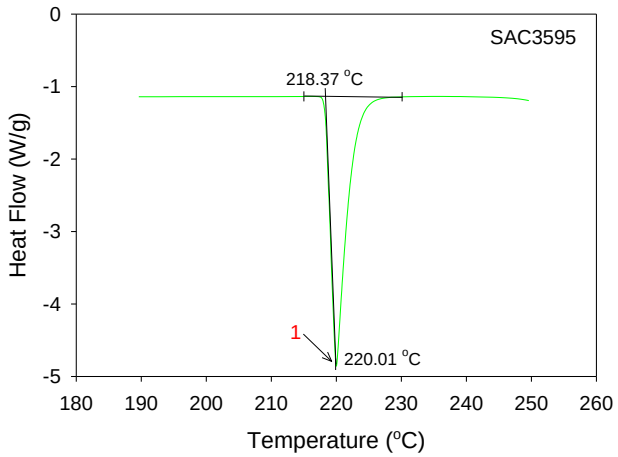

(f) SAC3595

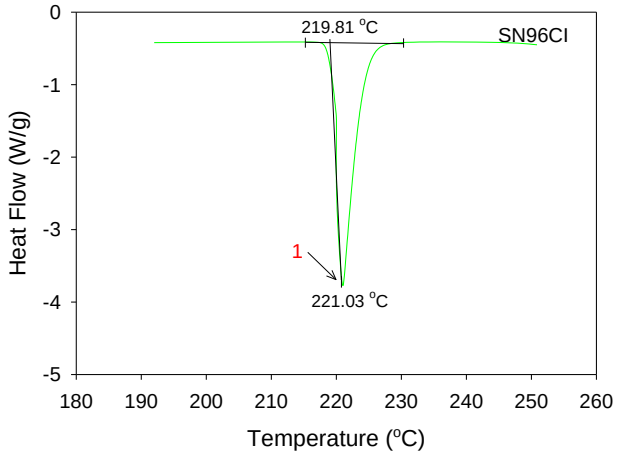

(g) SN96CI

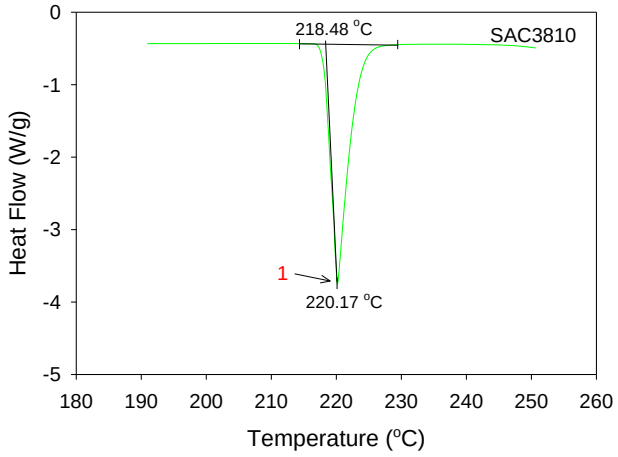

(h) SAC3810

Figure 7.1 DSC Analysis of Lead Free Solder Alloys

Alloy	Melting Temperature (^oC)	Pasty Range (^oC)	Major Phase Reaction
SACX	218.78	9.86	1) $Ag_3Sn^{(s)} + Cu_6Sn_5^{(s)} + Sn^{(s)} \rightarrow L$ 2) $Cu_6Sn_5^{(s)} + Sn^{(s)} \rightarrow L$
SAC105	220.47	9.01	1) $Ag_3Sn^{(s)} + Cu_6Sn_5^{(s)} + Sn^{(s)} \rightarrow L$ 2) $Cu_6Sn_5^{(s)} + Sn^{(s)} \rightarrow L$
SN100C	231.92	2.83	1) $Cu_6Sn_5^{(s)} + Sn^{(s)} \rightarrow L$
Sn-0.7Cu	230.49	1.12	1) $Cu_6Sn_5(s) + Sn^{(s)} \rightarrow L$
SAC-Zn	220.34	2.67	1) $Ag_3Sn^{(s)} + Cu_6Sn_5^{(s)} + Sn^{(s)} \rightarrow L$
SAC3595	220.01	1.64	1) $Ag_3Sn^{(s)} + Cu_6Sn_5^{(s)} + Sn^{(s)} \rightarrow L$
SN96CI	221.03	1.22	1) $Ag_3Sn^{(s)} + Cu_6Sn_5^{(s)} + Sn^{(s)} \rightarrow L$
SAC3810	220.17	1.69	1) $Ag_3Sn^{(s)} + Cu_6Sn_5^{(s)} + Sn^{(s)} \rightarrow L$

Table 7.1 Melting Temperature and Pasty Range of Solders of Interest

7.3 Effect of Aging on Phase Coarsening

As shown in a typical micrograph of a ternary Sn-Ag-Cu (SAC) solder alloy (Figure 7.2), the microstructure of SAC solders consists of primary β-Sn dendrites, and a honeycomb structure of uniformly dispersed fine precipitates over the β-Sn matrix throughout the bulk solder material. A closer look at the SAC solder (Figure 7.3) shows the different morphology of intermetallic compounds (IMCs) that exist and distribute around the β-Sn dendrite arms. Furthermore, by correlating the results from qualitative elemental mapping (Figure 7.4) with quantitative EDX analysis (Figure 7.5) conducted on the particles of interest (pointed out by red arrows in both figures), two types of IMCs were identified: (1) needle-shaped ε-Ag_3Sn; (2) scallop-shaped η-Cu_6Sn_5.

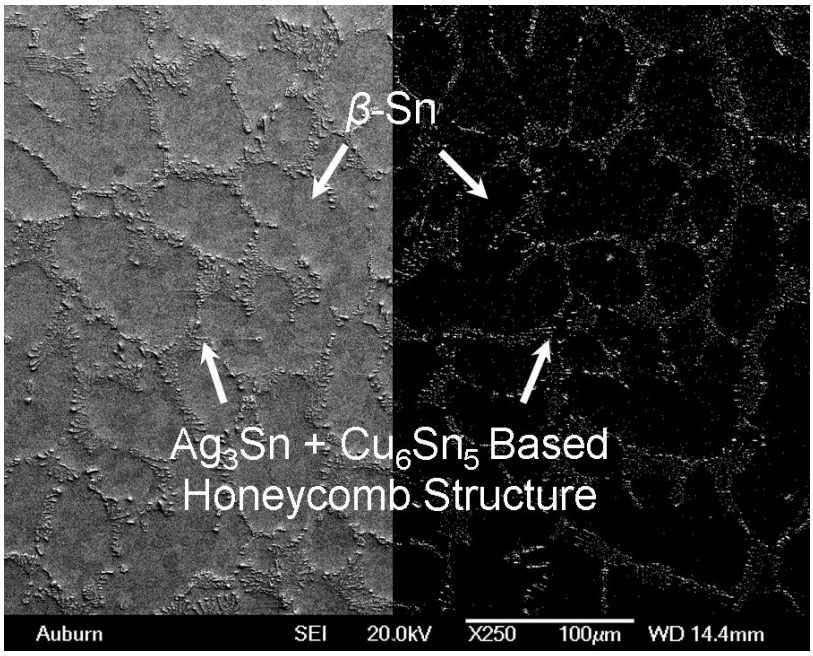

Figure 7.2 Typical Metallography of a Sn-Ag-Cu Solder
(SACX, As Reflowed, 250X)

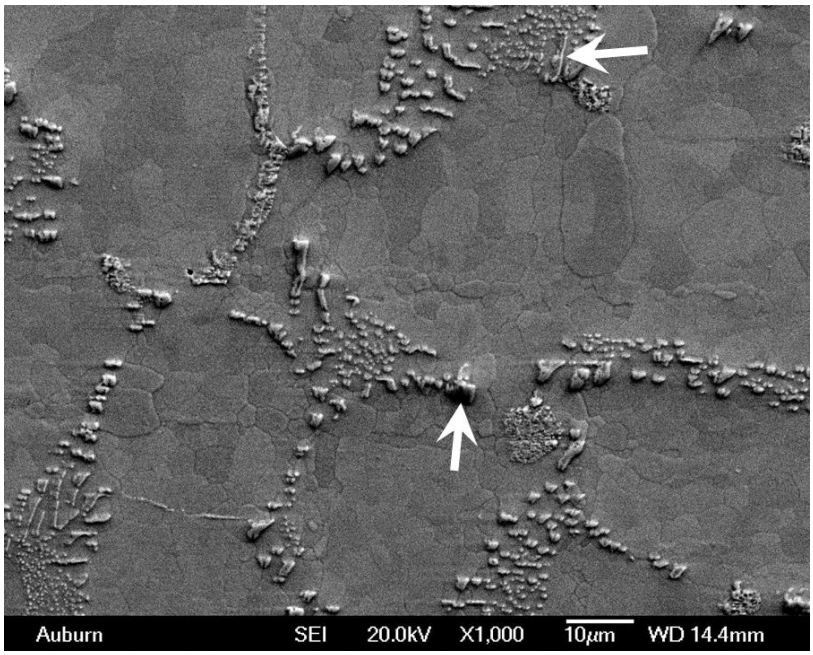

Figure 7.3 Typical Morphology of Intermetallic Compounds in a SAC Solder
(SACX, As Reflowed, 1000X)

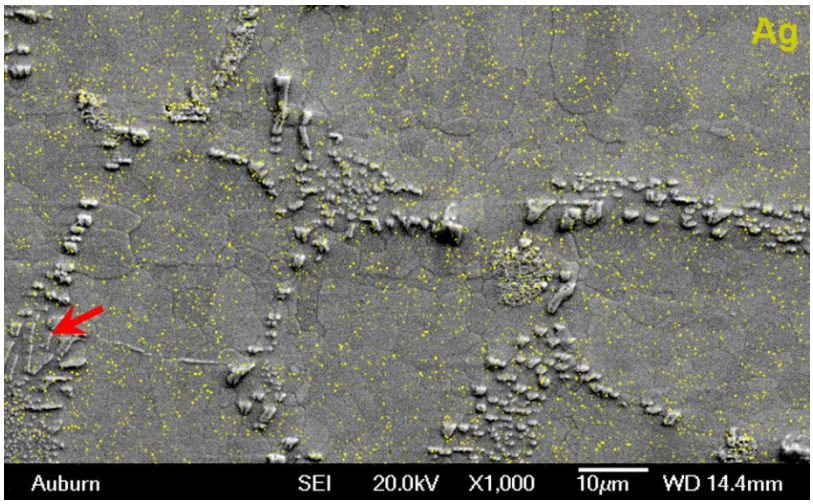

(a) Ag

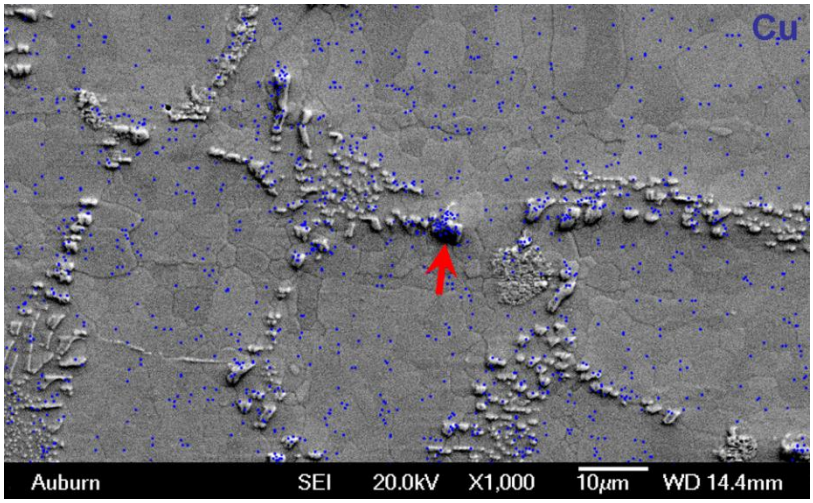

(b) Cu

Figure 7.4 Elemental Distribution Maps for SACX Solder and EDX Spots

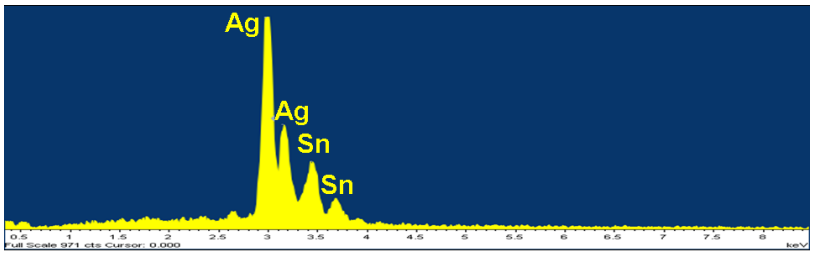

Element	Weight %	Atomic %
Ag L	72.02	73.90
Sn L	27.98	26.10
Totals	100.00	100.00

(a) Needle-Shaped Precipitates Distributed on β-Sn Matrix

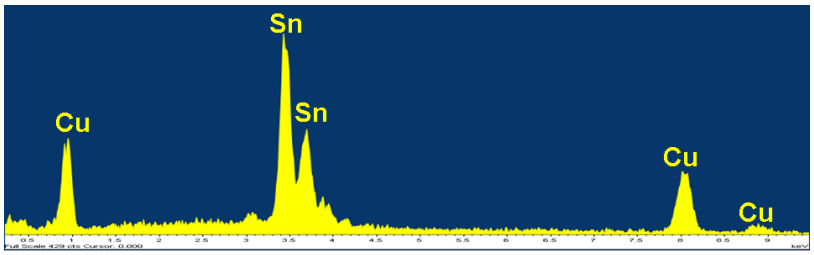

Element	Weight %	Atomic %
Cu K	36.32	51.60
Sn L	63.68	48.40
Totals	100.00	100.00

(b) Scallop-Shaped Precipitates Distributed on β-Sn Matrix

Figure 7.5 EDX Analysis of Typical IMCs in a SAC Solder Alloy

Aging causes phase coarsening in SAC solder alloys, which consists of growth, coalescence, and dispersing of IMCs with increased isothermal exposure [54, 55]. Microstructure evolution with different aging durations for SACX solder is pictured in Figures 7.6-7.7 (250X and 1000X magnifications, respectively). In this study, the water quenched SACX specimens were aged at 100 ^{o}C for up to 60 days and then prepared

according to the molding and polishing procedure described in Chapter 3. In general, it can be seen that the number of IMCs decreases while the average particle size increases with an increased aging time. For the first 2-3 days of aging, the microstructure of SACX evolved significantly so that the honeycomb structure in the as-quenched SACX sample could not be easily distinguished. Instead, a vast number of randomly distributed IMCs were observed and the microstructure evolution entered a steady state. Fine IMC particles gradually dispersed away from their original locations to the grain boundaries and conglomerated as aging progressed (Figure 7.8(b)). As a result, large IMCs were expected to emerge in the microstructure. Figure 7.9 is an example of an extreme case where a gigantic Cu_6Sn_5 IMC was captured. This particle measured approximately 20 μm in diameter.

Similar aging time effects were also found in reflowed SACX solders. In addition, the effect of aging temperature was examined through a parametric study on the reflowed samples. The SEM micrographs in Figure 7.10 were taken on both non-aged and aged samples. In this study, two aging temperatures (T = 25, 125 ^{o}C) and four aging durations (t = 0, 1, 3, 6 months) were considered. This resulted in a total of 7 different aging conditions (note that microstructure for zero-aging will be identical for the two aging temperatures, as shown in Figure 7.10(a)). By comparing the graphs with the same aging time, it is observed as expected that the microstructure evolved much more significantly with an increased aging temperature. The microstructure of SACX aged for 1 month at 125 ^{o}C appeared to be much more coarsened than that of SACX exposed to 6 months of room temperature aging. In fact, this result can be verified by using the Arrhenius relationship. According to Eq. 4.9, an acceleration factor (AF) of 1211X was

estimated (note that according to Table 4.4, the activation energy Q is approximated to be 70kJ for reflowed SACX solder):

$$AF = e^{\frac{Q}{R}\left(\frac{1}{T_1}-\frac{1}{T_2}\right)} = e^{\frac{70k}{8.314}\left(\frac{1}{298}-\frac{1}{398}\right)} = 1211 \tag{7.1}$$

Therefore, theoretically it takes 1211 months of aging at room temperature for SACX solder to achieve the same microstructure that occurs for aging of 1 month at 125 ^{o}C.

More importantly, the observations of the aging induced microstructure evolution of SACX solder alloy can explain the observed degradation in the material properties. As stated before, due to the high homologous temperature, SAC solder materials are thermally activated even at room temperature, which results in the dispersing, coalescence, and growth of phases with time. Therefore, the IMCs, as the second phase particles in the microstructure of a SAC alloy, gradually lose their effectiveness in pinning moving dislocations caused by external stresses. Hence, as aging progresses, weaker pinning effects from precipitates cause the reduction in resistance to deformation and finally leads to the losses in strength and stiffness, as well as the increases in the creep rate of the SAC solder material.

Another observation is that the cooling rate during solidification greatly affects the initial microstructure. By comparing Figure 7.6(a) to Figure 7.10(a), it can be seen that faster cooling rate during solidification yields finer IMC particles and smaller β-Sn dendrites. Therefore, the findings in Chapter 6, where water quenched solder samples possessed better material properties than reflowed samples, can be easily explained.

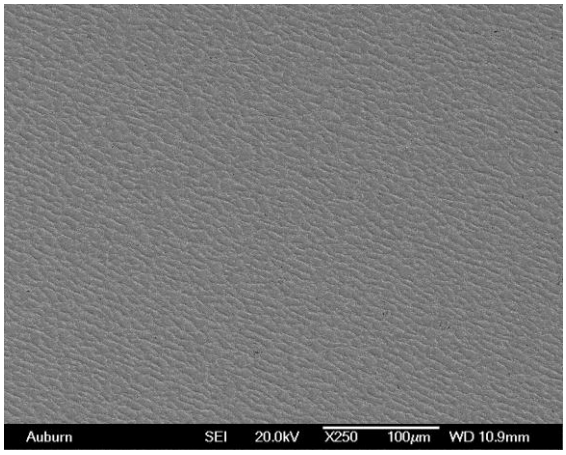

(a) Non-aged (As W.Q.)

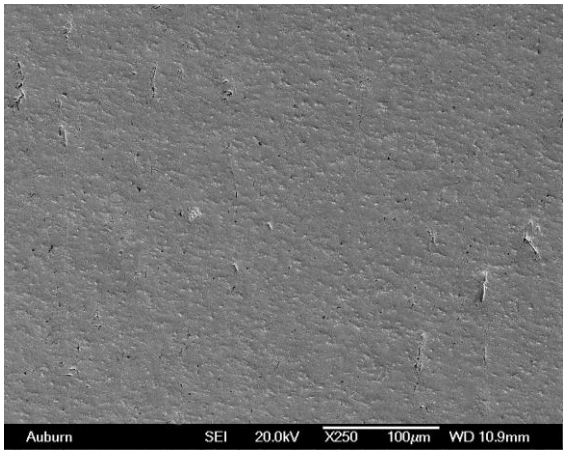

(b) 1 day

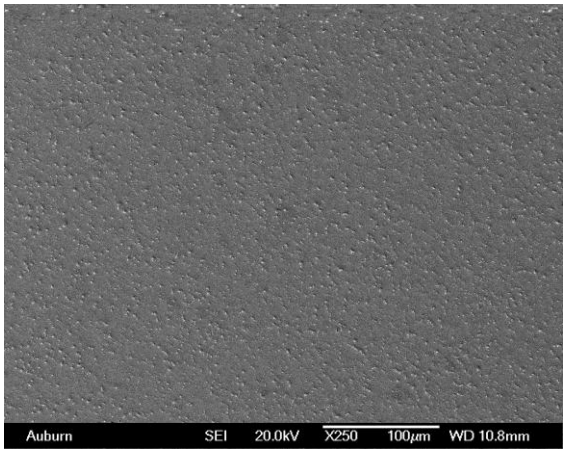

(c) 2 days

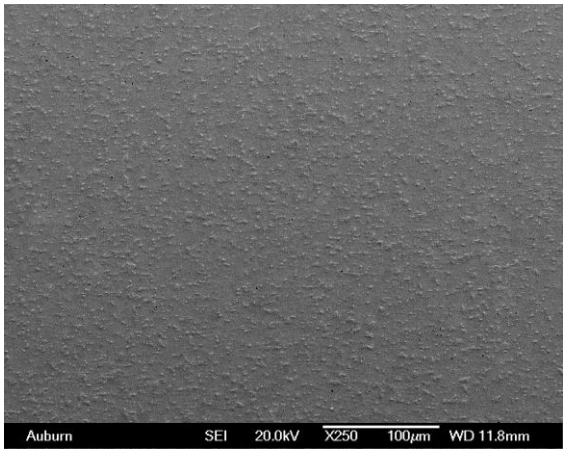

(d) 3 days

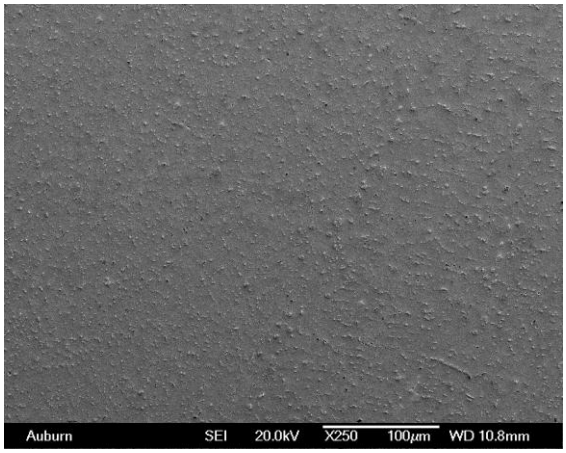

(e) 6 days

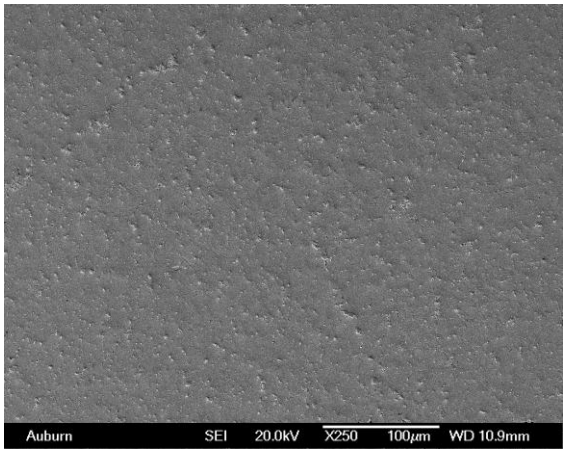

(f) 9 days

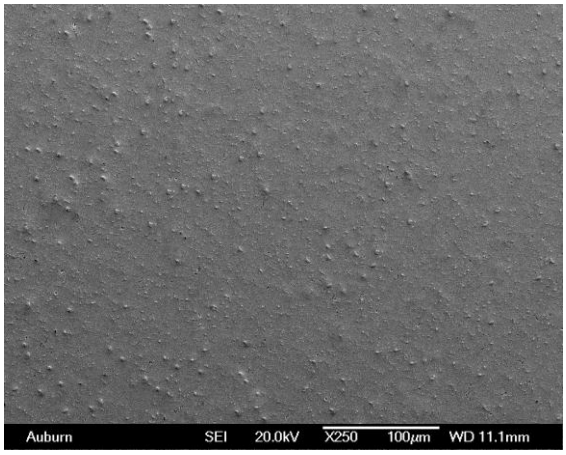

(g) 15 days

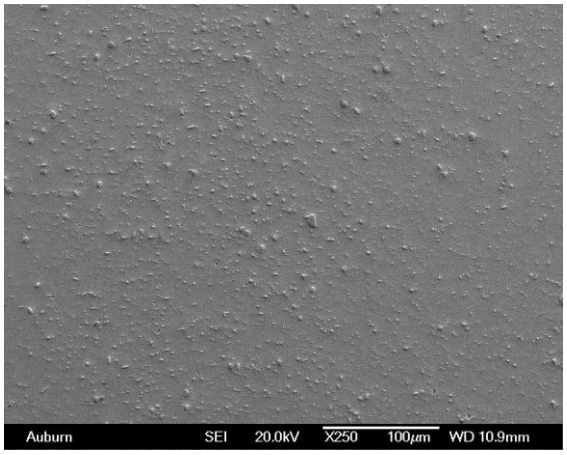

(h) 20 days

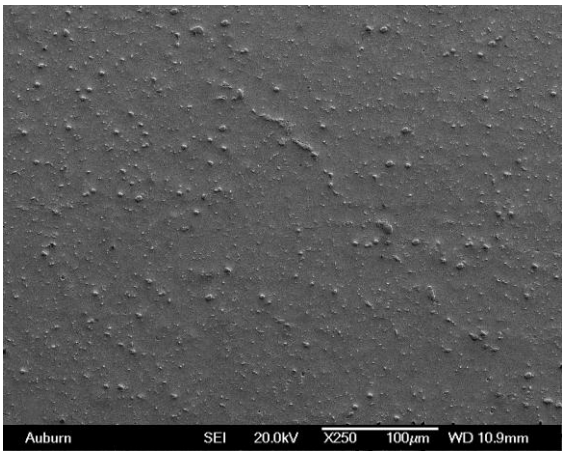

(i) 30 days

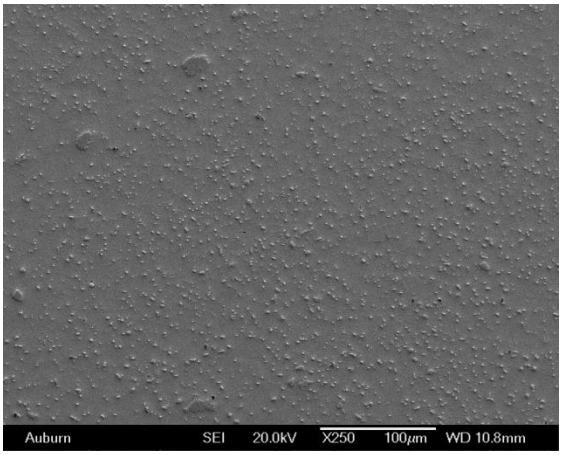

(j) 60 days

Figure 7.6 Microstructure Evolution of SACX with Aging
(250X, W.Q., Aged at 100 ^{o}C)

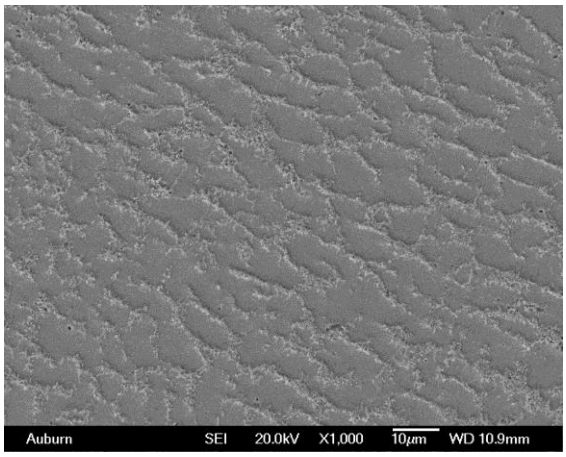

(a) Non-aged (As W.Q.)

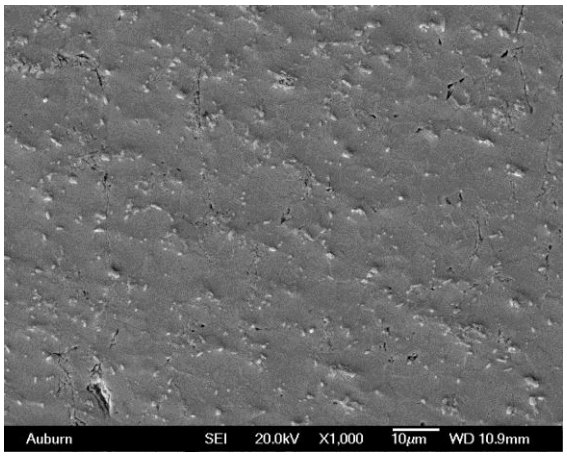

(b) 1 day

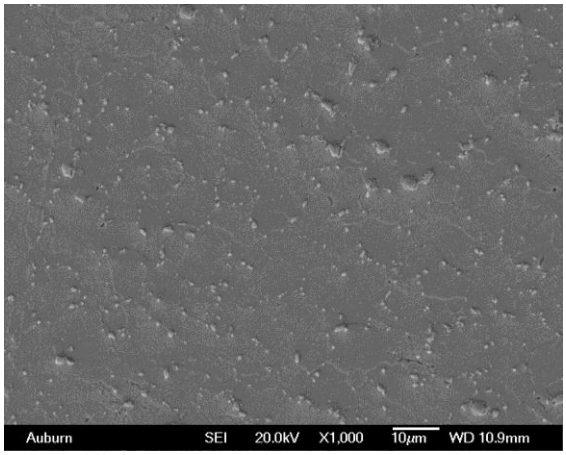

(c) 2 days

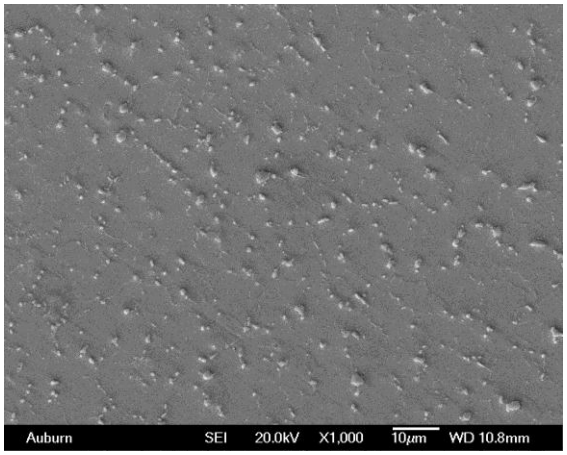

(d) 3 days

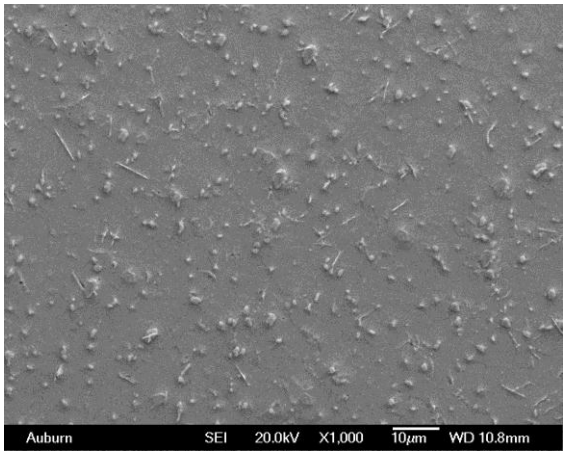

(e) 6 days

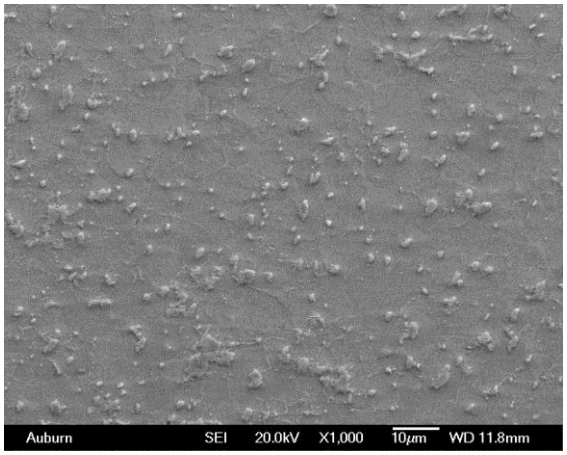

(f) 9 days

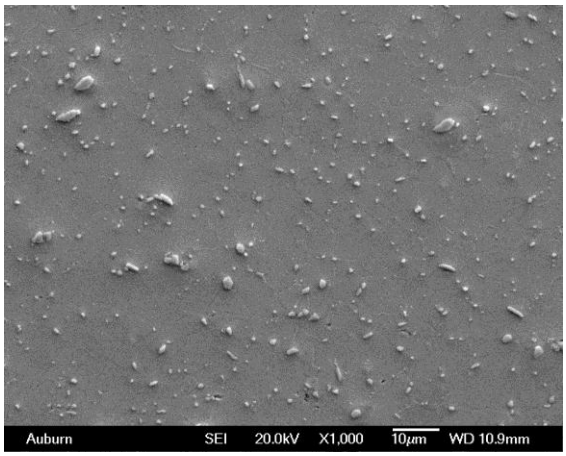

(g) 15 days

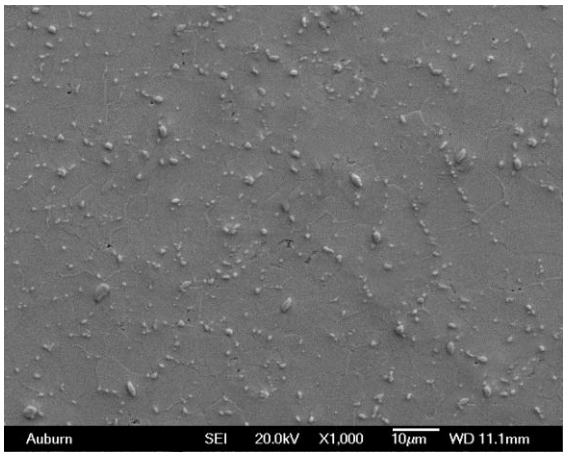

(h) 20 days

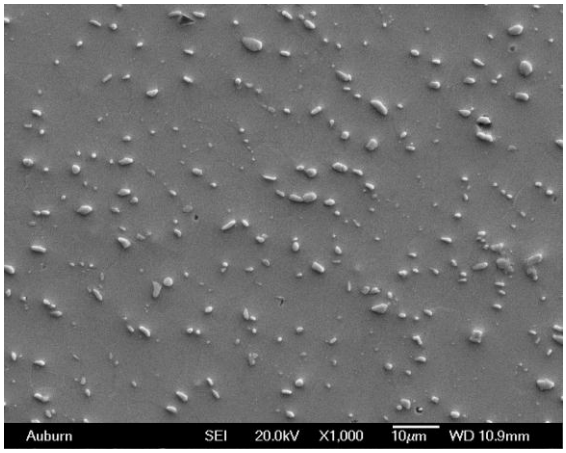

(i) 30 days

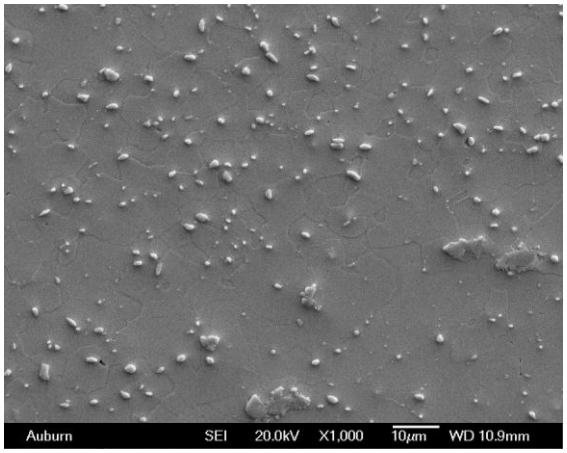

(j) 60 days

Figure 7.7 Microstructure Evolution of SACX with Aging
(1000X, W.Q., Aged at 100 ^{o}C)

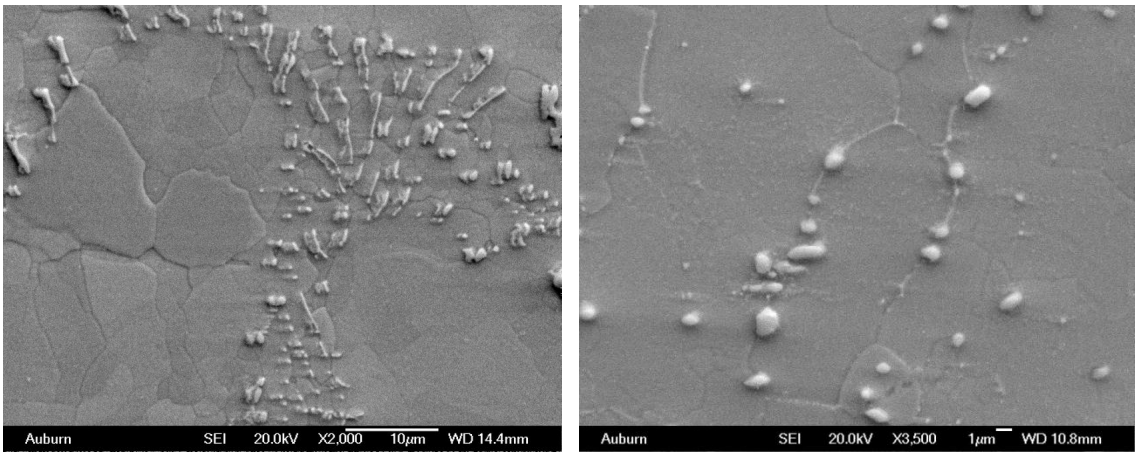

(a) Non-aged (b) Aged

Figure 7.8 Distribution of IMC Particles in SACX before/after Aging

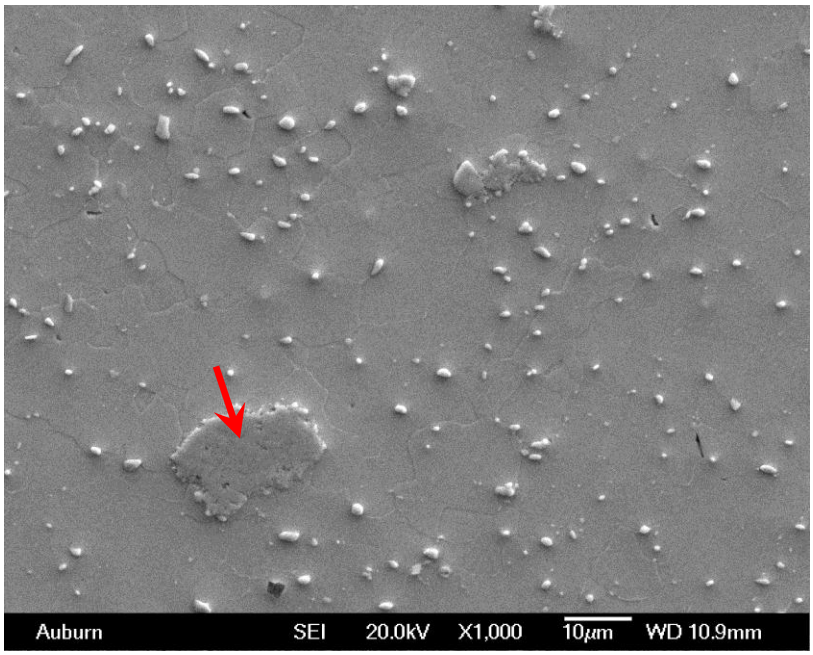

Figure 7.9 Extremely Large Cu_6Sn_5 IMC Particle
(W.Q., Aged at 100 ^{o}C for 60 days)

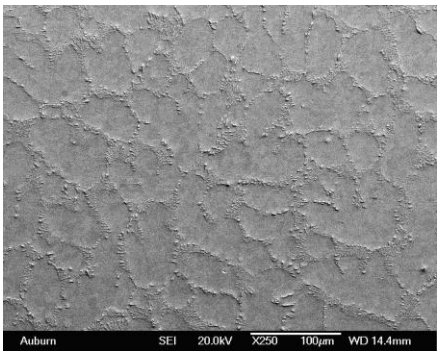

(a) As Reflowed

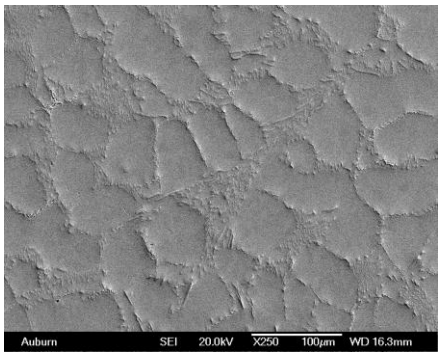

(b) 1 Month at 25 ^{o}C

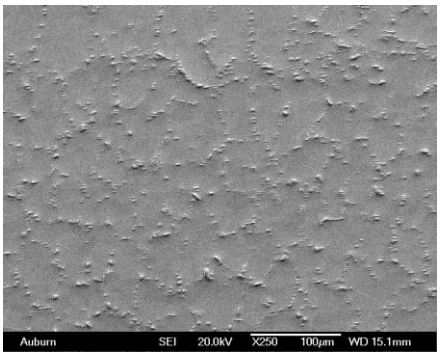

(c) 1 Month at 125 ^{o}C

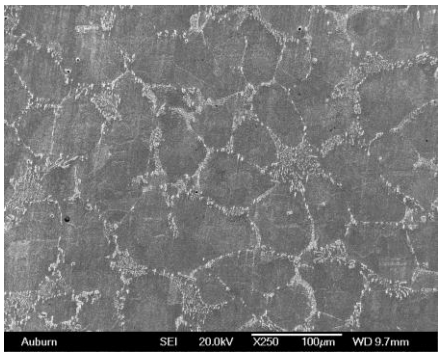

(d) 3 Months at 25 ^{o}C

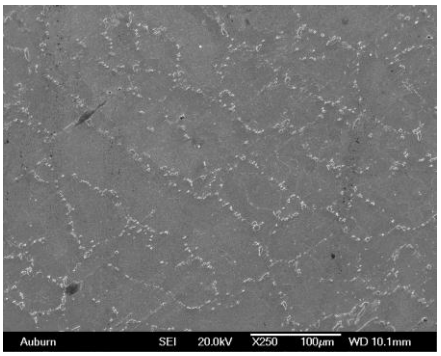

(e) 3 Months at 125 ^{o}C

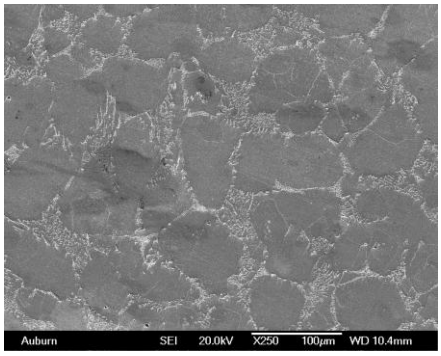

(f) 6 Months at 25 ^{o}C

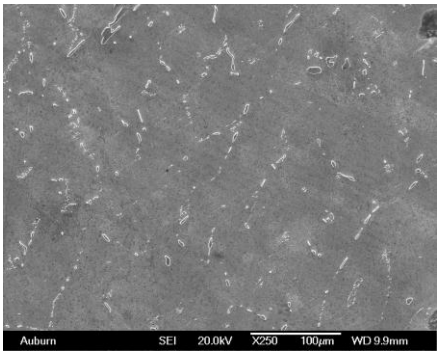

(g) 6 Months at 125 ^{o}C

Figure 7.10 Microstructure Evolution of SACX with Aging (250X, R.F.)

7.4 Effect of Aging on Grain Growth

Aging has also been reported to be a driving force for grain growth in many alloys. However, for all bulk solder samples in this dissertation, aging induced grain growth was hardly noticed. In contrast, significant sub-grain growth with aging was captured and quantitatively measured.

A typical grain structure in a SACX solder specimen is depicted in Figure 7.11. The first graph consists of 21 pictures that were individually taken by using an OLYMPUS BX60 optical microscope equipped with an analyzer/polarizer. In this cross-polarized picture, grains with different orientations can be obviously distinguished, and for better presentation, each grain has been colored as shown in Figure 7.11(b). Note that the observation area captured in these two graphs is approximately 3 × 10 mm, resulting in an estimate of the average grain size in a reflowed SACX specimen to be 0.55 mm in diameter.

One interesting observation is that some grain boundaries contain a zig-zag shape. Similar results were discussed by Kumar, *et al.* [122]. In this case, the grain boundary serration is largely caused by the difference in the growth orientation of the secondary β-Sn dendrite arms, as can be seen in the two enlarged polarized pictures in Figure 7.12. According to the theory of cross polarization, high contrast in color represents a large misorientation of the grain boundary. As indicated in the figures, two types of grain boundary are observed, i.e. high angle grain boundary (HAGB, whose misorientation is greater than 11^{o}) and low angle grain boundary (LAGB, whose misorientation is smaller than 11^{o}). When subject to stresses, grain boundaries, as defects in crystal structure, are acknowledged to be preferred sites for crack initiation and propagation due to their

relatively low bonding and stress concentration. On the other hand, grain boundaries are also known for their capability in blocking the movements of dislocations. Therefore, such information on grain structure will be useful to explain the mechanical and failure behavior of SAC solders.

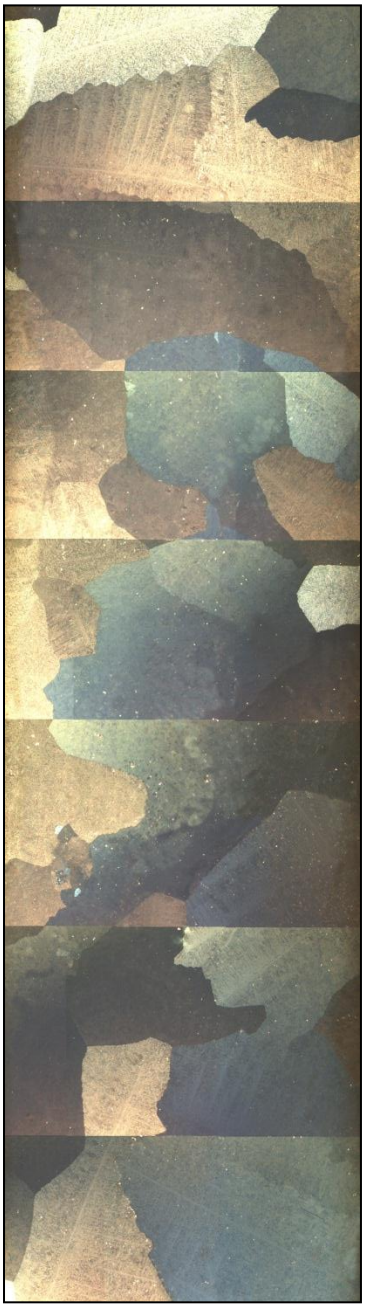

(a) Polarized Optical Micrograph

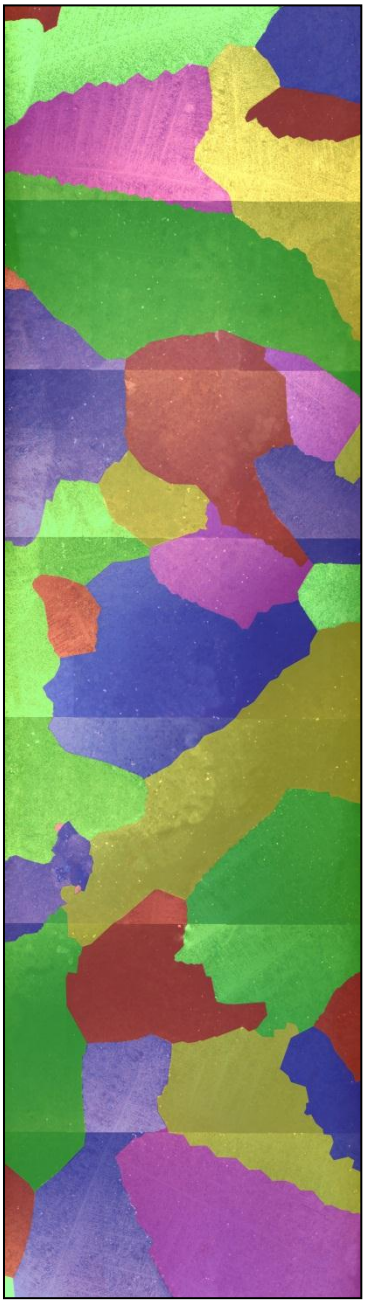

(b) Grains with Different Orientation

Figure 7.11 Grain Structure in a SACX Specimen

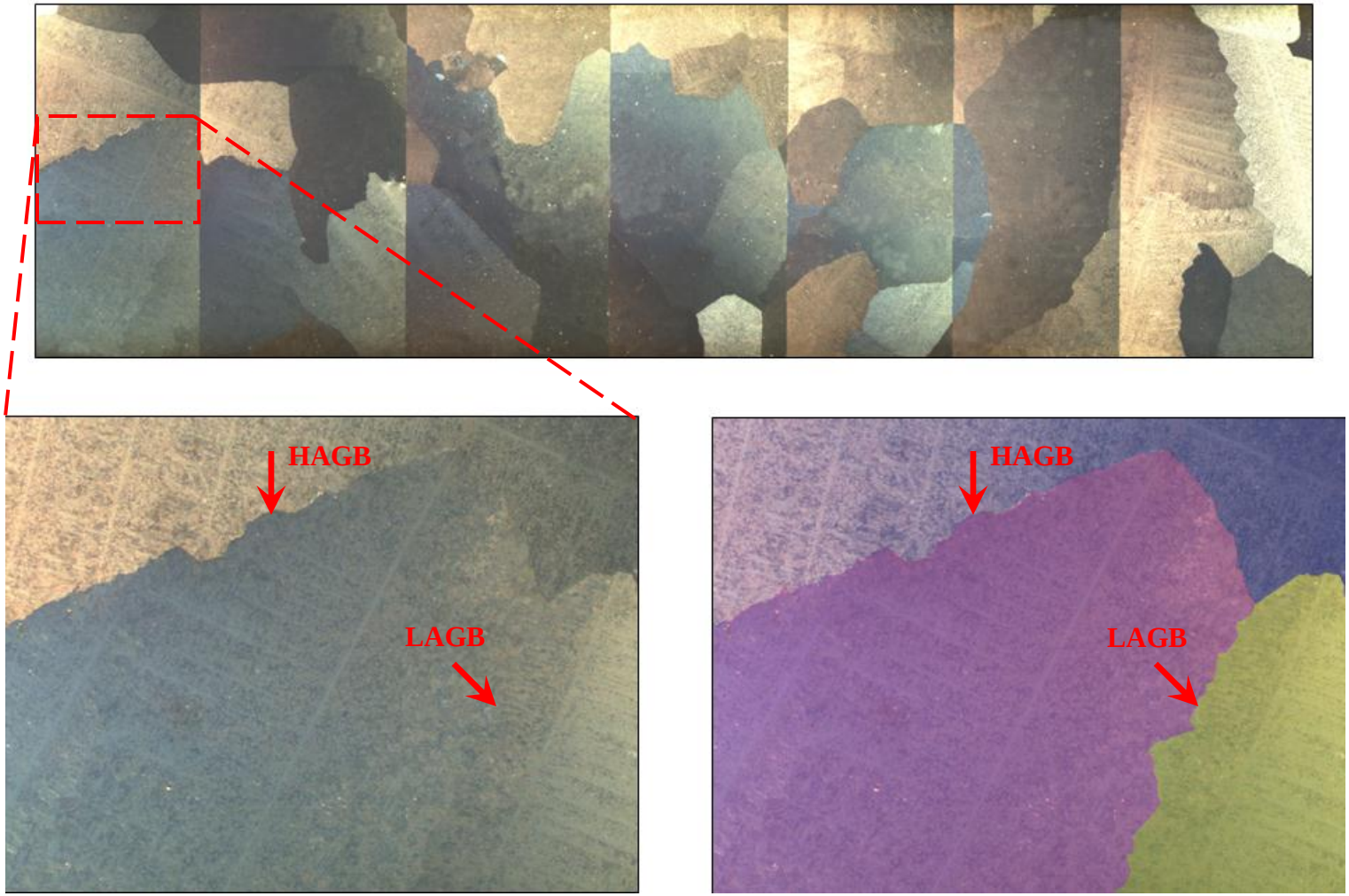

Figure 7.12 Typical Types of Grain Boundaries and Grain Boundary Serration

However, the effects of aging on grain growth for SAC alloys are not as obvious as those for phase growth discussed in the previous section. No significant evolution with aging was observed at the grain scale. Instead, dramatic changes in the sub-grain size with aging were captured for the SACX alloy. Compared to LAGB, sub-grains possess an even smaller grain boundary misorientation (< 1^o, typically 0.6^o). Such small differences in angles are not easily observed in a polarized optical microscope. However, the sub-grain boundaries can be inspected if an appropriate etchant was used. Figure 7.13 illustrates typical sub-grains in an etched SACX sample. The average sub-grain size was approximated to be 3 μm, which is around 200 times smaller than the average grain size (550 μm). In Figure 7.14, it is demonstrated that sub-grains in the SAC-Zn solder grow notably as aging progresses, and the growth is even more dramatic with increased aging temperature. Quantitatively (see tabulated values in Table 7.2), the average sub-grain size in an as-reflowed SAC-Zn solder sample was approximated to be 4 μm; after one month of room temperature aging, the size was almost tripled (11 μm). However, the average size increased to 22 μm for elevated temperature aging (125 ^{o}C). In fact, similar trends were observed for all solders of interest in this dissertation.

It is widely acknowledged that smaller/finer grain size enhances the ability for the solid to disrupt the motion of dislocations, and thus improves the strength of the material. This phenomenon has been empirically represented by the Hall-Petch relationship (Eq. 4.2), stating that the yield strength of a material is inversely proportional to its grain size. In fact, this relationship also holds for sub-grains. Since it has been demonstrated that aging is attributed to the growth of sub-grains in size, the observation in Chapter 4 that the yield strength of solder materials degrades with aging can thus be explained.

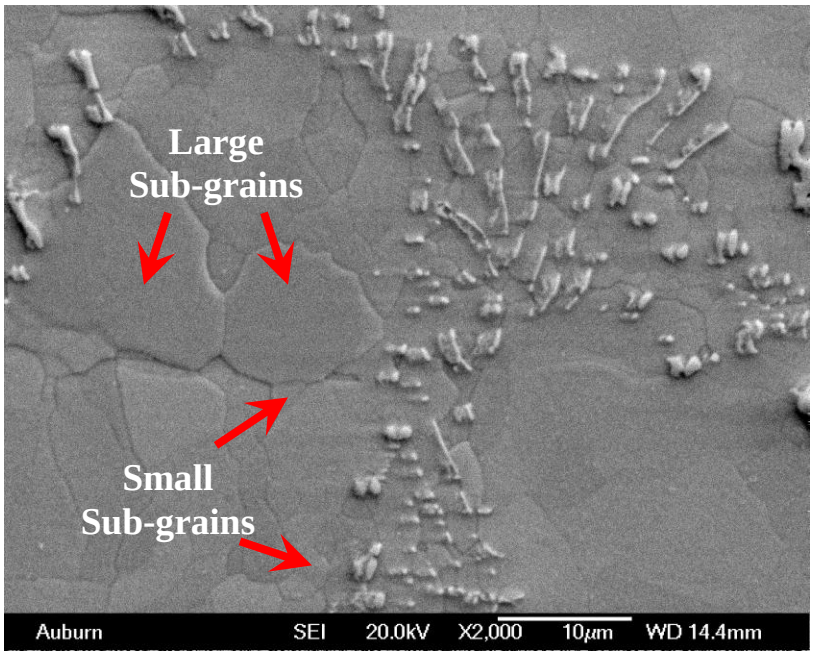

Figure 7.13 SEM Micrograph of Sub-Grain Structure in SACX

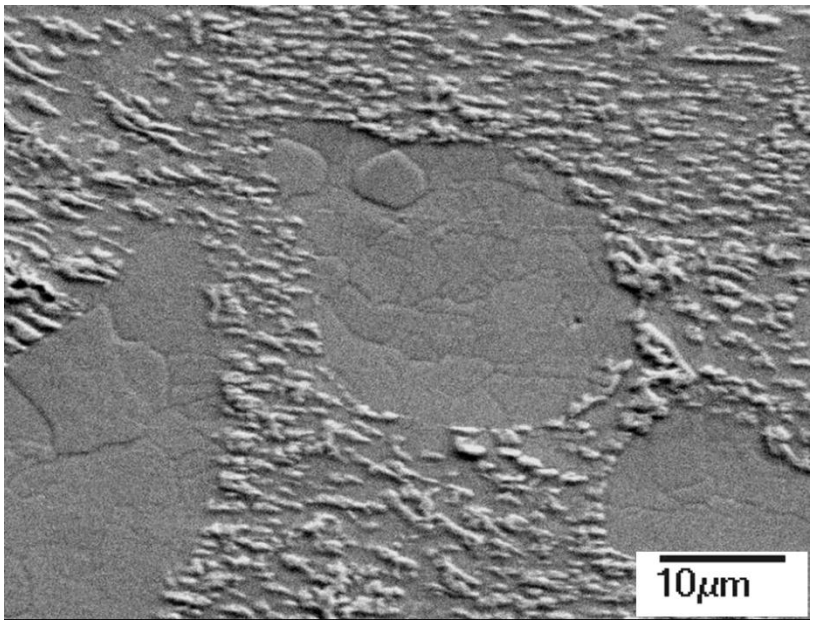

(a) As Reflowed

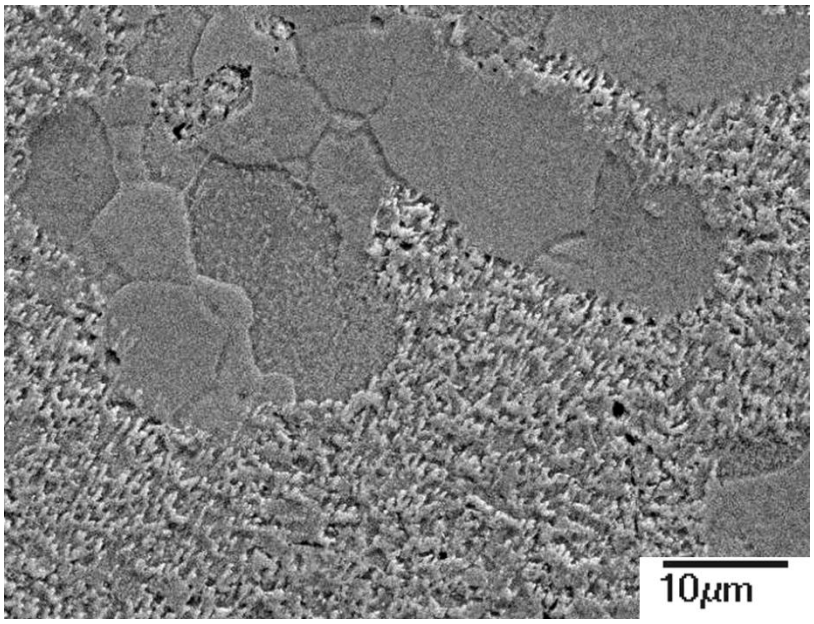

(b) 1 Month at 25 ^{o}C

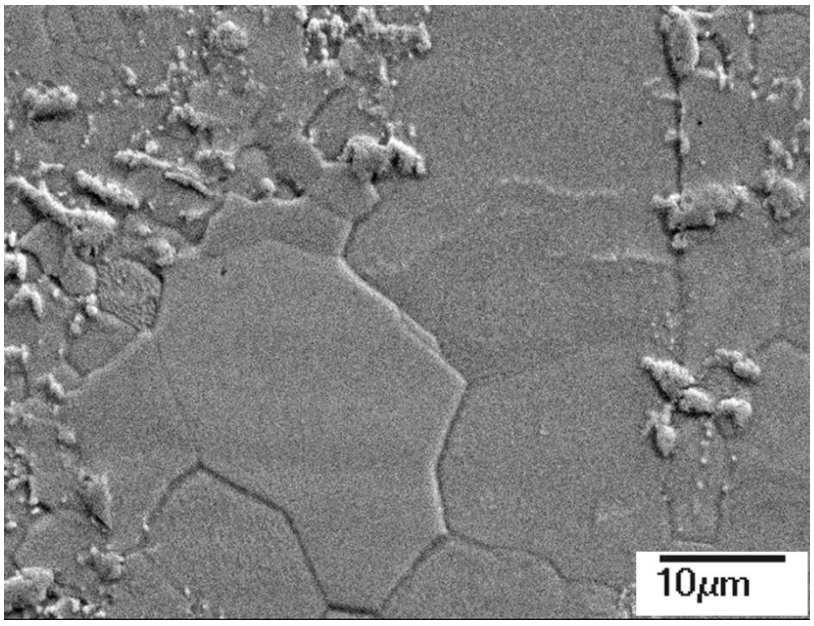

(c) 1 Month at 125 ^{o}C

Figure 7.14 Sub-Grain Growth with Aging in SAC-Zn

	No Aging	1 Month @ 25 ^{o}C	1 Month @ 125 ^{o}C
Sub-grain Size (μm)	4	11	22

Table 7.2 Sub-Grain Size of SAC-Zn under Various Aging Conditions

7.5 Effect of Dopants on Aging Induced Microstructure Evolution

As discussed earlier, aging has been ascribed to expedite the coarsening of microstructure and thus negatively impacted the material properties of lead free solder alloys. In an attempt to effectively reduce aging induced degradation, several strategies may be considered:

(1) Refinement of β-Sn dendrites;

(2) Mitigation of the coalescence and coarsening of precipitates;

(3) Inhabitance of grain/sub-grain growth.

According to the results from Chapter 5, it has been demonstrated that the enhancement of aging resistance of solder materials can be achieved by adding small addition of alloying elements, such as Bi, Ni, Zn, and Co. In this section, the refining mechanisms of dopants are investigated.

7.5.1 Bi

Extensive studies have been conducted on SACX (X = 0.1% Bi) solder material regarding to aging effects. For material characterization, it has been demonstrated that SACX solder possessed better properties than SAC105 after long term aging despite of its coarsened as-solidified microstructure.

Figure 7.15 compares the initial (as reflowed) microstructure of SACX and SAC105. Attributed to its higher silver content, SAC105 has finer/smaller β-Sn dendrites and IMCs with a compacted honeycomb structure (relative to SACX), and thus results in better initial material properties of SAC105 solder for no-aging condition. However, as aging progresses, the IMC particles in the SAC/SACX solders gradually lose their abilities to block moving dislocations due to the phase coarsening. Therefore, after long-

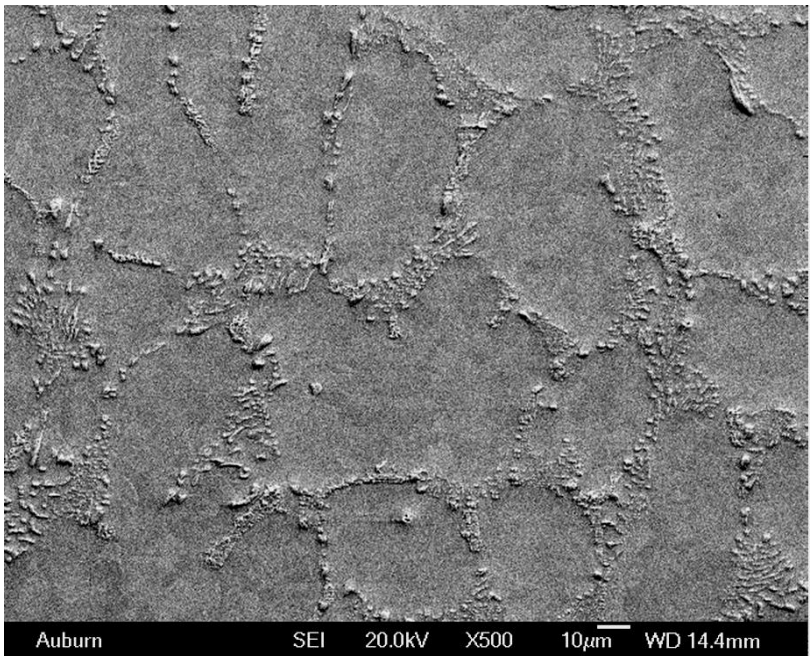

(a) SACX

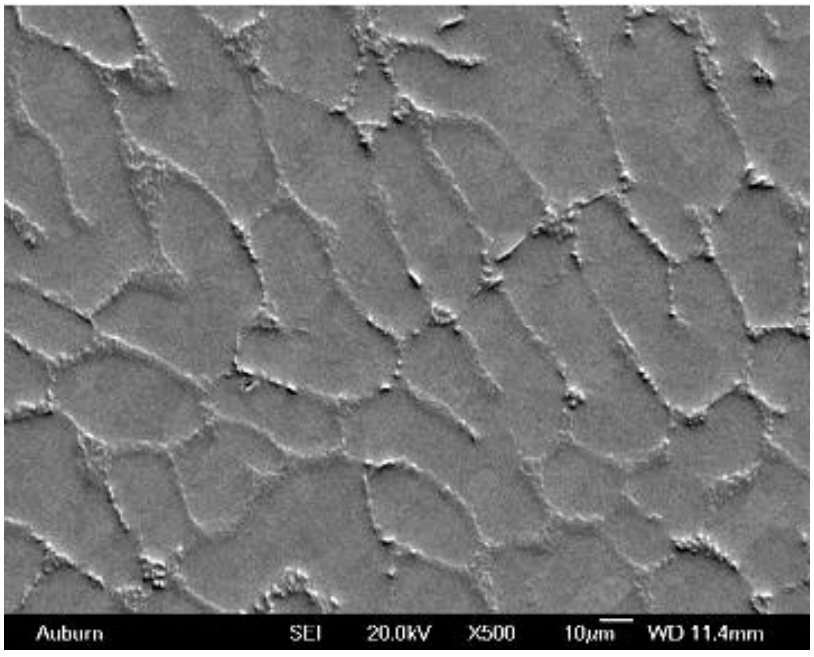

(b) SAC105

Figure 7.15 As-Reflowed Microstructure of SACX and SAC105

term aging, the strengths of low silver content solders, such as SACX and SAC105, largely are determined by their primary phase, namely, β-Sn matrix. As expected, β-Sn dendrites in SAC105 solder are observed to coarsen/grow with aging [112]. However, for the SACX solder material, the degradation of β-Sn dendrites is offset by adding Bi. Due to the large solid solubility of Bi in Sn, dissolved Bi atoms were observed to be uniformly distributed in the β-Sn matrix, as shown in the EDX mapping in Figure 7.16. Thus, there is improved strength of the Sn matrix by a solid solution strengthening (SSS) mechanism. Furthermore, the Sn-Bi binary phase diagram in Figure 7.17 also indicates that the solubility of Bi increases dramatically with temperature. As a result, this strengthening effect is expected to be even more significant at higher aging temperatures.

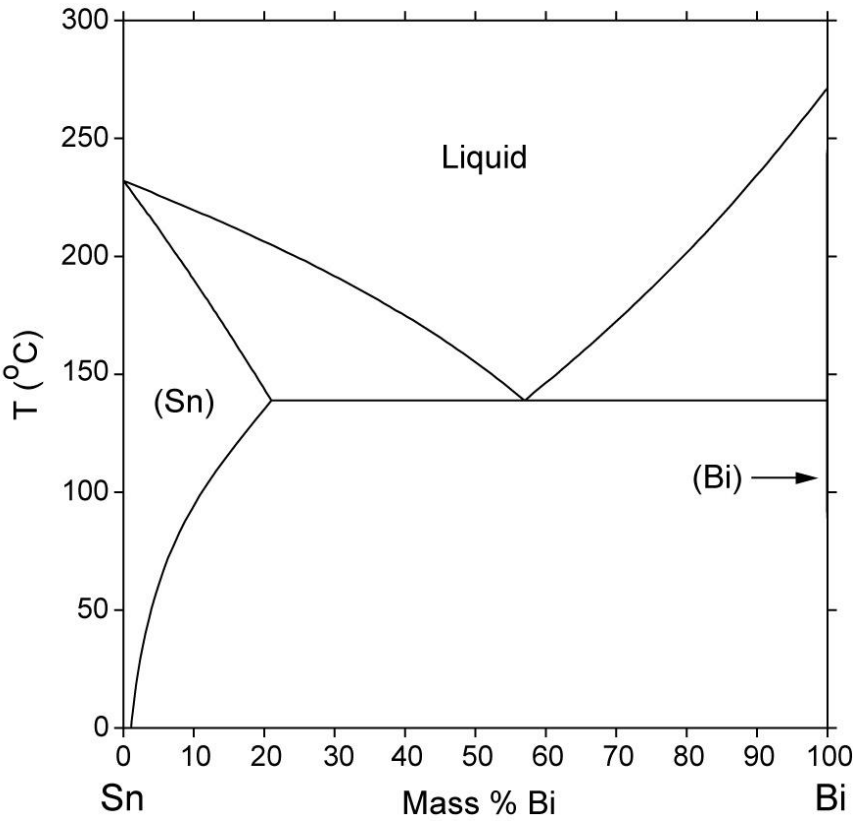

(http://www.metallurgy.nist.gov/phase/solder/bisn-w.jpg)

Figure 7.16 Sn-Bi Binary Phase Diagram

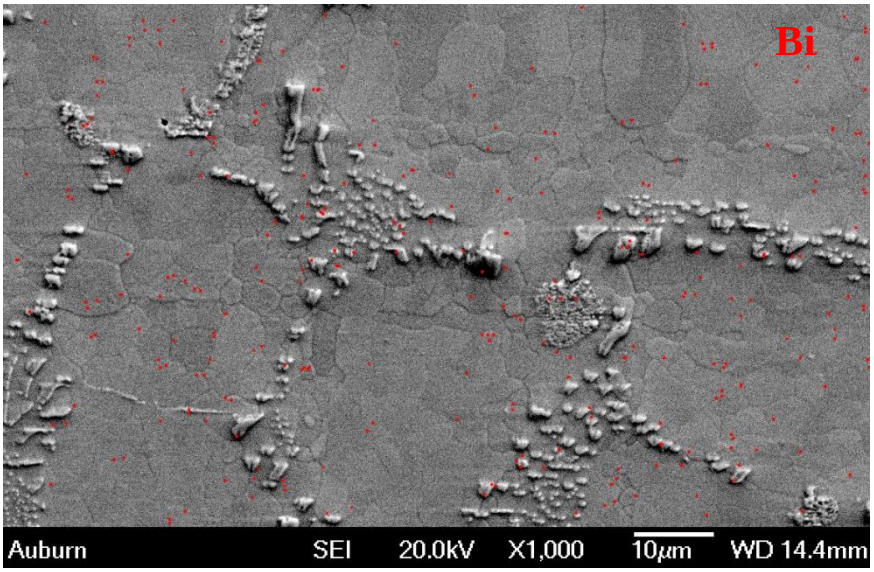

Figure 7.17 Distribution of Bi in a SACX Solder Sample (1000X, R.F., Non-aged)

7.5.2 Ni

SN100C is a well-known Ag-free solder for wave soldering. By replacing 0.05% Cu with Ni in the eutectic Sn-0.7Cu, the aging resistance of the solder is significantly enhanced. As shown in Figure 7.18, the aging induced microstructure evolution of SN100C is almost negligible when compared to Sn-0.7Cu. In contrast, IMC particles in the eutectic Sn-Cu solder are significantly coarsened even under room temperature isothermal exposure (Figure 7.19). Several literatures have also documented the observations that micro-alloying of Ni can successfully inhibit the allotropic transformation of Cu_6Sn_5 [23], and thus ensure the integrity of major IMCs in the microstructure. In the absence of Ni, hexagonal closed packed (HCP) Cu_6Sn_5 transformed to the monoclinic form upon cooling below 186 ^oC. This transformation is accompanied by 26% of volume change that could lead to possible micro-voids/cracks inside the bulk solder, resulting in the loss of stiffness and strength of the solder material.

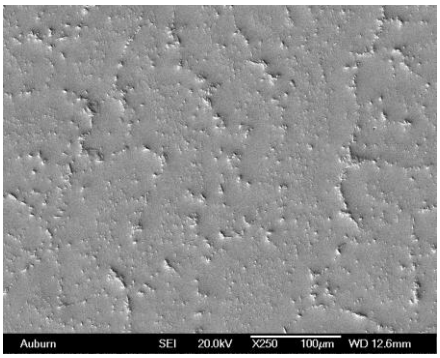

(a) As Reflowed

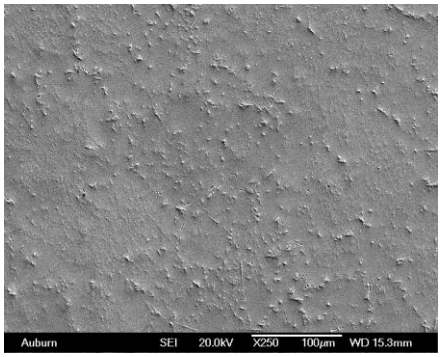

(b) 1 Month at 25 ^{o}C

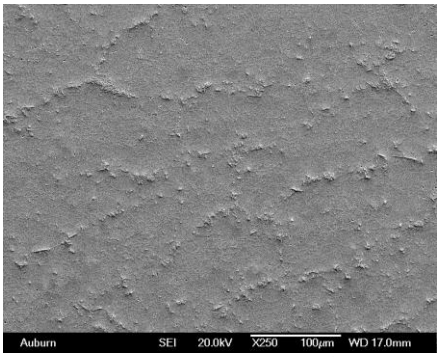

(c) 1 Month at 125 ^{o}C

Figure 7.18 Microstructure Evolution of SN100C with Aging (250X, R.F.)

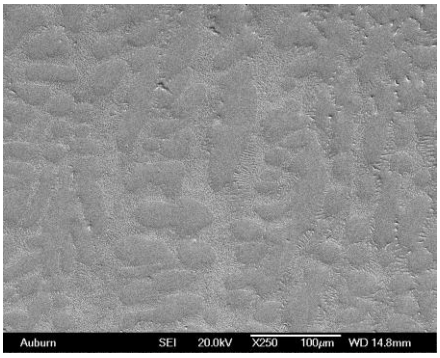

(a) As Reflowed

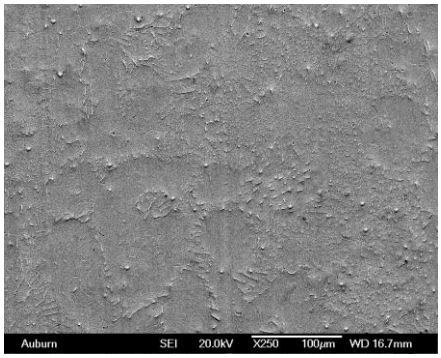

(b) 1 Month at 25 ^{o}C

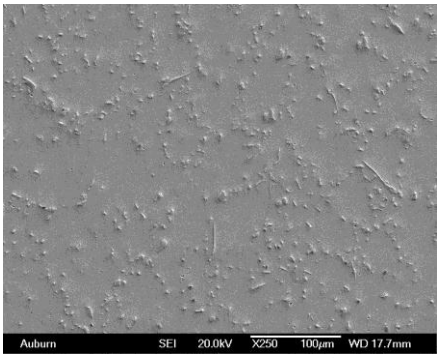

(c) 1 Month at 125 ^{o}C

Figure 7.19 Microstructure Evolution of Sn-0.7Cu with Aging (250X, R.F.)

In fact, there exists a Sn-Ni IMC (Ni_3Sn_4) according to phase diagram, as shown in Figure 7.20. However, no evidence has been shown that Ni_3Sn_4 is formed in the bulk sample used in this study. Instead, Figure 7.21(a) captured a ternary Cu-Ni-Sn IMC particle. Similar to Cu_6Sn_5, this type of IMC largely takes a pie shape in morphology. Quantitatively, the atomic ratio of Ni + Cu to Sn is approximated to be 6 to 5, indicating that the ternary IMC can be recognized as $(Cu_{6-x}Ni_x)Sn_5$. Due to the similar atomic size (128 pm for Cu and 124 pm for Ni) and same crystal lattice structure (FCC), Ni atoms from β-Sn matrix can occupy the vacancies created by the diffusion of Cu in the Cu_6Sn_5 lattice. Meanwhile, it has also been demonstrated based on energy and density states calculations that stoichiometric ternary $Cu_{6-x}Ni_xSn_5$ compounds are more stable

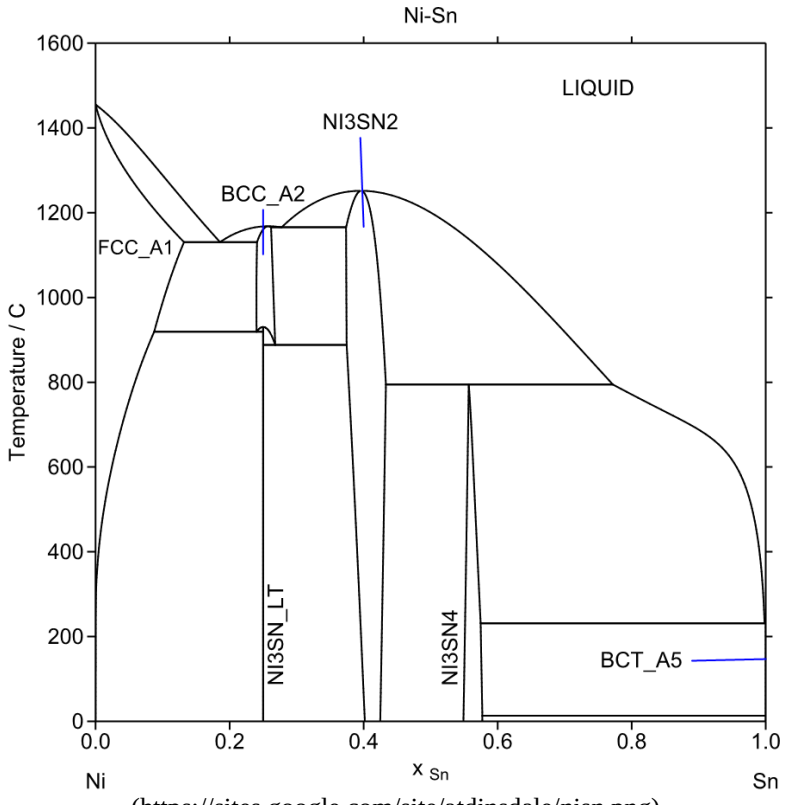

(https://sites.google.com/site/atdinsdale/nisn.png)

Figure 7.20 Sn-Ni Binary Phase Diagram

than Cu_6Sn_5 [123]. Since the phase stability of Cu_6Sn_5 is notably enhanced by the presence of Ni, a small variation in mechanical properties of solder material with aging is anticipated, as manifested in Chapter 5. On the other hand, however, as the addition of Ni is based on the cost of Cu, fewer Cu_6Sn_5 IMC particles are formed in SN100C solder, causing the lower strength of material when compared to Sn-0.7Cu.

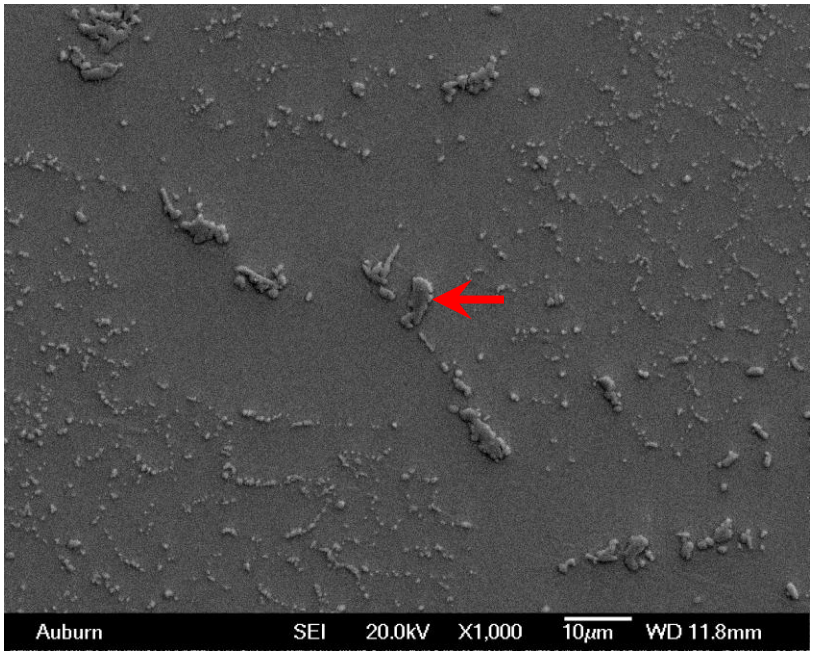

(a) EDX Spot

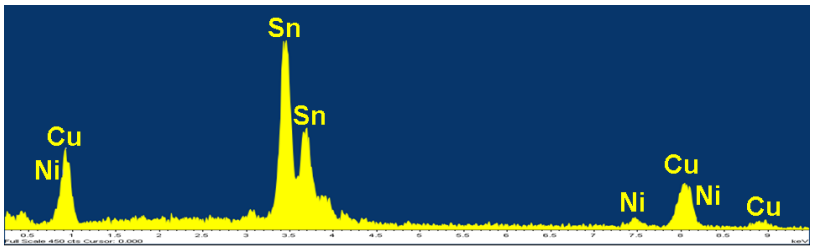

Element	Weight%	Atomic%
Ni K	3.49	5.30
Cu K	34	47.74
Sn L	62.51	46.96
Total	100	100

(b) EDX Analysis

Figure 7.21 EDX Spot and Analysis of IMC Particle in SN100C

7.5.3 Zn

Aging induced microstructure evolutions of SAC-Zn and SAC3595 are illustrated in Figures 7.22-7.23. It is observed that the average and the variance of IMC particle size in SAC-Zn solder are much smaller after aging when compared to SAC3595, although both solders have similar initial microstructures. Several large and severely coarsened IMC particles were found in SAC3595 sample as shown in Figure 7.23(c), but no such large particles were observed in SAC-Zn solder with the same aging condition, as shown in Figure 7.22(c).

The ability of Zn in stabilizing the microstructure is ascribed to its strong affinity with Cu. As illustrated in elemental mapping for Zn in SAC-Zn solder (Figure 7.24), the distribution of Zn atoms is favorably near/in the IMC region. According to the Cu-Zn binary phase diagram (Figure 7.25), there exist several possible phases in Cu-Zn crystal structure, i.e. brass. The formation of these phases can effectively slow down the diffusion rate of Cu within β-Sn matrix, and thus improve the microstructure stability of Sn-rich solder [124]. Furthermore, it has also been documented that the minor Zn addition can reduce the amount of undercooling during solidification process and thereby suppress the formation of large Ag_3Sn IMC particles [125]. Therefore, ascribed to the refined as-solidified microstructure and enhanced microstructure stability, it is obvious that the SAC-Zn solder possesses better material properties than SAC3595, as discussed in Chapter 5.

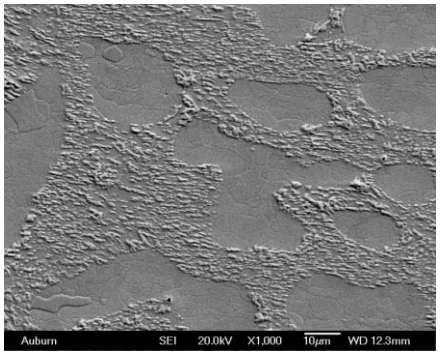

(a) As Reflowed

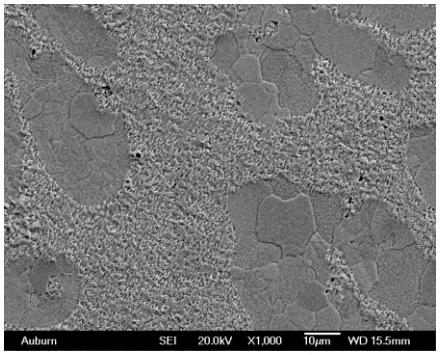

(b) 1 Month at 25 ^{o}C

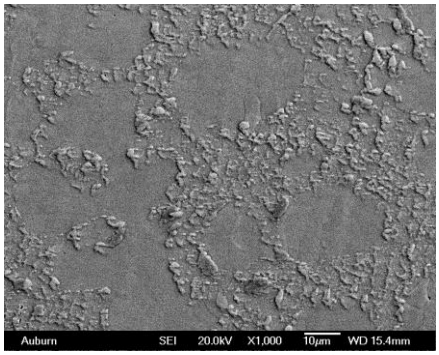

(c) 1 Month at 125 ^{o}C

Figure 7.22 Microstructure Evolution of SAC-Zn with Aging (1000X, R.F.)

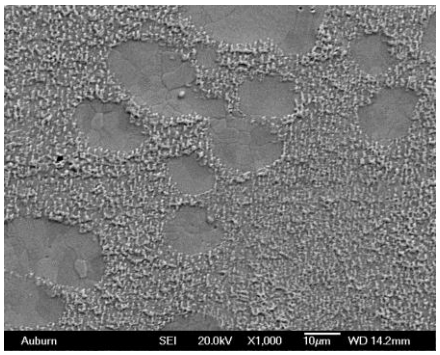

(a) As Reflowed

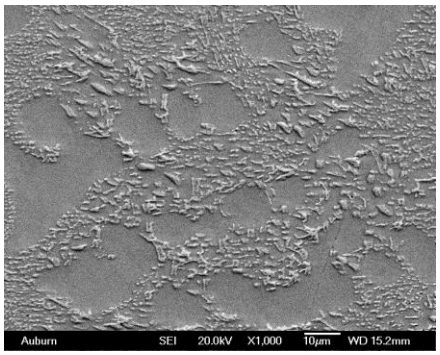

(b) 1 Month at 25 ^{o}C

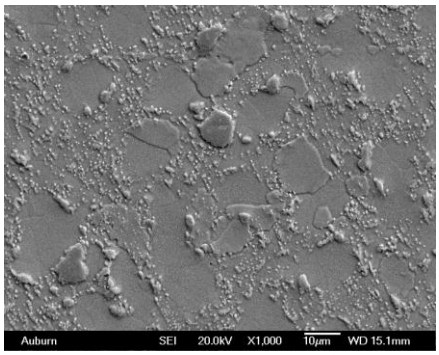

(c) 1 Month at 125 ^{o}C

Figure 7.23 Microstructure Evolution of SAC3595 with Aging (1000X, R.F.)

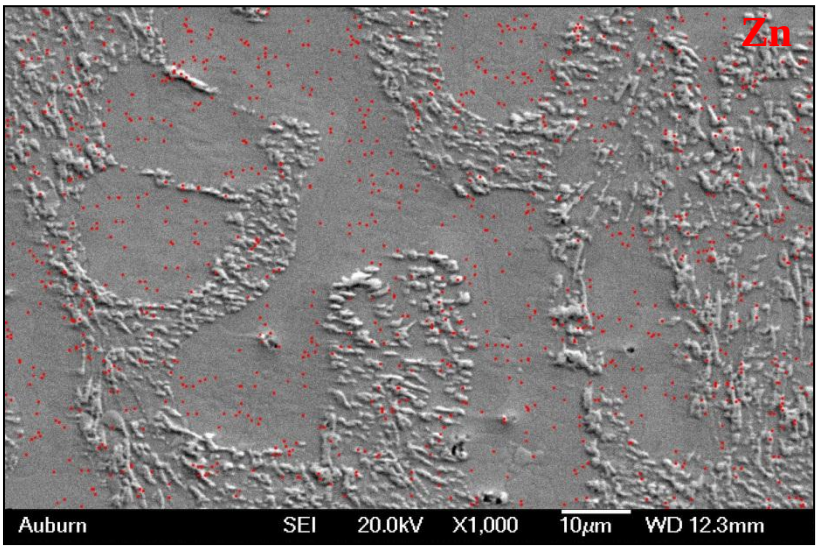

Figure 7.24 Distribution of Zn in a SAC-Zn Solder Sample (1000X, R.F., Non-aged)

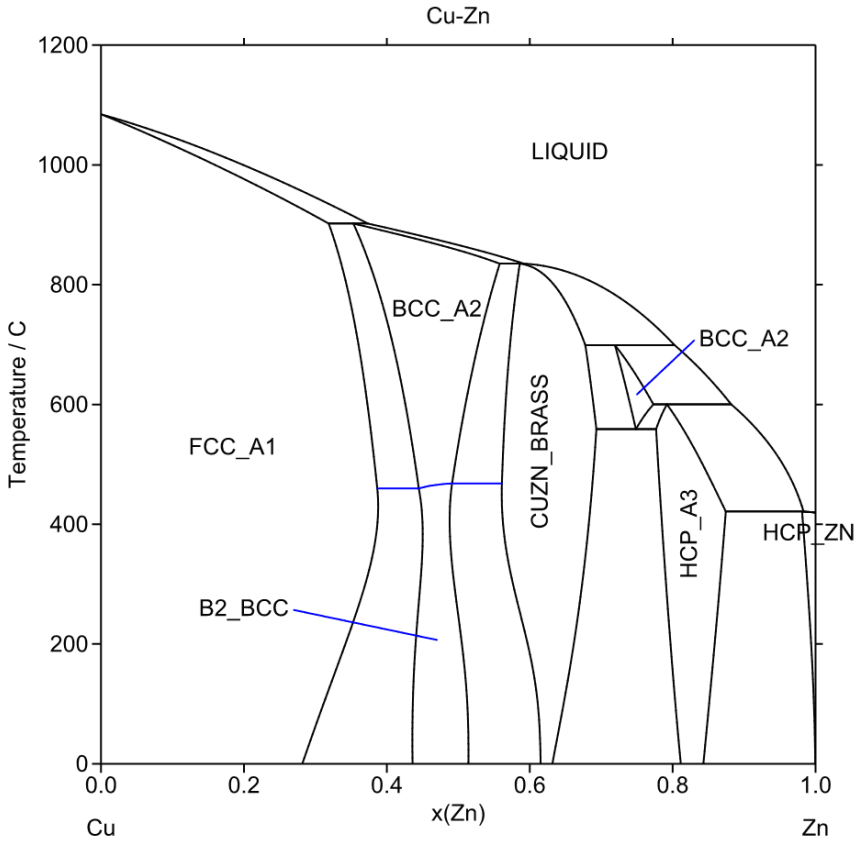

(https://sites.google.com/site/atdinsdale/cuzn.png)

Figure 7.25 Cu-Zn Binary Phase Diagram

7.5.4 Co

Figure 7.26-7.27 illustrate the microstructure of SN96CI and SAC3810 solder alloys under different aging conditions, showing the apparent coalescence and growth of the IMC particles in SAC3810 solder after aging than those in SN96CI solder.

Similar to Ni, the addition of Co can remarkably hinder the diffusion of Cu in Sn. According to the result of EDX analysis in Figure 7.28, the majority of Co were found in a ternary $(Cu_{6-x}Co_x)Sn_5$ IMC, taking a scallop morphology. Even though the addition of Co is merely about 0.05% in weight, the atomic percentage of Co in the ternary IMC is measured to be 10% on average. Since Co also has a similar atomic size as Cu (128 pm for Cu and 125 pm for Co), the vacant Cu sites in Cu_6Sn_5 crystal can be taken by Co without introducing any lattice distortion. Therefore, the vacancy diffusion of Cu is hampered, resulting in the slower growth of Cu_6Sn_5 IMC particles with aging in SN96CI solder than in SAC3810.

However, by comparing Figure 7.26(a) to 7.27(a), it is suggested that the Co addition leads to an increase in size of β-Sn dendrites and a shrinkage in area of eutectic/IMC phase. In general, the strength and stiffness of Sn-rich solder alloys is determined by the volume fraction of IMC phase. Therefore, less IMC phase regions of SN96CI solder result in the decrease of material properties when compared to SAC3810. Moreover, as shown in Figure 7.29, several large IMC platelets can be observed and identified as $CoSn_3$, according to the phase diagram (Figure 7.30) and EDX analysis. However, since the addition of Co is at the expense of Cu, formation of $CoSn_3$ may further reduce the properties due to the lower modulus (94 GPa for α-$CoSn_3$ [126] and 112 GPa for Cu_6Sn_5 [127]) and undesirable morphology when compared to Cu_6Sn_5.

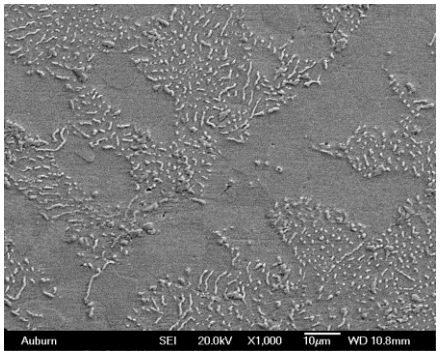

(a) As Reflowed

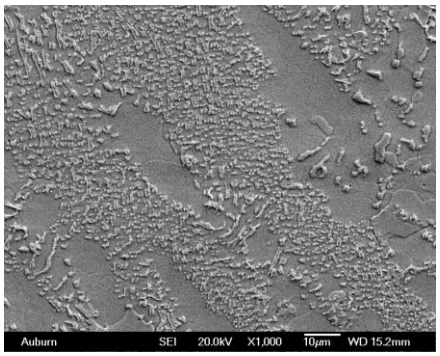

(b) 1 Month at 25 ^{o}C

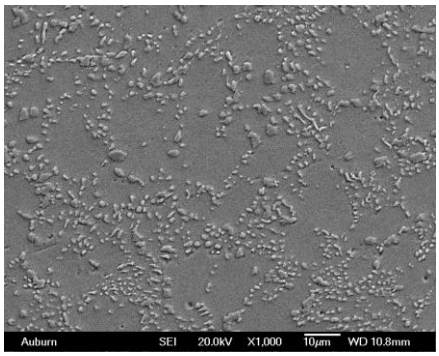

(c) 1 Month at 125 ^{o}C

Figure 7.26 Microstructure Evolution of SN96CI with Aging (1000X, R.F.)

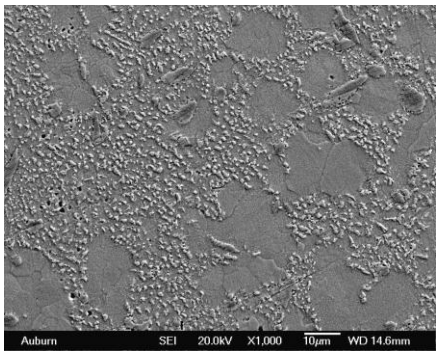

(a) As Reflowed

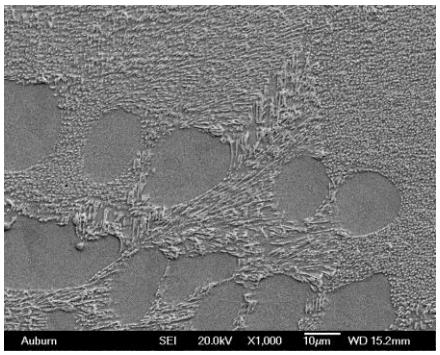

(b) 1 Month at 25 ^{o}C

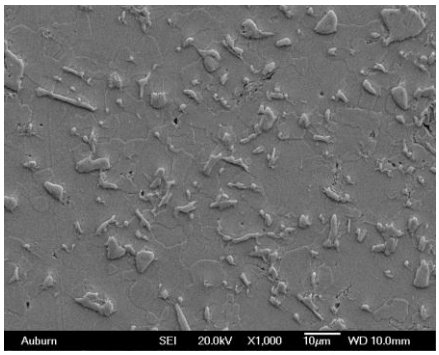

(c) 1 Month at 125 ^{o}C

Figure 7.27 Microstructure Evolution of SAC3810 with Aging (1000X, R.F.)

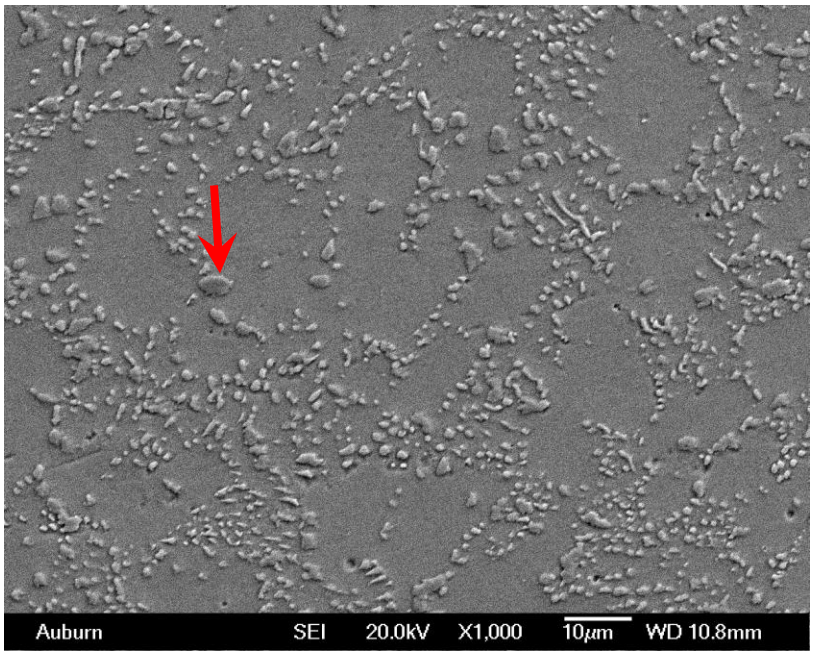

(a) EDX Spot

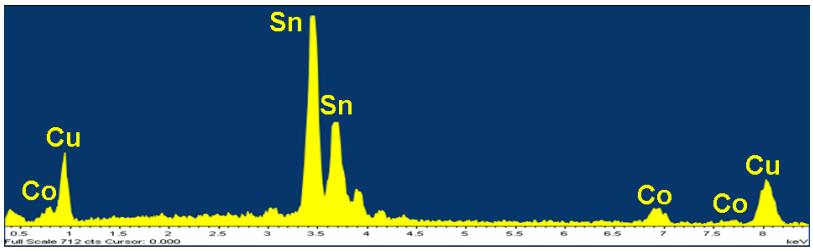

Element	Weight%	Atomic%
Co K	5.85	9.22
Cu K	25.23	36.86
Sn L	68.92	53.92
Total	100	100

(b) EDX Analysis

Figure 7.28 EDX Spot and Analysis of Sn-Co-Cu IMC Particle in SN96CI

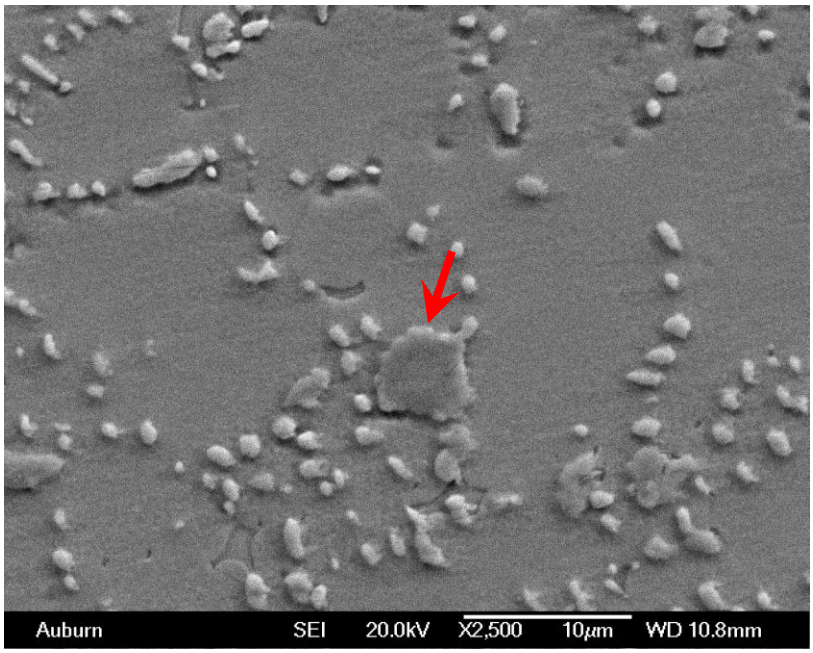

(a) EDX Spot

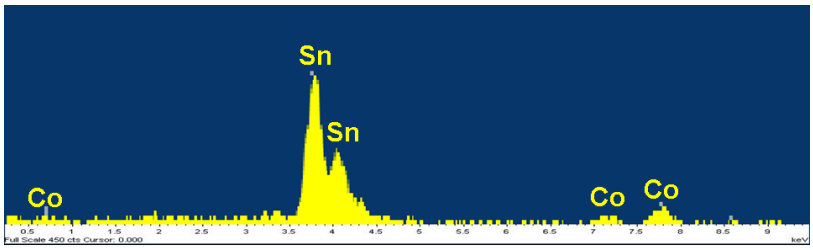

Element	Weight%	Atomic%
Co K	14.35	25.21
Sn L	85.65	74.79
Total	100	100

(b) EDX Analysis

Figure 7.29 EDX Spot and Analysis of Sn-Co IMC Particle in SN96CI

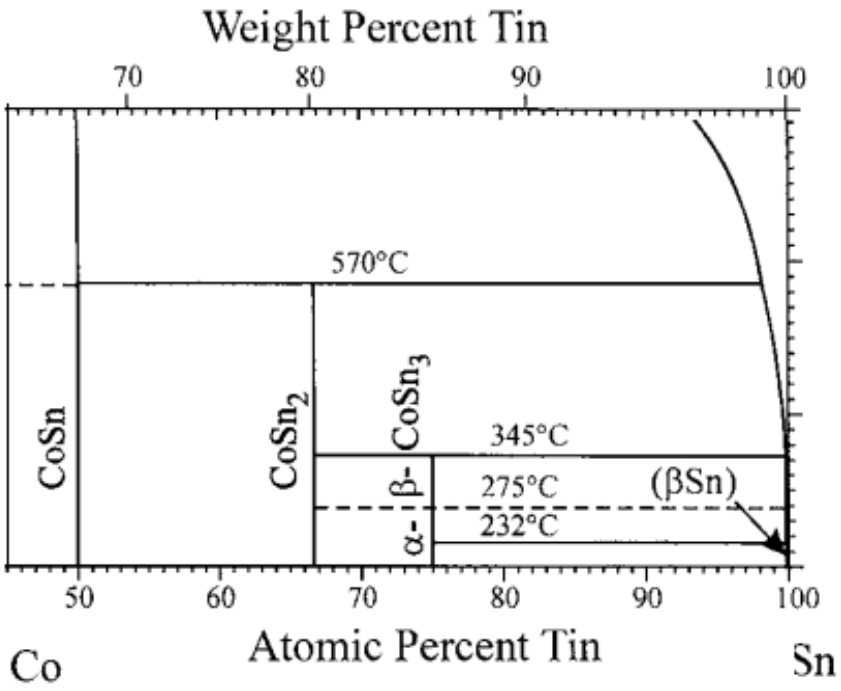

Figure 7.30 Enlarged Sn-Co Binary Phase Diagram in Sn Side

7.6 Aging Induced Relaxation of Residual Stress in Solder Alloys

Recently, a vast body of studies has been focusing on the effect of residual stress on ATC reliability of lead free solder joints. Largely introduced during solidification, the residual stress in solder joints has been reported to accelerate the formation of Kirkendall voids, and finally results in micro-cracking or failure of the package. However, few work has been done regarding to residual stress evolution with aging. In fact, heat treatment such as annealing (aging) has been used to reduce the residual stress for a long time. In the case of lead free solders, there is still no clue whether the changes in residual stress is the cause of aging induced degradation in material properties. In this study, a non-destructive stress measurement technique was utilized to examine the effect of aging on residual stress relaxation in solder materials.

In order to produce the maximum residual stress within the material, water quenching cooling profile was adapted during solidification process. The measurements were conducted on a SACX sample by using Bruker Discover D8 General Area Detector Diffraction System (DADDS). Note that the sample was subject to different isothermal exposures prior to test, including non-aging (as quenched), moderate aging (15 days at 125 ^{o}C) and severe aging (30 days at 125 ^{o}C).

Figure 7.31 depicts the brief introduction to methodology of residual stress determination by XRD. A collimated X-ray beam of wavelength λ is focused onto a specimen and the number of X-rays diffracted (diffracted intensity) is counted as the angle between the X-ray tube and X-ray detector θ is changed. This allows the construction of a plot of diffracted intensity vs. 2θ. From these peaks the lattice spacing, *d*', which will vary from stressed to non-stressed materials, can be determined using the Bragg equation:

$$n\lambda = 2d'\sin\theta \tag{7.2}$$

where λ is the wavelength of the incident X-ray; n is a constant; and θ is the diffraction angle.

Stress magnitudes are determined through measurement of changes in the materials lattice spacing *d*, due to the presence of a stress. From knowledge of the non-stressed lattice spacing, any stresses present can then be calculated using established equations:

$$\frac{d_{\phi\psi} - d_0}{d_0} = \frac{1+\nu}{E}\sigma_\phi \sin^2\psi \tag{7.3}$$

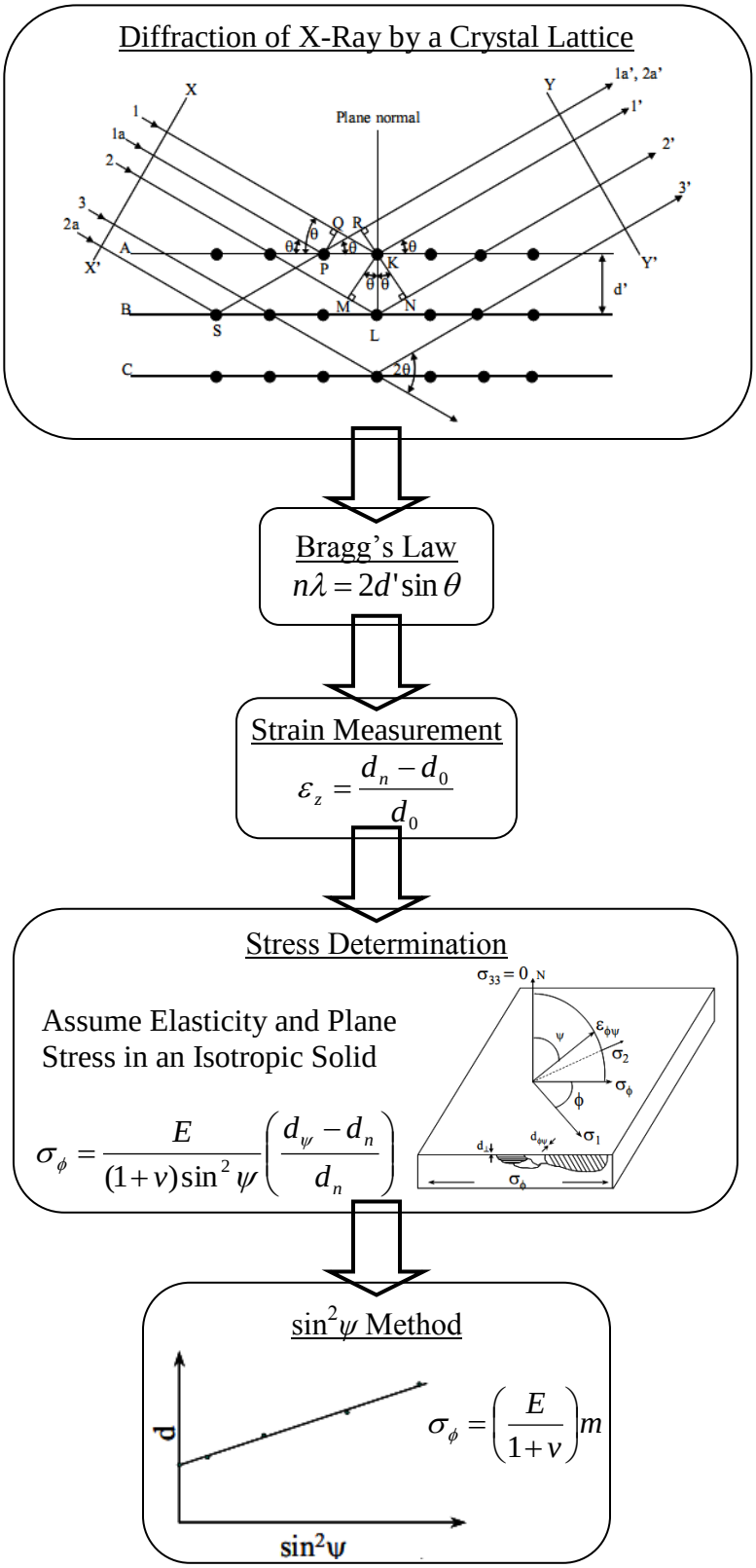

Figure 7.31 Brief Introduction to Methodology of Residual Stress Determination by XRD

where $d_{\Phi\Psi}$ represents inter-planar spacing in the direction defined by Φ and Ψ; d_0 the inter-planar spacing for unstressed material; v, E Poisson's ratio and Young's modulus, respectively; and σ_Φ the surface stress defined by the angle Φ.

Then, by repeating several measurements regarding to different Ψ, the residual stress can be indirectly determined by calculating the slope m for the plot of d vs. $\sin^2\Psi$ for a given set of Miller Indices (indices for crystal lattice structure) at each location on the specimen:

$$\sigma_\phi = \left(\frac{E}{1+v}\right)m \tag{7.4}$$

In the current study, {3 1 2} plane was selected for all measurements due to its ideal multiplicity and peak location for Sn-rich solder material (Figure 7.32), ensuring to eliminate the oscillation in the $\sin^2\Psi$ plot. The measurements were conducted under four different Ψ tilt angles (Ψ = 0, 15, 30, 45^o), with eight frames for each Ψ. In each frame, the scanning route was set to be 6 mm in length, and located in the middle of the sample, as illustrated in Figure 7.33. Furthermore, since the peak location of {3 1 2} is expected to be 79.5^o for SACX, only data with 2θ angle in the range from 73.5^o to 85.5^o were collected. The experimentally measured effective modulus of SACX was used in residual stress calculation, and v is approximated to be 0.3. Moreover, the crystalline anisotropic factor was set to be 1, assuming isotropy of SACX solder material. In summary, the parameter settings are tabulated in Table 7.3.

Figure 7.34 is a typical 2D-XRD pattern for SACX solder material. Instead of the even intensity distribution around the Debye ring, only several sporadic bright spots can be observed in the diffraction pattern, indicating the large grain size (at least 100 μm)

within the test specimen. However, it is still possible to integrate the intensity around a small section of the ring to reduce (but not eliminate) these intensity variations.

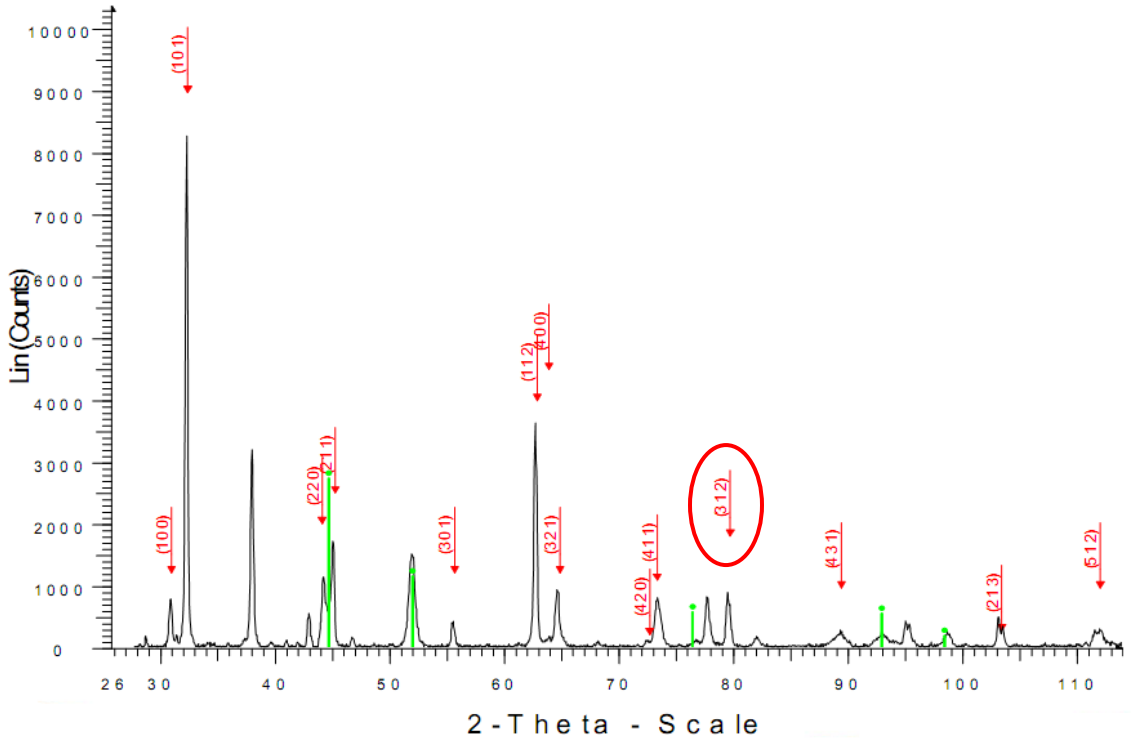

Figure 7.32 Typical Peaks for Crystallographic Planes of Sn-Rich Solder Alloys

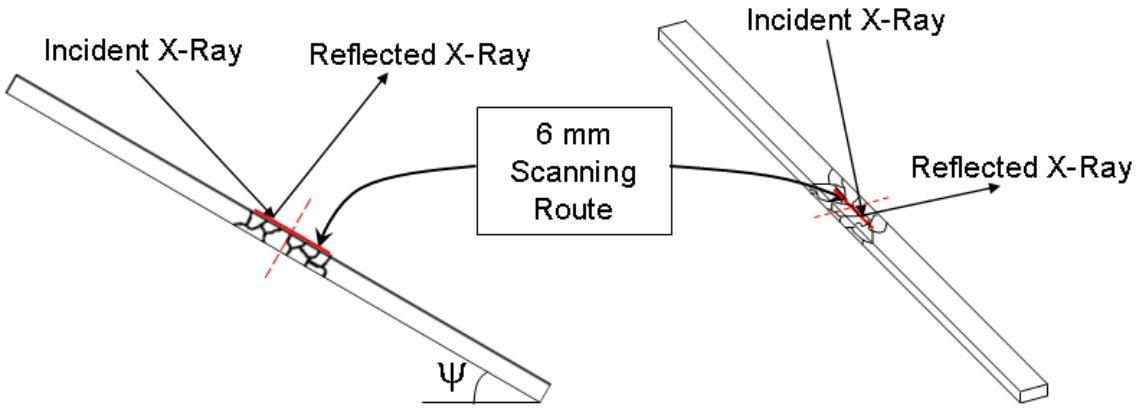

Figure 7.33 Schematic Illustration of Scanning Routes on a SACX Sample

Settings	Parameters
{H K L}	{3 1 2}
Ψ (^{o})	0, 15, 30, 45
Frames for each Ψ	8
Scanning Length (mm)	6
Starting 2θ (^{o})	73.5
Ending 2θ (^{o})	85.5
Starting χ(^{o})	-96.2
Ending χ (^{o})	-82.9
Step Size (^{o})	0.05
v	0.3
Arx	1
Φ (^{o})	0

Table 7.3 Settings for Residual Stress Measurement Using 2D-XRD

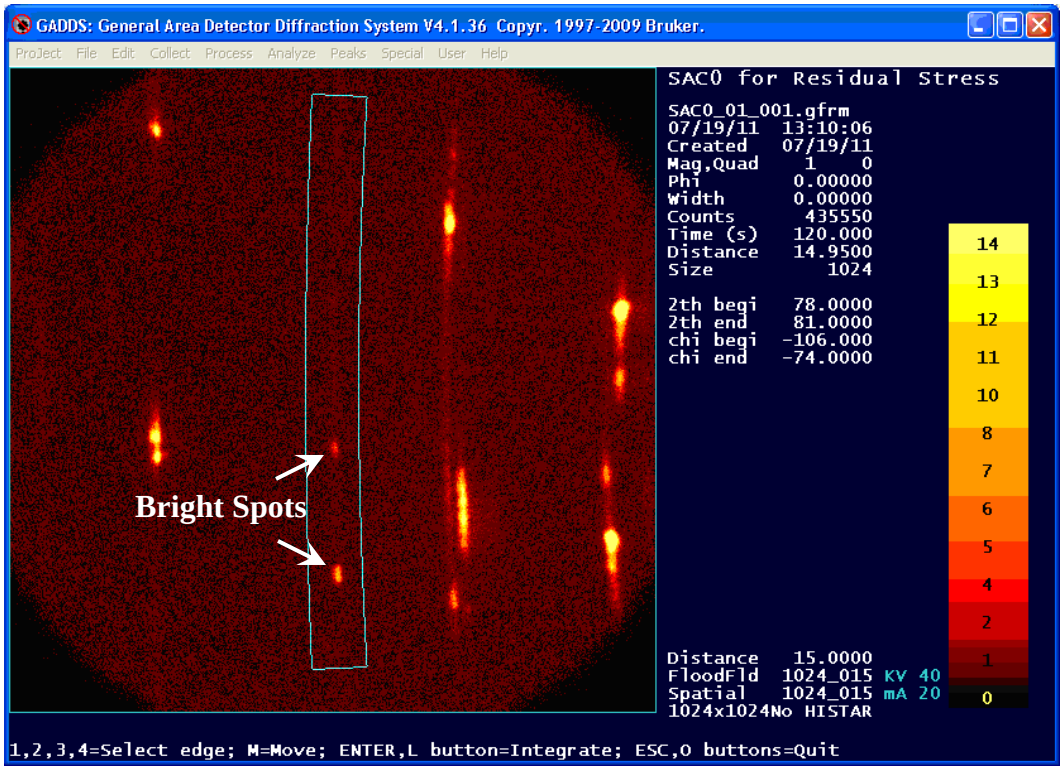

Figure 7.34 Typical 2D X-Ray Diffraction Pattern for a SACX Sample

After calculating the actual lattice spacing from each frame and estimating the slope *m* according to $\sin^2 \Psi$ plot, the average residual stress was estimated to be -37.24 MPa with a standard deviation of 29.99 MPa for an as-quenched SACX solder sample, as shown in Figure 7.35. The negative average value indicated the residual stress within the specimen appeared to be compressive, while the large variance was mainly caused by:

(1) large grain size in the sample;

(2) approximation of isotropy;

(3) micro-strains and inter-granular strains.

Referring to the grain structure of the testing specimen illustrated in Figure 7.36, it is evident that the grain size is so large (750 μm) that only four grains were examined on half of the scanning route. In common cases, residual stress is assumed to be uniformly distributed in each single grain, although stresses may vary significantly within different grains. Statistically, specimen with larger grains (fewer grains in a fix volume) provides inadequate number of observations, attains large variance in estimation, and finally reduce the precision to achieve reliable result from XRD residual stress analysis.

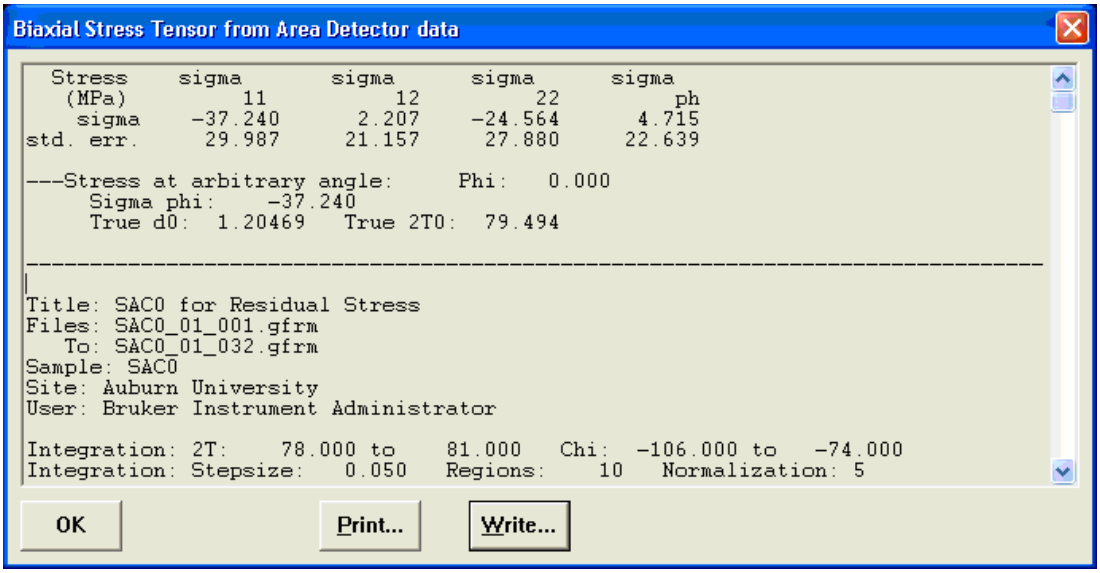

Figure 7.35 Example of Output for Residual Stress Analysis

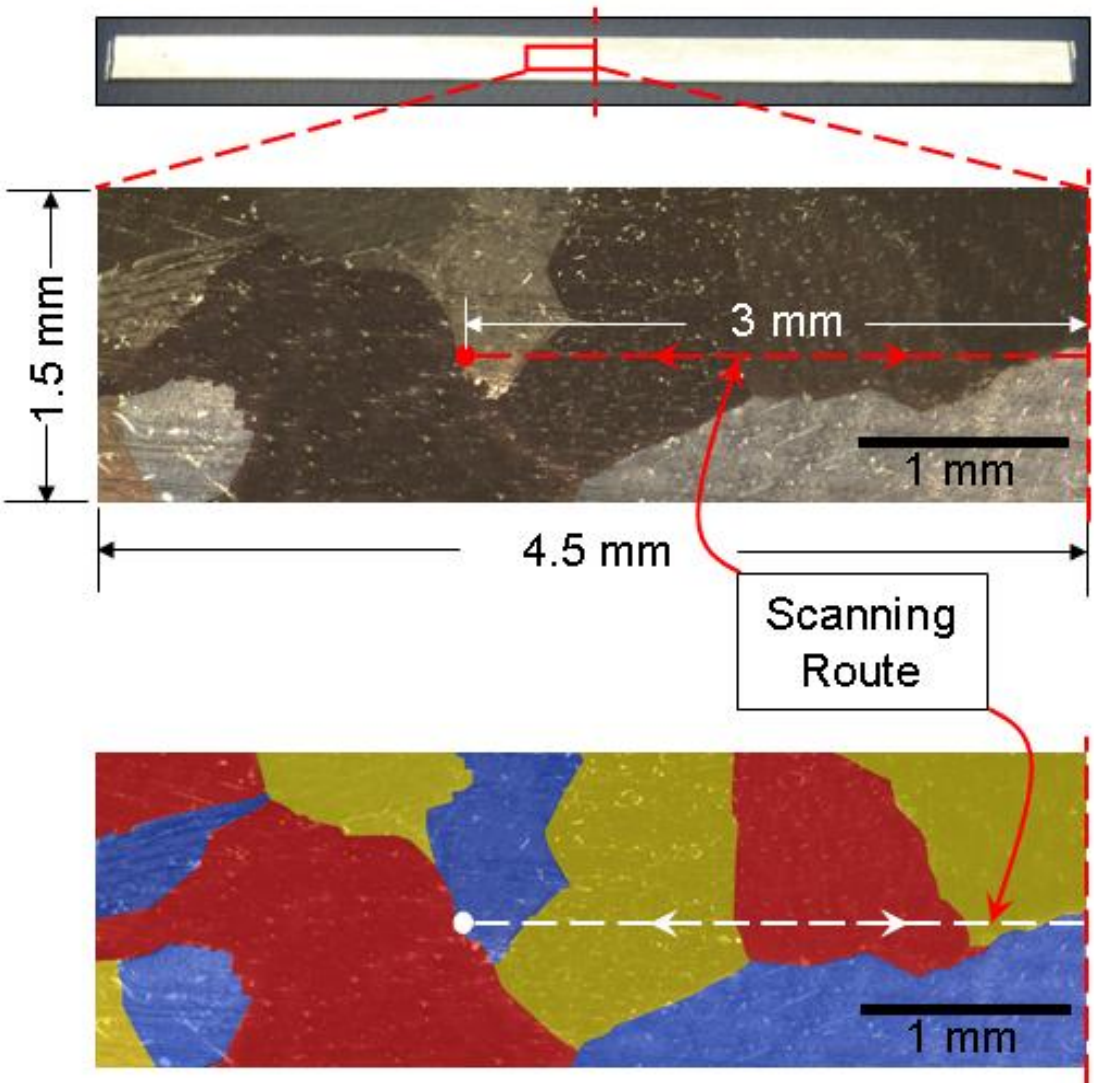

Figure 7.36 Polarized Optical Graph of Grain Structure in a SACX Sample

Similar measurements were also conducted on the same SACX sample after aging at 125 ^{o}C for 15 and 30 days, respectively. The variation in average residual stress with aging was plotted in Figure 7.37, inferring that the average compressive residual stress within the specimen diminishes as aging progresses. This observation may also explain the aging induced degradation in material properties of lead free solder materials. Due to the existence of large compressive stress established in the initial microstructure after solidification, extra forces are needed to deform the samples in tensile or creep test. However, heat treatment such as annealing, or isothermal aging in this case, relieves the residual stress within the specimen. As a result, lower external stresses are required to produce the same deformation for nearly stress-free solder specimens after aging. Therefore, a loss in strength for aged solders is expected when compared to as-solidified samples.

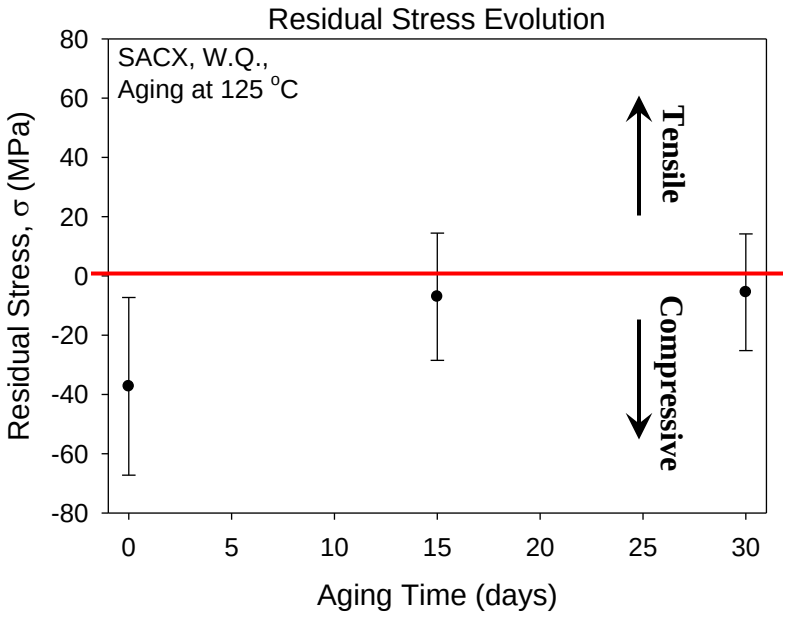

Figure 7.37 Variations in Residual Stress with Aging in a SACX Sample

7.7 Summary and Discussion

In this chapter, the melting behavior and major phase reactions during solidification were studied by performing DSC analysis on all solders of interest. In addition, the aging effects on intrinsic responses of solder materials were investigated so that aging induced degradation of material properties can be fully understood. In summary, the study was conducted from the following three aspects:

(1) aging effects on phase coarsening;

(2) aging effects on grain/sub-grain structure;

(3) aging effects on internal residual stress.

Firstly, it has been demonstrated that the microstructure evolves with aging for all solder alloys in this study. In more details, both primary phase (β-Sn matrix) and secondary phase (IMCs) grow in size as aging progresses. There exist two types of IMCs in standard SAC alloys, i.e. needle-shaped Ag_3Sn and scallop-shaped Cu_6Sn_5. The dispersing, coalescing and coarsening of the both types of IMCs with aging were observed. In addition, it is also found that aging temperature appears to have a more significant effect on the microstructure evolution of lead free SAC solders. It is believed that the coarsened IMC particles cannot effectively block the movement of dislocations and thus caused the reduction in material properties.

Secondly, the grain structure of SAC solders was examined by optical microscope with cross-polarizer. Large grains can be seen even in the as-quenched SAC alloys, but the growth of the grains was not obvious. In contrast, aging effects were found to have a strong impact on the sub-grain growth of SAC alloys. Correlating with Hall-Petch relationship, it is suggested that aging increases the sub-grain size of the solder, and thus

results in the loss of yield strength.

Thirdly, the residual stresses introduced by fast cooling rate during solidification were also observed to change with aging. By utilizing 2D-XRD system, the residual stresses within grains were measured on the same SACX sample subject to different aging conditions. The result suggests the existence of large compressive stresses in the as-quenched solder sample, but the stresses gradually diminished with an increased aging time.

The effect of dopants on aging induced microstructure evolution was also examined by comparing the results to the "standard" solders in this study. It can be concluded that the aging resistance was improved for all doped solders, even though the enhancing mechanisms are different. In general, the reduction of aging effects can be realized by:

(1) refining β-Sn dendrites, i.e. Bi;

(2) mitigating the coalescence and coarsening of IMCs, i.e. Ni, Zn, Co;

(3) inhibiting grain/sub-grain growth.

CHAPTER 8

CONCLUSIONS

8.1 Literature Review

An extensive review has been performed on three major topics in solder material characterization including aging effects, X-additive modification, and constitutive modeling.

Aging effects are acknowledged to be responsible for the large discrepancies existing in the mechanical property databases for solder materials. A vast body of studies has already demonstrated that isothermal aging is the root cause for the ever-changing microstructure of lead free solders and thus gives rise to the softening effect on the material properties. Most lead free solders, especially the Sn-Ag-Cu solder family, experience dramatic loss in strength (both tensile and shear), stiffness and creep resistance as aging progresses. This effect was found to be exacerbated for elevated temperature exposure. With respect to soldered components on substrates, aging has also been extensively reported to accelerate the unfavorable interfacial IMC growth, cause the formation of Kirkendall voids, and result in the coarsening of the phases in bulk solder joints.

The effects of cooling profile and testing conditions on mechanical properties of solder alloys were also discussed through reviewing previous work. In general, fast cooling rates (i.e. water quenching) during solidification yield finer/smaller phases in the

microstructure, which in turn strengthens the solder material. However, quickly cooled samples may also exhibit more brittle behavior when subject to deformation, indicating a loss in strain-to-failure. Testing conditions such as strain rate, stress level, and testing temperature are also known to be key factors affecting the mechanical properties of solders. In general, higher strain rates during tensile tests cause strain hardening, and thus increase the strength and stiffness of the material. In creep testing, the response is highly accelerated by small increases in the applied stress loading. Softening effects in material properties have been reported for both tensile and creep tests performed under elevated temperatures.

In an attempt to optimize the performance of lead free solders (e.g. aging resistance, drop resistance, etc.) researchers have modified lead free solders by micro-alloying. The possible candidates of the X-additive include Bi, Zn, Co, Ni, Mn, Cr, Ge, Ti, Si, B, Al, In, etc. It has been demonstrated that appropriate amounts of additives will not only refine the grains, phases and IMC particles in the bulk solder joints, but also control the growth of interfacial IMC layers between the bulk joint and the copper pads on the substrate.

Lastly, four widely used constitutive models for viscoplastic materials were discussed. In particular, the Anand viscoplastic model, which successfully incorporates rate-dependent creep behavior with rate-independent plastic behavior during deformation, has been often adopted for solder materials. However, modifications to the Anond model will be necessary to incorporate aging effects.

8.2 Specimen Preparation and Experimental

A unique specimen preparation procedure was developed in this study to fabricate micro-scale uniaxial tensile specimens. All solder specimens were formed in glass tubes with rectangular cross-section by using a vacuum suction system. Two cooling profiles were adapted in this study, including water quenching and controlled reflow oven cooling. Typical uniaxial samples with nominal dimensions of 80 × 3 × 0.5 mm were utilized.

Uniaxial tensile and creep tests were performed by using a multifunctional microtester. In this study, the experimental data were modeled by empirical constitutive laws so that the corresponding mechanical properties of solder materials could be extracted.

Microstructure analysis was conducted on specimens that were taped upon pre-made epoxy stubs by using SEM and Normaski OM. DSC analysis was also performed to study melting/solidification behavior of solder alloys. Furthermore, residual stresses in the test samples were evaluated by using 2D-XRD technique.

8.3 Effect of Aging on Mechanical Properties of Lead Free Solder Alloys

The effects of aging on mechanical behavior have been examined by performing stress-strain and creep tests on SACX solder samples that were aged for various durations (0-12 months) at room temperature (25 ^{o}C), and several elevated temperatures (50, 75, 100, and 125 ^{o}C). Under each aging condition, a set of 10 tests were conducted for stress-strain testing while 5 tests were performed for creep testing. All tests were carried out by a micro-tester at room temperature (T = 25 ^{o}C). The experimentally measured stress-strain curves and creep curves were then fitted by using constitutive models

discussed in Chapter 3. The material properties (such as effective modulus, yield stress, ultimate strength, steady state creep rate, etc) under each aging condition were determined from the model fitting curves.

The variations of tensile and creep properties were observed as a function of aging (aging time and aging temperature). As expected, the mechanical properties and creep rates evolved (degraded) more dramatically when the aging temperature was increased. The recorded data also demonstrate that the majority of degradation occurs within first month of aging. Afterwards, the material properties continue to decrease by a linear manner with aging time.

A four parameter non-linear aging model fit well to the SACX creep data up to 6 months of aging; however, the extension of the model deviated from the experimental measurements of samples with 9 and 12 months of aging. The creep rate was found to be nearly constant after 6 months of isothermal exposure, and thus a saturation point for the degradation of the creep rate was reached.

Two models of aging for solder materials have been established. It has been shown that both models can interpret data well and estimate the material properties for a given aging temperature T and aging time t. Moreover, an aging indicator was proposed to quantitatively estimate the state of aging. This concept might be useful for applications such as life prediction of solder joints.

8.4 Enhanced Aging Response Using Doped Lead Free Solders

A wide selection of doped lead free solders was examined, and analogous tests were performed on the corresponding "standard" solders (without dopants) so that the effects of dopants on aging resistance of lead free solder materials could be studied.

In this study, a total of 9 different lead free solders were separated into 4 sets:

Set 1: SACX, SAC105 and SAC205

Set 2: SN100C, Sn-0.7Cu

Set 3: SAC-Zn, SAC3595

Set 4: SN96CI, SAC3810

In general, it is observed that dopants are able to improve aging resistance for lead free solders. Contrary to non-doped solders, the material properties of doped solders, including effective modulus (E), ultimate tensile strength (UTS), yield strength (YS) and steady state strain rate ($\dot{\varepsilon}$), stabilize quickly with aging. This result is more obvious for the tensile properties of the doped solders, which becomes nearly constant after 10-20 days of aging. In contrast, the tensile properties of the "standard" solders without dopants continue to degrade in a linear manner with time.

Additionally, some X-additives were discovered to improve the material properties of the solders. For example, due to the existence of 0.21 wt.% Zn, SAC-Zn solder has better stiffness and strength than "standard" SAC3595, as well as a more favorable creep resistance. Another example is that SACX (0.3% Ag) shows superior strength properties to SAC105 (1% Ag) after long-term aging at all aging temperatures regardless of its lower silver content.

In summary, aging effects have been reported to be universally detrimental to the material properties of lead free solders [45, 46, 48, 54, 103, 105, 106, 114-121]. Based on the test results reported in this chapter, it has been demonstrated that metallurgical approaches (e.g. doping) can reduce the effects of aging on the degradation of material

properties. These observations can be explained by using material science theories for mechanisms of dislocation movement, solid solution strengthening, etc.

8.5 Effect of Cooling Profile and Testing Condition on Mechanical Properties

The effects of solidification cooling profile and testing conditions on the material properties of SAC alloys have been examined by performing a series of tensile and creep tests. The specimens were prepared with two different types of cooling profile, namely, Water Quenching Profile and Reflow Profile. The testing specimens were subject to isothermal aging exposures (3 aging temperatures and up to 8 aging time durations) before testing. The tensile tests were performed at two different strain rates ($\dot{\varepsilon}$ = 0.01 and 0.001 sec^{-1}), while the creep tests were conducted under two different applied stresses (σ = 10 and 15 MPa).

It has been demonstrated that the higher cooling rate (water quenching) resulted in enhanced material properties for both SAC solder materials under the same testing condition. The water quenched samples have higher stiffness, better tensile and yield strength, as well as larger creep resistance than the analogous reflowed specimens. Although it is impossible to "water quench" real electronic packages, the water quenched data is still meaningful because it approaches the optimal case of extremely fine microstructure, and can serve as a guideline for design purposes. The effects of testing conditions (such as strain rate effect for tensile and effect of stress level for creep) were also presented in this chapter. The testing results in this study agreed with prior studies in the literature. Higher strain rates led to enhanced tensile performance for both SAC solder materials. Additionally, the steady state strain rate in creep has proven to be significantly sensitive to the applied stress level.

In general, it was found that neither the adoption of a different solidification cooling profile or the use of other testing conditions were able to reduce aging effects. In fact, the use of higher stress levels in creep tended to exacerbate the observed degradations due to aging.

8.6 Aging Induced Microstructure Evolution and Residual Stress Relaxation

The melting behavior and major phase reactions during solidification were studied by performing DSC analysis on all solders of interest. In addition, the aging effects on intrinsic responses of solder materials were investigated so that aging induced degradation of material properties can be fully understood. In summary, the study was conducted from the following three aspects:

(1) aging effects on phase coarsening;

(2) aging effects on grain/sub-grain structure;

(3) aging effects on internal residual stress.

Firstly, it has been demonstrated that the microstructure evolves with aging for all solder alloys in this study. In more details, both primary phase (β-Sn matrix) and secondary phase (IMCs) grow in size as aging progresses. There exist two types of IMCs in standard SAC alloys, i.e. needle-shaped Ag_3Sn and scallop-shaped Cu_6Sn_5. The dispersing, coalescing and coarsening of the both types of IMCs with aging were observed. In addition, it is also found that aging temperature appears to have a more significant effect on the microstructure evolution of lead free SAC solders. It is believed that the coarsened IMC particles cannot effectively block the movement of dislocations and thus caused the reduction in material properties.

Secondly, the grain structure of SAC solders was examined by optical microscope with cross-polarizer. Large grains can be seen even in the as-quenched SAC alloys, but the growth of the grains was not obvious. In contrast, aging effects were found to have a strong impact on the sub-grain growth of SAC alloys. Correlating with Hall-Petch relationship, it is suggested that aging increases the sub-grain size of the solder, and thus results in the loss of yield strength.

Thirdly, the residual stresses introduced by fast cooling rate during solidification were also observed to change with aging. By utilizing 2D-XRD system, the residual stresses within grains were measured on the same SACX sample subject to different aging conditions. The result suggests the existence of large compressive stresses in the as-quenched solder sample, but the stresses gradually diminished with an increased aging time.

The effect of dopants on aging induced microstructure evolution was also examined by comparing the results to the "standard" solders in this study. It can be concluded that the aging resistance was improved for all doped solders, even though the enhancing mechanisms are different. In general, the reduction of aging effects can be realized by:

(1) refining β-Sn dendrites, i.e. Bi;

(2) mitigating the coalescence and coarsening of IMCs, i.e. Ni, Zn, Co;

(3) inhibiting grain/sub-grain growth.

REFERENCE

[1] Vianco, T. P., "Development of Alternatives to Lead-bearing Solders," Proceedings of the Technical Program on Surface Mount International, San Jose, CA, 1993.

[2] Reed-Hill, R. E., Physical Metallurgy Principles, PWS Publishing Company, pp. 306-307, 1994.

[3] Wood, E. P., Nimmo, K. L. "In Search of New Lead-free Electronic Solders," Journal of Electronic Materials, Vol. 23(8), pp. 709-713, 1994.

[4] Hwang, J. S., Implementing Lead-Free Electronics, McGraw-Hill, 2004.

[5] Turbini, L. J., Munie, G. C., Bernier, D., Gamalski, J., Bergman, D. W., "Examining the Environmental Impact of Lead-free Soldering Alternatives," IEEE Transactions on Electronics Packaging Manufacturing, Vol. 24, pp. 4-9, 2001.

[6] IPC Roadmap: A Guide for Assembly of Lead-Free Electronics, IPC, Northbrook, IL 2000.

[7] http://www.jeita.or.jp/english/press/2002/1217/attached.htm.

[8] Qian, Z., Abhijit, D., Peter, H., "Creep and High-temperature Isothermal Fatigue of Pb-free Solders", Proc. IPACK, International Electronic Packaging Technical Conference, 2003.

[9] Lee, N. C., "Getting Ready for Lead Free Solders," Indium Corporate America, Utica, NY, USA.

[10] Abtew, M., Selvaduray, G., "Lead-free Solders in Microelectronics," Materials Science and Engineering Reports, Vol. 27, pp. 95-141, 2000.

[11] http://www.ameslab.gov/files/LeadFreeSolder_Foundation.pdf

[12] Furusawa, A., Suetsugu, K., Yamaguchi, A., Taketomo, H., "Thermoset Pb-Free Solder Using Heat-Resistant Sn-Ag Paste," National Technical Report, 1997.

[13] McCormack, M., Jin, S., "Improved Mechanical Properties in New, Pb-Free Solder Alloys," Journal of Electronic Materials, Vol. 23, pp. 715-720, 1994.

[14] McCormack, M., Jin, S., Kammlott, G. W., Chen, H. S., "New Pb-Free Solder Alloy with Superior Mechanical Properties," Applied Physics Letters, Vol. 63(1), pp. 15-17, 1993.

[15] http://www.farnell.com/datasheets/315929.pdf

[16] Liu, P. L., Shang, J. K., "Interfacial Embrittlement by Bismuth Segregation in Copper/Tin–Bismuth Pb-free Solder Interconnect", Journal of Materials Research, Vol. 16, pp 1651-1659, 2001.

[17] Habassis, H., Rutter, J. W., Winegard, W. C., "Phase Relationships in Bi-In-Sn Alloy Systems," Materials Science and Technology, Vol. 2, pp. 985-988, 1986.

[18] Nimmo, K., "Alloy Selection," Chapter 3 of Lead-free Soldering in Electronics: Science, Technology and Environmental Impact, edited by K. Suganuma, New York, Marcel Dekker, pp. 61-62, 2004.

[19] Loomans, M. E., Fine, M. E., "Tin-Silver-Copper Eutectic Temperature and Composition," Metallurgical and Materials Transactions A, Vol. 31(A), pp. 1155-1162, 2000.

[20] Moon, K. W., Boettinger, W. J., Kattner, U. R., Biancaniello, F. S., Handwerker, C. A., "Experimental and Thermodynamic Assessment of Sn-Ag-Cu Solder Alloys," Journal of Electronic Materials, Vol. 29, pp. 1122-1136, 2000.

[21] Zhu, Q. S., Zhang L., Wang Z. G., Wu S. D., Shang J. K., "Effect of Intermetallics Ag_3Sn on the Tensile Property of Sn3.8Ag0.7Cu Solder Alloy", Acta Metallurgica Sinica, Vol. 43(1), pp. 41-46, 2007.

[22] Ganesan, S., Pecht, M., Lead-free Electronics, Wiley-Interscience Publication, pp. 51-52, 2006.

[23] Nogita K., "Stabilisation of Cu_6Sn_5 by Ni in Sn-0.7Cu-0.05Ni lead-free solder alloys", Intermetallics, Vol. 18(1), pp. 145-149, 2010

[24] Che, F. X., Luan, J. E., Baraton, X., "Effect of Silver Content and Nickel Dopant on Mechanical Properties of Sn-Ag-Based Solders," Proceedings of the 58th Electronic Components and Technology Conference, pp. 485-490, 2008.

[25] Guo, F., Lee, J., Choi, S., Lucas, J., Bieler, T., Subramanian, K., "Processing and Aging Characteristics of Eutectic Sn-3.5Ag Solder Reinforced with Mechanically Incorporated Ni Particles," Journal of Electronic Materials, Vol. 30, pp. 1073-1082, 2001.

[26] Chen, Z. G., Shi, Y. W.; Xia, Z. D.; Yan, Y. F., "Study on the Microstructure of a Novel Lead-Free Solder Alloy Sn-Ag-Cu-RE and Its Soldered Joints", Journal of Electronic Materials, Vol. 31(10), pp. 1122-1128, 2002.

[27] Law, C. M. T., Wu, C. M. L. "Microstructure Evolution and Shear Strength of Sn-3.5Ag-RE Lead-free BGA Solder Balls," Proceedings of the Sixth High Density Microsystem Design and Packaging and Component Failure Analysis Conference, pp. 60-65, 2004.

[28] Dudek, M. A., Sidhu, R. S., and Chawla, N., "Novel Rare-Earth-Containing Lead-Free Solders with Enhanced Ductility," Journal of the Minerals, Metals and Materials Society, pp. 57-63, 2006.

[29] Pei M., Qu J. M., "Effect of Rare Earth Elements on Lead-Free Solder Microstructure Evolution", Proceedings of the 57th Electronic Components and Technology Conference, pp. 198-204, 2007.

[30] Pirondi, A., "Mechanical Failure in Microelectronic Packaging," Vol. IGF 13, Convegno IGF XIII Cassino, 1997.

[31] Hertzberg, R. W., Deformation and Fracture Mechanics of Engineering Materials, John Wiley & Sons Inc, 4th edition, 1996.

[32] Thornton, P. A., Colangelo V. J., Fundamentals of Engineering Materials, Prentice-Hall, Inc., pp. 227-229, 1985.

[33] Vianco P. T., "Fatigue and Creep of Lead-free Solder Alloys: Fundamental Properties," Chapter 3 of Lead-free Solder Interconnect Reliability, Edited by D. Shangguan, ASM International, pp. 67-106, 2006.

[34] Wiese, S., Schubert, A., Walter, H., Dudek, R., Feustel, F., Meusel, E., Michel, B., "Constitutive Behavior of Lead-free Solders vs. Lead-containing Solders - Experiments on Bulk Specimens and Flip-Chip Joints," Proceeding of the 51st Electronic Components and Technology Conference, pp. 890-902, 2001.

[35] McCabe, R. J., Fine, M. E., "Athermal and Thermally Activated Plastic Flow in Low Melting Temperature Solders at Small Stresses," Scripta Materialia, Vol. 39(2), pp. 189-195, 1998.

[36] Lau, J. H., Pao, Y. H., Solder Joints Reliability of BGA, CSP, Flip-Chip, and Fine Pitch SMT Assemblies, McGraw-Hill, 1997.

[37] Shi, X.Q., Wang, Z. P., Yang, J. Q., Pang, H. L. J., "Creep Behavior and Deformation Mechanism Map of Sn-Pb Eutectic Solder Alloy", Journal of Engineering and Material Technology. Vol. 125(1), pp. 81-89, 2003

[38] Evans, R. W., Wilshire, B., Creep of Metals and Alloys, the Institute of Metals, 1985.

[39] Weertman, J., "Steady-State Creep through Dislocation Climb," Journal of Applied Physics, Vol. 28, pp. 362-366, 1957.

[40] Herring, C., "Diffusional Viscosity of a Polycrystalline Solid," Journal of Applied Physics, Vol.21, pp. 437-445, 1950.

[41] Engelmaier, W., "Surface Mount Solder Joint Reliability: Issues, Design, Testing, Prediction," Workshop Notes, Engelmaier Associates, Inc., Mendham, NJ, 1995.

[42] Miner, M. A., "Cumulative Damage in Fatigue," Journal of Applied Mechanics, Vol. 12(3), pp. 159-164, 1954.

[43] Kilinski, T. J., Lesniak, J. R., Sandor, B. I., "Modern Approaches to Fatigue Life Prediction of SMT Solder Joints," Solder Joint Reliability Theory and Applications, Edited by J. H. Lau, Chapter 13, Van Nostrand Reinhold, 1991.

[44] Ma, H. T., Suhling, J. C., "A review of mechanical properties of lead-free solders for electronic packaging", Journal of Materials Science, Vol. 44(5), pp. 1141-1158, 2009.

[45] Medvedev, A. S., "Aging of Tin-Lead Solders and Joints Soldered by Them," Metallovedenie i Obrabotka Metallov, No. 7, pp. 16-23, 1956.

[46] Lampe, B. T. "Room Temperature Aging Properties of Some Solder Alloys," Welding Journal, Vol. 55(10), pp. 330-340, 1976.

[47] Ding, Y., Wang, C. Q., Tian, Y. H., Li, M. Y., "Influence of Ageing Treatment on Deformation Behavior of 96.5Sn3.5Ag Lead Free Solder Alloy During In Situ Tensile Tests," Journal of Alloys and Compounds, Vol. 428, pp. 274–285, 2007.

[48] Xiao, Q., Bailey, H. J, Armstrong, W. D., "Aging Effects on Microstructure and Tensile Property of Sn3.9Ag0.6Cu Solder Alloy," Journal of Electronic Packaging, Vol. 126(2), pp. 208-212, 2004.

[49] Ma, H., Suhling, J. C., Zhang, Y., Lall, P., Bozack, M. J. "The Influence of Elevated Temperature Aging on Reliability of Lead Free Solder Joints," Proceedings of the 57th Electronic Components and Technology Conference, pp. 653-668, 2007.

[50] Zhang, Y. F., Cai, Z. J., Suhling, J. C., Lall, P., Bozack, M. J., "The Effects of SAC Alloy Composition on Aging Resistance and Reliability," Proceedings of the 59th Electronic Components and Technology Conference, pp. 370-389, 2009.

[51] Chen, W. M., McCloskey, P., O'Mathuna, S. C., "Isothermal Aging Effects on the Microstructure And Solder Bump Shear Strength of Eutectic Sn37Pb And Sn3.5Ag Solders," Microelectronics Reliability, Vol. 46(5-6), pp. 896-904, 2006.

[52] Kim, K. S., Yu, C. H., Yang, J. M., "Aging Treatment Characteristics of Solder Bump Joint for High Reliability Optical Module," Thin Solid Films, Vol. 462-463, pp. 402-407, 2004.

[53] Anderson, I. E., Harringa, J. L., "Elevated Temperature Aging of Solder Joints Based on Sn-Ag-Cu: Effects on Joint Microstructure and Shear Strength," Journal of Electronic Materials, Vol. 33(12), pp. 1485-1496, 2004.

[54] Xiao, Q., Nguyen, L., Armstrong, W. D., "Aging and Creep Behavior of Sn3.9Ag0.6Cu Solder Alloy," Proceedings of the 54th Electronic Components and Technology Conference, pp. 1325-1332, 2004.

[55] Mysore, K., Chan, D., Bhate, D., Subbarayan, G., Dutta, I., Gupta, V., Zhao, J. H., Edwards, D. R., "Aging-Informed Behavior of Sn3.8Ag0.7Cu Solder Alloys," Thermal and Thermomechanical Phenomena in Electronic Systems, ITHERM, pp.870-875, 2008.

[56] Chavali, S., Singh, Y., Kumar, P., Subbarayan, G., Dutta, I., Edwards, D. R., "Aging Aware Constitutive Models for SnAgCu Solder Alloys," Proceedings of the 61st Electronic Components and Technology Conference, pp.701-705, 2011.

[57] Bansal, A., Lee, T. K., Liu, K. C., Xue, J., "Effects of Isothermal Aging and In-Situ Current Stress on The Reliability of Lead-Free Solder Joints," Proceedings of the 60th Electronic Components and Technology Conference, pp.1529-1535, 2010.

[58] Venkatadri, V., Liang, Y., Yan, X., Cotts, E., Srihari, K., Borgesen, P., "Accelerating The Effects of Aging on The Reliability of Lead Free Solder Joints in A Quantitative Fashion," Proceedings of the 59th Electronic Components and Technology Conference, pp.398-405, 2009.

[59] Mustafa, M., Cai, Z. J., Suhling, J. C., Lall, P., "The Effects of Aging on The cyclic Stress-Strain Behavior And Hysteresis Loop Evolution of Lead Free Solders," Proceedings of the 61th Electronic Components and Technology Conference, pp.927-939, 2011.

[60] Allen, S. L., Notis, M. R., Chromik, R. R., Vinci, R. P., "Microstructural Evolution in Lead-Free Solder Alloys: Part I Cast Sn–Ag–Cu Eutectic," Journal of Material Research, Vol. 19(5), 2004.

[61] Fix, A. R., Nüchter, W., Wilde, J., "Microstructural Changes of Lead-Free Solder Joints during Long-Term Ageing, Thermal Cycling and Vibration Fatigue", Soldering & Surface Mount Technology, Vol. 20(1), pp.13-21, 2008.

[62] Yao, P., Liu, P., Liu, J., "Interfacial Reaction and Shear Strength of SnAgCu–xNi/Ni Solder Joints during Aging at 150 ℃," Microelectronic Engineering, Vol. 86(10), pp. 1969-1974, 2009.

[63] Tu, P. L., Chan, Y. C., Hung, K. C., Lai, J. K. L., "Growth Kinetics of Intermetallic Compounds in Chip Scale Package Solder Joint," Scripta Material, Vol. 44, pp. 317-323, 2001.

[64] Vianco, P. T., Hlava, P. F., Kilgo, A.C., "Intermetallic Compound Layer Formation between Copper and Hot-Dipped 100In, 50In–50Sn, 100Sn and 63Sn37Pb Coatings," Journal of Electronic Materials, Vol. 23(7), pp. 583-594, 1994.

[65] Lee, Y. G., Duh, J. G., "Interfacial Morphology and Concentration Profile in The Unleaded Solder/Cu Joint Assembly," Journal of Materials Science, Vol. 10(1), pp. 33-43, 1999.

[66] Yoon, J. W., Lee, Y. H., Kim, D. G., Kang, H. B., Suh, S. J., Yang, C. W., Lee, C. B., Jung, J. M., Yoo, C. S., Jung, S. B., "Intermetallic Compound Layer Growth at The Interface Between Sn–Cu–Ni Solder and Cu Substrate," Journal of Alloys and Compounds, Vol. 381, pp. 151-157, 2003.

[67] Vianco, P. T., Kilgo, A. C., Grant, R., "Intermetallic Compound Layer Growth by Solid State Reactions between 58Bi-42Sn Solder And Copper," Journal of Electronic Materials, Vol. 24(10), pp. 1493-1505, 1995.

[68] Vianco, P. T., Rejent, J. A., "Properties of Ternary Sn-Ag-Bi Solder Alloys: Part I—Thermal Properties and Microstructural Analysis," Journal of Electronic Materials, Vol. 28(10), pp. 1127-1137, 1999.

[69] Yoon, J. W., Lee, C. B., Jung, S. B., "Growth of an Intermetallic Compound Layer with Sn-3.5Ag-5Bi on Cu and Ni-P/Cu during Aging Treatment," Journal of Electronic Materials, Vol. 32(11), 2003.

[70] Lee, C. B., Suh, S. J., Shin, Y. E., Shur, C. C., Jung, S. B., "The Growth Kinetics of Inter-metallic Compound Layer at the Interface between Sn–3.5Ag Base Solder and (Cu, Electroless Ni-P/Cu, Immersion Au/Ni-P/Cu) Substrate," Proceeding of 8th Symposium on Microjoining and Assembly Technology in Electronics, pp. 351–356, 2002.

[71] Choi, S., Bieler, T. R., Lucas, J. P., Subramanian, K. N., "Characterization of The Gowth of Intermetallic Interfacial Layers of Sn-Ag and Sn-Pb Eutectic Solders and Their Composite Solders on Cu Substrate during Isothermal Long-Term Aging," Journal of Electronic Materials, Vol. 28(11), pp. 1209-1215, 1999.

[72] Vianco, P. T., Erickson, K. L., Hopkins, P. L., "Solid State Intermetallic Compound Growth between Copper and High Temperature, Tin-Rich Solders-Part I: Experimental Analysis," Journal of Electronic Materials, Vol. 23(8), pp. 721-727, 1994.

[73] Yoon, J. W., Lee, C. B., Kim, D. U., Jung, S. B., "Reaction Diffusions of Cu_6Sn_5 And Cu_3Sn Intermetallic Compound in The Couple of Sn-3.5Ag Eutectic Solder And Copper Substrate," Metals and Materials International, Vol. 9(2), pp. 193-199, 2003.

[74] Xu, L. H., Pang, J. H. L., Prakash, K. H., Low, T. H., "Isothermal and Thermal Cycling Aging on IMC Growth Rate in Lead-Free and Lead-Based Solder Interface," IEEE Transactions on Components and Packaging Technologies, Vol. 28(3), pp. 408-414, 2005.

[75] Zeng, K. J., Stierman, R., Chiu, T. C., Edwards, D., Ano, K., Tu, K. N., "Kirkendall Void Formation in Eutectic SnPb Solder Joints on Bare Cu And Its Effect on Joint Reliability," Journal of Applied Physics, Vol. 97(2), 2004.

[76] Telang, A. U., Bieler, T. R., Lucas, J. P., Subramanian, K. N., Lehman, L. P., Cotts, E. J., "Grain-Boundary Character and Grain Growth in Bulk Tin and Bulk Lead-Free Solder Alloys," Journal of Electronic Materials, Vol. 33(12), pp. 1412-1423, 2004.

[77] Hu, Q., Lee, Z. S., Zhao, Z. I., Lee, D. L., "Study of Cooling Rate on Lead-Free Soldering Microstructure of Sn-3.0Ag-0.5Cu Solder," Proceedings of International Conference on Asian Green Electronics, pp. 156-160, 2005.

[78] Jeong, S. W., Kim, J. H., Lee, H. M., "Effect of Cooling Rate on Growth of the Intermetallic Compound and Fracture Mode of Near-Eutectic Sn-Ag-Cu/Cu Pad: Before and After Aging," Journal of Electronic Materials, Vol. 33(12), pp. 1530-1544, 2004.

[79] Liang, J., Dariavach, N., Shangguan, D., "Solidification Condition Effects on Microstructures and Creep Resistance of Sn-3.8Ag-0.7Cu Lead-Free Solder," Metallurgical and Materials Transactions A, Vol. 38(7), pp. 1530-1538, 2007.

[80] Anand, L., "Constitutive Equations for the Rate-Dependent Deformation of Metals at Elevated Temperatures," Journal of Engineering Materials and Technology, Vol. 104, pp. 12-17, 1982.

[81] Pang, J. H. L., Xiong, B. S., Che, F. X., "Modeling Stress Strain Curves For Lead-Free 95.5Sn-3.8Ag-0.7Cu Solder," Proceedings of the 5th EuroSimE Conference, pp. 449-453, 2004.

[82] Nie, X., Bhate, D., Chan, D., Chen, W., Subbarayan, G., Dutta, I., "Rate-Dependent Behavior of Sn3.8Ag0.7Cu Solder over Strain Rates of 10^{-6} to 10^{2} s^{-1}," Thermal and Thermomechanical Phenomena in Electronic Systems, pp. 676-682, 2008.

[83] Huang, M. L., Wang, L., "Effects of Cu, Bi and In on Microstructure and Tensile Properties of SnAg-X (Cu, Bi, In) Solders," Metallurgical and Materials Transactions A, Vol. 36(6), pp. l439-1446, 2005.

[84] Liu, P. L., Shang, J. K., "Interfacial Segregation of Bismuth in Cu/Sn-Bi Solder Interconnect," Scripta Meterialia, Vol. 44(7), pp. 1019-1023, 2001.

[85] Pandher, R. S., Lewis, B. G., Vangaveti, R., Singh, B., "Drop Shock Reliability of Lead-Free Alloys - Effect of Micro-Additives," Proceedings of the 57th Electronic Components and Technology Conference, pp. 669-676, 2007.

[86] Tateyama, K., Ubukata, H., Yamaoka, Y., Takahashi, K., Yamada, H., Saito, M., "Effects of Bi Content on Mechanical Properties and Bump Interconnection Reliability on Sn-Ag Solder Alloys," International Journal of Microcurcuits and Electronic Packaging, Vol. 23(1), pp. 131-137, 2000.

[87] Tegehall, P.E., IVF Project Report (ELFNET), 2006.

[88] Song, J. M., Huang, C. F., Chuang, H. Y., "Microstructural characteristics and vibration fracture properties of Sn-Ag-Cu-TM (TM = Co, Ni, and Zn) alloys," Journal of Electronic Materials, Vol. 35(12), pp.2154-2163, 2006.

[89] Anderson, I., Walleser, J., Harringa, J., Labbs, F., Kracher, A., "Nucleation Control and Thermal Aging Resistance of Near-Eutectic Sn-Ag-Cu-X Solder Joints," Journal of Electronic Materials, Vol. 38(12), pp. 2770-2779, 2009.

[90] Kang, S. K., Leonard, D., Shih, D. Y., Gignac, L., Henderson, D. W., Cho, S., Yu, J., "Interfacial Reactions of Sn-Ag-Cu Solders Modified by Minor Zn Alloy Addition," Journal of Electronic Materials, Vol. 35(3), pp. 479-485, 2006.

[91] Anderson, I., Cook, B., Harringa, J., Terpstra, R., "Sn-Ag-Cu solders and solder joints: Alloy development, microstructure, and properties," Journal of the Minerals, Metals and Materials Society, Vol. 54(6), pp. 26-29, 2002.

[92] Syed, A., Kim, T. S., Cho, Y. M., Kim, C. W., Yoo, M., "Alloying Effect of Ni, Co, and Sb in SAC Solder for Improved Drop Performance of Chip Scale Packages with Cu OSP Pad Finish," Electronics Packaging Technology Conference, pp. 404-411, 2006.

[93] Wu, C. M. L., Wong, Y. W., "Rare-Earth Additions to Lead-Free Electronic Solders," Journal of Materials Science: Materials in Electronics, Vol. 18(1), pp. 77-91, 2007.

[94] Dudek, M. A., Sidhu, R. S., Chawla, N., "Novel Rare-Earth-Containing Lead-Free Solders with Enhanced Ductility," Journal of the Minerals, Metals and Materials Society, Vol. 58(6), pp. 57-62, 2006.

[95] Liu, W. P., Lee, C. N., "The Effects of Additives to SnAgCu Alloys on Microstructure and Drop Impact Reliability of Solder Joints," Journal of The Minerals, Metals and Materials Society, Vol. 59(7), pp. 26-31, 2007.

[96] Amagai, M., Toyoda, Y., Ohnishi, T., Akita, S., "High Drop Test Reliability: Lead-Free Solders," Proceedings of the 54th Electronic Components and Technology Conference, Vol. 2, pp. 1304-1309, 2004.

[97] Johnson, G. R., Cook, W. H., "A Constitutive Model and Data for Metals Subjected to Large Strains, High Strain Rates and High Temperatures," Proceedings of the Seventh International Symposium on Ballistic, The Hague, The Netherlands, pp. 541-547, 1983.

[98] Zerilli, F. J., Armstrong, R. W., "Dislocation-Mechanics-Based Constitutive Relations for Material Dynamics Calculations," Journal of Applied Physics, Vol. 61(5), pp. 1816-1825, 1987.

[99] Bodner, S. R., Partom Y., "Constitutive Equations for Elastic-Viscoplastic Strain-Hardening Materials," Journal of Applied Mechanics, pp. 385-389, 1975.

[100] Khan, A.S., Huang, S., "Experimental and Theoretical Study of Mechanical Behavior of 1100 Aluminum in the Strain Rate Range 10^{-5}-10^{4}," International Journal of Plasticity, Vol. 8, pp. 397-424, 1992.

[101] Anand, L., "Constitutive Equations for Hot Working of Metals," Journal of Plasticity, Vol. 1, pp. 213–231, 1985.

[102] Hsuan, T. C., Lin, K. L., "Effects of Aging Treatment of Mechanical Properties and Microstructure of Sn-8.5Zn-0.5Ag-0.01Al-0.1Ga Solder," Materials Science and Engineering, A, Vol. 456, pp. 202-209, 2007.

[103] Chuang, C. M., Liu, T. S., Chen, L. H., "Effect of Aluminum Addition on Tensile Properties of Naturally Aged Sn-9Zn Eutectic Solder," Journal of Materials Science, Vol. 37(1), pp. 191-195, 2002.

[104] Ding, Y., Wang, C., Tian, Y., and Li, M., "Influence of Aging on Deformation Behavior of 96.5Sn3.5Ag Lead Free Solder Alloy During In Situ Tensile Tests," Journal of Alloys and Compounds, Vo. 428, pp. 274-285, 2007.

[105] Pang, J. H. L., Low, T. H., Xiong, B. S., Xu, L., and Neo, C. C.., "Thermal cycling aging effects on Sn–Ag–Cu solder joint microstructure, IMC and strength," Thin Solid Films, Vol. 462-463, pp. 370-375, 2004.

[106] Darveaux, R., "Shear Deformation of Lead Free Solder Joints," Proceedings of the 55th Electronic Components and Technology Conference, pp. 882-893, 2005.

[107] Wiese, S., Wolter, K. J., "Creep of Thermally Aged SnAgCu Solder Joints," Microelectronics Reliability, Vol. 47, pp. 223-232, 2007.

[108] Dutta, I., Pan, D., Marks, R. A., Jadhav, S. G., "Effect of Thermo-mechanically Induced Microstructural Coarsening on the Evolution of Creep Response of SnAg-based Microelectronic Solders," Materials Science and Engineering A, Vol. 410-411, pp. 48-52, 2005.

[109] Cai, Z. J., Zhang, Y. F., Suhling, J. C., Lall, P., Johnson, R. W, Bozack, M. J., "Reduction of Lead Free Solder Aging Effects Using Doped SAC Alloys,"

Proceedings of the 60th Electronic Components and Technology Conference, pp.1493-1511, 2010.

[110] Zhang, Y. F., Cai, Z. J., Suhling, J. C., Lall, P., Bozack, M. J., "The Effects of Aging Temperature on SAC Solder Joint Material Behavior and Reliability," Proceedings of the 58th Electronic Components and Technology Conference, pp.99-112, 2008.

[111] Darveaux, R., Banerji, K., "Fatigue Analysis of Flip Chip Assemblies Using Thermal Stress Simulations and A Coffin-Manson Relation," Proceedings of the 41st Electronic Components and Technology Conference, pp. 797–805, 1991.

[112] Zhang, Y. F., "The Effects of Aging on the Mechanical Behavior of Lead Free and Mixed Formulation Solder Alloys," Ph.D. Dissertation, Auburn University, 2010.

[113] Kim, K. S., Huh, S. H., Suganuma, K., "Effects of Intermetallic Compounds on Properties of Sn-Ag-Cu Lead-Free Soldered Joints," Journal of Alloy and Compounds, Vol. 352(1-2), pp. 226-236, 2003.

[114] Miyazawa, Y., Ariga, T., "Microstructural Change and Hardness of Lead Free Solder Alloys," Proceedings of the 1st International Symposium on Environmentally Conscious Design and Inverse Manufacturing, pp. 616-619, 1999.

[115] Miyazawa, Y., Ariga T., "Influences of Aging Treatment on Microstructure and Hardness of Sn-(Ag, Bi, Zn) Eutectic Solder Alloys," Materials Transactions of the Japan Institute of Metals, Vol. 42(5), pp. 776-782, 2001.

[116] Chilton, A. C., Whitmore, M. A., Hampshire, W. B., "Fatigue Failure in a Model SMD Joint," Soldering and Surface Mount Technology, Vol. 3, pp. 21-24, 1989.

[117] Gagliano, R. A., Fine, M. E., Vaynman, S., Stolkarts, V., "Shear Testing of Solder Joints: The Effect of Various Parameters on the Maximum Shear Stress of Eutectic Tin-Lead Solder," Advanced Materials for the 21st Century: Proceedings of the 1999 Julia R. Weertman Symposium, pp. 107-116, 1999.

[118] Coyle, R. J., Solan, P. P., Serafino, A. J., Gahr, S. A., "The Influence of Room Temperature Aging on Ball Shear Strength and Microstructure of Area Array Solder Balls," Proceedings of the 50th Electronic Components and Technology Conference, pp. 160-169, 2000.

[119] Tsui, Y. K. , Lee, S. W., Huang, X., "Experimental Investigation on the Degradation of BGA Solder Ball Shear Strength Due to Room Temperature Aging," Proceedings of the 4th International Symposium on Electronic Materials and Packaging, pp. 478-481, 2002.

[120] Lee, S. W., Tsui, Y. K., Huang, X., Yan, C. C., "Effects of Room Temperature Storage Time on the Shear Strength of PBGA Solder Balls," Proceedings of the 2002 ASME International Mechanical Engineering Congress and Exposition, pp. 1-4, 2002.

[121] Ma, H. T., Suhling, J. C., Lall P., Bozack, M. J., "Reliability of the Aging Lead-free Solder Joint," Proceedings of the 56th Electronic Components and Technology Conference, pp. 849-864, 2006.

[122] Kumar, K. S., Reinbold, L., Bower, A. F., Chason, E., "Plastic Deformation Processes in Cu/Sn Bimetallic Films," Journal of Material Research, Vol. 23(11), 2008.

[123] Yu, C., Liu, J., Lu, H., Li, P., Chen, J., "First-Principles Investigation of the Structural and Electronic Properties of $Cu_{6-x}Ni_xSn_5$ (x=0, 1, 2) Intermetallic Compounds," Intermetallics, Vol. 15(11), pp. 1471-1478, 2007.

[124] Lu, M. H., Shih, D. Y., Kang, S. K., Goldsmith, C., Flaitz, P., "Effect of Zn Doping on SnAg Solder Microstructure and Electromigration Stability," Journal of Applied Physics, Vol. 106(5), 2009.

[125] Kang, S., Shih, D. Y., Leonard, D., Henderson, D., Gosselin, T., Cho, S. I., Yu, J., Choi, W., "Controlling Ag_3Sn Plate Formation in Near-Ternary-Eutectic Sn-Ag-Cu Solder by Minor Zn Alloying," Journal of the Minerals, Metals and Materials Society, Vol. 56(6), pp. 34-38, 2004.

[126] Gao. F., Cheng, F. J., Nishikawa, H., Takemoto, T., "Characterization of Co-Sn intermetallic compounds in Sn-3.0Ag-0.5Cu-0.5Co lead-free solder alloy," Materials Letters, Vol. 62, pp. 2257-2259, 2008.

[127] Deng, X., Koopman, M., Chawla, N., Chawla, K., "Young's modulus of (Cu, Ag)–Sn intermetallics measured by nanoindentation," Materials Science and Engineering A, Vol. 364(1-2), pp. 240–243, 2004.

APPENDIX A

VALIDATION OF MODEL FOR AGING EFFECTS ON MECHANICAL PROPERTIES OF SAC SOLDERS BY USING ADAPTIVE NEYMAN TEST

A.1 Parametric Non-linear Regression and Residual Analysis

Variations of yield stress (YS) for SACN05 (N = 1, 2, 3, 4) solders were modeled as a function of aging by the following parametric nonlinear curve fitting procedure:

(1) Obtain σ_{ys} from each uniaxial tensile test from all aging conditions

(2) Perform a Least Square fit to the collected data by the proposed model (Eq. A.1, which is a more formal expression of Eq. 4.1 in statistics aspect)

$$YS = YS_{\infty} + (C_0 + C_1 e^{-\frac{Q}{RT}} t)^{-\frac{1}{2n}} + \varepsilon, \qquad \varepsilon \sim \left(0, \sigma^2\right) \tag{A.1}$$

Table A.1 lists the estimated constants for all SAC series solders and sum of square errors of the model. Residual analysis was also performed on each alloy, as shown in Figure A.1-A.4. According to the result of Shapiro-Wilk test at α = 0.05, the residuals of SAC305 and SAC405 were found to be normally distributed (0.12 and 0.12 respectively) while those of SAC105 and SAC205 were not (0.01 and 0.03 respectively).

	YS_{∞}	C_0	C_1	Q (kJ)	n	*SSE*
SAC105	11.62	1.50×10^{-4}	1.6×10^{12}	96.22	1.95	802.7479
SAC205	16.17	1.61×10^{-4}	6.9×10^{9}	83.42	1.76	758.2741
SAC305	16.83	1.70×10^{-4}	4.4×10^{7}	68.56	1.71	731.2150
SAC405	17.99	1.77×10^{-4}	2.9×10^{5}	55.07	1.67	707.7834

Table A.1 Constants of Model for Yield Stress vs. Aging for SACN05

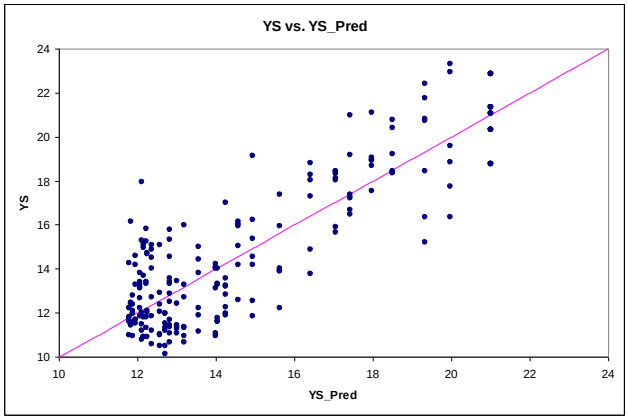

(a) YS vs. YS_Pred

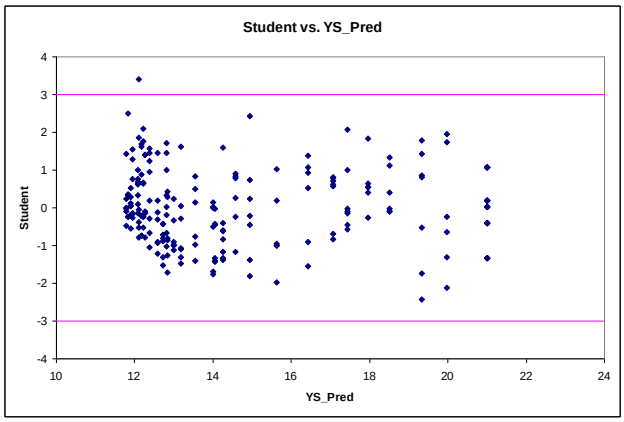

(b) Student Resid vs. YS_Pred

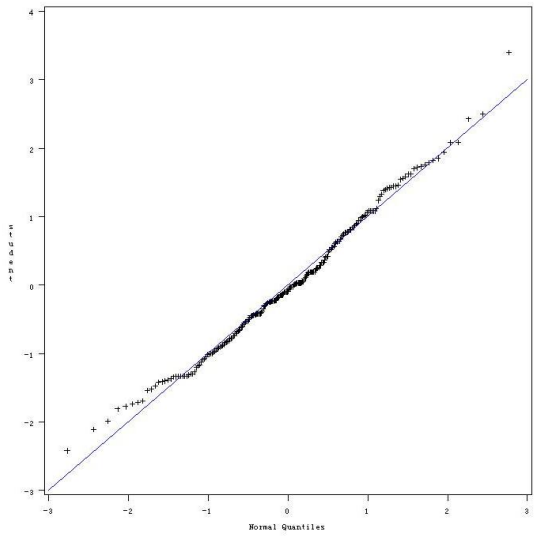

(c) Q-Q Plot

Figure A.1 Residual Analysis for Non-linear Regression (SAC105)

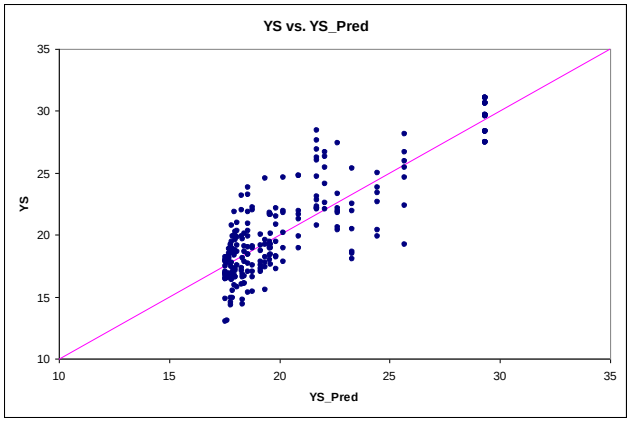

(a) YS vs. YS_Pred

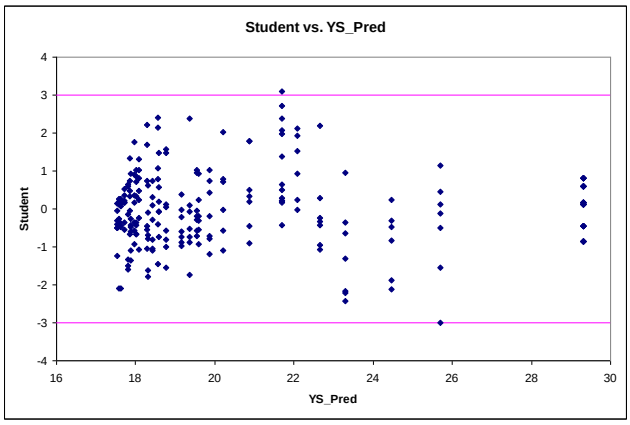

(b) Student Resid vs. YS_Pred

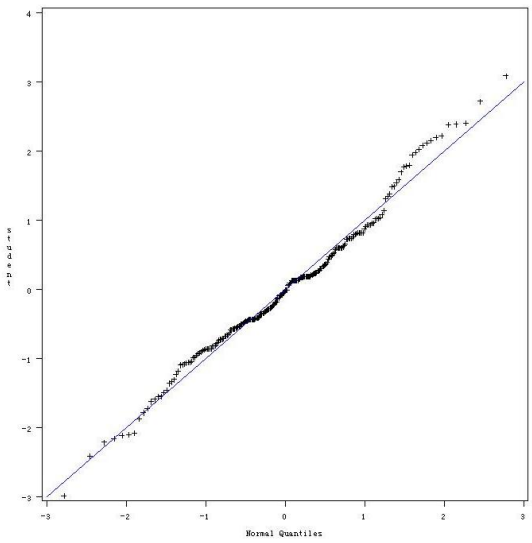

(c) Q-Q Plot

Figure A.2 Residual Analysis for Non-linear Regression (SAC205)

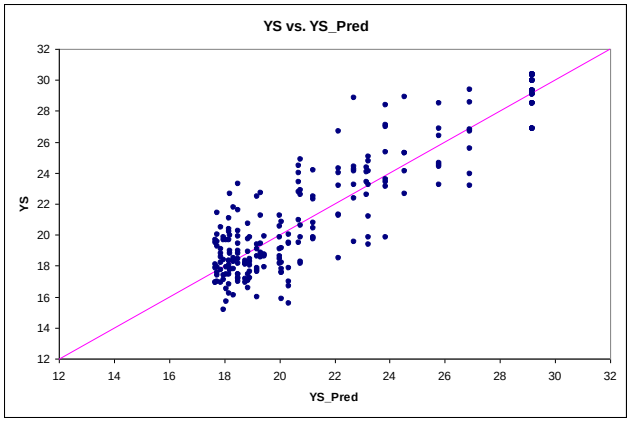

(a) YS vs. YS_Pred

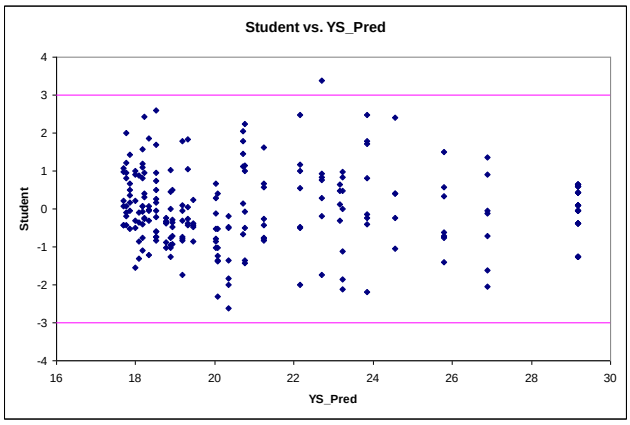

(b) Student Resid vs. YS_Pred

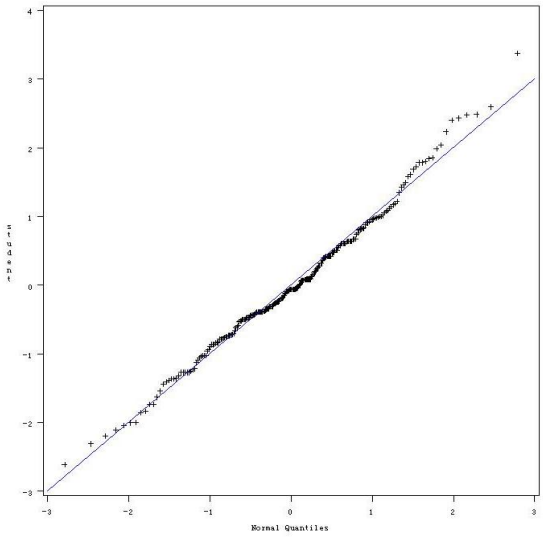

(c) Q-Q Plot

Figure A.3 Residual Analysis for Non-linear Regression (SAC305)

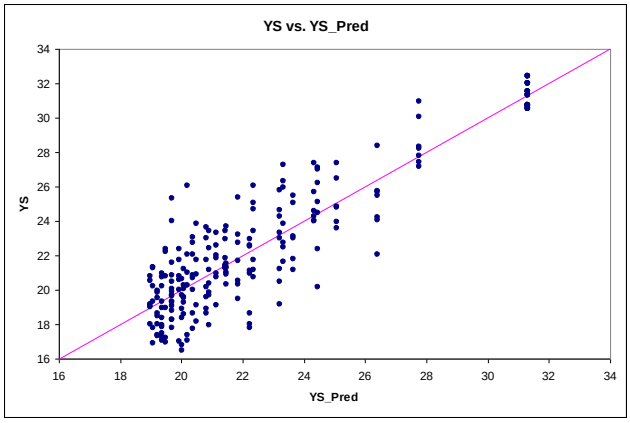

(a) YS vs. YS_Pred

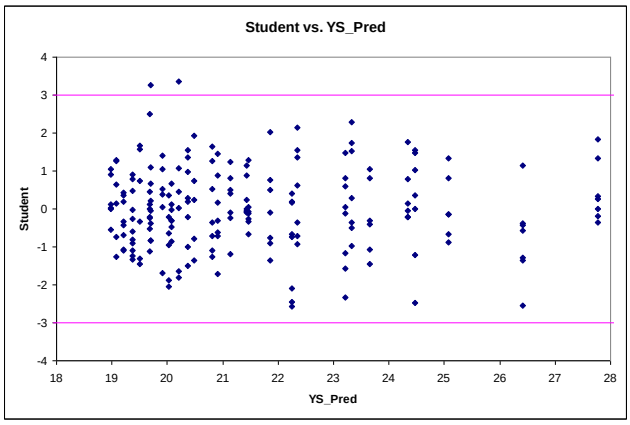

(b) Student Resid vs. YS_Pred

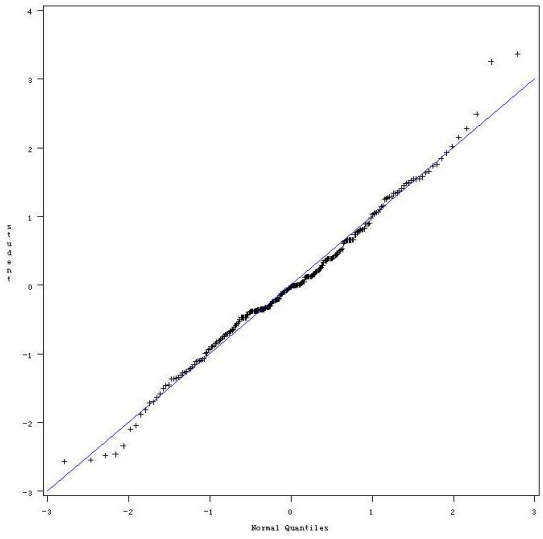

(c) Q-Q Plot

Figure A.4 Residual Analysis for Non-linear Regression (SAC405)

A.2 Adaptive Neyman Test and Thin Plate Spline Smoothing

The Adaptive Neyman test was also performed to test the goodness of fit of the nonlinear model. Similar to other test statistics, the basic idea of A-N test is that the residuals should be mostly zero bias if the proposed parametric model fits data adequately. As discussed by Fan and Huang [A1], let $(\boldsymbol{x}_1, Y_1),\ldots,(\boldsymbol{x}_n, Y_n)$ be independent observations from a population,

$$Y = m(x) + \varepsilon, \qquad \varepsilon \sim (0, \sigma^2) \tag{A.2}$$

where $\boldsymbol{x}$ is a p-dimensional vector and $m(\cdot)$ is a smooth regression surface. Let $f(\cdot, \theta)$ be a given parametric family. The null hypothesis and its corresponding saturated non-parametric alternative are:

$$\begin{aligned} H_0 &: m(\cdot) = f(\cdot, \theta) \qquad \text{for some } \theta \\ H_1 &: m(\cdot) \neq f(\cdot, \theta) \qquad \text{for all } \theta \end{aligned} \tag{A.3}$$

Meanwhile, let $\eta = (\eta_1,...,\eta_n)^T$, where $\eta_i = m(x_i) - f(x_i, \theta_0)$, the problem becomes

$$H_0 : \eta = 0 \text{ vs. } H_1 : \eta \neq 0 \tag{A.4}$$

which is based on the observation of residual vector. Then, the techniques for independent samples such as the adaptive Neyman test continue to apply [A2]. The resulting residual vector $\hat{\varepsilon}$ is estimated from a least squares fit and then, the discrete Fourier transformation (DFT) was applied to $\hat{\varepsilon}$. Therefore, the transformed residual vector $\hat{\varepsilon}^* = (\hat{\varepsilon}_1^*,..., \hat{\varepsilon}_n^*)^T$ can be calculated as:

$$\begin{aligned} \varepsilon_{2j-1}^* &= \sqrt{\frac{2}{n}} \sum_{i=1}^{n} \cos\left(\frac{2\pi ij}{n}\right) \hat{\varepsilon}_i, \\ \varepsilon_{2j}^* &= \sqrt{\frac{2}{n}} \sum_{i=1}^{n} \sin\left(\frac{2\pi ij}{n}\right) \hat{\varepsilon}_i, \qquad j = 1,...,[n/2] \end{aligned} \tag{A.5}$$

Note that an additional term $\varepsilon_n^* = \sqrt{\frac{2}{n}}\sum_{i=1}^{n}\widehat{\varepsilon}_i$ is needed if *n* is odd.

Meanwhile, the residuals are needed to be ordered before using the adaptive Neyman test because the A-N test statistics depend on the order of the residuals. A desired ordering should smoothen the sequence $\{m(x_i) - f(x_i,\theta_0)\}_{i=1}^{n}$ as good as possible for the given function *m*, and the large Fourier coefficients are focusing on low frequencies. As suggested by Fan [A1], one possible approach to ordering the residuals is to first assign a score s_i to the *i*th observation and then order the observations according to the rank of s_i. In this work, the problem is considered from the viewpoint of principal component (PC) analysis [A3]. Let ***S*** be the sample covariance matrix of the covariate vectors $\{x_i, i = 1,\ldots,n\}$. Then, the ordered eigenvalues $\lambda_1,\ldots,\lambda_p$ of **S** can be computed with corresponding eigenvectors $\xi_1,\ldots,\xi_p$. Denote $z_{i,k} = \xi_k^T x_i$ is the score for the *i*th observation on the *k*th sample PC, and λ_k to be the sample variance of $\{z_{1,k},...z_{n,k}\}$. Since $x_i - \bar{x} = z_{i,1}\xi_1 + z_{i,2}\xi_2$ (p=2 in this case), where $\bar{x}$ is the sample average, the sample score of variation may be obtained by:

$$s_i = \frac{1}{n-1}\sum_{k=1}^{2}\lambda_k z_{i,k}^2 \tag{A.6}$$

By ordering the transformed residual vector $\widehat{\varepsilon}^*$ according to S_i, the adaptive Neyman test statistic is defined as

$$T_{AN,1}^* = \max_{1\le m\le n}\frac{1}{\sqrt{2m\widehat{\sigma}_1^4}}\sum_{i=1}^{m}\left(\widehat{\varepsilon}_i^{*2} - \hat{\sigma}_1^2\right), \tag{A.7}$$

$$T_{AN,2}^* = \max_{1\le m\le n}\frac{1}{\sqrt{m\widehat{\sigma}_2^2}}\sum_{i=1}^{m}\left(\widehat{\varepsilon}_i^{*2} - \hat{\sigma}_1^2\right), \tag{A.8}$$

where $\hat{\sigma}_1^2 = \frac{1}{n-I_n}\sum_{i=I_n+1}^{n}\widehat{\varepsilon}_i^{*2} - \left\{\frac{1}{n-I_n}\sum_{i=I_n+1}^{n}\widehat{\varepsilon}_i^{*}\right\}^2$ and $\hat{\sigma}_2^2 = \frac{1}{n-I_n}\sum_{i=I_n+1}^{n}\widehat{\varepsilon}_i^{*4} - \left\{\frac{1}{n-I_n}\sum_{i=I_n+1}^{n}\widehat{\varepsilon}_i^{*2}\right\}^2$.

According to Fan's article [A1], I_n is given by [n/4]. The null hypothesis will be rejected when $T_{AN,i}^{*}$ is large. Note that $T_{AN,1}$ is good if the noise is normally distributed while $T_{AN,2}$ will be more robust against the normality assumption. Additionally, the test statistics may also be normalized as:

$$T_{AN,j} = \sqrt{2\log\log n}\,T_{AN,j}^{*} - \left\{2\log\log n + 0.5\log\log\log n - 0.5\log(4\pi)\right\}$$

for j = 1,2. (A.9)

Table A.2 tabulated the calculated adaptive Neyman test statistics. According to Fan [A4], the critical value of A-N test is 3.89 at a confidence level of $\alpha = 0.05$ for sample size near 200. Therefore, the nulls failed to be rejected for all models.

On the other hand, a nonparametric regression was also performed to validate the proposed nonlinear model. In this study, thin-plate (TP) spline smoothing technique was used to interpolate the behavior of the sample and the results were compared to the proposed model, as shown in Figure A.5.

	$T_{AN,1}$	$T_{AN,2}$
SAC105	2.73	3.34
SAC205	2.68	2.38
SAC305	2.59	2.73
SAC405	-2.30	-2.28

Table A.2 – Adaptive Neyman Test Statistic Values for SACN05 Solders

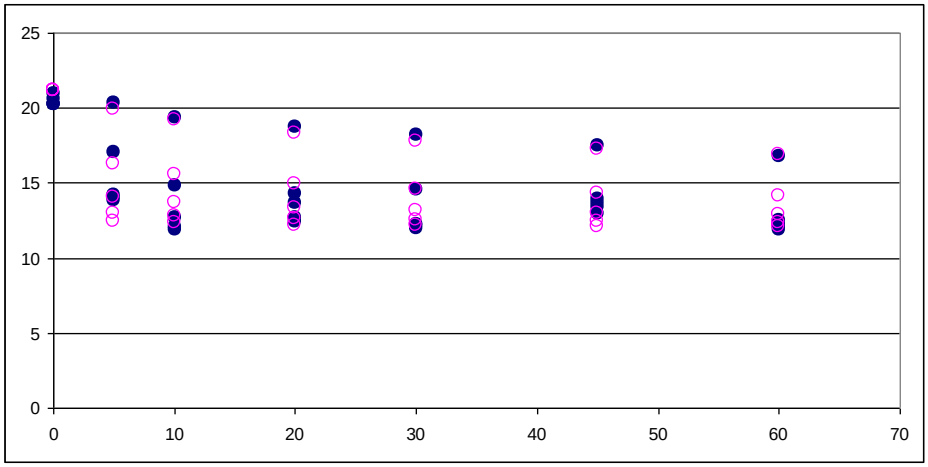

(a) SAC105

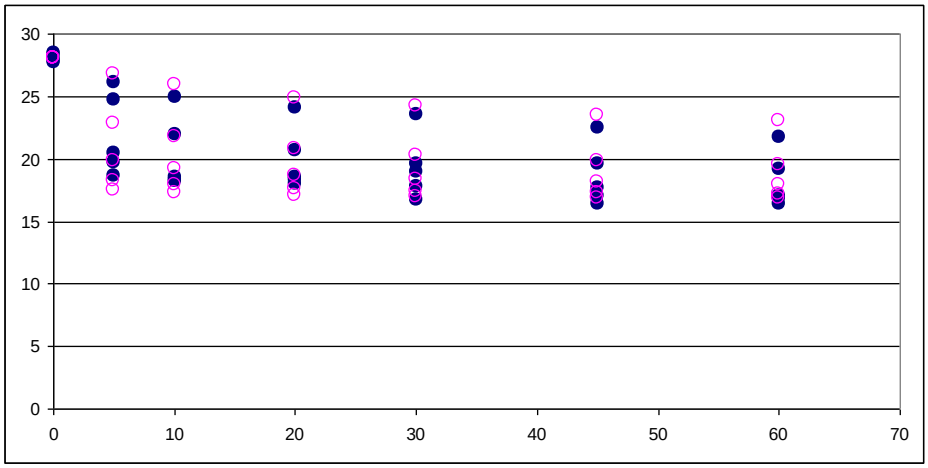

(b) SAC205

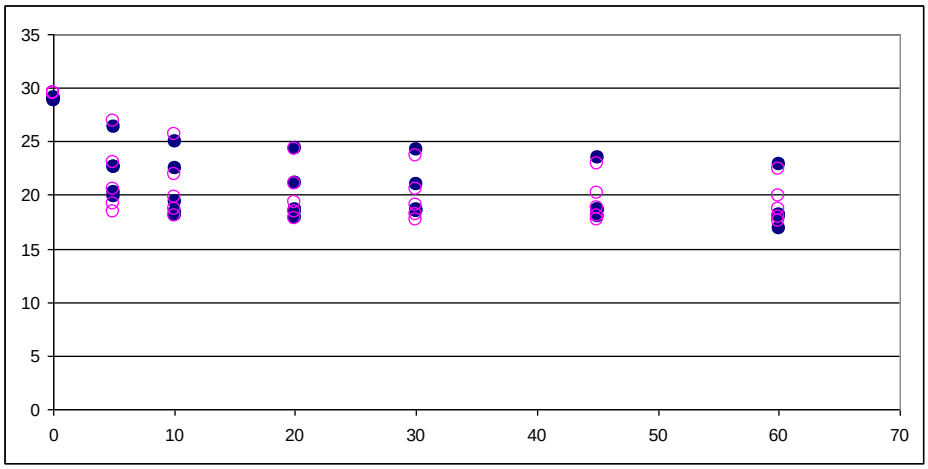

(c) SAC305

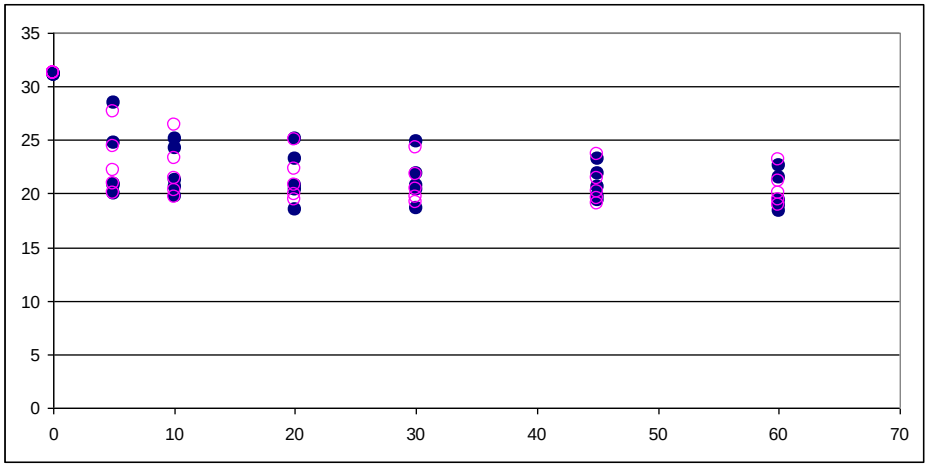

(d) SAC405

Figure A.5 – Thin Plate Spline versus Proposed Nonlinear Model
(Blue – TP Spline; Pink – Proposed Model)

A.3 Conclusions

A five-parameter nonlinear model was validated by Adaptive-Neyman (A-N) test. The experimental data is also compared by predictions from thin plate moving spline smoothing.

A.4 Reference

[A1] Fan, J., Huang, L., "Goodness-of-Fit Test for Parametric Regression Models," Journal of the American Statistical Association, Vol. 96, pp. 640-652, 2001.

[A2] Fan, J., "Test of Significance Based on Wavelet Thresholding and Neyman's Truncation," Journal of the American Statistical Association, Vol. 91, 674–688, 1998.

[A3] Jolliffe, I .T., Principal Component Analysis, New York: Springer-Verlag, 1986.

[A4] Fan, J., Lin, S. K., "Test of Significance When Data Are Curves," Journal of the American Statistical Association, Vol. 93, 1007–1021, 1996.

APPENDIX B

EMPIRICAL AGING MODELS AND CONSTANTS

B.1 Empirical Model and Constants for $\dot{\varepsilon}$ vs. Aging

Model: $\log \dot{\varepsilon} = C_0 + C_1 t + C_2 \left(1 - e^{-C_3 t}\right)$

Model Constants:

Constants / Temperature	C_0	C_1	C_2	C_3
25 ^{o}C	-14.93	0.38	1.92	3.23
50 ^{o}C	-14.93	0.37	3.40	5.02
75 ^{o}C	-14.93	0.35	4.29	4.64
100 ^{o}C	-14.93	0.34	4.55	4.68
125 ^{o}C	-14.93	0.33	4.89	5.32

Table B.1 SACX, R.F., Aged 0-6 Months

Constants / Temperature	C_0	C_1	C_2	C_3
SN100C	-9.81	3.32×10^{-3}	1.05	0.07
Sn-0.7Cu	-12.98	2.88×10^{-3}	2.91	0.53
SAC-Zn	-17.33	3.11×10^{-3}	1.81	0.24
SAC3595	-17.23	5.04×10^{-3}	3.06	0.58
SN96CI	-16.41	3.55×10^{-3}	2.92	0.25
SAC3810	-17.74	5.44×10^{-3}	3.25	0.21

Table B.2 Steady State Creep Rate, R.F., Aged at 100 ^{o}C for 0-6 Months

B.2 Empirical Model and Constants for Tensile Properties vs. Aging

Model: $y(E,UTS,YS) = C_0 + C_1 t + C_2\left(1 - e^{-C_3 t}\right)$

Model Constants:

Constants / Temperature	C_0	C_1	C_2	C_3
SN100C	26.49	3.30×10^{-3}	1.57	0.14
Sn-0.7Cu	24.95	2.27×10^{-3}	1.27	0.30
SAC-Zn	35.72	1.30×10^{-2}	4.82	0.29
SAC3595	34.94	1.35×10^{-2}	5.06	0.42
SN96CI	35.42	7.42×10^{-3}	7.16	0.31
SAC3810	38.95	1.44×10^{-2}	7.56	0.14

Table B.3 Elastic Modulus, R.F., Aged at 100 ^{o}C for 0-6 Months

Constants / Temperature	C_0	C_1	C_2	C_3
SN100C	21.49	2.03×10^{-3}	4.50	0.19
Sn-0.7Cu	25.08	1.58×10^{-2}	2.69	0.78
SAC-Zn	45.92	1.25×10^{-2}	12.62	0.20
SAC3595	42.95	1.27×10^{-2}	12.42	0.41
SN96CI	39.16	1.37×10^{-2}	8.33	0.58
SAC3810	47.82	1.77×10^{-2}	15.37	0.30

Table B.4 Ultimate Tensile Stress, R.F., Aged at 100 ^{o}C for 0-6 Months

Constants / Temperature	C_0	C_1	C_2	C_3
SN100C	17.25	9.83×10^{-4}	3.68	0.17
Sn-0.7Cu	18.63	8.71×10^{-3}	2.22	0.25
SAC-Zn	36.22	7.38×10^{-3}	10.08	0.41
SAC3595	32.21	7.66×10^{-3}	8.87	0.52
SN96CI	32.00	1.06×10^{-2}	8.68	0.75
SAC3810	35.11	1.14×10^{-2}	10.35	0.29

Table B.5 Yield Stress, R.F., Aged at 100 ^{o}C for 0-6 Months